



**ScuDo**  
Scuola di Dottorato - Doctoral School  
WHAT YOU ARE, TAKES YOU FAR



**UNIVERSITÀ  
DEGLI STUDI  
DI TORINO**

Doctoral Dissertation  
Doctoral Program in Urban and Regional Development  
XXXIII Cycle

# **Generation of a Land Cover Atlas of environmental critic zones using unconventional tools**

**Elena Belcore**

\*\*\*\*\*

## **Supervisors**

Prof. Marco Piras, Supervisor  
Prof. Alessandro Pezzoli, Co-Supervisor

## **Doctoral Examination Committee:**

Prof. Emanuele Lingua, Referee, Università degli Studi di Padova  
Dr. Frédéric Berger, Referee, Institut national de recherche en sciences et technologies pour l'environnement et l'agriculture  
Dr. Edyta Wozniak, Space Research Centre of Polish Academy of Sciences  
Prof. Fabio Giulio Tonolo, Referee, Politecnico di Torino  
Prof. Milan Kopal, Referee, University of Ljubljana

Politecnico di Torino  
April 2021

This thesis is licensed under a Creative Commons License, Attribution - Noncommercial - NoDerivative Works 4.0 International: see [www.creativecommons.org](http://www.creativecommons.org). The text may be reproduced for non-commercial purposes, provided that credit is given to the original author.

I hereby declare that, the contents and organisation of this dissertation constitute my own original work and does not compromise in any way the rights of third parties, including those relating to the security of personal data.

A handwritten signature in black ink that reads "Elena Belcore". The signature is written in a cursive style with a dotted line underneath it.

Elena Belcore  
Torino, April 2021

# Summary

During the last decades, the World's population witnessed an exponential intensification of Natural Hazards, such as floods, droughts, fires, and landslides, affecting urban and natural areas. Most of these phenomena have been attributed by the scientific community to the effects of climate change and the lack of environmental planning and management. In planning for natural risk reduction and prevention, monitoring the most vulnerable areas has become crucial for policymakers. Mainly, high-resolution analysis plays a pivotal role in forecasting natural hazards and in understanding resilience-related processes. Nevertheless, monitoring activities can be resources consuming and limited by extreme conditions. This is particularly true in those areas of the World characterized by a lack of infrastructures, peculiar land morphology, extreme climate conditions, and large-scale homogeneous land cover. In these critical areas, emerging technologies can be a powerful tool to monitor the processes taking place in areas affected – and potentially affected – by natural hazards and detecting Land Cover (LC). This research aims to propose a methodology for the multi-resolution, multi-temporal, and multi-thematic analysis of LC in the spotlight of natural hazards, providing a very high-resolution land cover Atlas of the areas of the World that are considered critical for the reasons mentioned above.

The atlas has a new level of detail to ensure meaningful information to data users. The maps are built upon the data collected through emerging technologies and analyzed through machine learning algorithms. The methodology is tested for two natural hazards: floods and rockfalls. The test areas are Tillabery in the sub-Saharan region of Niger and the subalpine regions of Alpine Arch.

# Acknowledgment

And I would like to acknowledge the ROCKTHEALPS and ANADIA 2.0 projects which supported the development of this research.

*I would like to dedicate  
this thesis to  
Professor Angela Calvo*

*Who first addressed me through research's  
bittersweet path.*

# I. Declaration of originality

I hereby declare that this Ph.D. thesis entitled "**Generation of a Land Cover Atlas of environmental critic zones using unconventional tools**" was carried out by me for the degree of Doctor of Philosophy in Urban and Regional Development under the guidance and supervision of Professor Dr. Marco Piras and Professor Dr. Alessandro Pezzoli, in the Politecnico di Torino, Italy. The interpretations put forth are based on my reading and understanding of the original texts, and they are not published anywhere in the form of books, monographs, or articles. The other books, articles, and websites I have used are acknowledged at the respective place in the text. For the present thesis, which I am submitting to the University, no degree or diploma or distinction has been conferred on me before, either in this or any other University.

# Contents

<b>I. Declaration of originality</b> .....	v
<b>II. List of Tables</b> .....	x
<b>III. List of Figures</b> .....	xvi
<b>IV. Acronyms</b> .....	xxiv
<b>1. Introduction</b> .....	<b>1</b>
1.1 Keywords.....	6
<b>2. Land Cover mapping and its role in environmental studies and regional planning</b> .....	<b>7</b>
2.1. Climate Change and planning against climatic risk: Sendai Framework .....	9
2.1.1. Land cover as a proxy of climate change and environment indicator .....	12
2.2. Criticalities of Land Cover monitoring.....	14
<b>3. Sensors and tools for Land Cover Generation</b> .....	<b>19</b>
3.1. Sensors for remote sensing .....	19
3.1.1. Optical sensors.....	20
3.1.2. Satellite .....	27
3.1.3. UAV .....	29
3.1.4. GNSS receivers .....	39
3.1.5. Some considerations about UAVs and satellite imagery .....	42
3.2. Tools for data elaboration: proprietary and FOSS software .....	43
<b>4. Classification of optical imagery, literature review</b> .....	<b>45</b>
4.1. Definition of classes.....	48
4.2. Pixel-based and object-oriented classifications .....	51
4.2.1. Single epoch and multi-temporal classification .....	54
4.3. Feature extraction and feature selection .....	55
4.3.1. Feature extraction .....	56

4.3.2.	Feature selection .....	63
4.4.	Type of classification algorithms.....	66
4.4.1.	Supervised and Unsupervised classifications .....	67
4.4.2.	Parametric and non-parametric classifiers.....	70
4.4.3.	Machine Learning classifiers for Land Cover .....	81
4.4.4.	Selection of the training samples for supervised classification	83
4.5.	Accuracy assessment methodologies and measures .....	86
4.5.1.	Error matrix and its derived measures.....	87
4.5.2.	Measures for the assessment of the segmentation process of object-based classifications .....	90
4.6.	Lesson learned .....	91
<b>5.</b>	<b>Pre-processing of images .....</b>	<b>93</b>
5.1.	Satellite optical imagery .....	94
5.1.1.	Geometric correction .....	95
5.1.2.	Absolute correction .....	96
5.1.3.	Absolute atmospheric correction.....	97
5.1.4.	Topographic correction .....	99
5.2.	UAV-derived imagery: SfM for orthophoto generation.....	103
<b>6.</b>	<b>Study areas and materials .....</b>	<b>112</b>
6.1.	Study area A, protection forests of Alpine arch: ROCKTHEALPS project .....	112
6.2.	Study area B, Sub-Saharan areas along Sirba River: ANADIA 2.0 project .....	115
6.3.	Tools and Hardware.....	119
6.3.1.	Hardware: UAV-mounted optical sensors.....	119
6.3.2.	Satellite sensors .....	129
6.4.	Tools for data processing.....	131
6.4.1.	Image processing and classification .....	132
6.4.2.	Structure from Motion.....	134
6.4.3.	GNSS post-processing Service.....	134
<b>7.</b>	<b>Case study A: Alpine Arch forest.....</b>	<b>135</b>
7.1.	UAV- ITD.....	135



7.1.1.	Class identification .....	136
7.1.2.	Data collection and pre-processing .....	140
7.1.3.	Methods .....	146
7.1.4.	Results .....	153
7.1.5.	Discussion.....	159
7.2.	Satellite .....	162
7.2.1.	Data collection and pre-processing .....	163
7.2.2.	Methods .....	180
7.2.3.	Results and discussion.....	183
<b>8.</b>	<b>Case study B: Sirba River in South-west Niger .....</b>	<b>192</b>
8.1.	Classification of UAV imagery for the identification of Temporary Surface Water Bodies (TSWB).....	193
8.1.1.	Data collection.....	195
8.1.2.	Data pre-processing.....	211
8.1.3.	Methods .....	213
8.1.4.	Accuracy assessment .....	216
8.1.5.	Results .....	217
8.1.6.	Discussion and conclusion .....	220
8.2.	Satellite .....	223
8.2.1.	Materials and methods.....	223
8.2.2.	Results .....	230
8.2.3.	Discussion and conclusions.....	234
8.3.	Land Cover using UAV imagery .....	235
8.3.1.	Classes identification.....	237
8.3.2.	Methods .....	238
8.3.3.	Results .....	244
8.3.4.	Discussion and conclusions.....	247
8.4.	Comparison to existing LC classifications .....	249
8.5.	Atlas applications in Disaster Risk Reduction planning.....	253
<b>9.</b>	<b>Conclusion and future vision .....</b>	<b>255</b>
<b>10.</b>	<b>PhD publications .....</b>	<b>283</b>
<b>11.</b>	<b>Appendix A.....</b>	<b>284</b>
<b>12.</b>	<b>Appendix B.....</b>	<b>286</b>
<b>13.</b>	<b>Appendix C.....</b>	<b>292</b>

<b>14. Appendix D</b> .....	<b>293</b>
<b>15. Appendix E</b> .....	<b>294</b>
<b>16. Appendix F</b> .....	<b>295</b>
<b>17. Appendix G</b> .....	<b>296</b>
<b>18. Appendix H</b> .....	<b>297</b>

## II. List of Tables

<b>Table 1.</b> According to Land Cover (LC) and Land Use (LU) rules, classification labels of some sample areas.....	3
<b>Table 2.</b> List of the LC maps in the Atlas. The spatial and spectral resolutions are referred to as the raw input data of the classifications. The number of considered classes correspond to the number of sub-classes, and the page indicates where to find the final map products. ....	6
<b>Table 3.</b> Criteria for Land Cover Classification Systems described by (Anderson, 1976) and author’s comments.....	8
<b>Table 4.</b> Existing land cover datasets and their main characteristics: producer, geographical coverage (global does not include poles), spatial resolution in meters, the span time (the time range dataset used for the classification), and the archived overall accuracy declared by the producer. Only dataset with a spatial resolution below 1000m were taken into consideration. ....	9
<b>Table 5.</b> Most popular commercial VHR and HR satellites. The table shows the main characteristics and parameters. The interval bands are referred to as panchromatic. (P) Indicates payment services and (F) the free to download ones. The temporal resolution varies based on the inclination of the satellite on the earth’s surface. V in spatial resolution means “visible”, PAN means “panchromatic” and MS means “multispectral”. *SPOT, Sentinel, and Landsat programs’ specifications are considered for the latest satellite in orbit (SPOT-7, sentinel-2B, and Landsat-8) with an exception for the launch date, which takes into consideration the first satellite of the constellation in orbit. **16 days for Landsat 8 and 16 for Landsat 7, but with eight days-offset. ....	28
<b>Table 6.</b> Evaluation of UAV platforms performances in geomatics applications. The evaluation ranges from 1 (very low) to 5 (very high), n.a. means “not available”. It was adapted from the work of (Nex and Remondino, 2014). ....	32
<b>Table 7.</b> Examples of optical cameras commonly used on UAVs for RGB image acquisition. The price is expressed using the following scale: \$ = 100 – 600\$; \$\$ = 600 – 2000\$ ; \$\$\$ = >2000\$.....	33
<b>Table 8.</b> Examples of optical cameras commonly used on UAVs for NIR image acquisition. The price is expressed using the following scale: \$ = 100 – 600\$; \$\$ = 600 – 2000\$ ; \$\$\$ = >2000\$.....	34
<b>Table 9.</b> Examples of optical cameras commonly used on UAVs for multispectral image acquisition. The price is expressed using the following scale: \$ = 100 – 600\$; \$\$ = 600 – 2000\$ ; \$\$\$ = >2000\$. ....	35

<b>Table 10.</b> Factors influencing a UAV survey and some recommendations to improve the quality of the acquisition. The recommendations are focused on forest surveys, (Iglhaut et al., 2019). .....	39
<b>Table 11.</b> comparative analysis of FOSS and proprietary software, adapted from (Singh et al., 2015). .....	44
<b>Table 12.</b> Advantages and disadvantages of Pixel-based and Object-oriented classification systems.....	52
<b>Table 13.</b> List of some of the most applied radiometric indices grouped according to their application. ....	58
<b>Table 14.</b> Advantages and disadvantages of feature selection algorithms, grouped in feature importance methods, feature subset assessment methods, and miscellaneous methods (Ma et al., 2017b). ....	65
<b>Table 15.</b> Machine learning algorithms are implemented in some of the most used image classification software by author's analysis in 2020. ....	82
<b>Table 16.</b> Some examples of most applied topographic correction methods and coefficients. The table shows the mane, the type of correction, and a brief description.....	101
<b>Table 17.</b> Most popular software for SfM-MVS workflow. The type (meant as aerial or terrestrial), the file output format, the operating system, and the price are analyzed. The pricing should be interpreted carefully. It referrers to single-user license in April 2020. Source: <a href="https://all3dp.com/">https://all3dp.com/</a> .....	109
<b>Table 18.</b> Components of the Raspberry-based device .....	122
<b>Table 19.</b> Geometric calibration results.....	123
<b>Table 20.</b> Dark frame assessment per band for different ISO settings. ....	126
<b>Table 21.</b> Distances between Raspberry reflectance values of the green band and Hyperspectral ones. The data are referred to as sample pixels of the calibration panels. ....	127
<b>Table 22.</b> Difference between the Band NoIR of the raspberry NoIR and one of the hyperspectral bands between 630nm and 880nm ion the 5 sample points selected for the comparison. ....	129
<b>Table 23.</b> Spatial resolution and bandwidth of Sentinel-2A (S2A) and Sentinel-2B (S2B). .....	130
<b>Table 24.</b> Author's experience over the image processing software used in this work. ....	133
<b>Table 25.</b> Classifications that interest the Alpine arch area. ....	135
<b>Table 26.</b> UAV and LiDAR systems' advantages and disadvantages for the acquisition of data in forested areas with UAV for the Individual Tree crown Detection (ITD) from literature and authors' personal experience.....	138

<b>Table 27.</b> Characteristics of the sensors of the flights.....	142
<b>Table 28.</b> Characteristics of the three flight plans (Num. = Number). .....	142
<b>Table 29.</b> Estimated residuals on the GCPs and CPs and characteristics of the obtained dense point clouds (where N = Number and RMSE=Root Mean Square Error).....	144
<b>Table 30.</b> Algorithms, parameters, and computational time are used for the segmentation. The input band is the Hölder exponent image.....	148
<b>Table 31.</b> Computational time Graphic restitution of each step (algorithm) of the segmentation process. Figures in blue have no classification. The class <i>Trees</i> is green; the class <i>Other</i> is yellow, the class <i>Temporary</i> is red.....	155
<b>Table 32.</b> Results from the Visual evaluation of the Hölder exponent segmentation. ....	156
<b>Table 33.</b> Root Mean Square Error, the Average and the % of an error on the Average, of the Perimeter, the Area, and the Compactness metrics of the Hölder exponent segmentation and the validation datasets .....	156
<b>Table 34.</b> Summary statistics of the Over-segmentation index (OS), the Under-segmentation index ( <i>US</i> ), the Completeness index ( <i>D</i> ), the Jaccard index ( <i>J</i> ), and the Distance between centroids.....	157
<b>Table 35.</b> Sentinel 2 level 1C and 2A images of the classification dataset ..	165
<b>Table 36.</b> List of datasets used for the Dark Object Subtraction (DOS) accuracy evaluation.....	167
<b>Table 37.</b> Bands of Sentinel-2 imagery considered in the DOS accuracy analysis.....	167
<b>Table 38.</b> $r^2$ values for 2017, 2018, 2019 and aggregated (total) distributions of $\Delta 2A-EE$ . ....	172
<b>Table 39.</b> Results of the Kolmogorov-Smirnov significance test carried out for the overlap area .....	174
<b>Table 40.</b> Percentage of validated topographic correction for 1C level dataset .....	178
<b>Table 41.</b> Percentage of validated topographic correction for 2A level dataset .....	178
<b>Table 42.</b> Derivative features are calculated for each epoch. They are divided into 4 groups: histogram-based, radiometric, edge extractor, and textural.....	179
<b>Table 43.</b> Classes of Land Cover considered in this work. ....	180
<b>Table 44.</b> Input datasets for the training layer and the translation to the reference classes. ....	181
<b>Table 45.</b> Aggregation methods comparison. ....	183

<b>Table 46.</b> Correlation analysis of radiometric-based features. The dark green cells indicate a correlation coefficient >0.85. ....	184
<b>Table 47.</b> Correlation analysis of textural and edge-detector features. The dark green cells indicate a coefficient >0.85. ....	185
<b>Table 48.</b> Importance analysis of the textural features. The features that exclusion caused increasing on the OA of 0.01 points were considered less important (negatively affecting the classification). ....	186
<b>Table 49.</b> Producer's and User's accuracies and F1 score for the classification with and without textural features. ....	187
<b>Table 50.</b> Producer's and User's accuracies and F1 score for the classification on tile K. ....	189
<b>Table 51.</b> Producer's and User's accuracies and F1 score for the classification on the overlapping area between tiles Q and K. ....	189
<b>Table 52.</b> Classifications that interest the South-Niger area. ....	192
<b>Table 53.</b> Main characteristics of the sensors and the flights performed on Larba Birno and Tourè.....	196
<b>Table 54.</b> Summary of the main characteristics of the three services. *calculated on 10Mb file. ....	199
<b>Table 55.</b> Files in the CSRS-PPP results folder and their contents. The * indicates the files available since August 2018. ....	200
<b>Table 56.</b> Characteristics of the positions of the base receivers (Stations) analyzed. * gg/mm/yyyy format .....	204
<b>Table 57.</b> Differences between the coordinates estimated by CSRS, APPS, and AUSPOS in WGS84/UTM 31N system for each sample station. ....	204
<b>Table 58.</b> $\sigma$ , 95% confidence, values estimated for full-time acquisitions...205	205
<b>Table 59.</b> $\sigma$ , 95% confidence, estimated for acquisition time reduced to 1-hour. ....	206
<b>Table 60.</b> Difference between the coordinates estimated by CSRS, APPS, and AUSPOS in WGS84/UTM 31N system for each sample station (1hour stationing). ....	206
<b>Table 61.</b> $\sigma$ values, 95% confidence, values estimated for acquisition time reduced to 0.5-hour. ....	208
<b>Table 62.</b> Difference between the coordinates estimated by CSRS, APPS, and AUSPOS in WGS84/UTM 31N system for each sample station (acquisition time 0.5-hour). ....	208
<b>Table 63.</b> Main characteristics of YKRO. Source: IGS website .....	209
<b>Table 64.</b> Differences between the estimated and reference (IGS) coordinates of the YKRO station .....	209

<b>Table 65.</b> Description of the characteristics of the GNSS surveys in Larba Birno and Tourè. The Delta is the difference between the base station's measured coordinates and the estimated coordinates by Precise Point Positioning. ....	211
<b>Table 66.</b> RMSE value of the ground control points (GCPs).....	212
<b>Table 67.</b> RMSE value of the checkpoints (CPs) .....	212
<b>Table 68.</b> The parameters set of the ground classification algorithm. Maximum degree angle describes the maximum slope of the study area expressed in degree; Maximum distance in the maximum distance between the ground and the highest feature in the scene; Cell size in the side size of the most extended cell in which are no detectable ground points (i.e. very dense woods, big buildings). ....	213
<b>Table 69.</b> Pixels distribution (percentage) of the NDWI raster within the identified classification. Column 1 shows the class's name, column two the interval of values describing the class (low-value $\leq$ DN < higher-value), in column three, are reported the pixel distribution in each class in Tourè village analysis, while the fourth column presents the NDWI pixels distribution of Larba Birno. ....	217
<b>Table 70.</b> DN distribution within the reclassified raster of depressions for the villages of Tourè and Larba Birno .....	217
<b>Table 71.</b> Larba: comparison between ground inspection TSWB and DTM-detected .....	220
<b>Table 72.</b> List of Sentinel-2 images used in the classification. ....	224
<b>Table 73.</b> Classes on the classification in South Niger. ....	226
<b>Table 74.</b> Derivative features are calculated for each epoch. They are divided into 5 groups: histogram-based, radiometric, edge extractor, textural. And elevation.....	228
<b>Table 75.</b> Tests run over five scenarios that differ in the number of input features in the classification selected according to their importance value (see Figure 95). The parameters considered for the best scenario evaluation are the out-of-bag error (oob) and the overall accuracy (OA). ....	230
<b>Table 76.</b> OA achieved on single classification. The underlined classifications were excluded from the aggregation.....	231
<b>Table 77.</b> Tests run over 5 scenarios that differ in the number of input features in the classification selected according to their importance value. The parameters considered for the best scenario evaluation are the out-of-bag error (OOB) and the overall accuracy (OA).....	232
<b>Table 78.</b> DOS influences over the classifications. ....	232
<b>Table 79.</b> Error matrix of the aggregated multi-temporal classification. ....	233
<b>Table 80.</b> Error matrix of the stacked multi-temporal classification. ....	234
<b>Table 81.</b> Features selected for the segmentation and the classification.....	239

<b>Table 82.</b> Segmentation ruleset applied for the Land Cover OBIA classification of Tourè village.....	241
<b>Table 83.</b> Visual assessment metrics of the segmentation of the buildings in Niger case study.....	245
<b>Table 84.</b> Area-based quantitative assessment of the segmentation of the buildings in Niger case study. * lower values means better segmentation. ....	245
<b>Table 85.</b> Root Mean Square Error of the Area and the Perimeters of the house objects in Niger study area.....	246
<b>Table 86.</b> Error matrix of Object-bases classification of Tourè along Sirba River (Niger).....	246
<b>Table 87.</b> Error matrix of the CLC 2018 (reference) and Alpine Classification. To facilitate the reading, the values are reported in square kilometres. ....	250
<b>Table 88.</b> Conversion classes between ESA Africa LC and Sirba LC. ....	251
<b>Table 89.</b> Error matrix of the ESA LC Africa (reference) and Sirba Classification. To facilitate the reading, the values are reported in square kilometres.....	253



### III. List of Figures

**Figure 1.** The priorities of the Senday Framework, (UNDRR, 2015)..... 11

**Figure 2.** Scheme of a general optical sensor.  $M$  and  $N$  are the dimensions of the image, which is proportional to the dimension of the sensor ( $m$  and  $n$ ). Modified from (Oliveira et al., 2019). .....20

**Figure 3.** Process of remote sensing, describing the steps from the hypothesis formulation to the information. It considers the main existing remote sensing techniques. The highlighted points represent the parts of the process applied in this work (Revised from Introduction to remote sensing, Jensen 1987) .....21

**Figure 4.** Global shutter (left) and rolling shutter (right) functioning. The global shutter at time  $t_l$  exposes the entire frame, while the rolling shutter at  $t_l$  exposes only one line out of  $n$ . .....22

**Figure 5.** Two widespread effects of rolling shutter sensors. An example of the distortions caused by the rolling shutter of a fast-moving object (car) is on the left. On the right, the distortion caused by the rolling shutter is used for capturing an image of a static scene (fence) from a moving means. CC BY-SA 4.0 via wikimedia. ....23

**Figure 6.** Representation of the CCD sensors that have only one converter of charge. The charges are moved within the sensor photocells to reach the converter, from <https://meroli.web.cern.ch>. .....24

**Figure 7.** Representation of the CMOS sensors that have one small converter for each photocell. The conversion of charge happens in the photocell fastening the image acquisition process. From <https://meroli.web.cern.ch>. .....24

**Figure 8.** Electromagnetic spectrum. Optical sensors are generally sensitive to the visible (400nm) till the Short Wave Infrared (SWIR) (3000nm), (Akhroufi and Bendada, 2013). .....25

**Figure 9.** Example of sensor sensitivity. The spectral sensitivity represents in the graph is of Multispec 4C camera by Sensefly, (Sensefly, 2014). .....26

**Figure 10.** Bayer filter. Each cell stores data of Blue (B), Green (G), or Red (R) information. Then, each color band is interpolated to fill the data gap, (Campbell and Wynne, 2011). .....26

**Figure 11.** UAV classification is based on the height range and the maximum distance, according to (van Blyenburgh, 1999). .....31

<b>Figure 12.</b> a) Example of lighter than air UAV. The balloon with an inboard sensor; b) Example of multirotor UAV. This is an exacopter (6 propellers) produced by DJI called MATRICE 600; c) Example of fixed-wing UAV eBee classic. ....	31
<b>Figure 13.</b> Main variables that should be taken into consideration on mission planning phase. ....	36
<b>Figure 14.</b> Example of lateral and forward overlap of a UAV flight. Image modified from <a href="https://www.nrcan.gc.ca/">https://www.nrcan.gc.ca/</a> . ....	37
<b>Figure 15.</b> Three main strategies for GNSS data acquisition exist: absolute positioning, relative positioning, and differential positioning. Adapted from <a href="http://fig.net/">http://fig.net/</a> . ....	42
<b>Figure 16.</b> Graphic representation of the classification process (simplified). On the left the representation of a raster single band image and of the classified image (right). Similar values of the left image have been grouped for a class in the image on bright. Class “A” is defined by bright values (>6) and class “B” describes the dark pixels (< 3). (Campbell and Wynne, 2011). ....	45
<b>Figure 17.</b> Graphical restitution of pixel vector in the multiband image. In this case, the highlighted pixel is the vector [23 42 89 94]. (Campbell and Wynne, 2011) .....	46
<b>Figure 18.</b> The general workflow of the classification structure as identified by (Lu and Weng, 2007) and (Campbell and Wynne, 2011). This methodology is particularly adapted for supervised classification algorithms. The image pre-processing step is analyzed in Chapter 5. ....	48
<b>Figure 19.</b> An example of increasing thematic detail. a) is the analysed area; b) is the analysed area classified as "vegetation"; c) in the classification distinguish between grassland (light green), forest (dark green) and shadows (black); d) is more thematically detailed classification where single tree crowns are detected (red outlines). ....	49
<b>Figure 20.</b> Example of a classification system. It is composed of classes (grasslands, Forests, Rivers, Stream, Lakes, Sea, Metal roofs, Brick roofs, Concrete roofs), subclasses (broadleaves and conifers), and macro classes (Vegetation, Water, and Urban areas) organized in a hierarchical system. ....	50
<b>Figure 21.</b> A graphic example of the segmentation process. Pixels with homogeneous information (in this case, spectral information) are grouped to form polygons (or objects) with specific characteristics. ....	52
<b>Figure 22.</b> Main steps for the pixel-based and OBIA classification, starting from a ready-to-classify input dataset. ....	53
<b>Figure 23.</b> Graphical restitution of feature extraction and feature selection processes. Features A, B, C, and D are the spectral information. The feature	

extraction identifies new features E, F, G, and H that are a function of A, B, C, and D data. The feature selection process identifies the most significant and essential features for the classification (B, D, F, G, and H). .....56

**Figure 24.** Example of a distribution histogram. On the abscissae, the digital number (DN) values and on the ordinates the frequency of DN values. ....57

**Figure 25.** Representation of Kurtosis. Image source: <https://community.sw.siemens.com> .....59

**Figure 26.** Representation of the Skewness (or skew). Image source: Diva Jain, CC BY-SA 4.0 <<https://creativecommons.org/licenses/by-sa/4.0/>>, via Wikimedia Commons .....59

**Figure 27.** Visual representation of neighborhoods. The black pixel is the object of reference, and it is defined by (n, m) size. The Surrounding grey pixels constitute its 3 x 3 neighborhoods. The white pixels delimit the 5 x 5 neighborhood (which includes the 3 x 3 neighborhood).....60

**Figure 28.** Two examples of fractals in (a) the Roman broccoli, Source treccani.it (b) Norway fjords. Source: <http://paulbourke.net/> .....62

**Figure 29.** Classification algorithms are grouped according to the assumption of the data distribution and on the type of learning. ....67

**Figure 30.** Main steps of the unsupervised and supervised classification process. ....69

**Figure 31.** Example of CART classifier. It represents four layers-decision trees, where Layer 1 is the Root node, and Layer 4 is the Leaf node where the class is assigned to the unit of classification in the exam. ....74

**Figure 32.** Optimum separation plane (hyperplane) and support vectors data that define it. (Salah, 2017b).....76

**Figure 33.** Example of a simple SVM decision tree (a) and a multiclass decision using SVM classifiers in parallel with final decision logic (b). (Richards, 2013).77

**Figure 34.** Structure of Random Forest classifier. It is composed of n trees with a different number of nodes. Each tree defines a class for each element to be classified, and the most frequent (majority voting) is the final class assigned to the element. Modified from Venkata Jagannath, CC BY-SA 4.0 .....80

**Figure 35.** Example of error matrix. The elements on the diagonal are the correctly classified samples. ....88

**Figure 36.** Simplified scheme of needed data corrections and calibrations due to the atmosphere. Satellite-mounted sensors collect data in the form of radiance that needs to be transformed into reflectance at the surface (or bottom-of-atmosphere). The UAV-mounted sensor is not subjected to atmosphere distortions

because they are close to the Earth’s surface. Modified from (Young et al., 2017). .....	94
<b>Figure 37.</b> Potential workflow for the correction of the satellite images. Not all the steps are always necessary. The figure is adapted from the work of Young et al. (2017). .....	95
<b>Figure 38.</b> Shadow's effect depending on sun elevation and position. From <a href="https://www.youtube.com/watch?v=LgZbhogv9Q8">https://www.youtube.com/watch?v=LgZbhogv9Q8</a> . The proposed example regards some trees, but the same effects exist over hills and mountains. .....	100
<b>Figure 39.</b> Structure from Motion technique. The acquisition of moving (black cameras) to get data from a static object (red dots) creates a 3D model (Iglhaut et al., 2019). .....	103
<b>Figure 40.</b> Geometric calibration workflow. .....	105
<b>Figure 41.</b> Camera calibration defines the relation between the sensor, real-world, and image reference frames and calculates the camera's intrinsic and extrinsic parameters. .....	106
<b>Figure 42.</b> Example of the effects of positive and negative radial distortions on an image. Adapted from <a href="https://it.mathworks.com">https://it.mathworks.com</a> . .....	106
<b>Figure 43.</b> Structure from Motion processing steps, (Wu et al., 2012). .....	107
<b>Figure 44.</b> SfM-MVS workflow for the generation of the Dense Point Cloud, (Seitz et al., 2006). .....	108
<b>Figure 45.</b> The study area in Cesana Torinese .....	114
<b>Figure 46.</b> Timeline of land surveys in the Alps region. .....	115
<b>Figure 47.</b> Sirba River in Niger country .....	116
<b>Figure 48.</b> Example of local architecture. Aerial view. .....	117
<b>Figure 49.</b> CORS in Africa continent. The dots indicate the stations that provided raw observations to the International GNSS Service (IGS) in the last ten days. The map is daily updated. This image is referred to the 17 January 2020. Source: International GNSS Service (IGS). .....	118
<b>Figure 50.</b> Land surveys in the Tillaberi region. .....	119
<b>Figure 51.</b> Spectral response of Canon Powershot S110 NIR. Since the NIR filter was removed, the NIR channel is broad and encompasses the visible electromagnetic spectrum. Source: Sensefly .....	121
<b>Figure 52.</b> Raspberry-based device used in this study .....	122
<b>Figure 53.</b> Known-size chessboard used for the geometric calibration .....	123
<b>Figure 54.</b> Raspberry Pi camera spectral response. Source: Pagnutti et al., 2017 .....	124
<b>Figure 55.</b> Histograms of frequency for the DN of dark frame assessment at 100 ISO (for Band 1, 2 and 3) and 600 ISO (for Band 1, 2 and 3). .....	125

<b>Figure 56.</b> Picture of the calibration scene taken by the NoIR camera. On the left, the calibration target comprises four panels (white, light grey, dark grey, and black). On the right side of the picture, a plant. At the bottom of the picture is visible, the irradiance sensor of the hyperspectral.....	127
<b>Figure 57.</b> Plots of spectral signatures on the SONAP (grey dots) and the Raspberry NoIR (orange squares). The wavelength is on the x-axis, while the reflectance (0-1 scale) on the y-axis. ....	128
<b>Figure 58.</b> Pushbroom sensor functioning. Modified from <a href="http://fao.org">http://fao.org</a> ....	131
<b>Figure 59.</b> The study area in Cesana Torinese. The light blue circles are the CPs and the orange squares are the GCPs. ....	142
<b>Figure 60.</b> Resulting RGN orthomosaic. ....	144
<b>Figure 61.</b> The procedure used to calculate the Hölder exponent $\alpha$ , adapted from Figure 1b in (Aleksandrowicz et al., 2016).....	147
<b>Figure 62.</b> Possible cases of the relation between reference crowns (blue border) and segmented crowns (red border).....	150
<b>Figure 63.</b> (a) and (d) Details of RGB dataset; (b) and (e) Detail of RGN dataset of the same area presented in (a) and (d); (c) and (f) Map of the Hölder exponents determined for the area presented in (a) and (d). The Hölder exponent layer restitution is in greyscale visualization, where 0 is black, and 1 is white. The shadows are mitigated, and the single crowns are easily identified as well as the grassland that are large areas of low DNs.....	154
<b>Figure 64.</b> Detail of the delineation of single crowns (red border) on RGB orthomosaic. The red square in the bottom-right corner indicates the sample area's location within the entire study area. ....	154
<b>Figure 65.</b> Distribution of the Jaccard index (y-axis) values according to the Crown size (x-axis).....	158
<b>Figure 66.</b> The plot of the Over-segmentation index (OS), Under-Segmentation index (US), Completeness index (D), Jaccard index (J), and the distance between centroids (CD) calculated on the Hölder exponent dataset and the validation datasets (Spectral information, NDVI, Sum Variance textural information, CHM, and the mixed input data).....	159
<b>Figure 67.</b> Tiles T31TGK (western tile, blue) and tile T32TLQ (eastern tile, red). The study area Cesana Torinese indicated by the yellow pointer lies in the overlap between T31TGK and T32TLQ. ....	164
<b>Figure 68.</b> Example of outliers. The test points 7 and 63 are placed on the cloud-masked area (Digital Number 0), while point 68 is located on non-masked clouds due to the cloud-masking algorithm's inaccuracy, and it has Digital Number over 1000. ....	168

<b>Figure 69.</b> Graphs of $\Delta 2A - EE$ of 2017. The distributions are represented in different graphs for the visible, red-edge, NIR, and SWIR bands.....	169
<b>Figure 70.</b> Graphs of $\Delta 2A - EE$ of 2018. The distributions are represented in different graphs for the visible, red-edge, NIR, and SWIR bands.....	170
<b>Figure 71.</b> Graphs of $\Delta 2A - EE$ of 2019. The distributions are represented in different graphs for the visible, red-edge, NIR, and SWIR bands.....	171
<b>Figure 72.</b> Graphs of $\Delta 2A - EE$ of 2017, 2018, and 2019. The distributions are represented in different graphs for the visible, red-edge, NIR, and SWIR bands. ....	173
<b>Figure 73.</b> Spectral signature obtained by the median value of each point of vegetation (from CLC) of Earth Engine DOS, 2A and 1C datasets .....	175
<b>Figure 74.</b> a) RGB visualization of a sample area; b) hillshade+CLC visualization; c) example of a pair of points on two mountainsides (orange and blue points). ....	177
<b>Figure 75.</b> Classification of tile Q. ....	187
<b>Figure 76.</b> Some detail of the tile classification in high-altitude mountainous areas ( left, scene 1) and lowlands (right, scene 2). Images a.1 and a.2 show the RGB orthophoto (Source: Bing Satellite); b.1 and b.2 shows the classification; c.1 and c.2 shows the overlapping of the orthophoto and the classification (low opacity). ....	188
<b>Figure 77.</b> The changes in F1-score for each class through the epochs (tile no., on the abscissae). ....	188
<b>Figure 78.</b> Left: UAV system built by Drone Africa Service. Right: Detail of the UAV body. It is visible that the Raspberry Pi sensor is mounted on the UAV system. 3.5 inches screen and the GPS receiver. ....	196
<b>Figure 79.</b> Sample pictures of the same area in Larba Birno acquired by Sony-ILCE-5100 and Raspberry Pi. The SONY picture (6000x3000 pixels) has a 2.5 cm/pixel resolution and is in RGB. The raspberry picture (2592x1933 pixels) has a 6 cm/pixel resolution, and it is visualized in NIR Green Red. ....	197
<b>Figure 80.</b> Section of Sirba River interested by the survey. The green squares identify the locations of the stations along the river. The circled ones are analysed in this contribute. ....	198
<b>Figure 81.</b> APPS service upload webpage. ....	201
<b>Figure 82.</b> AUSPOS service upload webpage.....	202
<b>Figure 83.</b> Graphical analysis of the $\sigma$ values of East, North, and Up coordinates of the three services, obtained considering the full acquisition time. ....	207

<b>Figure 84.</b> The workflow of the orthophoto and Digital Terrain model generation.....	212
<b>Figure 85.</b> On the left, a detail of the ground classification was performed on the point cloud on Tourè. The brown area is the one classified as “ground” by the Photoscan algorithm. Right: extract of the non-interpolated DTM of Tourè. ....	213
<b>Figure 86.</b> Simplified representation of fill sinks algorithms functioning, the depressed areas (i.e., DN value 4) are rise up based on the neighborhood. Depending on the algorithm used, the number of neighbor cells considered may vary. ....	215
<b>Figure 87.</b> Graphic restitution of the decision tree structure applied for the identification of TSWB.....	215
<b>Figure 88.</b> Detail of the depressions identified through the DTM analysis in Larba Birno. The small and shallow depressions are DTM artifacts created by the roughness of the soil. Some depressions are well defined (blue spots), while others are noisy due to irregularities on the ground due to mud and water. ....	218
<b>Figure 89.</b> Example of matched TSWB between the ground inspection (green polygon) the DTM-derived (pink polygon). ....	219
<b>Figure 90.</b> a) RGN visualization of the Temporary Surface Water Body (TSWB) in Larba Birno. b) Match of NDWI-based (green) and DTM-based (blue) TSWBs.....	219
<b>Figure 91.</b> Sample TSWB in Larba Birno. A scene is extracted from the orthophoto. B scene shows the information originated from the DTM analysis. In this case, the NDWI analysis results in the total absence of water. From picture A, it is possible to identify the loam residuals in correspondence with the potential TSWB. Moreover, the path seems to be created in order to avoid TSWB. ....	220
<b>Figure 92.</b> TSWB detected by NDWI analysis (green features) and partially developed under a tree crown. It was not detected by the DTM method. ....	222
<b>Figure 93.</b> (a) RGB mosaic on sentinel 1C data, DOS applied; (b) RGB mosaic on sentinel 1C data, DOS applied, and topographically corrected. The correction excessively alters the data over the plateaux, but also in the plane areas. ....	225
<b>Figure 94.</b> The workflow of the classification. Red arrows indicate the DOS processing, while the blue ones indicated the processing without DOS correction. ....	229
<b>Figure 95.</b> GINI importance of the extracted features.....	230
<b>Figure 96.</b> Example of the aggregated multi-temporal classification (left) and the stacked multi-temporal classification (right). ....	233
<b>Figure 97.</b> Classification legend structure composed of 4 macro-classes (Buildings, Bares soils, Vegetation, and Water); 10 classes and two sub-classes (Grass and agricultural lands). ....	238

<b>Figure 98.</b> Position of the reference objects within the study area.....	243
<b>Figure 99.</b> Possible relations between reference crowns (yellow outline) and segmented crowns (blue outline) .....	244
<b>Figure 100.</b> a) example of segmentation in a sample area, and b) its classification. ....	244
<b>Figure 101.</b> Detail of the segmentation process. The yellow square indicates two objects of mixed class: grassland and wet areas. ....	247
<b>Figure 102.</b> Example of land cover spectral variability within households ‘yards. ....	248
<b>Figure 103.</b> Examples of Alpine LC and Corine LC in plane area and mountainous zone; a1. Bing satellite view with Google labels of Padana plain; a2. Alpine LC classification and Google labels; a3. CLC2018 classification and Google labels. b1. Bing satellite view with Google labels of montaneous area (Valle Stura di Demonte, Italy); b2. Alpine LC classification and Google labels; b3. CLC2018 classification and Google labels. ....	251
<b>Figure 104.</b> Sirba River area classified according Sirba LC (top) and ESA LC (bottom). ....	252
<b>Figure 105.</b> Extract from Tourè village (Niger) flood risk analysis considering the buildings exposed to four level of flood risk (Green, Yellow, Orange and Red) and water stagnation. ....	254



## IV. Acronyms

AICS: Italian Agency for development and cooperation

ALS: Aerial Laser Scanner

AMP: Agisoft Metashape Professional

ANADIA II: AdattameNto Ai cambiamenti climatici: prevenzione Delle catastrofi e sviluppo agrIcolo per la sicurezza Alimentare

APPS: Automatic Precise Positioning Service

AUSPOS - AUStralia's On-Line Static GPS POsitioning Service

BAI: Burn Area Index

BOA: Bottom Of Atmosphere

CHM: Canopy Height Model

CMR Clay Minerals Ratio

CORS: Continuously Operating Reference Stations

CSRS: Canadian Spatial Reference System

DDV: Dense Dark Vegetation

DN: Digital Number

DRR: Disaster Risk Reduction

ESA: European Space Agency

EVI: Enhanced Vegetation Index

FIR: Far InfraRed

GEE: Google Earth Engine

GEMI: Global Environment Monitoring Index

GIS: Geographic Information Systems

GNSS: Global Navigation Satellite System

GPS: Global Positioning System

HR: High Resolution

ICE: Internal Combustion Engine

ITD: Individual Tree Detection

LC: Land Cover

LCC: Land Cover Change

LCCS: Land Cover Classification System

LCS: Land Change Science

MDDV: Modified Dense Dark Vegetation

NASA: National Aeronautics and Space Administration

NDBI: Normalized Difference Built Up Index

NDPI: Normalized Difference Pond Index

NDTI: Normalized Difference Turbidity Index

NDVI: Normalized Difference Vegetation Index

NDWI: Normalized Difference Water Index

PPP: Precise Point Positioning

PVI: Perpendicular Vegetation Index

RINEX: Receiver INdependent EXchange format

RMSE: Root Mean Square Error

ROCKTHEALPS: Harmonized ROCKfall natural risk and protection forest mapping in the ALPine Space

RTK: Real-Time Kinematic

RVI: Ratio Vegetation Index

SAVI: Soil Adjusted Vegetation Index

SCS: Sun-Canopy-Sensor

SfM: Structure from Motion

SODA: Sensor Optimized for Drone Applications

SRM: Structural Risk Minimization

SRWI: Simple Ratio Water Index

TLS: Terrestrial Laser Scanner

TOA: Top Of Atmosphere

UAV: Unmanned Aerial Vehicles

UN: United Nations

VHR: Very High-Resolution satellites

WASH: WATER Sanitation and Hygiene

# Chapter 1

## Introduction

Land Cover (LC) maps are representations of the real land cover and describe the covering of the Earth's surface at a certain time using well-defined features. They result from the classification process, which is an abstract representation of land cover at a given time using diagnostic criteria. The classification is defined as (Sokal, 1974):

*"The ordering or arrangement of objects into groups or sets on the basis of their relationships."*

LC is generally meant as the physical cover on the Earth's surface (FAO, 2000). If we strictly consider the definition, only the vegetation and human-made features should be considered covers, since bare rock or bare soil describes land itself rather than land cover. However, the scientific community recognizes under the term land cover also bare soil and water. Land Cover is often confused with land use; although the terms are often used interchangeably, their actual meanings are quite distinct.

Land use describes the cover but the human's usage of the cover. It is defined by the arrangements, activities, and inputs that people undertake in a specific land cover type to produce, change, or maintain it. Land use refers to the purpose the land serves. For example, "bare sandy soil" is a cover term, while "recreation area" or "beach" refers to the use of a sandy cover. "Recreation area" is a land use term that may apply to different land cover types: for instance, grasslands like urban parks, bare red soil like a tennis court, etc. (Table 1), (FAO, 2000).




Mapping Land Cover has many applications, and it is fundamental for Earth monitoring studies, resource management, and planning. According to the agreement on Disaster Risk Reduction of the United Nations document, also known as the Sendai framework (UNDRR, 2015), the Earth observation data are fundamental and relevant for reducing disaster risk. To meet climate planning and natural hazard monitoring, Very High Resolution (VHR) data are needed, and they must be repeatable, replicable, standardized, and affordable. Usually, land cover properties are measured via remote sensing using specific techniques from which LC is interpreted with ancillary data or *a priori* knowledge. These classification techniques are commonly ascribable to Machine Learning (ML) classification algorithms. The classification techniques are part of complex classification systems composed of several steps that result in the Land Cover maps. These systems, called Land Cover Systems (LCS) or Land Cover Classification Systems (LCCS), consist of specific methodologies that regulate, among the others, the nature of input data, the selection of the classes to group the objects of the classification in, the classification algorithms, the modality of validation, and the characteristics of the restitutions.

Nowadays, there is a scarcity of tools and methodology able to provide LCS information to satisfy VHR monitoring requirements. The main reasons are ascribable to:

- **Lack of exhaustive research** that analyzed the entire process of VHR Land Cover data extraction, considering the LCS as a whole from the selection of proper sensors for data collection to the LC map restitution;
- **Lack of adequate low-cost technologies** able to provide the LCS users with the VHR data;
- **Need for optimization** of the VHR Land Cover map generation process;
- **Lack of standardized methodology** for VHR Land Cover detection for mapping landscape-complex areas;
- Most of the present solutions are **not replicable and automatic**.

This framework emerges from the need for new technologies and tools to create VHR LC maps according to well-defined and shared methodologies that consider multi-temporal, and multi-thematic aspects of Land Cover classifications.

**Table 1.** According to Land Cover (LC) and Land Use (LU) rules, classification labels of some sample areas.

	<b>LC</b>	<b>LU</b>
	Grasslands	Recreation area
	Bare red soil	Recreation area
	Bare sandy soil	Recreation area

These considerations naturally give rise to the following questions that have been the starting point of this investigation:

- How can reliable spatial data for climate planning be obtained?
- Which is the most i) low-cost, ii) standardized, iii) replicable, and iv) high-resolution way to get information regarding natural risk?
- Which is an adequate LCS for natural risk monitoring?
- Which are the main limitations related to the standard classification methodology applied to VHR?
- Does the literature address these limits?
- Is there a solution to mitigate or remove them?

Answering these questions led to this thesis's development, which analyzes the methodology for the generation of Land Cover Maps of critical areas at high thematic, temporal, and spatial detail. This work is focused on the optimization of the Land Cover map process: from the data collection to the final result. The idea behind this work is that it is possible to simplify the classification process of VHR resolution imagery and semi-automatically generate high thematic detailed LC maps with a multi-temporal approach using few input features, with low computational effort, new technologies, and open and free software. As far as the author's knowledge, it does not exist exhaustive work that analyzed the entire process of Land Cover data extraction considering the selection of the proper sensor from the flight to the Land cover Map restitution, especially for Unmanned Aerial Vehicles (UAVs) systems. The VHR imagery LC classification is a relatively emerging field, mainly applied in critical areas, even though critical areas are the ones that may benefit more from it. The case studies analyzed in this work are two critical areas located in the Alpine Arch and the Sub-Saharan region of Niger. These areas are bonded by the heterogeneous land cover, the challenging environmental conditions, and being prone to specific natural hazards (respectively, rockfall and floods). These common aspects are the significant constraints to the data collection and data analysis. The final product of this work is a multi-resolution LC Atlas of natural hazards-prone areas of the World. The classification system is tailored according to the planning-related needs for risk reduction as identified by the planners.

This thesis was possible thanks to the data collected within two pilot projects: ANADIA 2.0 and ROCKTHEALPS. Even if the pilot projects' study areas are geographically distant, they share the focus on natural hazard prevention. The

possibility of working on specific natural hazards (i.e., rockfalls and floods) in such different environments has been an opportunity to validate the methodology developed in this research, demonstrating its broad applicability.

A further aim of the research is to minimize human intervention into the Land Cover classification process. Automation had been one of the most relevant obstacles faced during the investigation since it requires high computational power and the harmonization of the variables and algorithms for classification. Google Earth Engine (GEE) platform provided the needed computational power, and it is a no-cost service provided by Google. The harmonization of the algorithms and the classification steps was possible thanks to the knowledge and the inputs of the Earth Observation research group of the Space Research Center of Poland (CBK-PAS). Professor Edyta Wozniak supported this investigation in the development of the harmonized steps for optical imagery classification. During the five months of research in CBK premises, the classification methodology structure for satellite imagery was created. It is entirely coded in the Google Earth Engine API platform.

The final result is an atlas composed of three Land Cover Maps of the Sub-Saharan region and two LC maps of the Alpine arch case study. The maps differ in resolution and thematic detail. Two maps are realized using Sentinel-2 data, with 10 m of spatial resolution. The remaining maps are realized with UAV datasets. Table 2 lists the available maps in the atlas.

The manuscript is organized into nine chapters (considering introduction and bibliography). Chapter 2 provides a literature overview of the relation between climate planning, land cover, and the current complexity and constraints in land cover monitoring. Chapter 3 analyses the existing data collection tools for LC mapping and presents the workflow to realize this research. Chapter 4 analyzes the existing algorithms for the LC classification. Chapter 5 analyses the pre-processing of optical data for the generation of Land Cover Maps. The pilot projects and the test areas of the study are presented in Chapter 6. Chapters 7 and Chapter 8 concern the description of used sensors and their calibrations, the information gathering surveys and the pre-classification analysis performed on the dataset, the classification, its validation, and the generation of the LC Atlas respectively for the Alpine Arch (Chapter 7) and the Tillaberi region (Chapter 8). A general discussion on the proposed methodology's effectiveness that summarises the archived results and underlines future potential investigation directions planning is presented in Chapter 9.



**Table 2.** List of the LC maps in the Atlas. The spatial and spectral resolutions are referred to as the raw input data of the classifications. The number of considered classes correspond to the number of sub-classes, and the page indicates where to find the final map products.

Case study	LC map name	Data source	Spatial resolution (m)	Spectral resolution (nm)	Number of LC classes	Type of classification	Appendix
Sub-Saharan	Satellite_1	Sentinel-2	10	492– 2202 (13 bands)	7	Pixel-based	G
	UAV_1	UAV-mounted optical sensors	0.06	400-900 (6 bands)	11	Object-oriented	H
	UAV_2						
Alpine Arch	Satellite_2	Sentinel-2	10	492– 2202 (13 bands)	12	Pixel-based	D
	UAV_3	UAV-mounted optical sensors	0.10	450-850 (6 bands)	1, single tree crown	Object-oriented	C

## 1.1 Keywords

Keywords: LC (Land cover); Land Cover Classification; Landscape Complexity; Machine Learning; Random Forest; Optical sensors; UAV (Unmanned Aerial Vehicles); GEE (Google Earth Engine); Natural Hazards; Critical areas; Alpine arch; Sub-Saharan; Low-cost; FOSS.

## **Chapter 2**

# **Land Cover mapping and its role in environmental studies and regional planning**

The Land Cover (LC) classifications order the objects on the Earth's surface into groups. These groups are called classes, and their definition should be clear, precise, possibly quantitative, and based upon objective criteria (FAO, 2000). Land cover classification systems (LCCS) should use classes that can be applied at any spatial scale or detail level (scale independence). Moreover, the classification needs to be source independent, which means that it must be applied independently of the data collection methodology (satellite, UAV, field survey, etc.). The classification classes and their descriptions constitute the legend of a classification. It depends on the area of application of the classification: a legend is the application of a classification in a specific area using a defined mapping scale and a specific dataset. Therefore, a legend may contain only a proportion, or sub-set, of all the possible classes of the classification. The legend is scale- and cartographic representation-dependent. Indeed, mixed mapping units are not rare if the elements composing this unit are too small to be delineated independently.

Moreover, the legend is data- and mapping methodology- dependent. The sensors used for the data collection strongly influences these aspects, as explained in Chapter 3. During the last decades of the 19<sup>th</sup> century, when satellite information for LC monitoring was a new-born approach to LCCS and still not consolidated, ten criteria that LCCS should meet to be applied to satellite imagery were identified

(Anderson, 1976). Some of these criteria can be generally applied to the classification systems based on optical imagery and they are described in Table 3.

**Table 3.** Criteria for Land Cover Classification Systems described by (Anderson, 1976) and author's comments.

N.	Criteria	Comments
1	The minimum level of interpretation accuracy in the identification of land use and land cover categories from remote sensor data should be at least 85 percent.	This first criterion is generally acceptable, although the classification accuracy also depends on the system's complexity and the landscapes. From 1976 till today have been produced LC maps less than 85% accuracy, although these classifications provided novel methodologies, a new level of detail and extension. Some examples can be found in Table 4.
2	The accuracy of interpretation for the several categories should be about equal.	This criterion is still valid and sharable. All the classes in an LCCS should have very similar accuracies.
3	Repeatable or repetitive results should be obtainable from one interpreter to another and from one time of sensing to another.	The repeatability of LCCS and, generally, of classification methodology is a fundamental aspect of LC analysis. Especially through time. Indeed, the monitoring and the study of landscape evolution are based on comparing different time LC comparison to detect changes.
4	The classification system should be applicable over extensive areas.	The statement refers to the spatial replicability of the classification. Indeed, at an equal data source, an LCCS should provide the analyst with coherent results when applied to different areas characterized by the same landscape conditions. LCCS created for desert areas will not provide a significant result from its application in coastal areas.
5	The categorization should permit vegetation and other types of land cover to be used as surrogates for activity.	The classes, or categories, of LCCS should be exact and scale-independent to guarantee their use and interpretation by different users.
6	The classification system should be suitable for use with remote sensor data obtained at different times of the year.	The statement refers to temporal replicability. The LCCS should provide the analyst with reliable results of LC from datasets of different sending time.
7	Effective use of subcategories that can be obtained from ground surveys or from the use of larger-scale or enhanced remote sensor data should be possible.	The classes, or categories, of the LCCS should be organized in a multi-level structure that can be modified and integrated with subcategories at any moment.
8	Aggregation of categories must be possible.	Similarly to point 7, the LCCS should be organized in a multi-level structure that can be modified and aggregated in macro-classed at any moment.
9	A comparison with future land cover data should be possible.	LCCS should include and present the results to guarantee the comparison to future LC maps.
10	Multiple uses of land should be recognized when possible.	This aspect is valid only for Land Use maps.

Modern LCS satisfy most of these criteria. Today, several LC information exists, and it is open access. The table 4 lists the most used existing land cover datasets and their main characteristics—only dataset with spatial resolution below 1000m are presented.

**Table 4.** Existing land cover datasets and their main characteristics: producer, geographical coverage (global does not include poles), spatial resolution in meters, the span time (the time range dataset used for the classification), and the archived overall accuracy declared by the producer. Only dataset with a spatial resolution below 1000m were taken into consideration.

LC dataset	Producer	Coverage	Spatial resolution	Reference period	Declared accuracy
Global Land Survey (GLS)	USGS and University of Maryland	Global	30 m	2000 – 2012	91%
Climate Change Initiative (CCI) Land Cover V2	ESA	Global	300 m	/	75%
MCD12Q1 0.5 km MODIS-based Global Land Cover Climatology	NASA	Global	500 m	2001-2010	/
USGS – Global Land Cover Characterization (GLCC)	USGS	Global	1000 m	1992 - 1993	67% accuracy.
Globe Land 30	National Geomatics Centre of China	Global	30 m	2000 - 2010	80%.
UN FAO Global Land Cover Network (GLC-SHARE)	FAO	Global	1000 m	/	80%
CORINE land cover	Copernicus	Europe	100 m (2018)	1985, 2000, 2006, 2012, 2018	≥ 85%
ESA Climate Change Initiative Land Cover Sentinel-2 Prototype	ESA	Africa	20 m	2016	/

## 2.1. Climate Change and planning against climatic risk: Sendai Framework

In the last years an exponential intensification of natural hazards all over the World has been detected (IPCC, 2012), affecting the safety of persons and communities as a whole (UNDRR, 2015). Besides, small-scale disasters are more

frequent and intense (IPCC, 2012). Climate change and poorly planned development are considered the drivers of this intensification (in frequency and intensity) of hazards (UNDRR, 2015). In this framework, the need for planning to forecast and reduce disasters is unneglectable. Indeed, the United Nations (UN) recognize the importance of planning against climate change. To more effectively protect persons, communities, and countries, their livelihoods, health, cultural heritage, socioeconomic assets, and ecosystems (UNDRR, 2015). Thus, monitoring the World's areas that are more vulnerable to natural hazards has become crucial all over the World. In order to reduce disaster risk, effective tools and relevant data are needed. According to the agreement on Disaster Risk Reduction of the United Nations document, the Sendai framework (UNDRR, 2015), the collection of satellite data (i.e., Earth observation programs) and *in situ* information should be promoted encouraging tools for the management of geographic data, such as the Geographic Information Systems (GIS).

The Sendai Framework for Disaster Risk Reduction 2015-2030, with its seven targets and four priorities for action, was adopted at the Third UN-World Conference on Disaster Risk Reduction on March 18, 2015 (Figure 1). It was endorsed by the UN General Assembly on June 3, 2015. The Sendai Framework is a 15-year, voluntary, non-binding agreement which recognizes that the State has the primary role to reduce disaster risk but that responsibilities are to be shared with other stakeholders including local government and the private sector. It aims for the following outcome: the substantial reduction of disaster risk and losses in lives, livelihoods and health and in the economic, physical, social, cultural and environmental assets of persons, businesses, communities and countries.

The targets focus on substantial reductions in *i)* disaster mortality, *ii)* the number of affected people, *iii)* direct economic losses, and *iv)* reducing damage to critical infrastructure and disrupting basic services. The Sendai Framework also seeks a substantial increase in *v)* national and local disaster risk reduction strategies by 2020, *vi)* enhanced cooperation in developing countries and *vii)* a substantial increase in multi-hazard early warning systems, disaster risk information, and assessments. The Sendai Framework identifies four priorities.

Understanding disaster risk requires relevant data from different sources, such as satellite information and land survey data (priority 1, Figure 1). Those data must be collected and analyzed with innovative tools and new technologies and managed and elaborated on sharing-information platforms. As in point (f) of priority 1 of the document:

*“To promote real time access to reliable data, make use of space and in situ information, including geographic information systems (GIS), and use information and communications technology innovations to enhance measurement tools and the collection, analysis and dissemination of data”.*

In this framework, this thesis presents a methodology for the collection of reliable LC data from satellite imagery, new technologies, such as Unmanned Aerial Vehicles (UAV), and performant data analysis platforms. The LC legend is tailored to Natural Hazard monitoring. It is fundamental to understand the deep connection between geophysical hazards and Land Cover.

Priority 1. Understanding disaster risk: Disaster risk management needs to be based on an **understanding of disaster risk in all its dimensions** of vulnerability, capacity, exposure of persons and assets, hazard characteristics and the environment. Such knowledge can be used for risk assessment, prevention, mitigation, preparedness, and response.

Priority 2. Strengthening disaster risk governance to manage disaster risk: **Disaster risk governance at the national, regional and global levels is very important** for prevention, mitigation, preparedness, response, recovery, and rehabilitation. It fosters collaboration and partnership.

Priority 3. Investing in disaster risk reduction for resilience: **public and private investment in disaster risk prevention and reduction through structural and non-structural measures are essential** to enhance the economic, social, health and cultural resilience of persons, communities, countries and their assets, as well as the environment.

Priority 4. Enhancing disaster preparedness for effective response and to “Build Back Better” in recovery, rehabilitation, and reconstruction: The growth of disaster risk means there is a need to strengthen disaster preparedness for response, take action in anticipation of events, and ensure capacities are in place for effective response and recovery at all levels. **The recovery, rehabilitation, and reconstruction phase is a critical opportunity to build back better, including through integrating disaster risk reduction into development measures.**

**Figure 1.** The priorities of the Senday Framework, (UNDRR, 2015)

### **2.1.1. Land cover as a proxy of climate change and environment indicator**

Disaster mapping has been instrumental in our understanding of climate planning. Risk models represent reality but are only as good as the data used (UNISDR 2015, Magliocca 2013). Effective mapping requires good resolution data in terms of space and time. LC is a valuable tool for monitoring risky areas (Lacoste et al., 2008). Indeed, the systematic study of LC, also named Land Change Science (LCS), helps understand natural hazards, disaster risk, and resilience-related processes. Therefore, to achieve a general understanding of natural hazards and their consequences across different places and times, a synthesis of local land change knowledge collected at varying scales and diverse methods is required (Magliocca et al., 2015).

Natural hazards can be the cause and effect of land cover. It can cause uncontrolled and unmanaged expansions in areas poorly planned, but at the same time, the lack of planning may exacerbate the harmful effects of climate change (increasing the frequency of extreme climatic events) (Pyke and Andelman, 2007). Indeed, the Earth's albedo (Earth's surface reflectance) directly depends on the land cover, and its variation can lead to changes in micro-climate and climate (Dale, 1997). The changes in climatic conditions are not the unique cause of land cover change, but the alteration in land management practices and land use (e.g., agricultural intensification or deforest for cropland) performs a lead role in the phenomenon. The distribution of vegetation strongly depends on the Earth's climate; thus, the alterations in its distribution are a proxy of climate change monitoring. Land cover changes influence and reshape most of Earth's elements cycles by modifying water and energy interrelation with the troposphere and consequentially distorting greenhouse gas and sinks (Townshend et al., 2008). As support of this thesis, land cover characteristics represent the dynamic evidence of ongoing Earth surface processes as part of a global change, which includes the loss of biodiversity and ecosystem functions (due to phenomena such as deforestation, desertification, and unmanaged urbanization) leading to the intensification of extreme natural events (Lacoste et al., 2008). For these reasons, land cover change data have long been used to drive land surface models in climate, water, and ecosystem models (Lacoste et al., 2008), providing predictions and reliable scenarios for the researcher who furnishes synthesized (and elaborated) information to policy-makers. These, based on the information gathered on LCS patterns, may act with strategic applications of specific management practices to increase the resilience of vulnerable ecological systems and facilitate climate adaptation (Pyke and Andelman, 2007). This statement underlines how experts and planners cover a vital role in interpreting the

environmental and ecological impacts of climate change and developing strategies for adaptation (Pyke and Andelman, 2007). Nevertheless, several practical limits to the use of LC-based tools exist, introducing essential considerations regarding the reliability and the effectiveness of data and, consequentially, the information used in climate planning.

Nowadays, enormous quantities of land observations data are collected and regularly used for climate and environmental decision-making, but the lack of global (or regional) standardization of data gathering and elaboration processes makes comparisons between different source data difficult, impeding, or even obstructing, the understanding of land processes at a global scale. As an example, the same land change phenomenon may be interpreted in several ways due to the vast diversity of scientific approaches (Magliocca et al., 2015). Several methods exist for LC analysis, which applies qualitative, quantitative, or both methods. Besides the disharmonized LC methodologies, the insufficiency of data impedes an adequate forecast of disasters' effects and adaptive planning. Frequently, reliable and constant observations are insufficient, and decisions are based on experts' estimations, interpolations, or information extrapolated from spatially incomplete information. Consequentially, the identification, assessment of and solutions to environmental problems are still underdeveloped by our observational capacity, even though several international conventions, such as the Sendai framework, the UN Sustainable Development Goals, and the UN New Urban Agenda (UN, 2016; UNDRR, 2015), and programs explicitly require such information (Townshend et al., 2008). The scientific community defines natural hazards in two classes: the biological natural hazards and the geophysical (Burton et al., 1993). The firsts are connected to biology and epidemiology and embrace hazards, such as spreading infections, human, animal, and plant disease. Geophysical natural hazards are mainly connected to geology and meteorology. Some examples are landslides, eruptions, floods, and wildfires. In this thesis, only geophysical hazards are analyzed. As illustrated in paragraph 2.1, page 9, monitoring natural hazards activities have a crucial role in Disaster Risk Reduction (DRR). In the Natural Hazard Encyclopaedia, monitor is defined as follow (Jaboyedoff et al., 2013):

*“The verb ‘to monitor’ comes from the Latin ‘monere’ which means to warn. In geosciences, it means to watch carefully at a hazardous situation and to observe its evolution and changes over a period of time. It is also used to define the activity of a device that measures periodically or continuously sensitive states and specific parameters”.*



Thus monitoring means detecting the changes in hazardous situations and tracking the evolution of the parameters that influence the phenomenon and the ones that are influenced by it.

Monitoring geophysical natural hazards is undertaken through specialist data gathering and communication systems, exploration, site visits, and collaborative studies of current and historical events. In past times, the only way to periodically measure those changes was via land survey, but, thanks to the new technologies, today, hazards can be remotely monitored. These techniques are ascribable to the class of remote sensing. The two methodologies are not mutually exclusive: nowadays, monitoring activities are often realized via remote sensing and validated through direct data collection in the field (Kustas and Norman, 1996; Rogan and Chen, 2004; Shalaby and Tateishi, 2007; Sobrino and Raissouni, 2000; Zhang et al., 2003). In this work, both phases (remote data collection and validation) are taken into consideration. The LC establishes the baseline for monitoring and provides the ground cover information for baseline thematic maps (Natural Resources Canada, 2016).

## **2.2. Criticalities of Land Cover monitoring**

As underlined previously, Land Cover plays a key role in environmental monitoring, but also in many other disciplines, such as sustainable land management, land resource monitoring, urban vegetation mapping landscape ecology, and climate-related researches (Feng et al., 2015; Rizeei et al., 2016; Sekertekin et al., 2017; Shelestov et al., 2017; Turner and Gardner, 2015). The wide spectrum of land cover maps' applications makes them highly demanded (Carrasco et al., 2019; Delalay et al., 2019; Sekertekin et al., 2017; Thanh Noi and Kappas, 2018).

Land Cover maps are commonly derived from machine learning classifications of satellite optical imagery, which represents one of the prevalent applications of remote sensing, and many authors have described it (Achard et al., n.d.; Aksoy et al., 2009; Baamonde et al., 2019; Carrasco et al., 2019; Delalay et al., 2019; Ghamisi et al., 2019; Herold et al., 2008; Rizeei et al., 2016; Sekertekin et al., 2017; Shelestov et al., 2017; Sidhu et al., 2018; Thanh Noi and Kappas, 2018; Yu et al., 2014). In the last decades, satellite land cover research has spread, followed by Unmanned Aerial Vehicles (UAV) for image classification. According to the literature review of (Yu et al., 2014), who analyzed 6771 papers on land cover, 87.9% of existing works have been realized starting from 2000.

This exponential growth is attributable to four main factors:

- i. The availability of free satellite datasets (such as Landsat and Sentinel) (Yu et al., 2014)
- ii. New Earth observation programs and missions (such as Sentinel) (Yu et al., 2014)
- iii. The diffusion and affordability of more powerful analysis devices (Gavish et al., 2018)
- iv. The development of more sophisticated classification algorithms that permit the reduction of human contribution in LC analysis (Gavish et al., 2018)

Indeed, LC classification has taken significant steps forward: a wide range of free satellite medium-high optical imagery, reduction of the cost of UAV, specific classification algorithms, many processing platforms and machines with more and more high computational power are now available (Carrasco et al., 2019; Khatami et al., 2016; Lu and Weng, 2007; Rizeei et al., 2016; Sidhu et al., 2018; Yu et al., 2014). Apparently, besides the increasing Land Cover application, the past twenty years have been witnesses of a general growth of the classifications' accuracy (Yu et al., 2014). Besides today's achievements and high availability of information, the generation of land cover maps through remote sensing techniques still faces some major constraints. Taking apart the limitations regarding the analyst's choices (and his/her experience), such as the design of the classification methods, the selection of appropriate algorithms, eventually the identification of correct and significant training sample, which will be explored in Chapter 4, the remaining constraints can be grouped in environmental constraints and technical constraints. The environmental constraints regard the typical characteristics related to the area to be classified. Indeed the major limits depend on the landscape's complexity, namely the topography, the degree of heterogeneity of the land cover, the seasonality, and the climatic conditions. On the other side, the technical constraints are related to the limit of the technology and the tools necessary for the Land Cover Maps generation.

The technical constraints depend on the characteristic of the sensor selected for the data collection. Thus, they vary according to the sensor selected by the analyst. Since several sensor data sources are readily available, the analyst has more choice to select suitable remotely sensed data for a specific study, taking into consideration the relative limitations (Lu and Weng, 2007). Along with the technical characteristics, the economic condition is another essential factor that affects the selection of remotely sensed data and the time and labor devoted to the

classification process, thus affecting the quality of the classification results (Lu and Weng, 2007). Another critical factor affecting the classification data selection is the atmospheric condition (Lu and Weng, 2007). The frequent cloudy or rainy conditions prevent the collection of useful data. The satellites-mounted sensor can capture the images even with rainy or partially cloud covers, but they would result in low-quality data. In the case of total cover, the optical data cannot be used for LC classification, and in the case of partial cover, the missing data can be integrated with time-close information (Carrasco et al., 2019; Dorren et al., 2003). Generally, aerial sensors are not affected by partially clouded data, but they are susceptible to windy and rainy conditions.

Consequently, the areas of the World in which such conditions are frequent are hard-to-map through remote sensing. For example, the rainy season in tropical areas and the desert of sub-deserted areas in which sand storms and the presence of earth particulates in the air may alter the sensed data's spectral value. The weather conditions are limits to the collection of good-quality data, although, even with data collected with good meteorological conditions, it is possible to face criticalities in the classification process. This is the case of heterogeneous areas, in which in few adjacent pixels, different classes exist. This condition decreases the accuracy of the classification. Heterogeneous land is frequent in mixed forests, grasslands, and farmlands (Herold et al., 2008; Yu et al., 2014). (Yu et al., 2014) defined heterogeneity as land cover complexity and indicator for the mapping difficulty of a particular location. Earth's most difficult-to-map areas have not been frequently mapped. Besides the heterogeneity of the land cover, the homogeneity of the land cover types' spectral response is an additional limiting factor. Similar spectral characteristics of land cover classes may complicate the classification process. This is particularly evident for the single-epoch classification of plantations using medium-resolution data (Eisavi et al., 2015). For example, summer crops can be classified as orchards and pastures. The built-up areas may be easily confused with the soils because both are highly-reflectance surfaces. In some areas of the World, the buildings are constructed with local laterite, and buildings' discrimination from bare soils can be very challenging. The intra-annual phenological patterns may help in distinguish the classes. Indeed, some areas present an annual-based land cover change cycle, which can be integrated into the classification ad multi-temporal approach to mitigate the confusion of similar spectral types. For example, agricultural lands in temperate areas have different land cover during the spring and the autumn seasons. Using images collected during the autumn and the spring can significantly help discriminate between crops (Eisavi et al., 2015).

In some areas, the inclusion of spring images allows discrimination between urban areas and soils, which are usually covered by grass in the spring (Eisavi et al., 2015). On the other hand, some land covers' high seasonality might represent a limitation for the generation of orthomosaics and, consequentially, for the classification. The atmospheric disturbance and the high seasonal variability are the main environmental constraints of the land cover classification and the topography variation.

The topography may influence the classification in two ways: by altering the spectral values in satellite imagery, especially in steep areas, and distorting the image, especially in UAV imagery. These alterations are caused by high slopes, such as steep mountainous sides.

Practically, the spread shadows are the main effect of the topography on satellite imagery (Dorren et al., 2003). Shaded areas have lower spectral values, and the classification algorithm might not assign shaded pixels to the correct class. It is not rare that shaded pixels are classified as water. This aspect concern mainly the satellite data more than the UAV because of the extension of the study areas. Generally, UAVs cover smaller areas in which the light condition is uniform.

The image distortion is rare neither. The distorted images can alter the area's texture, making such information not usable as a class discriminant for the classification. For example, the topography-derived distortions alter the spectral value and mismatch data captured from different points of view. This may prevent the correct co-registration of different bands (or datasets). For what concerns the UAV, distorted photograms reduce the accuracy of the Structure from Motion (SfM) -sourced products (i.e., orthophoto and Digital Terrain Models). The topography limitations are partially solved in the pre-processing phase with the topographical correction (presented in chapter 5, paragraph 5.1.4 page 99), even if the classifications might still encounter problems with some spectral types (Dorren et al., 2003) (see the application of topographic correction in Alpine Arch case study, paragraph 7.2, page 162).

Additional factors related to the study environment's specificity are the ease of data collection in the field. In complex landscapes, ground samples are not easy to realize, because in steep mountainous terrain it is very time and labor consuming to obtain such a dataset (Dorren et al., 2003). In some remote areas, the lack of communication infrastructures and/or prohibitive and extreme climatic conditions (poles, deserts) may increase the difficulty for data in field data collection, as happened in the study in Niger (paragraph 8.1, page 193). These unfavorable conditions can be exacerbated by emergencies, like during (or immediately after) natural hazards. The data collection to train and validate models is the limiting

factor for efficient land cover maps generation. Thus, to fully realize the data revolution's potential, it needs to optimize limited and expensive ground-truth data (Gavish et al., 2018).

# Chapter 3

## Sensors and tools for Land Cover Generation

### 3.1. Sensors for remote sensing

Remote sensing encompasses all the techniques for information gathering about objects or areas from a distance that does not include direct contact between the sensor for data collection and the source of data (Chuvienco, 2016). Remote sensing is described in *Introductory Digital Image Processing* (Cowell, 1997; Jensen and Lulla, 1987) as:

*“The art, science, and technology of obtaining reliable information about physical objects and the environment, through the process of recording, measuring and interpreting imagery and digital representations of energy patterns derived from non-contact sensor systems.”*

It is a tool or technique similar to mathematics that uses optical sensors to measure the amount of Electro-Magnetic Radiation (EMR) exiting an object or geographic area from a distance and then extracts valuable information from the data using mathematic and statistical measures. It functions in harmony with the mapping sciences' spatial data-collection techniques or tools, including cartography and Geographic Information Systems (GIS) (Clarke, 2001). Remote sensors can be passive or active. Passive sensors respond to external stimuli. They collect energy that is reflected or emitted from a surface (Earth's surface). The most common source of radiation detected by passive sensors is reflected sunlight (NOAA, 2019).

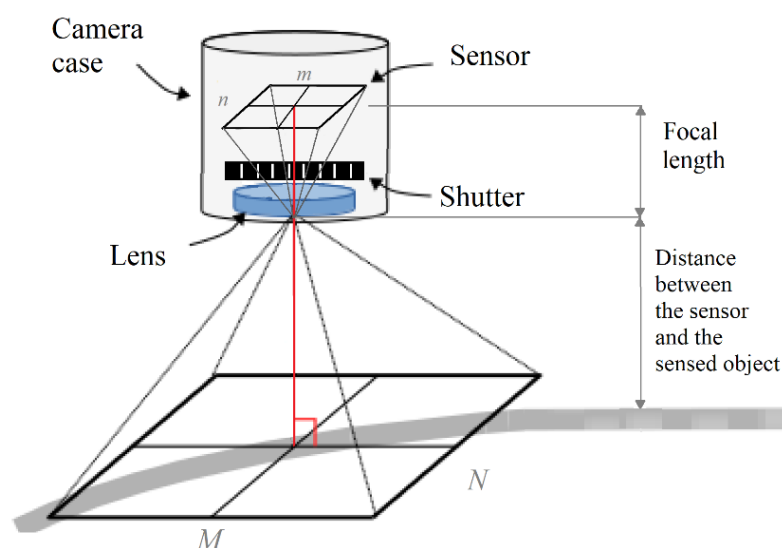
In contrast, active sensors use internal stimuli to collect data about Earth. Active sensors emit the stimuli and record the reflected energy of the stimuli. For example, a LiDAR remote sensing system projects a laser on Earth's surface and measures the time that it takes for the laser to reflect back to its sensor. The raw data of remote

sensing analysis are EMR values of a specific area stored in a fixed-size pattern depending on the acquisition sensor's resolution. EMR values can be collected by different sensors, which in turn can be supported by aerial or terrestrial means. LC usually employs nadiral information collected through aerial means. Figure 3 (Jensen and Lulla, 1987) schematizes the remote sensing process, identifying four steps in *i)* statement of the problem, *ii)* Data Collection, *iii)* Data-to-information, *iv)* Information presentation. For each step, the passages applied in this research are highlighted. This work focuses on passive remote sensing, using only optical multispectral data deriving from sensors installed on satellites and UAV. The Global Navigation Satellite System (GNSS) technique has been used to georeference the multispectral data. The next paragraphs provide an overview of the above mentioned means and sensors.

### 3.1.1. Optical sensors

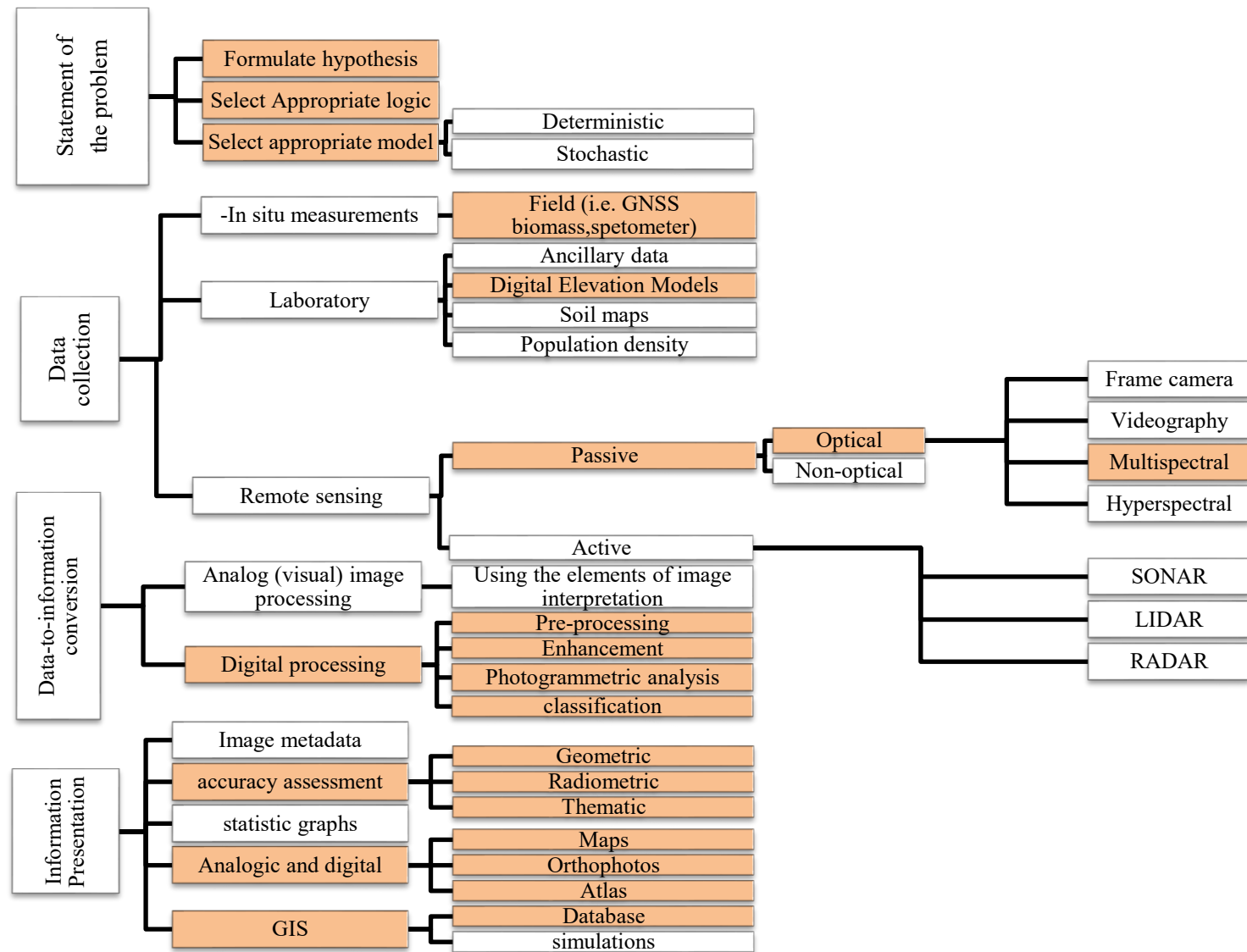
The digital image is a matrix composed of many thousands of single elements, each too small to be individually detected by the human eye. It is acquired using digital optical sensors that record photons reflected from defined portions of Earth's surface. These portions constitute the single unit of the image and are called pixels and together compose the array of discrete brightness that form an image (Campbell and Wynne, 2011). The acquisition of aerial images relies on the digital optical sensor. These sensors are composed of essential components that are common to satellite-mounted, UAV-mounted, and terrestrial sensors (Figure 2):

- i) a lens to gather light to form a scene in real-world;
- ii) a sensor (or detector), which is a light-sensitive surface to record the image;
- iii) a shutter that controls the entry of light;
- iv) a camera case (or body) contains the other components together and maintains them in their correct position.



**Figure 2.** Scheme of a general optical sensor.  $M$  and  $N$  are the dimensions of the image, which is proportional to the dimension of the sensor ( $m$  and  $n$ ). Modified from (Oliveira et al., 2019).

**Figure 3.** Process of remote sensing, describing the steps from the hypothesis formulation to the information. It considers the main existing remote sensing techniques. The highlighted points represent the parts of the process applied in this work (Revised from Introduction to remote sensing, Jensen 1987)

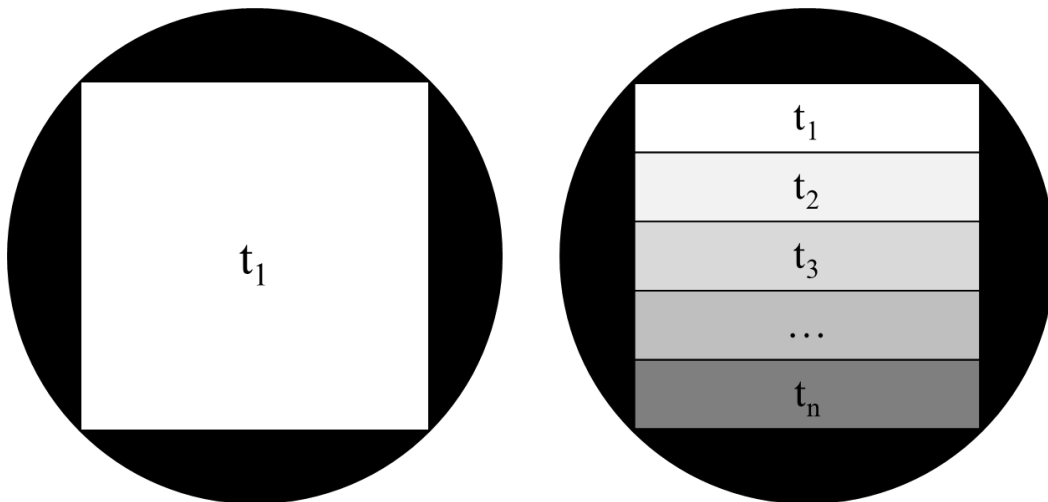




In photogrammetry, the Ground Sample Distance (GSD) is the single-pixel projection onto the Earth's surface. The focal length ( $h$ ) of the selected sensor and the dimension ( $d$ ) of  $m \times n$  size of the sensor, and the distance between the sensor and the sensed object (which in the case of aerial means, it is the height of the flight,  $H$ ) define the GSD according to the following relation (equation 1 ):

$$GSD = \frac{d \times H}{h} \quad [ 1 ]$$

The shutter is a device that allows the light to enter the camera and reach the sensor by opening and closing. Depending on the opening time, a certain quantity of light hits the sensor and influences the final result. Digital cameras can be embedded with a rolling shutter or a global shutter. The global shutter allows the sensor to be entirely exposed simultaneously, and it is generally associated with specific sensors called CCD (see next paragraph). The rolling shutter exposes the sensor line-by-line in the below-second interval, instead of the entire image at once. It is commonly associated with CMOS sensors (Figure 4).



**Figure 4.** Global shutter (left) and rolling shutter (right) functioning. The global shutter at time  $t_1$  exposes the entire frame, while the rolling shutter at  $t_1$  exposes only one line out of  $n$ .

The rolling shutter may cause distortion when the sensed object is fast-moving. This happens because the sensed object moves/changes when the shutter moves from time  $t_n$  to  $t_{n+1}$ . Consequentially, the distortion can be because also if the scene is static, but the means of acquisition is moving, such as images captured from cars and aerial vehicles. Figure 5 shows the typical effects of a rolling shutter.

Two main typologies of digital sensors exist, and they are classified according to the nature of the detector chip. Detectors are chips made of light-sensitive substances that generate minute electrical currents when they intercept photons from the lens. They create an image from the matrix of brightness proportional to the strengths of the electrical charges that reach the focal planes (Campbell and Wynne, 2011). Detectors can be Charged-Coupled Devices (CCDs) or Complementary Metal Oxide Semiconductor (CMOS) chips.

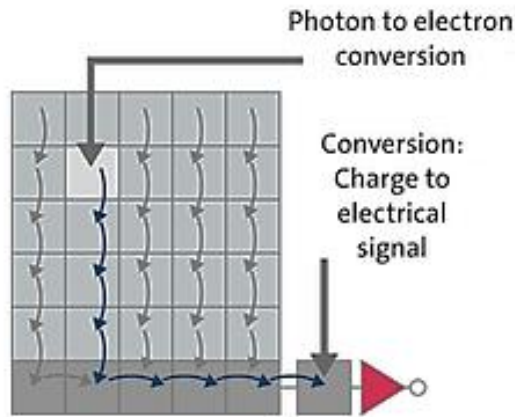


**Figure 5.** Two widespread effects of rolling shutter sensors. An example of the distortions caused by the rolling shutter of a fast-moving object (car) is on the left. On the right, the distortion caused by the rolling shutter is used for capturing an image of a static scene (fence) from a moving means. CC BY-SA 4.0 via wikimedia.

CCDs are formed from light-sensitive material embedded in a silicon chip. They are tiny, usually around  $1\mu\text{m}$  in diameter, and organized in arrays to form a micro-circuit. The light-sensitive part of CCD is stimulated by the photons filtered by the lens (i.e., photodiode). Each CCD transforms the photon stimuli into an electrical charge. Once all the CCD has a small charge, it is transported to an amplifier and then to a transformer to be quantified and converted into a numerical value (Figure 6). CCDs have been widely applied for scientific purposes because they are compact and easily transported and embedded in moving vehicles. Moreover, CCDs are efficient in detecting photons also in reduced light conditions and respond linearly to brightness. Thus they produce a high-quality picture. These aspects influence the use of CCDs in aerial photogrammetry, which has been relied on CCD-based linear arrays to acquire imagery line by line as the satellite's motions carry the field of view forward along the flight track.

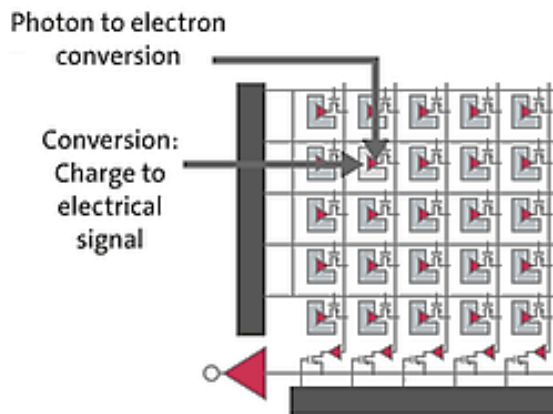
Contrary to CCDs, the CMOS sensors do not expose all the pixels (each photodiode) to the light simultaneously, but a single line at a time. While data from a line are transferred and stored, the next line is exposed. Therefore, pixels within

a CMOS image are not exposed simultaneously, but the data storage is relatively quick.



**Figure 6.** Representation of the CCD sensors that have only one converter of charge. The charges are moved within the sensor photocells to reach the converter, from <https://meroli.web.cern.ch>.

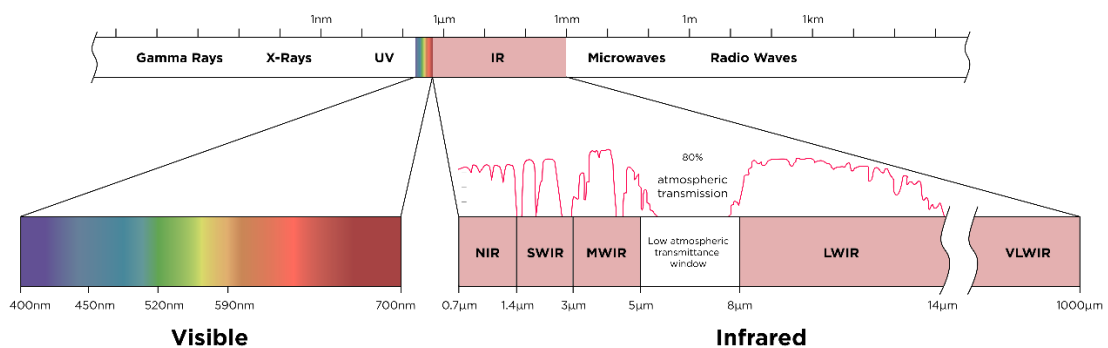
CMOS are composed of one sensor for each resulting pixel, and the quantification and conversion is realized at a single sensor level and not by an amplifier. They can be assembled with fewer components and generally require less power than CCDs. These aspects make CMOS widely used for low-cost and low power requirements devices (Figure 7).



**Figure 7.** Representation of the CMOS sensors that have one small converter for each photocell. The conversion of charge happens in the photocell fastening the image acquisition process. From <https://meroli.web.cern.ch>.

Today CMOS sensors dominate the image detectors market. Because they ensure good data quality with minimum data consumption in rather quick acquisition time. Nevertheless, CCD still dominates the space applications; for example, a CCD sensor is mounted on Sentinel 5 satellite and Hubble telescope.

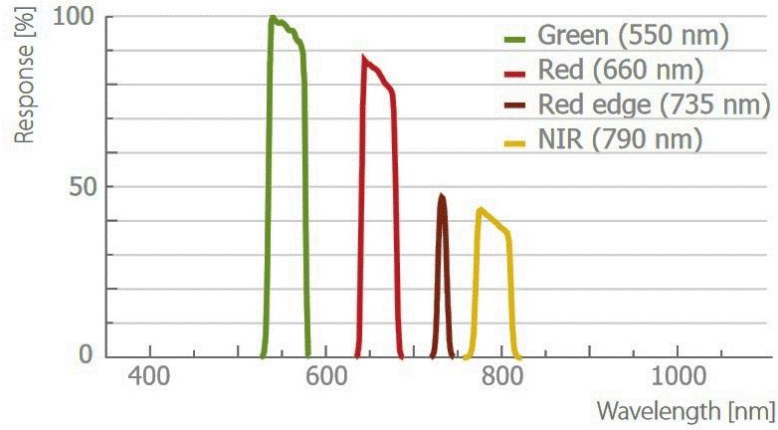
Regardless of the type of detector, optical sensors are sensitive to a specific portion of the electromagnetic spectrum (Figure 8) that usually encompasses the visible spectrum (with a maximum in the green region) and the InfraRed (IR). Most sensors can capture imagery in visible light that is perceptible to the human eye. Optical visible light cameras operate in the wavelength range, approximately from 400 to 700 nm (Pádua et al., 2017).



**Figure 8.** Electromagnetic spectrum. Optical sensors are generally sensitive to the visible (400nm) till the Short Wave Infrared (SWIR) (3000nm), (Akhluofi and Bendada, 2013).

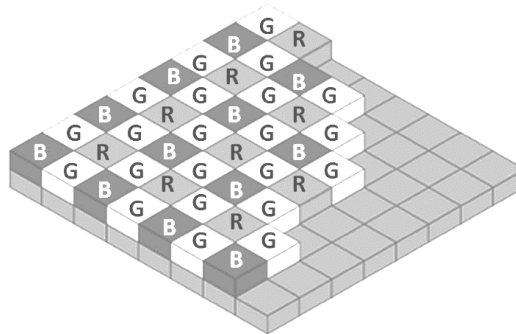
For remote sensing purposes, the digital sensors must have spectral sensitivities focused on a narrow range of wavelengths of the electromagnetic spectrum. The sensitivity of a sensor is defined as spectral detail or spectral resolution. It indicates the portions of the electromagnetic spectrum that stimulate the sensor. Each portion has an image output called *band*. The set of outputs from each band of the same sensor is defined as a multi-band image. The aspects that describe the spectral resolution of a sensor are the peak of sensitivity for each band and the bandwidth. The peak allows the analyst to describe a specific feature from a spectral point of view, while the bandwidth indicates the precision of the band's spectral description. For example, the *Flavescence dorée* is a vineyard disease which is spectrally manifested by a decrease of the reflectivity between 500 nm and 700 nm and an increase of reflectivity between 800 nm and 1300 nm (Al-Saddik et al., 2019). To correctly monitor the effect of *Flavescence dorée* a sensor sensitive to the spectral range affected by the disease is needed. Moreover, the bandwidth should precisely describe that range. Particularly a band that peaks at 600 nm and has a bandwidth

of 200 nm would be acceptable for monitoring *Flavescence dorée* (Al-Saddik et al., 2019).



**Figure 9.** Example of sensor sensitivity. The spectral sensitivity represents in the graph is of Multispec 4C camera by Sensefly, (Sensefly, 2014).

Sensors can achieve band information using multiple cameras/lines (one per band) or the Bayer filter (Remondino, 2011). Bayer filter is a specialized filter applied to select the wavelengths that reach each pixel. A Bayer filter is specifically designed to allocate 50% of the pixels in an array to receive a specific wavelength (generally the green for the visible light sensor, because the human eye is susceptible to green light) and 25% each to other wavelengths.



**Figure 10.** Bayer filter. Each cell stores data of Blue (B), Green (G), or Red (R) information. Then, each color band is interpolated to fill the data gap, (Campbell and Wynne, 2011).

The missing values for the omitted pixels for each band are then interpolated (or extrapolated). For example, the blue recorded pixels are used to interpolate the blue values omitted in the array and complete the blue band. Bayer filter has been optimized and primarily used for NIR cameras (Campbell and Wynne, 2011).

Another essential aspect of optical sensors is the number of pixels composing the sensor. The number of pixels of the sensor indicates the number of photodiodes (in CMOS sensors), which is proportional to the final pixel's spatial resolution. This aspect is particularly important in aerial images since the number of pixels, and the sensor defines the Ground Sample Distance during the acquisition (Equation 1). The optical sensors can be embedded in different platforms for data acquisition. Only satellite and Unmanned Aerial Vehicles (UAV) will be analyzed for the purpose of this thesis. The optical sensors embedded on satellite platforms are built *ad hoc* and have the specific characteristics to function outside the Earth's atmosphere.

### 3.1.2. Satellite

In the last two decades, land quantitative synthesis analysis has been frequently realized via remote sensing using satellite imagery (Anderson, 1976; Herold et al., 2008; Leone et al., 1995; Wu and Li, 2009; Yuan et al., 2009). Remote sensing techniques via satellite imagery had been a revolutionary and powerful tool for monitoring the Earth's surface on a global, regional, and local scale, providing important information regarding coverage and cover features.

The Earth observation constellation of satellites continually provides a broad collection of optical imagery, which differs in terms of spatial, spectral, radiometric, and temporal resolutions. The *National Aeronautics and Space Administration* (NASA) of the United States and the *European Space Agency* (ESA) provide public access to satellite imagery collections of most of their constellations. The range of available and free products are continually increasing. Since the launch of the first civil satellite for Earth observation (NASA Landsat mission in 1972), the satellite image's spatial resolution has dramatically improved, making the GSD reaching 0.10 m at the nadir in panchromatic images (Al-Wassai and Kalyankar, 2013; Maglione, 2016).

The resolution is defined as:

*“The ability of an entire remote-sensing system to render a sharply defined image.”*

(Jensen and Lulla, 1987)

Nevertheless, satellite optical sensor limitations are most often a severe drawback. Even if satellite platforms have a frequent revisit time, no single sensor offers at the same time the optimal spectral, spatial, and temporal resolution for

detailed scale analysis. Table 5 contains an overview of the existing Optical satellite imagery products and their main resolution characteristics.

**Table 5.** Most popular commercial VHR and HR satellites. The table shows the main characteristics and parameters. The interval bands are referred to as panchromatic. (P) Indicates payment services and (F) the free to download ones. The temporal resolution varies based on the inclination of the satellite on the earth's surface. V in spatial resolution means “visible”, PAN means “panchromatic” and MS means “multispectral”. \*SPOT, Sentinel, and Landsat programs’ specifications are considered for the latest satellite in orbit (SPOT-7, sentinel-2B, and Landsat-8) with an exception for the launch date, which takes into consideration the first satellite of the constellation in orbit. \*\*16 days for Landsat 8 and 16 for Landsat 7, but with eight days-offset.

Commercial satellite	Launch	Orbit (km)	Coverage swath (km)	Spatial Resolution (m)	Temporal resolution (days)	Interval Bands (µm)	Note
IKONOS-2 (P)	1999	681	11.3	PAN: 0.82 Ms: 3,28	3	0.335-0.900	mission ended in 2008
QuickBird-2 (P)	2001	350	16.8	PA: 0,61 MS: 2,4	2-12	0.305-1.053	mission ended in 2015
SPOT (1-7) (P)	2001*	822	60	PAN: 1,5 MS: 6	26	0.380-0.710	SPOT 7 ongoing
GeoEye-1	2008	681	5.3	V: 0.50 MS: 2	<3	0.350-0.800	active
WorldView-4 (P)	2016	613	13.1	V: 0.30 MS: 1,2	1.1-3.5	0.450-0.800	active
Rapid eye (P)	2008	630	77	V: 6.5 MS: 6.5	5.5	0.440-0.850	Retired in 2020
Sentinel-2 (F)	2015*	786	290	V: 10 MS: 20	5	0.442-2.202	active
Landsat (7-8) (F)	1972*	703	185	V: 30 MS: 30	8**	0.433-1.390	active

Many events can be studied by analyzing satellite imagery, but the extracted information can be ineffective for small-scale and punctual-shaped phenomena. Free satellite data are available at fixed time intervals (i.e., temporal resolution), preventing a complete analysis of the hazard for lack of data regarding the study period or bad weather conditions (ESA, 2019; NASA, 2019). The increasing number and improving the quality of space-borne sensors have altered the capacity to observe land change (Turner et al., 2007), reducing the information across time

and space. In fact, while satellite imagery is fundamental for a large scale, it is strongly limited for detailed classification (Magliocca et al., 2015). The satellite imaging still depends on atmospheric conditions, although extensive archives are now available, often with stereo-pairs for geomatics applications. This is a gap-filler that brings photogrammetric methodologies closer to traditional remote sensing (Remondino, 2011). Moreover, the satellite data provide information about the top layer covering the land, excluding the lower layers' information (vertically developed environments, 45° imagery). In the framework of natural hazard monitoring and detailed land cover studies, the need for new tools for high-precision (better resolutions) is not negligible.

### 3.1.3. UAV

The UVS international<sup>1</sup> define Unmanned Aerial Vehicles (UAVs) as generic aircrafts designed to operate with no human pilot on-board. UAVs are known by several names. Among the others, *Unmanned Aerial Systems* (UAS), *aerial robot*, *Remotely-Piloted Aerial Systems* (RPAS), or simply *drones* are the most popular terms. UAVs' usage has gained approval in the scientific community for different applications related to acquiring information, becoming common in a wide range of applications, and geospatial research (D'Oleire-Oltmanns et al., 2012). The cost-effectiveness of these technologies (compared to traditional ones, such as field surveys and aerial photos from aircraft) is partially responsible for UAVs' increasing popularity. An additional factor contributing to their popularity is that they can be equipped with several sensors, such as optical and hyperspectral camera, Laser, SAR, IMU, GPS (D'Oleire-Oltmanns et al., 2012; Hruska et al., 2012; Skoglar et al., 2012). Today, using only a simple optical Near InfraRed and visible sensor grants the possibility to apply several radiometric indexes, performing meaningful analysis useful for most scientific applications.

The numerous applications of UAVs in the geospatial realm generally fall under the *detailed mapping* activities. Contrary to traditional ground surveys, UAVs can cover large areas in a relatively short time (Banu et al., 2016). Moreover, the cost-effectiveness and low time consumption allow frequent repetition of surveys to facilitate the multi-temporal studies and monitoring activities. Compared to satellite systems, UAVs can acquire imagery more often than satellites, allowing users to collect information whenever moment (e.g., immediately after extreme events, specific punctual conditions, etc.). Besides these innovative aspects, UAVs'

---

<sup>1</sup> UVS is a non-profit international association focused on UAV activities, <http://www.uvs-international.org/>



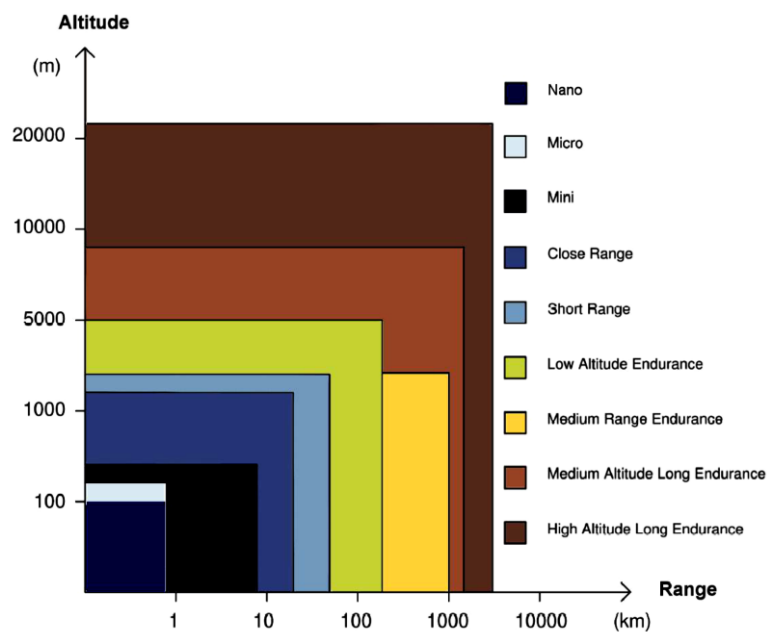
flights are strongly conditioned and limited by the low-atmospheric conditions: heavy rain, strong winds, and fog may impede the data collection.

Additionally, UAVs are limited in the equipment that they can carry onboard (Paneque-Gálvez et al., 2014), and the autonomy of the survey depends on the battery system. In some areas of the world, traditional field surveys can be problematic. This is particularly true in areas where dangers to personnel exist. For example, in post-hazard areas in which structures have collapsed or explosions have occurred (Towler et al., 2012). UAV system has been widely used in these dangerous conditions, like in Fukushima after the nuclear reactor explosion. Considering that UAVs are generally cheaper and more versatile than traditional remote-sensing techniques, they can be a valuable alternative for acquiring imagery and other physical parameters before, during, and after a natural hazard event (Giordan et al., 2017).

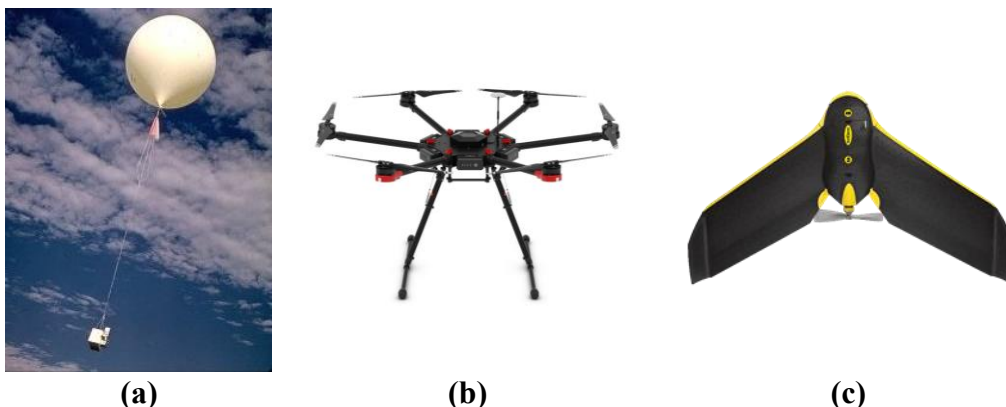
UAVs systems' continuous and fast evolution has made necessary the constant categorization of such systems by the scientific community. There is not a unique and universal classification of UAVs (Colomina and Molina, 2014; Nex and Remondino, 2014), although UAV systems are usually classified according to the weight-based system (i.e., Maximum Take-Off Weight, MTOW), and the flight range (Colomina and Molina, 2014). The flight range is meant as the farthest operating distance from the location of the ground control. The MTOW indicates the maximum weight (the entire system, sensors included) that allows the drone to take off. One of UAVs' first proposed classifications is based on the flight range and the MTOW (van Blyenburgh, 1999). The *Medium Range Endurance* group encompasses the UAVs that can fly over the stratosphere. They are complex technologies and are only allowed to fly under specific special regulations by ultra-qualified teams, generally military units. The *close-short-medium-range* UAVs are characterized by a MTOW between 150 and 1250 kg and an operating range between 10 km and 70 km. Finally, the *nano-micro-mini* UAV class is defined by low flying altitudes and an operative range of fewer than 10 km. Quick operational deployments characterize these systems; they are allowed to fly lower than national ceilings of segregated airspaces. The power autonomy is generally less than two hours, and the MTOW is 30 kg. The *nano-micro-mini* UAVs represent the largest group, and they are broadly used in the detailed mapping. It is worth underling that the MTOW specifications may vary from country to country depending on the national legislation. Figure 11 shows the distribution of drones based on the height range and the maximum distance (van Blyenburgh, 1999).

An alternative classification adopted for the UAVs regards the physical features, and it is possibly the most frequently used in the geomatics realm. This

classification is based on the technology adopted for the flight (Nex and Remondino, 2014). The UAVs group *lighter than air*, do not need engines nor fuel to flight (e.g., kites, balloons) (Figure 12a). The *multirotor* group includes the UAVs equipped with propellers. They can be either electric or with a combustion engine (e.g., single-rotor, multi-rotor, multicopter). The structure often reminds of helicopters (Figure 12b). Finally, *fixed wings* are able to fly thanks to structures similar to the ones of airplanes, based on the physical lift force (Figure 12c).



**Figure 11.** UAV classification is based on the height range and the maximum distance, according to (van Blyenburgh, 1999).



**Figure 12.** a) Example of lighter than air UAV. The balloon with an inboard sensor; b) Example of multirotor UAV. This is an exacopter (6 propellers) produced by DJI called MATRICE 600; c) Example of fixed-wing UAV eBee classic.

In geoscience applications, mini- and micro- UAVs are the most used systems in both multirotors and fixed-wings type. Although they are both efficient for mapping purposes, they differ in several aspects. Due to their structure and the engines' redundancy, the multi-rotors systems are more stable than fixed-wings systems. Moreover, they can be flexibly piloted, allowing the pilot to collect with ease information from different angles (i.e., oblique acquisitions). On the contrary, fixed-wings systems can acquire only nadiral information, but their endurance is generally higher than their maximum flight altitude, making it possible to cover larger areas at an equal time of flight.

Fixed-wings cannot hover on a fixed point, but they are generally more user-friendly and easy to use, as long as the systems are integrated with GNSS systems for take-off and landing. Fixed wings can land only horizontally; thus, they need a clean and non-obstacle space, which can be challenging in some areas (e.g., cities, forests). On the other hand, multi-rotors can perform the vertical landing in less space. Both can be equipped with different sensors, limited by the maximum payload and the available power. (Nex and Remondino, 2014) proposed a table to summarize the main characteristics and differences between fixed-wing and multi-rotor systems with electric and Internal Combustion Engine (ICE). Table 6 proposes the same analysis but considering electric motors only and the advancement of UAVs' technologies till today.

**Table 6.** Evaluation of UAV platforms performances in geomatics applications. The evaluation ranges from 1 (very low) to 5 (very high), n.a. means “not available”. It was adapted from the work of (Nex and Remondino, 2014).

	<b>Lighter than air</b>	<b>Rotatory</b>	<b>Fixed-wings</b>
Payload	3	4	3
Wind resistance	4	3	2
Minimum speed	4	4	2
Flying autonomy	n.a.	2	3
Portability	3	3	2
Landing distance	4	4	3


The spreading applications of UAVs are also attributable to the versatility of the technology and the possibility of being equipped with many different sensors, with the limit of the size and the weight. Besides the fundamental navigation sensors, the most common sensors are cameras, multispectral sensors (Baluja et al., 2012; Berni et al., 2009.; Kelcey and Lucieer, 2012) and LiDAR (Light Detection and Ranging) (Chisholm et al., 2013; Tulldahl et al., 2015; Wallace et al., 2012). UAVs can fly autonomously, using an integrated GNSS system, stabilizer platform,

and data collection sensors. However, on-board sensors' choice must be compatible with the UAV's payload capacity and the application requirements. Some of the most sought-after characteristics of on-board sensors are the low-costing (Aden et al., 2013; Kingston and Beard, 2003), the customizability, and the lightweight. Several low-cost optical multiband sensors have entered into the market in the last few years, providing UAV-users with several solutions. Besides these, inexpensive alternatives to commercial radiometric sensors exist. UAV can benefit from a large scale of mass-market cameras to professional-grade cameras with prices varying accordingly. In the next paragraphs will be briefly presented today available sensors that can be embedded into UAV systems. They are presented in groups based on their spectral sensitivity: visible, InfraRed, Thermal, and Multispectral.

### *RGB sensors*

The RGB cameras acquire the visible part of the electromagnetic spectrum and do not differ from sensors for non-photogrammetric purposes. Recent UAV models have an RGB camera embedded in the UAV system and synchronized with it. In this way, the pilot has direct control over the camera during the flight. Table 7 displays some examples of the currently used RGB cameras suitable for UAV and generally for photogrammetric applications.



**Table 7.** Examples of optical cameras commonly used on UAVs for RGB image acquisition. The price is expressed using the following scale: \$ = 100 – 600\$; \$\$ = 600 – 2000\$ ; \$\$\$ = >2000\$.

Name	Type		Embedd ed in the UAV system	Spectral resolution	MP	Price
S.O.D.A.	BSI CMOS		Yes, eBee	RGB	19.9	\$\$
Sony ILCE- 5100	APS-C CMOS		No	RGB	20	\$
Phantom 4 Advanced	CMOS		Yes, phantom DJI	RGB	20	\$\$

### *Infrared sensors*

The infrared portion of the electromagnetic spectrum ranges from around 700 nm (Near InfraRed) to 10,000,000 nm (Far InfraRed, FIR), covering longer wavelengths than the visible spectrum. The boundaries of the infrared spectrum, between NIR and visible from one side and between FIR and microwave on the other, are still discussed (Pádua et al., 2017). The spectrum approximately between 700 nm and 850 nm represents the NIR region, and it is typically where plants have the highest reflectance. This makes the NIR information crucial for most vegetation-related studies, such as agriculture, forestry, algae monitoring, etc. NIR sensors are frequently used in precision agriculture and constitute the basis for vegetation analysis. Healthy vegetation that is actively growing and producing energy from photosynthesis absorbs in red (the red light stimulates photoreceptors of the chlorophyll) and reflects more in the NIR region. Vegetation with very low reflectance in the red channel and very high in the NIR channel can be defined as strongly photosynthetic and thus very healthy. Most of the standard commercial cameras have filters blocking NIR. However, it is relatively easy to transform an RGB camera into a NIR camera by removing the filter and replacing it with one that is filtering the visible red, green, or blue bands. Table 8 shows some RGN camera in which the IR blocking filter was removed.

**Table 8.** Examples of optical cameras commonly used on UAVs for NIR image acquisition. The price is expressed using the following scale: \$ = 100 – 600\$; \$\$ = 600 – 2000\$ ; \$\$\$ = >2000\$.

Name	Type		Embedded in UAV	Spectral resolution, band width	MP	Price
Mapir 3N	Sony Exmor R IMX117 CMOS		No	R: 655 nm, n.a. G: 550 nm, n.a. N: 850 nm, n.a.	12	\$
Canon S110 NIR	back-illuminated CMOS		Yes, EBee Classic	R: 625 nm, 100nm G: 550 nm, 100nm N: 850 nm, 150nm	12.1	\$\$

While NIR is totally invisible and imperceptible for humans, FIR can be experienced as heat. Thermal cameras operate approximately in the spectrum at wavelengths from 5000 to 14,000 nm. Each pixel's intensity can be transformed into a temperature measurement. Thermal cameras have several applications,

although NIR cameras are much more expensive, and the spatial resolution is much lower (Mejias et al., 2015).

### *Multispectral sensors*

NIR and RGB sensors can be combined together in multispectral sensors. Multispectral and hyperspectral cameras, meant as devices with more than three acquisition channels, have become commercially available in recent years. Multispectral sensors are usually sensitive between the visible and the infrared, focusing on the Red-Edge (that refers to the portion of the Electromagnetic spectrum between visible light and NIR in which some plants are particularly active). Recently, also ultraviolet light and thermal bands have been included in multispectral sensors. (Nebiker et al., 2008) compared a multispectral camera and a low-cost NIR camera showing significant differences. As expected, the multispectral sensor provided good results, consistent with the reference values obtained by a hyperspectral spectrometer, while the low-cost camera showed a reasonable correlation with the multispectral system with some significant biases. However, high spatial resolution low-cost cameras proved to be useful for the qualitative monitoring of crops, including disease detection. Table 9 presents three examples of multispectral cameras.

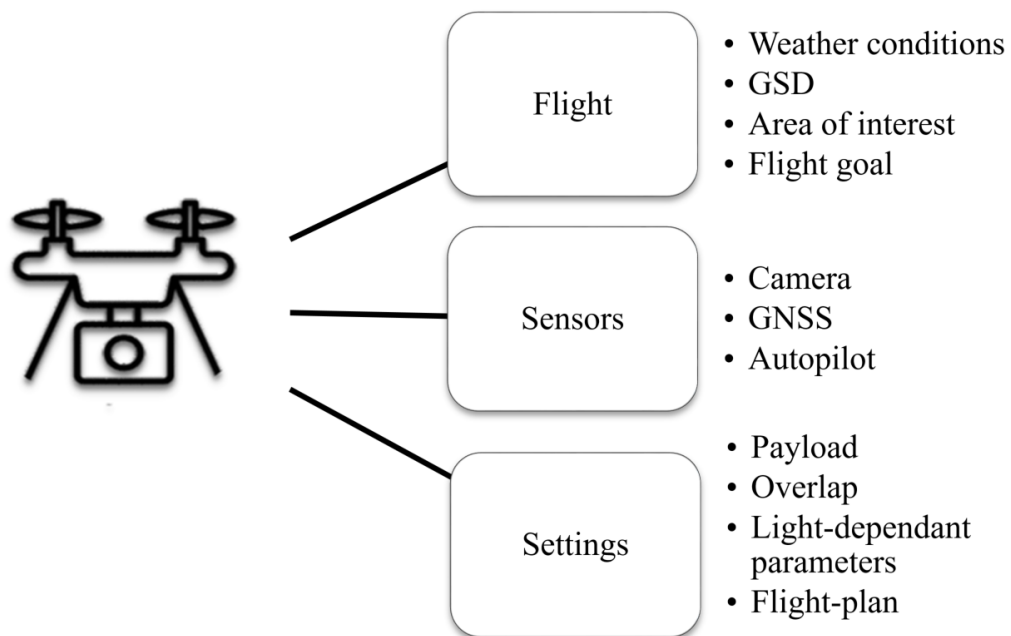
**Table 9.** Examples of optical cameras commonly used on UAVs for multispectral image acquisition. The price is expressed using the following scale: \$ = 100 – 600\$; \$\$ = 600 – 2000\$ ; \$\$\$ = >2000\$.

Name	Type		Embed ded in UAV	Spectral resolution, band width	MP	Price
Slantra nge	Si CMOS		<b>Yes</b> DJI matrice	1) Red wide: 620 nm, 110 nm 2) Green: 520 nm, 110 nm 3) Blue: 470 nm, 110 nm 4) Red Edge: 715 nm, 30 nm 5) Red narrow: 650 nm, 40 nm 6) NIR: 850 nm, 70 nm	3.2	\$\$\$
multiS PEC	CMOS		<b>Yes</b> eBee classic	1) Green: 550 nm, 50 nm 2) Red: 660 nm, 50 nm 3) Red Edge: 735 nm, 40 nm 4) NIR: 790 nm, 50 nm	1.2	\$\$\$
P4 multis pectral	CMOS		<b>Yes</b> Phanto m 4	1) Red: 650 nm ± 16 nm 2) Green: 560 nm ± 16 nm 3) Blue: 450 nm ± 16 nm 4) Red Edge: 730 nm ± 16 nm 5) NIR: 840 nm ± 26 nm	2.08	\$\$\$

Multispectral cameras sense few wide bands compared with hyperspectral cameras, capable of sensing hundreds of narrow bands, up to 2 nm in wavelenght. These cameras are the most innovative optical sensors that can be mounted on UAVs. Although, they have different functioning and structure with respect to traditional multi-band sensors. For this reason, they are not analyzed in this work.

### *Characteristics of the UAV flight and planning*

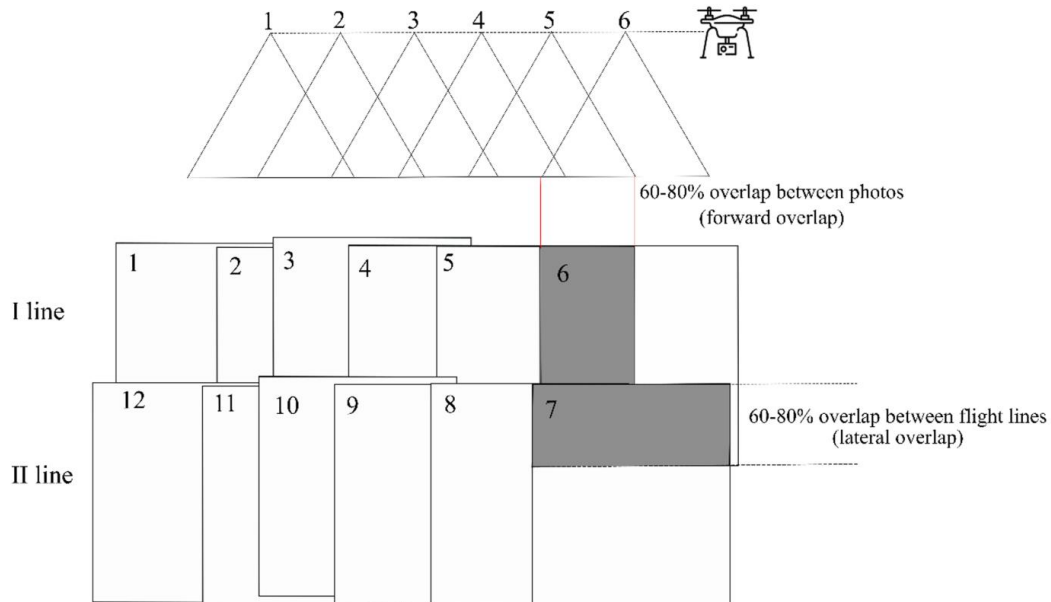
A fundamental aspect of UAV data collection for geomatics applications is the flight planning or mission plan. The planning phase aims to find the balance between the data requirements and the available UAV platform, the sensors, and the survey's goal. It is generally realized in a laboratory using specific software. The input data are the knowledge of the area of interest, the needed Ground Sample Distance (GSD), the type of datum (multispectral, NIR, thermal, etc), the available UAV platform, and the information needed from the survey (**Figure 13**).



**Figure 13.** Main variables that should be taken into consideration on mission planning phase.

The camera perspective centers (or waypoints) are computed fixing the forward (or longitudinal) and lateral (or transversal) overlap of the flight-lines, which generally ranges between 60% and 80%. The overlaps it is fundamental for the Structure from Motion (SfM) technique (paragraph 3, page 103). Large overlaps

compensate for aircraft instability (typical of mini UAVs) to reach enough overlaps for finding the conjugates for the SfM process. To achieve small GSDs high overlaps and low-altitude flights are usually needed (Figure 14).



**Figure 14.** Example of lateral and forward overlap of a UAV flight. Image modified from <https://www.nrcan.gc.ca/>.

Once the mission is planned, it is possible to realize the flight. It can be manual, autonomous, or assisted. These three flight modalities differ in the number of inputs of the pilot during the flight. Experience shows that a careful design of the UAV trajectory (lines, height, speed, etc.) and a flexible real-time mission management capacity (flying directions, sensor configuration, triggering events, etc.) are instrumental in achieving productive and safe acquisition missions (Colomina and Molina, 2014). The GNSS navigation device is a fundamental component for the autonomous flight (take-off, navigation, and landing) and guides the image collection. The GNSS, along with the navigation system, can facilitate image acquisition. The autopilot performs a flight according to the planning and communicates with the platform during the mission. It is worth mentioning that these GNSS systems have been proven to be sufficient for auto-piloting but not for accurate georeferencing (Piras et al., 2010).

UAVs equipped with double-frequency GNSS for RTK positioning exist. These systems can improve the quality of positioning to a decimeter level, but they are expensive solutions (Nex and Remondino, 2014).



Besides the above mentioned principal aspects, in mission planning, several secondary aspects should be taken into consideration:

- i) The **characteristics and the size of the area to be covered** in relation to the space needed for the take-off and the landing and any obstacles or obstructions present in the area;
- ii) The **flying height variations** according to the topography of the surveyed area;
- iii) The **required and available payload** in relation to the expected final result;
- iv) The **overlapping images** from multiple locations and angles (acquisition of the same feature from multiple angles to reduce occlusions and systematic errors);
- v) The **features to be reconstructed should be visible at least in three images** (five or six images for dense vegetation);
- vi) The **illumination conditions**, the scene must be sufficiently illuminated (constant lighting is preferable);
- vii) The **features of interest** should be fixed (e.g., no movement from branches in the wind).

In mission planning, the users have many parameters that vary depending on the equipment and pursued results. For some equipment, the users have full control during the flight (e.g., ISO, shutter speed), although several other can only be estimated in the planning phase. The factors influencing the success of a UAV survey (meant as the planning and data collection as a whole) can be divided into four categories (Iglhaut et al., 2019), as presented in Table 10.

**Table 10.** Factors influencing a UAV survey and some recommendations to improve the quality of the acquisition. The recommendations are focused on forest surveys, (Iglhaut et al., 2019).

Category	Variable	Recommendations
Scene	Texture	High surface contrast to allow for small features detection
	Pattern repetition	Increase overlap and increase the number of geotags
	Moving features	Avoid, if possible.
	Occlusions	Increase overlap and viewing angles
Lighting conditions	Sun angle	Possibly high. Solar noon is ideal to avoid shading
	Weather	Overcast provides is acceptable for structural (RGB) surveys. For spectral surveys, a clear sky is recommended.
	Changing illumination	Avoid it if possible.
Camera parameters	Focal length	Wide but not too wide to minimize distortions. 28–35 mm is a good basis.
	Exposure	Well exposed.
	Aperture	f/8 an advisable default
	Shutter speed	High for reduced motion blur, but depends also on the ground speed (m/s)
	ISO	Low for min noise, auto-ISO an advisable default
	Pixel pitch	As high as is practical. Physical pixel size positively influences dynamic range and sensitivity
Survey characteristics	Overlap	High (> 80% forward and lateral). Especially for high patten reptition surveys to increase redundancy and matchability.
	View angles	Convergent for reduction of systematic errors (RGB) Parallel (Nadir) for multi-spectral sensing (reflectance)
	Survey range	With increasing distance to the object/scene (decreasing GSD) survey precision degrades. Increased GSD requires a higher overlap.

### 3.1.4. GNSS receivers

The accuracy of the position and the scale of a survey is determined by the referencing approach (e.g., direct georeferencing, manual scaling). When using Ground Control Points (GCPs) and direct georeferencing to obtain accurate results, the Global Navigation Satellite System (GNSS) is compulsory. GNSS refers to satellites' constellation providing signals from space that transmit positioning and timing data to GNSS receivers. The receivers then use this data to determine location. By definition, GNSS provides global coverage. Examples of GNSS

include Europe's Galileo, the USA's NAVSTAR Global Positioning System (GPS), Russia's Global'naya Navigatsionnaya Sputnikovaya Sistema (GLONASS), and China's BeiDou Navigation Satellite System (EGA, 2019). GNSS dual-frequency receivers are enhancements to the Global Positioning System (GPS), which provide improved location accuracy from 15 m to about 10 cm (they receive information from GPS and other constellations).

In the past years, GNSS systems have progressively overcome traditional survey methods, becoming standard tools in many sectors. Nowadays, GNSS systems play a lead role in data acquisition thanks to the increasing number of satellites, the low-costing, the efficiency, and the variety of available products. GNSS measures can be acquired through two primary modalities: static or kinematic. In the static survey, the GNSS receiver is positioned on each point to be measured for a few minutes, while in the kinematic survey, the receiver is continuously moving. A typical application of the static mode is the measurement of topographic network vertex, while the kinematic technique is employed mostly for rapid measurement of GCPs using RTK (Real-Time Kinematic) technique. Three main strategies for GNSS data acquisition exist: absolute positioning, relative positioning, and differential positioning (**Figure 15**).

The absolute positioning is the most straightforward strategy. Only one GNSS receiver is needed, which directly receive information from GNSS constellations. This strategy allows for the 5-10m precision, which is usually applied for navigation purposes and not for topographic applications.

In relative positioning, two receivers are used: one is positioned on a known-coordinates point, the second on an unknown-coordinates point. Both receivers positioning information from the GNSS constellations. This strategy aims to estimate the vector connecting the two receivers, which is called the baseline. The relative positioning required simultaneous observations and long stationing time (depending on the baseline length). In relative positioning, the coordinates are estimated *a posteriori*.

In differential positioning, two receivers are used: one is placed on a known-coordinates point (called Master), while the second receiver is placed on an unknown-coordinates point (called Rover). The position of the unknown-coordinates receiver can be established relative to the known-coordinates point by defining the baseline. The estimations are done in real-time thanks to the connection between the master and the rover (radio transmission, internet, GSM).

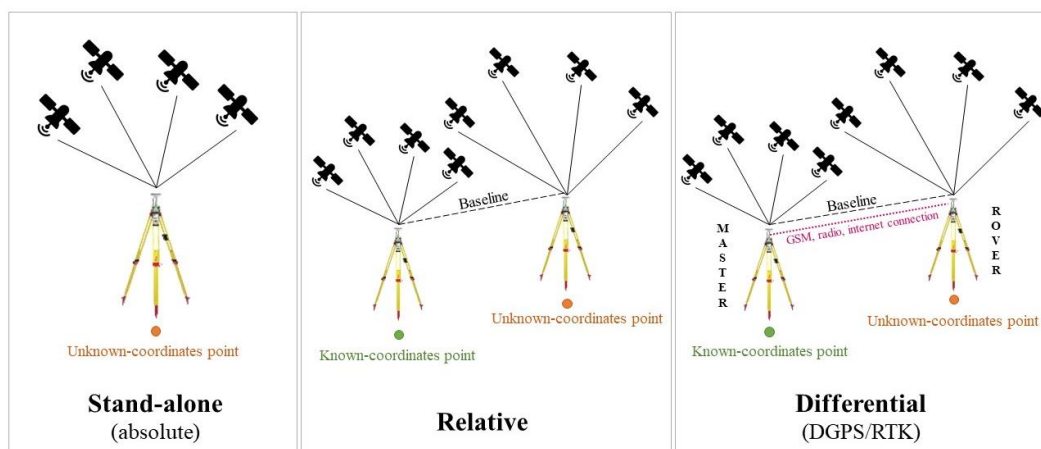
Indeed, from 2002 forward (Eren Kamil et al., 2009), Real-Time Kinematic networks (NRTK) have spread. These networks are composed of GNSS stations of known coordinates, called Continuously Operating Reference Station (CORS), and

managed by a network software installed in a control center. The introduction of the CORSs has allowed users to collect data in differential positioning using one GNSS multi-frequency receiver (instead of two). This is possible thanks to the direct connection between the CORS, through the control center, and the dual-frequency receiver. The NRTK has revolutionized the data acquisition modalities (Grejner-Brzezinska Dorota A. et al., 2007; Rizos, 2007). A dense network of permanent stations is available to process GNSS data (Kim et al., 2014). Despite today CORSs covering most of the world's countries, some areas are still not included in the network, such as some sub-Saharan countries (see paragraph 8.1., page 193). Considering the real-time positioning and the NRTK method, the rover receiver needs to be within a short distance (less than 60 km) from the reference stations. This is fundamental to minimize the distance-dependent errors induced by the troposphere, the ionosphere, and the orbital errors (El-Mowafy, 2012). This specific requirement can be an obstacle for the realization of NRTK surveys where there are no CORS within hundreds of kilometers (Elmezayen and El-Rabbany, 2019). A possibility to overcome the lack of CORS is resorting to two GNSS dual-frequency receivers in the rover-base modality. When a known-coordinates point for the “base” receiver is not available, post-processing operations to obtain the base's correct position is compulsory.

One of the most common post-processing methods is the PPP (Precise Point Positioning). To perform it, data regarding satellites' orbits and the ionosphere are needed to process the pseudo-range and carrier phase measures of GNSS multi-frequency receivers (Bisnath and Gao, 2009; Kouba and Héroux, 2001; Zumberge et al., 1997). These data are collected by permanent stations that can also be located very far from the surveyed area (Kouba and Héroux, 2001). In terms of East, North, and Up components, the PPP can provide centimeter-level precisions in static mode (Bisnath et al., 2003; Pan et al., 2015), if the phase ambiguities are fixed as integer values in a correct way (Collins and Bisnath, 2011; Ge et al., 2008). The precision of the PPP corrections is also strictly dependent on the measurement session's duration (Mohammed et al., 2018; Yigit et al., 2014). Its effectiveness for the estimation of the positions has been demonstrated by several authors (Gao et al., 2003; Gao and Shen, 2002; Kouba and Héroux, 2001; Zumberge et al., 1997), using precise orbits and satellite clocks from IGS (Gao and Chen, 2004; IGS, 2019) and many other providers (Jamieson Marian and Gillins Daniel T., 2018; Mohammed et al., 2018; Wang et al., 2018). Until some years ago, the satellites' data, the ionosphere information, and the specific software that are necessary to perform PPP were not easily obtainable, and consequentially the PPP limited to few expert users, such as academia and research institutes. Today the PPP technique has raised the

interest not only of the academia but also of industry and governments (Bisnath and Gao, 2009). In particular, the last ones have dedicated specific attention to PPP, and some of them shared the socio-economic benefits of PPP with the public, providing *ad hoc* coordinates online estimation services (Bisnath and Gao, 2009).

Regardless of the GNSS strategy adopted, the estimated-coordinates points are used for georeferencing the UAV-models (see paragraph 3, page 103). In this phase, it is fundamental to consider the precision and accuracy of the GNSS survey.



**Figure 15.** Three main strategies for GNSS data acquisition exist: absolute positioning, relative positioning, and differential positioning. Adapted from <http://fig.net/>.

### 3.1.5. Some considerations about UAVs and satellite imagery

The availability of optical remote sensed imagery is limited mainly by weather conditions and, specifically for UAV's aerial images, restrictions on flights. Indeed, among the satellites' technical constraints, the low temporal resolution is one of the most cited (Carrasco et al., 2019; Lu and Weng, 2007; Zhai et al., 2018). To date, most classification methods require input images with few clouds because the presence of cloud cover increases the difficulty of image analysis. However, satellites hardly meet the absence of cloud cover with low temporal frequency, especially in the areas particularly prone to clouds (e.g., monsoon season in tropical areas, autumn in temperate season). The limits caused by the low temporal resolution have been partially overcome with the introduction of medium-high resolution satellites that increase the free data available and make possible integrating the datasets from different acquisitions (Remondino, 2011). However,

integration and high-spatial-resolution require managing a large amount of data, and thus a large amount of storage, as well as significant computing power and time (Carrasco et al., 2019).

On the one hand, the available software may not be able to deal with this large volume of data, while on the other hand, the increased number of input variables may introduce additional complexity regarding the increase of computational time. Managing satellite datasets requires considerable data storage capability, and the high spatial resolution further increases this requirement. Indeed, the antinomy between spatial resolution and computational power is another pervasive technical constraint. During the last few years, some geographic cloud computing platforms that allow the analysis and storage of geographic data were born. These services (such as Google Earth Engine) decrease the computational and storage limits of satellite data processing (Farda, 2017; Kumar and Mutanga, 2018).

It is worth mentioning that satellite imagery is usually more expensive than aerial images (Remondino, 2011). Although they have low spectral resolution compared to satellite imagery, the UAVs' sensors are still very attractive. UAVs' sensors have a wide variety of camera configurations. The new satellite missions with 0.3 m spatial resolution (such as Cartosat-3 and GeoEye-2) will help keep the two technologies closer, particularly for mapping applications (Remondino, 2011).

### **3.2. Tools for data elaboration: proprietary and FOSS software**

Despite the Free and Open Source Software (FOSS) are not the focus of this work, whenever it was possible, they have been used. FOSS are free software which source-code is obtained under a specific license that permits users to use, modify, and improve a product or service. The users are allowed to redistribute the modified-code in the FOSS license. Usually, FOSS are considered in contraposition to proprietary software, which are associated with the copyright holder. Proprietary software has non-public source code, generally are created by private companies, and the users need to pay to use them. There has been significant discussion on the advantages and disadvantages of FOSS against proprietary software. The economic advantages and characteristics of FOSS are persuasive. Singh et al. (Singh et al., 2015) propose an interesting comparative analysis between FOSS and proprietary software. Table 11 proposes a similar analysis.

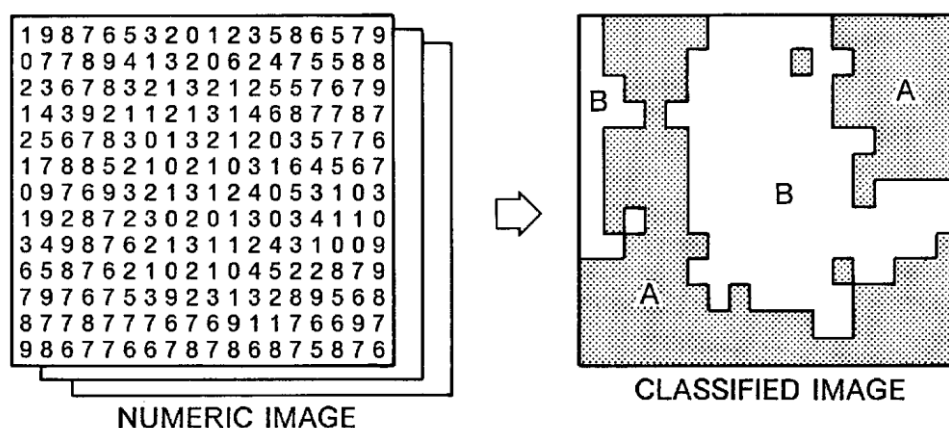
**Table 11.** comparative analysis of FOSS and proprietary software, adapted from (Singh et al., 2015).

<b>Factor</b>	<b>Free Open Source Software</b>	<b>Proprietary Software</b>
<b>Cost</b>	Although open source software vendors are increasingly charging for add-ons, additional administrations, and joining, there is no FOSS cost. Thus the final cost of ownership for FOSS may be equivalent to some proprietary software alternatives.	They are free. Users are charged for the whole work behind the software: programming, administrations, assistance, etc. Generally, the expense guarantees a more tweaked item from a trusted brand that incorporates more massive amounts of security and usefulness, continuous advancement, a more prominent capacity to scale, progressing preparing and packing, and a lower prerequisite for specialized abilities.
<b>Service and Support</b>	FOSS do not provide assistance or support to users. The user can consult specific online community systems and get support from forums and blogs.	Proprietary software suppliers offer progressing backing to clients, a key offering point for clients without specialized mastery.
<b>Innovation</b>	Open source programming empowers innovation by providing users with the opportunity to modify and suit the software, without confinement. This innovation can be transmitted to the community of the users of the software.	Proprietary software's source code is not available for users. This guarantees the security and the quality of the product. Proprietary software suppliers also customize their products for particular clients.
<b>Usability</b>	FOSS are generally created for expert users and specialists. Most FOSS are considered as hardly usable by the larger part of the computer users.	Proprietary software generally invest many resources in usability and user-friendly interfaces.
<b>Security and reliability</b>	Several developers develop FOSS code, and anyone can hinder the security of the software. On the other hand, this may represent an additional security level because more people are looking for potential vulnerabilities to be fixed.	Proprietary software is considered much more secure since it is developed in supervised and trackable conditions only by professional companies.
<b>Availability</b>	Open Source Software is freely available.	Proprietary software are accessible through the developing companies that own the rights. Often trial version or demo version is freely distributed too.
<b>Flexibility</b>	As organizations continually look to do more with less, adopting open source software can deliver greater flexibility.	When using proprietary software, it requires to keep upgrading both software and hardware. Updates must be installed (and paid) for the proper working.

# Chapter 4

## Classification of optical imagery, literature review

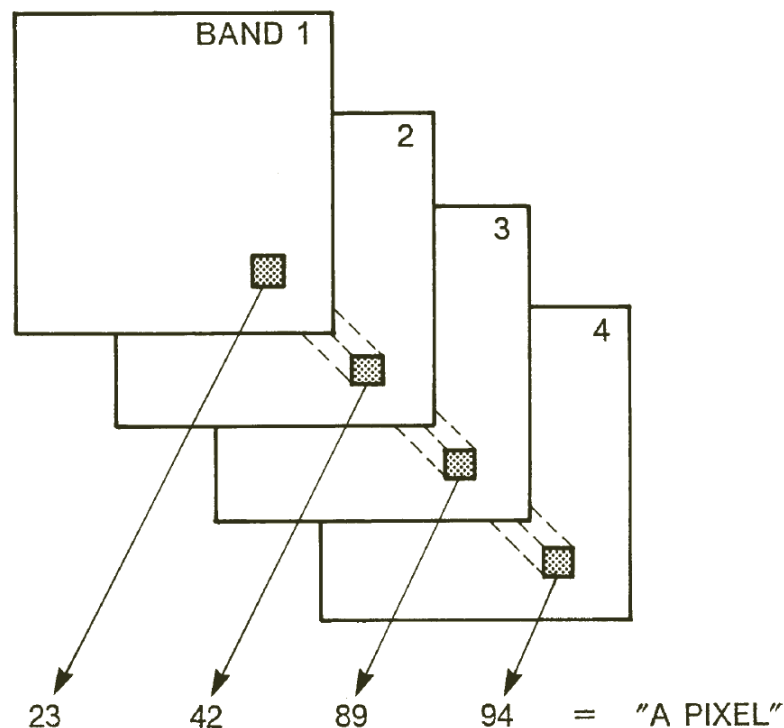
Image classification is one of the most basic operations of digital image processing (Campbell and Wynne, 2011; Jensen and Lulla, 1987). In simple terms, image classification is the process of distributing image into classes or categories of the analogous type by assigning each pixel to a meaningful category (Figure 16) (Campbell and Wynne, 2011).



**Figure 16.** Graphic representation of the classification process (simplified). On the left the representation of a raster single band image and of the classified image (right). Similar values of the left image have been grouped for a class in the image on bright. Class “A” is defined by bright values (>6) and class “B” describes the dark pixels (< 3). (Campbell and Wynne, 2011).



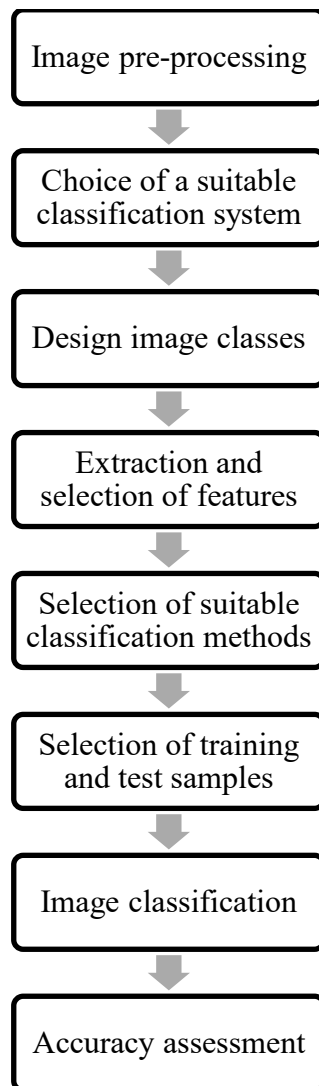
In other terms, it can be expressed as a computer-assisted analysis of images for information extraction. Thus, classification can also be defined as information extraction. In information extraction from multiband optical imagery, pixels are assumed to be individual units that carry several band values (Jawak et al., 2015). A pixel is a vector composed of several Digital Numbers (DN), one for each spectral band of the image Figure 17 (Campbell and Wynne, 2011; Salah, 2017a). In the multiband optical images process classification, the pixels of an image having comparable spectral values are assigned to one specific class. Classes should be homogenous (Campbell and Wynne, 2011) because, within the same image, pixels of one class differ spectrally from the pixels of another class. This is the idea behind image classification, different features on the Earth's surface have a different spectral reflectance (Campbell and Wynne, 2011). Thus the pixels that describe those features can be grouped in different spectral classes. In a map or a digital image, these classes constitute regions and results in a mosaic of consistent classes, each identified by a specific symbology.



**Figure 17.** Graphical restitution of pixel vector in the multiband image. In this case, the highlighted pixel is the vector [23 42 89 94]. (Campbell and Wynne, 2011)

In the field of Remote Sensing from optical imagery, numerous attempts have been made for developing a practical approach for the information extraction processes. The recent availability of a range of high resolution (HR) and Very-High resolution (VHR) images offers an advantage for more precise extraction of information by developing advanced classification schemes. Indeed, the classification is a complex process and requires consideration of many factors. Comprehensive and exhaustive reviews of Land Cover classification techniques and algorithms exist (Franklin and Wulder, 2002; Jawak et al., 2015; Jog and Dixit, 2016; Lu and Weng, 2007; Ma et al., 2017b; Salah, 2017a). Generally, the authors provide an overview of current practices and the existing classification methods and compare them. Most of them focus specifically on comparing classifiers (Jog and Dixit, 2016; Talukdar et al., 2020). The literature is rich in classification reviews on specific technique or techniques for Land Cover classification, such as Jawak who provide a review on the Land Cover supervised object-oriented classification focused on cryospheric application (Jawak et al., 2015). They focus only on most recent object-oriented classification methodologies (Ma et al., 2017b). More comprehensive analysis regarding the entire classification process is rarer in literature as much as the analysis of Land Cover classification methods for VHR imagery. The works of (Lu and Weng, 2007; Pandey et al., 2019; Thyagarajan and Vignesh, 2019) are the most complete, even if limited to the spaceborne-generated dataset. However, the remotely sensed data process classification is composed of several sub-processes, or steps, which are compulsory for relevant results (Campbell and Wynne, 2011; Lu and Weng, 2007; Salah, 2017a). Indeed, the classification itself is the core of the classification process, but it cannot exist without preparing the dataset, selecting the classes, and the accuracy assessment.

The present chapter provides an overview of the existing and most applied classification techniques for the LC maps' production, focusing on the entire classification process. The chapter is structured following the foremost steps of image classification. The order and steps of a classification workflow depend on the type of classification algorithm used, the nature of the input data, and the analyst's time and needs. This structure is developed basing on (Campbell and Wynne, 2011)'s steps for the classification process, initially proposed in "Introduction to Remote Sensing, fifth edition". It was then enriched following (Lu and Weng, 2007)'s classification main steps, which traces most of the land cover classification publications and many other authors share it (Jawak et al., 2015; Jog and Dixit, 2016; Salah, 2017a; Talukdar et al., 2020). The general strategy workflow adopted in this work is shown in Figure 18.

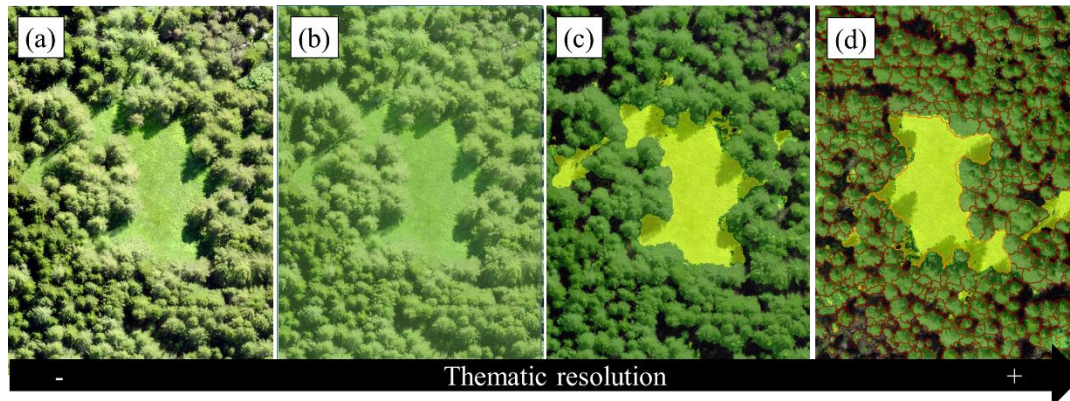


**Figure 18.** The general workflow of the classification structure as identified by (Lu and Weng, 2007) and (Campbell and Wynne, 2011). This methodology is particularly adapted for supervised classification algorithms. The image pre-processing step is analyzed in Chapter 5.

## 4.1. Definition of classes

Land Cover maps are composed of contiguous classes forming regions. According to the classification needs, meaning the needed study area's information, the analyst identifies them. Thus, the classes are the categories of interest to the data users (Campbell and Wynne, 2011). The classes represent the specific characteristics of the Land Cover, and they can be, for example, the different kinds of forest units, different kinds of soil, or the different kinds of land cover that provide information to planners and scientists who are the final users. The classes

that describe a particular aspect of the classified scene are high thematic resolution classes. For example, high thematic classes are forest burnt areas, landslides, or asbestos roof buildings. Low thematic resolution classes are generally easier to identify: they are directly visible on the image and spectrally uniform.



**Figure 19.** An example of increasing thematic detail. a) is the analysed area; b) is the analysed area classified as "vegetation"; c) in the classification distinguish between grassland (light green), forest (dark green) and shadows (black); d) is more thematically detailed classification where single tree crowns are detected (red outlines).

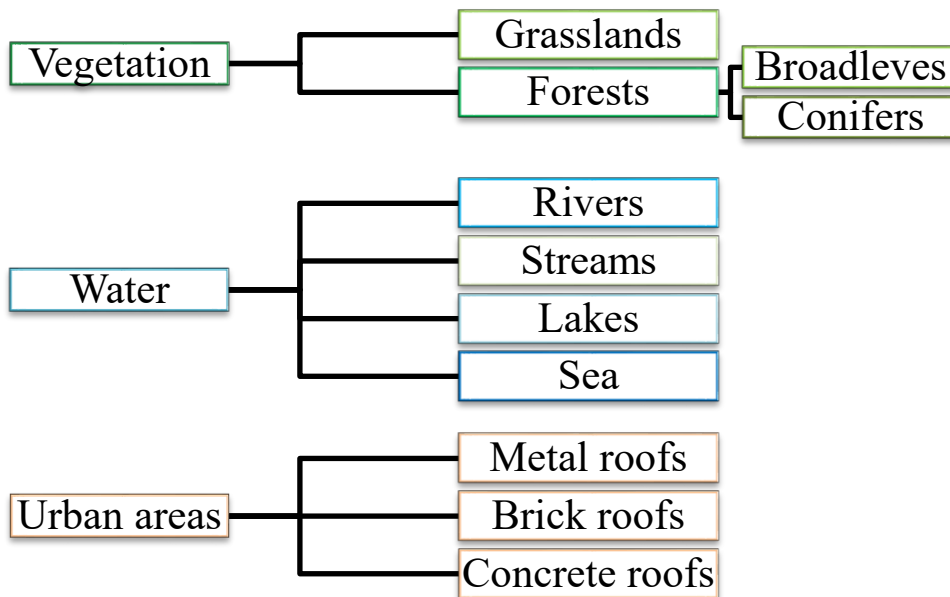
Unfortunately, it is not always so easy. Some very detailed classifications are not directly recorded on remotely sensed images, but they can be derived indirectly, using multiple aspects of the image. For example, the image cannot directly show soil types, but the analyst can identify and describe them considering the topography, the vegetation, the pixel reflectance, and other factors. Classes are strictly dependant on the spatial resolution of the image. A single pixel should capture the characteristics of the classification target (Torres-Sánchez et al., 2015). Classification targets smaller than the spatial resolution cannot be detected. For example, it is impossible to define a single tree from 30m spatial resolution imagery, but only the forested areas.

The classes of land cover are created based on spectral similarity. The pixels are grouped (manually or automatically) according to the DN values (or brightness) of single pixels on the images dataset. The classes are spectrally uniform and homogeneous categories. Thus, remote sensing Land Cover classification matches these spectral categories to informational categories. If the match can be made with confidence, then the information is likely to be reliable. If spectral and informational categories do not correspond, then the image is unlikely to be a useful source for that particular form of information (Campbell and Wynne, 2011).

In supervised classification, this aspect is defined during the preparation of the training sample before applying the classification algorithm. In contrast, for unsupervised classification, it is defined after applying the algorithm and the clustering (see paragraph 4.4, page 66 for the definition of supervised and unsupervised classifications).

Of course, classes can have little variations due to the natural variations within the class. For example, the land cover class “water” may include rivers, streams, sea, and lakes, which differ in spectral appearance. Moreover, the illumination and the shadowing produce additional variations even within otherwise spectrally uniform classes. These aspects are a source of inaccuracies in some environments, such as the mountainous areas.

Typical classification systems are composed of classes, subclasses, and macro classes organized in a hierarchical system. The subclasses are spectrally distinct groups that together may be assembled to form a class. Similarly, classes providing similar information can be grouped in macro-classes. For example, the class “forest” can be composed of the subclasses “conifers” and “broadleaves”, and being part of the macroclass “vegetation” with the “grasslands” (Figure 20).



**Figure 20.** Example of a classification system. It is composed of classes (grasslands, Forests, Rivers, Stream, Lakes, Sea, Metal roofs, Brick roofs, Concrete roofs), subclasses (broadleaves and conifers), and macro classes (Vegetation, Water, and Urban areas) organized in a hierarchical system.

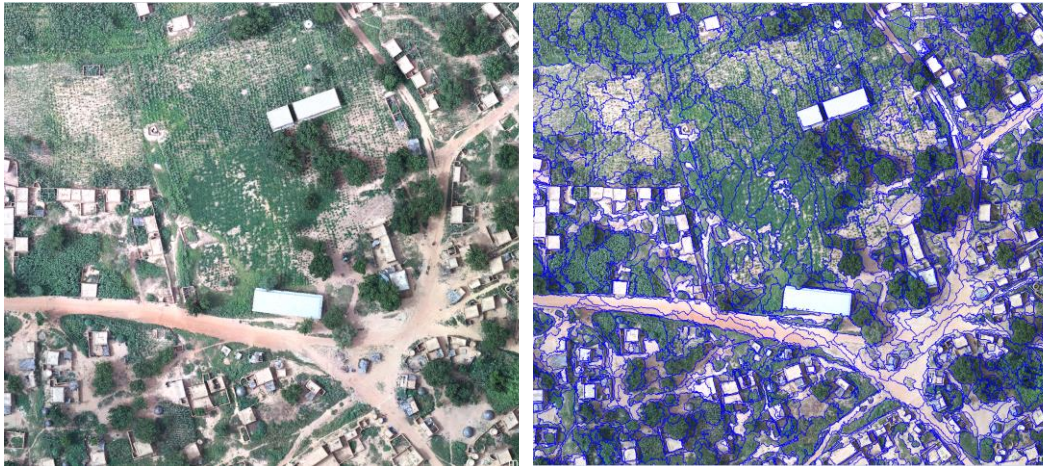
This hierarchical system helps the analyst in the organization of the information, but it can also be used as a stratagem for those homogeneous classes

from an informational point of view but inhomogeneous from a spectral point of view. Temporary subclasses are created, and in post-processing, merged in the hierarchically upper class of interest. For example, in the classification of “urban areas,” roofs of buildings can be made of spectrally different materials, such as metal, concrete, wood, or bricks. Even if distinguishing the buildings according to the single material is not informational relevant, the analyst does it to correctly describe the “urban area” class (Figure 20). The analyst treats spectral subclasses as distinct units during classification and displays several spectral classes under a single symbol for the final image or map.

## 4.2. Pixel-based and object-oriented classifications

The pixel has been the single unit of image classification since the early applications of Remote Sensing (Hussain et al., 2013; Lu and Weng, 2007; Rastner et al., 2014). As described in the previous paragraph, the pixel in multispectral images represents the atomic unit of the image, and it is a vector composed of Digital Numbers as much as the bands that compose the image. Most often, classifications and statistical operators are applied at the single pixel level. Each pixel is analyzed and labeled by the algorithm. This classification approach is called *pixel-based*. The pixel is the single and fundamental unit of image processing, but it is not a geographic unit. Indeed it is a cell of a grid that stores numbers and whose boundaries lack real-world correspondence (Hussain et al., 2013). This means that generally one pixel does not describe a geographical object. The representativeness of pixels depends on their projection in real space. When the pixel is bigger than the geographical object, the DN of the pixel will be the mixture of the reflectance values of the target object, and the surrounding ones. When the pixel size is smaller than the target, object its DN will be the reflectance of only a part of it, which may be non-representative of the entire object in case of high-spectral variability. The high reflectance variability within individual features and the number of classes present in the images, especially at the high-spectral resolution, has restricted the traditional per-pixel analysis (Hussain et al., 2013). A more recent image classification option is object-based image analysis (OBIA) (Whiteside et al., 2011).

This technique considers as the unit of the classification homogeneous groups of pixels instead of single pixels. Pixels are grouped based on their spectral characteristics and the geometrical properties of their spatial distribution (Figure 21). This phase is called segmentation, and it predates the classification itself, Figure 22 (Gao et al., 2018; Lu and Weng, 2007; Rastner et al., 2014).



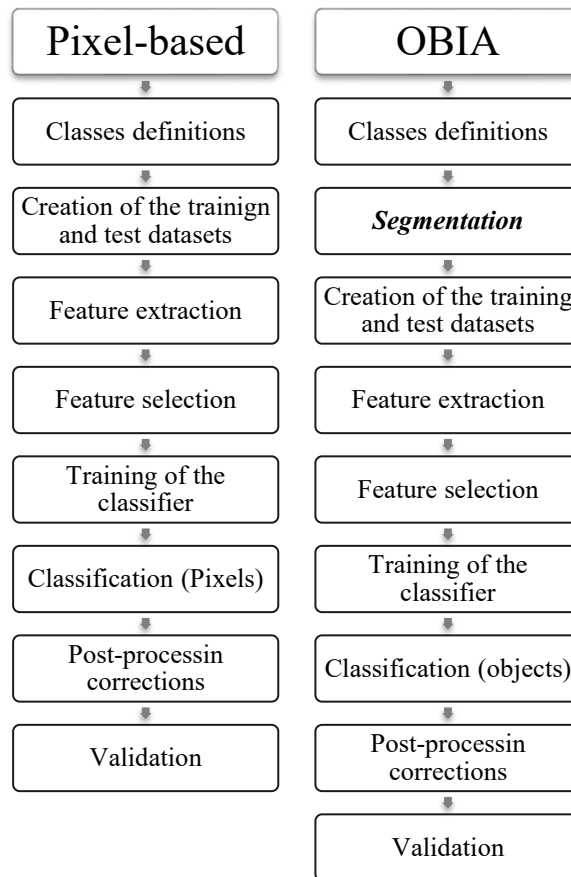
**Figure 21.** A graphic example of the segmentation process. Pixels with homogeneous information (in this case, spectral information) are grouped to form polygons (or objects) with specific characteristics.

**Table 12.** Advantages and disadvantages of Pixel-based and Object-oriented classification systems.

	Advantages	Disadvantages
Pixel-based	<ul style="list-style-type: none"> <li>▪ Lower sensitivity to selected threshold</li> <li>▪ Low computational time</li> <li>▪ Capture of details</li> <li>▪ Extensive area mapping of satellite images</li> <li>▪ Low computational power demand</li> </ul>	<ul style="list-style-type: none"> <li>▪ High amount of speckled pixels</li> <li>▪ Limited transferability</li> <li>▪ Expert knowledge requirement</li> <li>▪ Salt and pepper effect on VHR imagery.</li> </ul>
OBIA	<ul style="list-style-type: none"> <li>▪ Better accuracy on VHR imagery</li> <li>▪ No anesthetic effects (salt-and-pepper effect)</li> <li>▪ image objects can be created at various scales (e.g., from a single tree crown to groups of trees)</li> <li>▪ statistic attributes can be obtained from image objects deviation using the DN</li> </ul>	<ul style="list-style-type: none"> <li>▪ The final accuracy is strongly dependant on the segmentation process</li> <li>▪ The goodness of the segmentation is hard to assess</li> <li>▪ High computational cost (dependant on the no. of segments)</li> <li>▪ Still implemented in few software</li> <li>▪ High need for graphical restitution for the segmentation</li> </ul>

The segmentation is the core process of OBIA, and several steps generally characterize it. Starting with individual pixels, OBIA algorithms merge contiguous

pixels into groups (i.e., objects) based on three parameters: scale, shape, and compactness (Lu and Weng, 2007; Meneguzzo et al., 2013; Rastner et al., 2014). The objects should represent the land cover features (e.g., agricultural fields, buildings, and roads) (Hussain et al., 2013). Scale, shape, and compactness are user-defined parameters. The scale represents the degree of spectral heterogeneity allowed in each object. Generally, the higher the scale value (that is unitless), and larger the object will be because it is more heterogeneous (Hussain et al., 2013; Rastner et al., 2014). The compactness can be defined as the degree of similarity of a polygon to a circumference. The compactness parameter optimizes the resulting objects regarding the compactness.



**Figure 22.** Main steps for the pixel-based and OBIA classification, starting from a ready-to-classify input dataset.

In the VHR image classification realm, the OBIA approach dominance is undiscussed. However, its efficiency in medium-spatial resolution is questionable. The segmentation process of medium-spatial resolution datasets requires



experienced analysts and good intuition to ensure fully representative objects. It is computationally demanding, and the geometrical attributes of the objects are poorly significant (**Table 12**). Ontologically, OBIA allows the identification and extraction of real-world features more accurately and reliably from remotely sensed data only on more appropriate scales (Hussain et al., 2013).

#### **4.2.1. Single epoch and multi-temporal classification**

Assuming the availability of spectral data relative to the same target area but captured in a different time, it is possible to perform multi-temporal analysis. It is proved that the use of multi-temporal than single-date classification for Land Cover mapping increases accuracy with improved tools (Langley et al., 2001; Long et al., 2013; Ma et al., 2017b). The multi-temporal approach's main advantage is the possibility of using image data from different dates to better capture spectral diversity in the same Land Cover class. Namely, some covers are more prone to spectral variabilities than others are, such as agricultural fields, deciduous forests, and small rivers. The multi-temporal classification approach has been successfully used to map and monitor vegetation (Long et al., 2013). It has been applied largely in crops' phenological stages (Eisavi et al., 2015; Langley et al., 2001; Long et al., 2013), mapping wetlands (Corcoran et al., 2013), and semi-arid areas (Langley et al., 2001; Mohamed and El-Raey, 2019). Two main approaches for multi-temporal classification exist.

The first scheme used for multi-temporal analysis consists of stacking the input images of a different time and classify the entire dataset. This method is also called a multi-date approach (Ghamisi et al., 2019). The multi-date approach's main idea is to characterize pixels by stacking the feature vectors of the images acquired at different times. The classification is then carried out by training the classifiers to produce a map describing the land cover (Ghamisi et al., 2019). This method has been applied with a seasonal declination (Hepinstall-Cymerman et al., 2009; Long et al., 2013). Namely, the multi-temporal datasets are created on a (phenological, natural, or growing) season basis. The multi-date approach is broadly applied (Corcoran et al., 2013; Eisavi et al., 2015; Hepinstall-Cymerman et al., 2009). Although it is based on two essential assumptions:

- I. the considered image acquisition dates do not differ in cover classes (i.e., there is no change in land cover, for example, from Agricultural fields to built-up areas);
- II. the applied classification algorithm can model the data distributions' complexity (Ghamisi et al., 2019).

The second scheme used for multi-temporal analysis consists of classifying the land cover of each image of the time series separately, thus producing a land cover map for each available acquisition time. This approach permits explicitly identify eventual transitions in the land cover, and, mostly, it removes the assumption that there are no changes in cover between the considered dates. This methodology's principal limit is the need for training samples that can adequately represent all the classes in each image, thus excluding those associated with changes.

Indeed, a proper multi-temporal classification would require multi-temporal ground reference samples in both approaches. For this reason, great attention has been -and is still- devoted to the use of methods that address the limitations of the training set (Ghamisi et al., 2019).

Besides introducing a certain grade on uncertainty, the multi-temporal classification has two other strong constraints than single epoch classification. Working on large time-series requires handling more massive data sets and consequentially a demand of computational time and power (Langley et al., 2001), and when working with multi-temporal dates, the images need to be co-registered, calibrated, and atmospherically corrected.

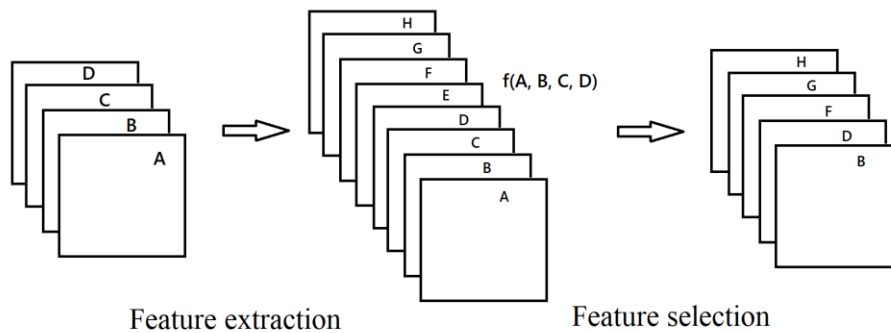
It is worth mentioning that the multi-temporal approach can have different meanings and roles according to the classification's goal. The multi-temporality may serve for the generation of a single land cover map; a land cover map for each item of the time series, thus producing a set of multi-temporal land cover maps; an annual or seasonal land cover map with classes that represent the behavior of the temporal signature of each pixel or region in the images in a year or season. Each of these methods requires extra attention and approach.

### **4.3. Feature extraction and feature selection**

The single unit of image classification, regardless of its nature (i.e., pixel or object), is characterized by several attributes deriving from the bands on the image to be classified. These bands are called features of the classification. Effective use of features as input data for a classification procedure can improve classification accuracy (Lu and Weng, 2007; Maxwell et al., 2018; Salah, 2017b). The basic features used in the optical-imagery classification process are the ones deriving from the spectral information of the image. For example, a Sentinel-2 input dataset consists of 13 spectral features (one per band) (ESA, 2019). Besides the spectral features, a wide variety of variables are available which includes, spectral-derived indices, processed images, textual information, height or surface roughness, non-spectral geographical information (ancillary data), and shape and size of objects (only for OBIA) (Lu and Weng, 2007; Salah, 2017b). These features can be derived

from elaborating one or more spectral bands or can have an external source, thus independent from the classified image's spectral information. The selection of the set of features for the classification process has a crucial role in absolute accuracy (Salah, 2017b; Thyagarajan and Vignesh, 2019). The feature extraction step within the classification process has two main functions: it allows one to identify and select the most useful features in the classification process, and it reduces the classification dimensionality and simplifies the model (Thyagarajan and Vignesh, 2019). Maxwell et al. (Maxwell et al., 2018) distinguish the two feature extraction and feature selection functions.

The feature extraction generates new features (variables) by combining information from the original features to provide more meaningful information than the one contained in the original variables (Maxwell et al., 2018; Thyagarajan and Vignesh, 2019). A well-known example is Principal Component Analysis (PCA), in which the original variables are transformed into uncorrelated variables. On the other hand, feature selection identifies a subset of the input features determined to be valuable for the classification (Maxwell et al., 2018). Figure 23 shows the combination of the two processes.



**Figure 23.** Graphical restitution of feature extraction and feature selection processes. Features A, B, C, and D are the spectral information. The feature extraction identifies new features E, F, G, and H that are a function of A, B, C, and D data. The feature selection process identifies the most significant and essential features for the classification (B, D, F, G, and H).

### 4.3.1. Feature extraction

The feature extraction begins from an initial set of measured data and forms a new feature. The diversification of the input features is crucial for a useful classification and can improve the final accuracy. For example, textural elements can facilitate Land Cover class discrimination (Jin et al., 2018; Lewiński et al., 2015; Zhang et al., 2003) and the histogram-based ones (Drzewiecki et al., 2013). The number of features depends on the level of thematic detail required for the final product and

the type of classifier. For practical reason, classification features are grouped according to their nature in:

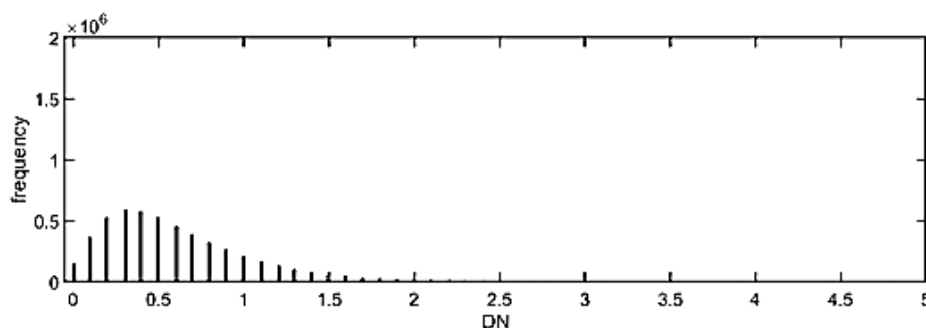
- I. Radiometric-based features
- II. Histogram-based features
- III. Textural-based features
- IV. Other features

#### *Radiometric-based features*

Radiometric –based features, or spectral features, include all those features resulting from the simple combination of other spectral bands. These features have been proven to effectively separate land cover categories with similar spectral signatures (Zhang et al., 2003). Generally, they are indices for the monitoring of specific characteristics of the environment. The most common and applied index is the Normalized Difference Vegetation Index (NDVI) (Jin et al., 2018; Merciol et al., 2019; Pelletier et al., 2016; Zhang et al., 2003), which is used for the discrimination of vegetation classes, also in multi-temporal classification approaches. Other radiometric-based standard features are the built-up indices, water indices and tasselled cap features (Pelletier et al., 2016). The radiometric indices should be extracted according the needs of the classification. For example, NDVI is indicated for the identification of mid-low vegetation, while the Enhanced Vegetation Index (EVI) is more appropriated for the identification of high-biomass regions. Table 13 lists some of the most common spectral indices in classification software (i.e. ENVI and Orfeo toolbox) grouped according their application.

#### *Histogram-based features*

Histogram-based features are indices that can be obtained from the density histograms of an image band. The density histogram on the band plots the DN values against their frequency (Figure 24). Some authors recognize the histogram-based features as textural describers.



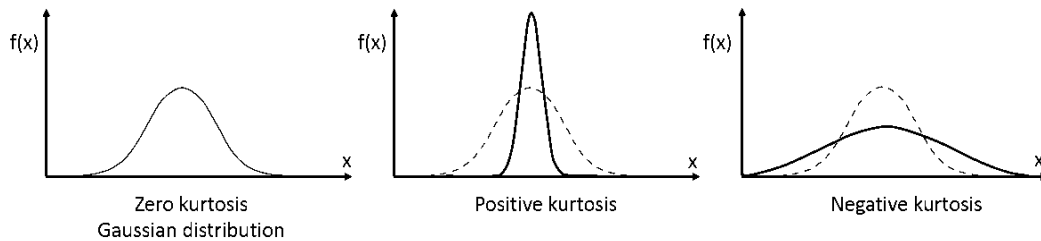
**Figure 24.** Example of a distribution histogram. On the abscissae, the digital number (DN) values and on the ordinates the frequency of DN values.

**Table 13.** List of some of the most applied radiometric indices grouped according to their application.

<b>Application</b>	<b>Acronym</b>	<b>Index</b>	<b>Reference</b>
Vegetation	NDVI	Normalized Difference Vegetation Index	(Rouse, 1973)
	RVI	Ratio Vegetation Index	(Pearson et al., 1972)
	PVI	Perpendicular Vegetation Index	(Richardson, 1977; Wiegand et al., 1991)
	SAVI	Soil Adjusted Vegetation Index	(Huete, 1988)
	GEMI	Global Environment Monitoring Index	(Pinty and Verstraete, 1992)
	EVI	Enhanced Vegetation Index	(Huete et al., 1994)
Water	SRWI	Simple Ratio Water Index	(Zarco-Tejada and Ustin, 2001)
	NDWI	Normalized Difference Water Index	(Gao, 1996)
	NDWI2	Normalized Difference Water Index	(Mcfeeters, 1996)
	NDPI	Normalized Difference Pond Index	(Lacaux et al., 2007)
	NDTI	Normalized Difference Turbidity Index	(Lacaux et al., 2007)
Built-up	NDBI	Normalized Difference Built Up Index	(Zha et al., 2003)
Fire	BAI	Burn Area Index	(Harris et al., 2011)
Soil	CMR	Clay Minerals Ratio	(Mallick, 1987)

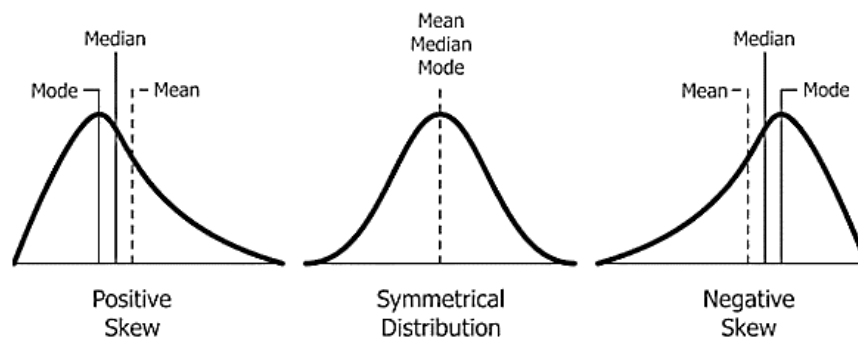
Mean, Variance, Skewness, and Kurtosis are some of the most applied and representative histogram-based features (Drzewiecki et al., 2013). Mean, and Variance are easily interpretable, in contrast to Kurtosis and Skewness. They represent the disparity deviation of a histogram when compared with a Gaussian

distribution. Kurtosis describes how sharply peaked a histogram is. This means that a Gaussian distribution has a Kurtosis of zero. A more peaked histogram than a Gaussian distribution has a positive kurtosis value (Figure 25).



**Figure 25.** Representation of Kurtosis. Image source: <https://community.sw.siemens.com>

Skewness describes the degree of asymmetry of a histogram. When the distribution is perfectly symmetrical, it has a skewness of zero. Asymmetrical distributions have positive or negative values. For example, a histogram with a long tail to the right has a positive skewness value, Figure 26.

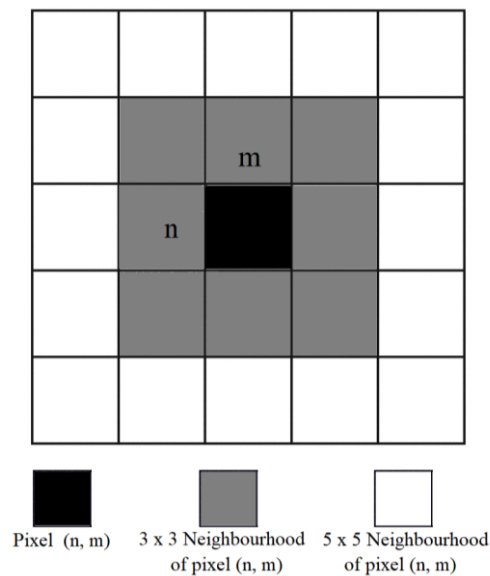


**Figure 26.** Representation of the Skewness (or skew). Image source: Diva Jain, CC BY-SA 4.0 <<https://creativecommons.org/licenses/by-sa/4.0/>>, via Wikimedia Commons

### *Textural-based features*

The inclusion of texture features can improve classification accuracy (Drzewiecki et al., 2013; Lewiński et al., 2015). Its role in the classification process has been recognized in numerous studies (Jin et al., 2018; Zhang et al., 2003). The texture refers to spatial variation in digital image spectral brightness due to spatial variation in the land surface (Berberoğlu et al., 2010). In satellite imagery, it is referred to as a specific spectral band and can be described as the frequency of tonal values (brightness or color) of neighboring pixels (Haralick et al., 1973). Because the texture concerns the neighborhood and can be related to a direction or a scale. The textural characteristic can be calculated on the entire image (called global

features), on an object within the image defined by segmentation process (OBIA classifications) or small groups of pixels formed by fixed or moving window (like kernels) (Drzewiecki et al., 2013; Lewiński et al., 2015). Generally, when operating on moving windows, kernel filters are constituted by  $n \times n$  size, where  $n$  is an odd number. The textural index value is calculated for the central cell (*pixel* ( $n, m$ ) in Figure 27) considering its relation with the  $n \times n$  neighborhood.



**Figure 27.** Visual representation of neighborhoods. The black pixel is the object of reference, and it is defined by ( $n, m$ ) size. The Surrounding grey pixels constitute its 3 x 3 neighborhoods. The white pixels delimit the 5 x 5 neighborhood (which includes the 3 x 3 neighborhood).

Texture analysis techniques can be divided into four groups (Lewiński et al., 2015): structural texture (e.g., mathematical morphology), statistical texture (e.g., image first-order and second-order statistics), model-based texture (e.g., fractals or multifractals) and transform texture extraction techniques (e.g., wavelets) (Lewiński et al., 2015). Statistical texture features are in turn categorized into the first order that relates to the intensity of the individual pixels, and into second-order that relates to the occurrence of neighboring pixels. Basically, first-order statistical parameters are directly based on histogram features of an image (histogram-based features), while the second-order textural features are based on the grey level co-occurrence matrix (GLCM) (Qadri et al., 2016).

The most popular textural analysis in 2D optical remote sensing is the grey level co-occurrence matrix (GLCM) (Jin et al., 2018; Lewiński et al., 2015; S.V.S.Prasad et al., 2015; Zhang et al., 2003). GLCM is calculated on subgroups of pixels or an

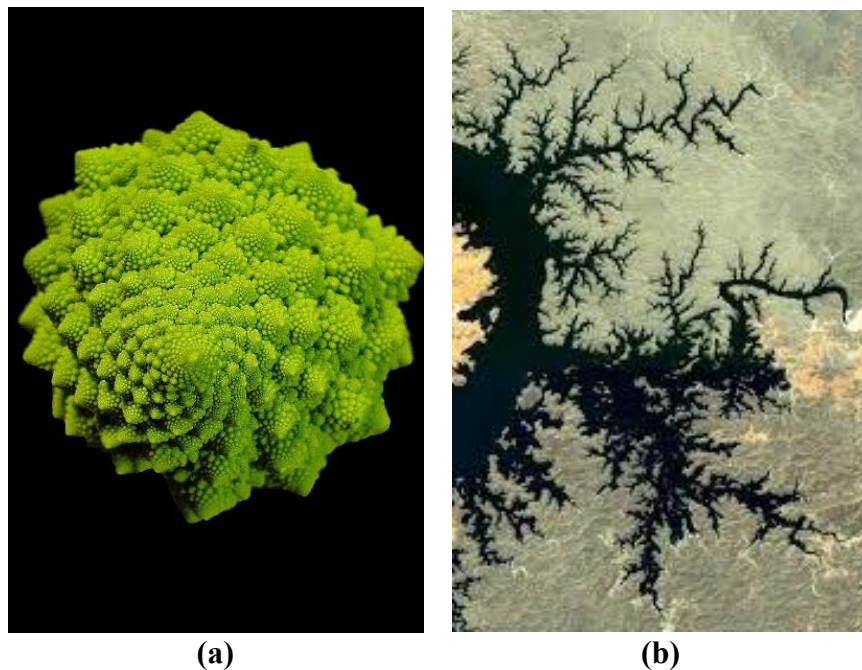
$n \times n$  filter. In GLCM, the number of columns and rows is estimated based on the number of grey levels in the image (Berberoğlu et al., 2010; Haralick et al., 1973). The GLCM matrix elements show the statistical estimated values that happen between the grey-level value and  $j$  at a special direction  $\theta$  and distance  $d$  (Haralick et al., 1973). Based on the Grey level co-occurrence matrix Haralick in 1973 (Haralick et al., 1973) proposed 14 measures (Angular Second Moment, Contrast, Correlation, Sum of squares, Inverse Difference Moment, Sum Average Sum Variance, Sum Entropy, Entropy, difference Variance, Difference Entropy, Information measure of correlation, Maximal correlation coefficient), which have been broadly applied on Land Cover classification studies and are now implemented in most of the existing classification software.

Two aspects need to be carefully addressed in the computation of textural features for land cover mapping: the size of  $n$  (size of the filter) and the base spectral information for the analysis (Jin et al., 2018). Indeed, too small  $n$  may not be able to detect the brightness variance within the neighborhood, but on the contrary, too large  $n$  may consider a non-representative area. Since the texture analyzes DN's variance in a specific area,  $n$  size also depends on the target land cover. For example, the coniferous forests may have a very different textural behavior compared to graveled soils. Similarly, some spectral bands can be more textured than others can. For example, the near-Infrared is expected to be more textured for a forest than the red band. This means that to distinguish effectively specific classes, it may be necessary to consider different  $n$  size and different spectral information. GLCM textural features are applied especially in HR and VHR imagery, mainly for the for vegetation structure modeling (Jin et al., 2018; Ostad-Ali-Askari et al., 2017) for the identification of built-up areas (Eslami and Mohammadzadeh, 2017; Jin et al., 2018; Lewiński et al., 2015).

Within model-based textural features, the fractal models are the most applied. Since the 1970s, the Mandelbrot fractals geometry models have been used in several image processing and classification processes. (Mandelbrot, 1982) defined as fractal the complex geometries that cannot be characterized by an integral dimension. Fractal objects can define and describe the irregular shapes of natural features and other complex objects that traditional Euclidean geometry fails to analyze (Lopes and Betrouni, 2009). Many authors have applied fractal geometry analysis to describe complex land surfaces, and the role of fractals in the improvement of classification accuracy has been proven by several researchers (Drzewiecki et al., 2013; Lewiński et al., 2015; Nowakowski et al., 2017). The applications of fractal techniques to image analysis rely heavily on the estimation of fractal dimensions. The fractal dimension,  $D$ , is a crucial parameter developed in



fractal geometry to measure complex objects' irregularity. Varieties of methods have been developed to compute the  $D$  of features. A comprehensive review of these methods is proposed by (Sun et al., 2006) and by (Lopes and Betrouni, 2009). The fractal dimension has been applied for segmentation too. (Zeide and Pfeifer, 1991) showed that tree crowns' fractal dimension could be useful in crown classification and foliage distribution within a single tree crown analysis. Nevertheless, (Sun et al., 2006) report some inaccuracy of the texture described by fractal dimension due to the complexity and inhomogeneous of optical dataset. This is the reason behind the recent application of multifractal formalism for image classification process (Aleksandrowicz et al., 2016; Lewiński et al., 2015; Sun et al., 2006).



**Figure 28.** Two examples of fractals in (a) the Roman broccoli, Source treccani.it (b) Norway fjords. Source: <http://paulbourke.net/>

The multifractal formalism states the extension of fractal theory, and it is connected with a group of parameters, which permit a more detailed characterization of the considered data (locally and globally). In particular, multifractal image analysis methods are based on the assumption that there is a measure defined in terms of pixel intensities. The local degree of regularity of this measure is described by singularity exponents (Hölder exponents), while the global regularity is summarized in the form of the multifractal spectrum (Stojić et al., 2006a; Vêhel and Mignot, 1994). Global multifractal characteristics have already

been applied to VHR optical data (Jenerowicz et al., 2019; Wawrzaszek et al., 2014), mostly to distinguish between different land cover types. One can also find their application in the context of the study of forest cover, such as in (Danila et al., 2019)'s work or to perform the segmentation of images of vegetation leaves diseases (Wang et al., 2013). In this work, the Holder exponent, a multifractal local measure of texture, is used (see paragraph 7.1, page 135). The local multifractal description by using Hölder exponents has been used rarely, mainly to perform segmentation of medical data (Stojić et al., 2006a; Véhel and Mignot, 1994), or in the change detection aspects of satellite images (Aleksandrowicz et al., 2016; Véhel and Mignot, 1994).

#### *Other features*

Besides the radiometric-based and textural features, other features can constitute the input dataset for the classification. This group encompasses all those features that are not computed from the spectral information of the original bands. These features are often called ancillary data, and they can be constituted of raster and vector information both. The most frequent are the Digital Elevation Models (Salah, 2017b), and its derived features such as height models (obtained as the difference between Digital Surface Models and Digital Terrain Models). Information deriving from census (population) road density, road coverage are often used too. Indeed, each information that can help separate specific classes can be used as long as the selected classifier tolerates a heterogeneous input dataset. For example, DEM can distinguish between built-up areas and bare soil, and population density to facilitate the identification of town and city.

### **4.3.2. Feature selection**

After the feature extraction process, the input dataset should carry significant and no-redundant information for the separability of classes (Thyagarajan and Vignesh, 2019). Nevertheless, feature extraction can result in a dimensionally large dataset, increasing the computational time for the classification and requiring a large amount of storage space. Thus, it can be necessary to reduce datasets' dimensionality without scarifying accuracy (Lu and Weng, 2007). Feature selection reduces the dimensionality of the input feature by decreasing the number of features in the classification. It aims to identify and remove redundant information so that the dataset can include maximum information using the minimum number of features (Campbell and Wynne, 2011). In fact, due to different capabilities in land-cover separability, a large number of features can lead to a lower classification accuracy compared to classification with a subset of those features (Hughes

paradox). This is particularly true when the subset features are chosen focusing on the features that are most important in discriminating the classes (Maxwell et al., 2018).

Additionally, feature selection simplifies the model, even if the accuracy does not improve. For example, a model that requires a small number of input variables is easily replicable or easily extrapolated to another area since a smaller number of features will need to be computed. Machine learning methods have been noted to be less affected by high dimensionality datasets than parametric methods. Indeed some algorithms are robust to high-dimensionality, such as Support Vector Machine and Random Forest (S.V.S.Prasad et al., 2015). Although a reduced feature space may not improve the interoperability of 'black box' classifiers, such as Support Vector Machine and Artificial Neural Networks, on the other hand, a reduced feature space may make the structure of a Decision Trees (DT) classifiers easier to understand (Maxwell et al., 2018). Regardless of the nature of the classification and the algorithm used, the feature selection should be effective (Thyagarajan and Vignesh, 2019). Feature selection can be realized with different techniques, such as principal component analysis (PCA), minimum noise fraction (MNF), transform discriminant analysis (TDA), decision boundary (DP), feature extraction (FE), non-parametric weighted feature extraction (NPWFE), wavelet transform (WT) and spectral mixture analysis (SMA) algorithms (S.V.S.Prasad et al., 2015; Thyagarajan and Vignesh, 2019).

PCA is one of the most applied method algorithms (Thyagarajan and Vignesh, 2019). It consists of the optimized linear combination of the original spectral features (i.e., bands) that can account for pixel values' variation within an image (Campbell and Wynne, 2011). PCA transforms the original variables into uncorrelated variables (Maxwell et al., 2018). In contrast, PCA analysis may require high computational capabilities, and, in the case of high dimensionality dataset, it is complicated to identify the correct linear combinations that prevent the decrease of the final accuracy. Feature selection can be realized with statistical analysis, such as average divergence, transformed divergence. Generally, the comparison of different combinations of selected variables is implemented (Lu and Weng, 2007).

Most feature selection methods rely on the feature importance assessment method, the feature subset assessment method, and other selection methods (Ma et al., 2017b). These analyses result in a chart of importance. The most important features occupy the top of the chart in the classification. Methods such as GINI, RF, Chi-square, and SVM-RFE, are broadly applied. Table 14 sums up the pro and cons of feature selection methods, as identified by (Ma et al., 2017b).

**Table 14.** Advantages and disadvantages of feature selection algorithms, grouped in feature importance methods, feature subset assessment methods, and miscellaneous methods (Ma et al., 2017b).

Category	Method	Advantages and disadvantages
Feature importance	Random Forest (RF)	Adaptable to the random forest only. It ensures the accuracy of the feature selection and generates sorted features.
	GINI	More efficient feature selection. It sorts the features, and it is easily combined with Decision trees. It is based on the impurity criterion.
	Support Vector Machine (SVM) /RF-RFE	Generate feature sorting results while achieving the best classification accuracy, generally combined with SVM and RF.
	Relief-F	Able to generate sorted features; independent of the classification model, difficult to determine optimal subsets.
	Chi-square	Able to generate sorted features and classification rules.
	Information Gain	Able to generate sorted features and classification rules, difficult to determine optimal subsets.
Feature subset assessment methods	CFS	Directly generate feature subsets, independent of the classification model, featuring fast processing speed.
	Wrapper (RF/SVM)	Easy adaptation to classifiers. Point-based cross-validation is adopted in most cases, susceptible to overfitting or over-adapting to classifiers. Time-consuming. They are usually applied in combination with RF and SVM.
Miscellaneous	JM distance	Able to generate classification distances amongst classes. They are generally used for rule-based classification or NN classifier.
	FSO	It is integrated into eCognition with easy use: black-box manipulation, lack of feature importance sorting. It is typically used for the NN classifier.
	GA	Black-box manipulation, lack of feature sorting results. Normally used for ANN classifier.

How feature selection affects the final accuracy is still uncertain regarding some classifiers (Ma et al., 2017b). For example, SVM seems to be insensitive to changes in the feature's dimensionality, although some studies found that SVM classification accuracy improved with decreased dimensions. Similarly, Random Forest's response to the dimensionality of the input dataset is not clearly defined. Some studies found that feature selection improves classification accuracy. On the other hand, others proved that the RF classifier is a more stable object-based remote sensing image classification method regardless of the feature selection application (Ma et al., 2017b). Although, these observations are focalized on the accuracy assessment without considering the computational time and the ease to reproduce the entire classification process.

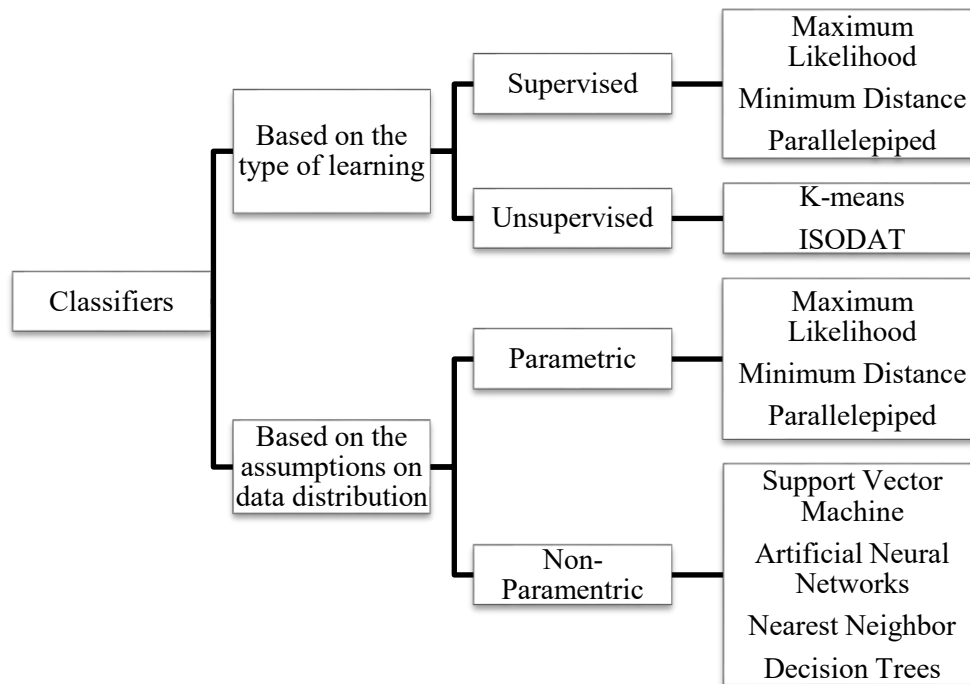
Defining the correct number of features in Land Cover classification is not possible without generalization. Generally, OBIA classification needs fewer features than pixel-based (less than 30) (Ghosh and Joshi, 2014; Guan et al., 2013; Ma et al., 2017b). The number of features also depends on the number of classes of the system and their thematic detail. In particular, a useful representative dataset for each class is vital for implementing an effective supervised classification (Lu and Weng, 2007).

#### **4.4. Type of classification algorithms**

A large variety of classification techniques and algorithms for the Land Cover mapping exists. Generally, these classifiers can be grouped into two categories according to their nature:

- I. supervised and unsupervised classifiers, based on the type of learning;
- II. parametric and non-parametric classifiers, based on assumptions on data distribution;

Figure 29 represents the distribution of some of the most popular classifiers in the two categories (Jawak et al., 2015; Lu and Weng, 2007). In the following paragraph, the two groups' discriminant aspects will be defined, and the main classification algorithms will be briefly analyzed.



**Figure 29.** Classification algorithms are grouped according to the assumption of the data distribution and on the type of learning.

#### 4.4.1. Supervised and Unsupervised classifications

##### *Unsupervised classifications*

Unsupervised classifications consist of the automatic identification by the classification algorithm of natural groups, or structures, within multispectral data. The units of the classification (pixels or objects) are grouped according to the similarity of the input features. This pixels-grouping phase is defined as *clustering*, and each group identified by the classifier is called a *cluster*. The definition of the clusters depends on the input parameters that usually are set by the analyst according to the information that he/she needs to extract from the dataset (see classes design paragraph), like the number of classes to identify and the part of the dataset to be issued (i.e., which band) (Campbell and Wynne, 2011; Salah, 2017a). The analyst needs to label the clusters identified by the classifier and, if necessary, merge the clusters representing the same information (i.e., class). The unsupervised classification is applied when identifying the training samples is hard to accomplish and/or the analyst has poor knowledge regarding the study region. This condition

is not frequent in Land Cover analysis, in which the supervised classification application still dominates. Recent and fascinating applications of unsupervised classification in Land Cover regard the Mars surface's mapping activities (Dundar et al., 2019; Jones et al., 2011; Ramachandra, 2019).

The study area's not required knowledge represents for sure one of the significant advantages of unsupervised classification. It is not required *a priori* knowledge of the area, but it is fundamental knowing how to interpret and label the cluster identified by the algorithm.

The unsupervised classifications have as recognized advantages as the minimization of human error, since human input is limited compared to supervised classifications. On the other hand, this aspect also has a negative connotation since it also lead to limited control of the analyst on the creation of classes, in their number and in their nature. This aspect is a substantial limitation when the target classes have high thematic detail.

The unsupervised classification can recognize unique classes. It means that even the small (in size and extent) classes that would be embedded in bigger classes in supervised classifications are clustered separately. On the other hand, clustering may identify non-informative groups that the analyst has to merge into other classes. Finally, unsupervised classification should be used carefully in multiresolution classification since some classes can change on a seasonal basis, and consequentially the grouping may change.

In this work, the unsupervised classification will be not further explored, neither in the literature review, nor in the applications presented in the next chapters. This choice is due to the poor control that the analyst has on the unsupervised classification, most of the Land Cover scientist shares this view, as the benefit of supervised classification in Land Cover are well known and shared by the scientific community.

### *Supervised classifications*

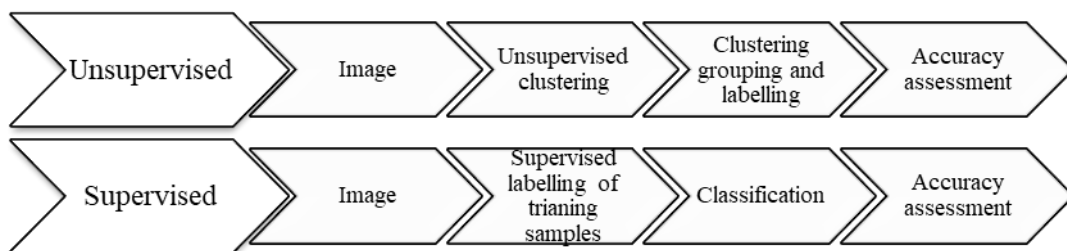
The Supervised classification consists of assigning a specific class to small representative sample pixels and using them to classify unknown class pixels. The sample pixels are located in training areas, or training fields identified by the analyst (Campbell and Wynne, 2011). The analyst must know *a priori* the location of the land cover type he/she is interested in and label them according to the information he/she needs to extrapolate from the dataset (Campbell and Wynne, 2011; Jawak et al., 2015; Salah, 2017b). Training areas should be homogeneous and must typify the spectral properties of the classes they represent. Each class corresponds to a specific spectral value used to guide the classification and train the classification

algorithm (Campbell and Wynne, 2011; Jawak et al., 2015). The reflectance value of each new pixel is compared to the sample pixels' spectral value and assigned to the most similar class. The analyst defines the classification algorithm (or the decision rules for each class) and provides the training data for each class to assist the classification.

In supervised classification procedure:

- I. the decision rules for each class are defined directly;
- II. training data (class prototypes) for each class are provided to assist the classification.

The main difference between the supervised and the unsupervised classification is the moment of data labeling. In unsupervised classification, the labeling happens after the grouping of data into different classes (clustering), while in supervised classification, the labeling happens before the grouping of the pixels of the entire image. Figure 30 shows the main logical steps of supervised and unsupervised classifications (Salah, 2017b).



**Figure 30.** Main steps of the unsupervised and supervised classification process.

In supervised classifications, the analyst controls a selected menu of classes tailored to a specific purpose and geographic region. This is crucial when there is the need to define specific classes, and, opposite of unsupervised classification facilitates the realization of multi-temporal classifications and high thematic resolution classifications. Additionally, the analyst does not have to match the clusters to maps and assign to each specific spectral response to a class because this aspect is addressed during the samples' selection. Even if supervised classification is usually more intuitive when there is knowledge of the study land cover, it has many disadvantages (Campbell and Wynne, 2011). First, the analyst, who imposes a classification structure on the data, forces the supervised classification in structure. Supervised classification may not identify special or unique categories if they are



not in the training data. This might result in less accurate classification since there is no match between the classes identified by the analyst and the “natural” classes, and the identified classes are heterogeneous. The training dataset is often first created based on the land cover class information instead of spectral information. For example, the sample area of class “conifers” can include high spectral information variability: different species composition, shade areas, the density of the stands, etc.

Moreover, the training dataset needs to represent the whole variety of every single class, and it cannot be representative. The principal limit of supervised classification, which to some extent is also the main advantage, is the high subjectivity of the results. Besides this, supervised classification is still the most applied in Land Cover analysis. The common supervised classification algorithms are the minimum distance (MD), Mahalanobis distance (MhD), parallelepiped (PP), maximum likelihood classifier (MXL), K-nearest neighbor (KNN), SVMs, and spectral angle mapper (SAM) (Jawak et al., 2015).

#### **4.4.2. Parametric and non-parametric classifiers**

In the last decades, several new classifiers have been created and introduced in Land Cover analysis. Even if all these classifiers have the same goal, their performances are affected by several factors such as choice of training samples, heterogeneity of study area, number of classes to identify (Jog and Dixit, 2016; Lu and Weng, 2007). As Figure 29 shows, another way to group the classification algorithms is according to the assumption of the data distribution: parametric and non-parametric

##### ***Parametric classifiers***

Parametric algorithms are based on the assumption that the classification parameters (i.e., classification dataset organized in spectral classes) are typically distributed and described by a Gaussian function. Thus, parametric classifiers assume that the mean and the covariance matrix represent the classification dataset (Lu and Weng, 2007). In other terms, they are based on the statistical probability distribution of each class. Traditional parametric classifiers provide excellent results as far as the input data is unimodal (Belgiu and Drăguț, 2016; Liu et al., 2011). However, parametric classifiers often lead to poor performance when this assumption is violated. In practice, if one class, or more, is multimodal, it may lead to poor performance by the resulting classifier (Chaudhuri et al., 2009). Some of the algorithms most applied and broadly used in Land Cover classification are the Maximum Likelihood and the minimum distance.

### *Maximum likelihood*

The Maximum likelihood is a supervised parametric classifier that uses statistics of second-order Gaussian probability distribution function (Jog and Dixit, 2016). This classifier is based on the Bayesian theory of probability and uses an array of patterns and a covariance matrix from a Gaussian distribution sample set (Salah, 2017b). It assigns each pixel to the appropriate class based on the pixel's probability values, which are computed by estimating the average and the variances of the training data (Campbell and Wynne, 2011). The maximum likelihood classifiers require large training dataset to allow accurate estimation of the mean vector and the variance-covariance matrix (Campbell and Wynne, 2011; Jog and Dixit, 2016; Salah, 2017b), which need to be highly homogeneous within each class (Campbell and Wynne, 2011). The input parameter should not be correlated to avoid the instability of the variance-covariance matrix's inverse matrix (Salah, 2017b). Generally, the Maximum likelihood requires intensive calculations, which is considered time-consuming (Campbell and Wynne, 2011; Salah, 2017b).

### *Minimum distance*

The minimum distance is a supervised parametric classifier based on the distance computed between the training data and the classified data. It uses the central values of the spectral data that form the training data as a mean to assign the pixel to class (Campbell and Wynne, 2011). The minimum distance between a single pixel and the sample cases represents the maximum similarity. Thus the pixel is assigned to the closest (less distant) class. The distance can be computed as Euclidean distance, Normalized Euclidean distance, or Mahalanobis distance (Jog and Dixit, 2016). This method has a low-computational requirement, but in its simplest form (Euclidean Distance), the minimum distance classifier is not always accurate because there is no provision for accommodating differences in variability of classes, and some classes may overlap. It is rarely applied in Land Cover classification, especially in its simplest form. The classifier in Mahalanobis distance form is still applied.

### *Parallelepiped*

It is a supervised classifier that defines the pixel class parallelepiped-shaped boxes for each class. Parallelepiped boundaries for each class are determined on the ranges of values within the training data to define regions within a multidimensional data space. These boundaries identify checks pixels of test images and determine the class of the pixel. The unclassified pixels' values are projected into the same space and assigned to the classes in which they fall into.

The parallelepiped method is fast and easy to run, but the overlap of training values may produce false results. The parallelepiped classifier has been one of the first classifiers applied to classify satellite imagery (Landsat) (Campbell and Wynne, 2011). It is now overcome and substitute by more accurate classifiers.

### *Non-parametric classifiers*

As suggested by the name, non-parametric classifiers do not assume a normal distribution of the dataset. Indeed, no statistical parameter is needed to separate the classes. This makes non-parametric classifiers particularly suitable for the incorporation of non-spectral data into a classification procedure. These basic aspects are the main reasons behind the increasing popularity of non-parametric classifiers in remote sensing. Sensed data are seldom normally distributed (Belgiu and Drăguț, 2016), and the application of non-spectral information has recently spread in the classification of complex landscapes.

Machine Learning (ML) algorithms can be found among the supervised non-parametric classification algorithms. Machine Learning classifiers are considered among the most reliable approaches for the classification of non-linear systems (Belgiu and Drăguț, 2016; Maxwell et al., 2018) and are increasingly used for the Land Cover analysis from Remote Sensed imagery (Belgiu and Drăguț, 2016; Lary et al., 2016; Maxwell et al., 2018; Rodriguez-Galiano and Chica-Rivas, 2014a). These classifiers produce better accuracy than traditional parametric classifiers (Maxwell et al., 2018; Yu et al., 2014), and they can be used not only for classification but also for regressions (Lary et al., 2016; Richards, 2013). Among the aspects that made them so appreciated in the last years there is their ability to learn complex patterns, even if they are non-linear, and deal with many parameters (Lary et al., 2016; Maxwell et al., 2018). Machine Learning classification algorithms are also appreciated for their low sensitivity to noisy datasets, for the possibility of integrating non-spectral-based information, such as Digital Elevation Models and categorical information (Rodriguez-Galiano and Chica-Rivas, 2014b; Rogan and Chen, 2004). Despite the evident advantages of machine learning techniques, the traditional parametric metrics are still widely applied (Maxwell et al., 2018). In 2014, (Yu et al., 2014) compared more than 1000 scientific manuscript on Land Cover analysis from Remote Sensed data and discover that around 30% of the analysis were realized using Maximum Likelihood classification, even if they smaller accuracy than ensemble machine learning methods (such as Random forest). The dominant popularity of parametric methods over ML is due to the high availability of classification software (Yu et al., 2014).

Among the ML Classifiers, CART, RF, k-Nearest Neighbour (k-NN), SVM, Artificial Neural Network (ANN) are some of the most popular and applied (Lary et al., 2016; Lu and Weng, 2007; Maxwell et al., 2018; Rodriguez-Galiano and Chica-Rivas, 2014b; Talukdar et al., 2020). In the next paragraph, their functioning and the main characteristics will be briefly expanded. For more detailed information, (Richards, 2013) and (Duda et al., 2012) s' works are recommended.

#### *Classification and Regression Trees (CART) classifier*

CART is a supervised non-parametric classification technique based on the creation of a series of decision trees (Richards, 2013). Decision trees (DT) are intuitive binary classifiers that recursively split the input data to achieve a certain result (classification) as specified by the analyst (Campbell and Wynne, 2011; Maxwell et al., 2018). For example, the data can be split according to a threshold over a specific variable. The splits are called nodes, and the first one is the root node. As for the structure of a tree, the classifier is constituted by several nodes that are repeated and connected to each other (like the branches of a tree) until reaching the target class (the leaf) (Figure 31). In the CART classification process, the entire unclassified dataset is fed to the root node and split in two groups according to the threshold, which should ensure the minimization of the mixture of classes in the two groups. For example, if there are six separate classes in the training set then we would expect the sub-groups to have pixels from fewer than six classes and, in some cases, hope that one sub-group might have pixels from one class only. The CART keep splitting the data into groups as we go down the tree structure, and the last node leads to groups containing pixels from only one class. This class represents a pure group, and it is represented by the leaf (Richards, 2013).

CART classifiers are recognized as having many advantages. The classification model can be visualized as a set of dichotomies (Campbell and Wynne, 2011; Maxwell et al., 2018; Richards, 2013). CART utilizes categorical data. Thus it can deal with ancillary data and non-linear distribution. Generally, the classification is rapid because no further complex mathematics is required, apart from creating the classification tree (Campbell and Wynne, 2011).

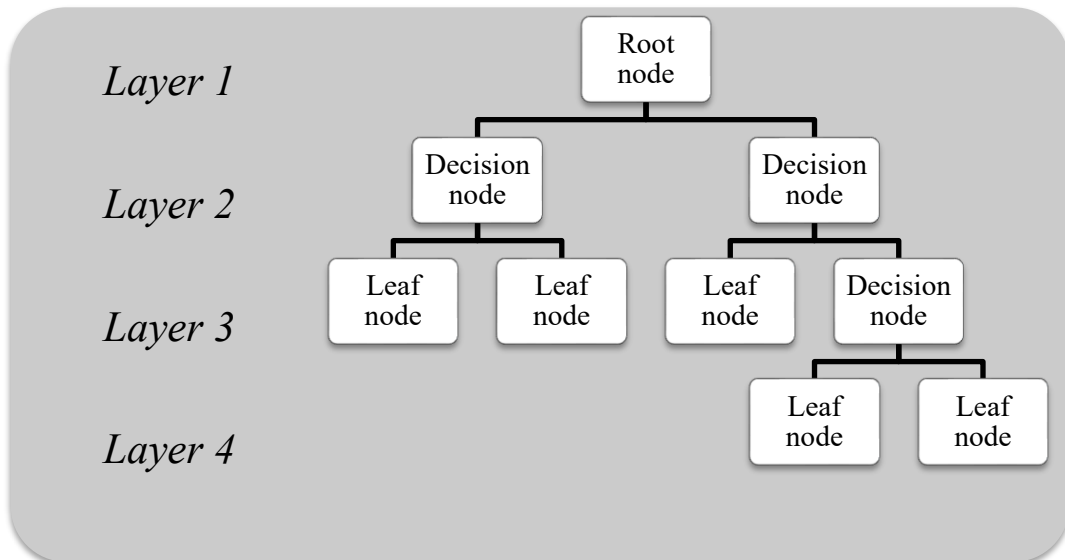
One of CART classifiers' main limits is the overfitting (Campbell and Wynne, 2011; Maxwell et al., 2018; Richards, 2013). The overfitting is a specific condition characterized by very high accuracy values when using many variables, but results that are tailored to specific datasets. The overfitting is usually addressed by removing one or more layers of splits (i.e., branches), creating a more concise, more robust, and generally applicable division rules system. This process is called “pruning” since it removes part of the decision tree branches. Generally, the pruning

reduces the accuracy of the training data but increases the unknown dataset's accuracy.

The CART classifiers require an accurate training dataset. It is essential to have equal size classes because the classifier performs better when the numbers of pixels in training data sets are approximately equal (Campbell and Wynne, 2011).

Besides the classification or decision tree, CART is also composed of the regression trees, which function is similar to the Decision trees, but the final leaves are constituted by continuing variable instead of discrete. Since the regressions are not the object of study of this work, they are not described and analyzed.

The CART tree growing methodology is possibly the most commonly encountered because it restricts and simplifies the possible options for how the decision nodes function. Only one feature is involved in each decision step, and a simple threshold rule is used in making that decision.



**Figure 31.** Example of CART classifier. It represents four layers-decision trees, where Layer 1 is the Root node, and Layer 4 is the Leaf node where the class is assigned to the unit of classification in the exam.

### *K-nearest neighbor*

k-Nearest Neighbour (k-NN) is a supervised non-parametric classifier. It is particularly simple in concept, and, unlike other machine learning classifiers, it does not need to be trained to produce a model (Campbell and Wynne, 2011; Maxwell et al., 2018; Richards, 2013). It is based on the assumption that pixels projected in the same spectral space and close to each other belong to the same class. The

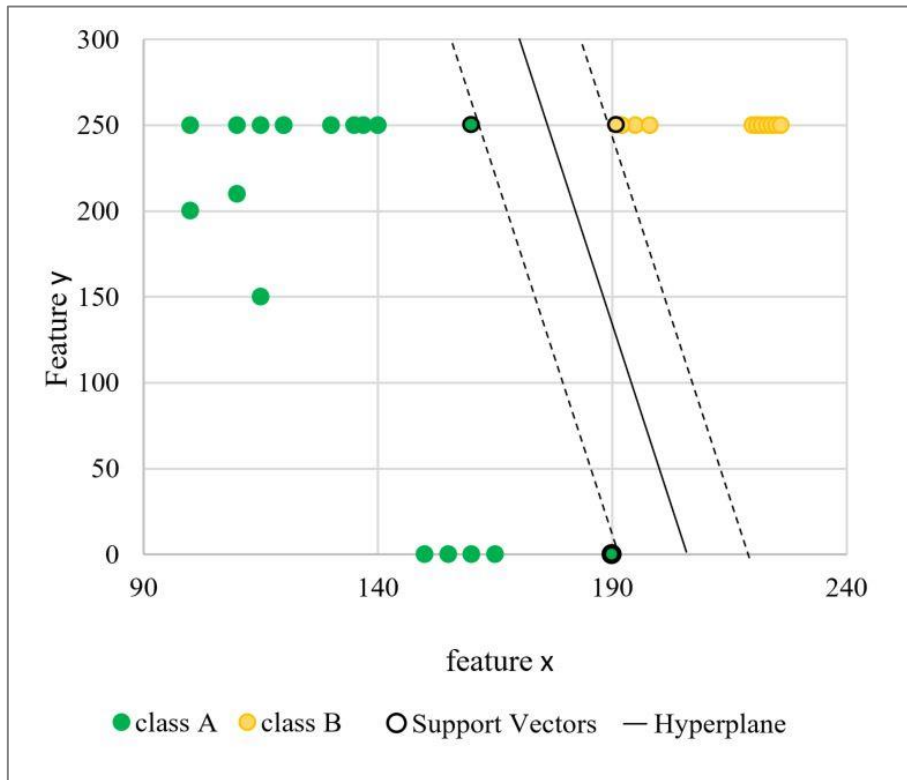
algorithm analyses each unclassified pixel, and it finds the k number of sample pixels that are closer to the unclassified one. The analyzed pixel is then assigned to the class represented by the most samples among the k neighbors (Campbell and Wynne, 2011). Typically, k is set to be a relatively small integer divisor. A small value of the k parameter produces a very complicated decision boundary, but on the other hand, a higher k will result in greater generalization (Maxwell et al., 2018). K-NN classifiers need consistent time for computation because they need to calculate each pixel's distance to the k neighbors. This is particularly true for large training datasets and spectral bands (Campbell and Wynne, 2011; Maxwell et al., 2018; Richards, 2013; Thyagarajan and Vignesh, 2019).

#### *Support Vector Machine (SVM)*

SVM is a non-parametric supervised machine learning technique that was introduced in remote sensing in 1998 to solve binary classification problems (Maxwell et al., 2018; Richards, 2013; Salah, 2017b; Talukdar et al., 2020). It is based on the concept of structural risk minimization (SRM), and it separates multidimensional data into two classes using hyperplanes (Figure 32). The hyperplanes define the class's margins, and they are identified to ensure the maximum space between the classes (Salah, 2017b; Talukdar et al., 2020). The hyperplanes should be equidistant on average from the sample points projected into the feature space (Richards, 2013). The definition of the hyperplanes is the first aim of the SVM algorithms. Support Vectors are the samples that delineate the hyperplanes (Maxwell et al., 2018). The SVM can support multiple continuous and categorical variables as well as linear and non-linear data distribution in different classes.

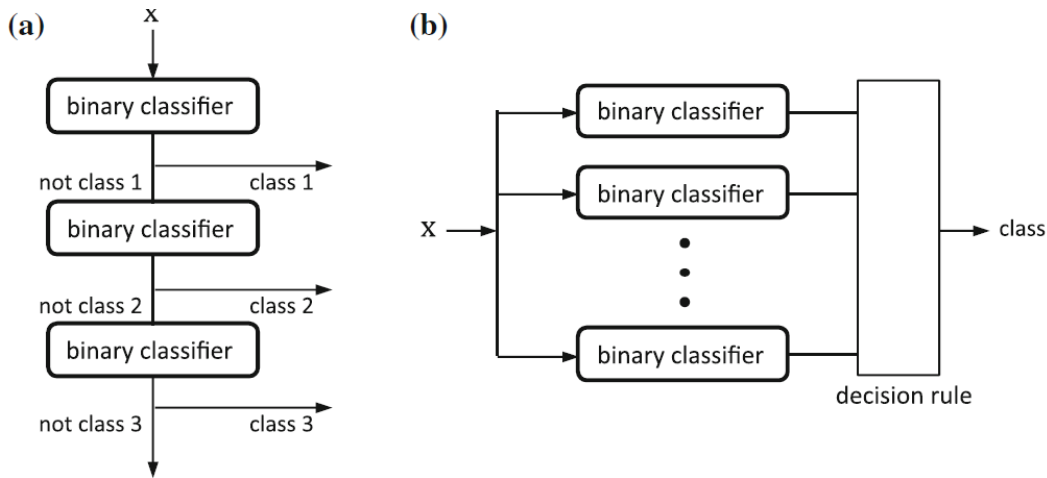
The SVM algorithm needs a proper kernel function to project the data from the input space into feature space to accurately establish the hyperplanes (can be non-linear) and minimize the classification errors. The selection of the kernel function represents the essential part of the SVM. Four kernels that can be used for SVM exist: i) Gaussian Radius Basis Function (RBF); ii) Linear; iii) Polynomial, and iv) Sigmoid (Quadratic). In remote sensing classification, the Gaussian RBF kernel is the most popular, and it has proved to be effective with reasonable processing times and accuracies (Maxwell et al., 2018; Salah, 2017b; Talukdar et al., 2020). In a perfect scenario, the training samples are correctly separated, and the hyperplanes are linear features. This is not always true. In the case of overlapping classes, the hyperplanes have soft margins, and observations can lay on the wrong side on the hyperplane if a cost, defined by the analyst, is respected (Maxwell et al., 2018; Salah, 2017b). Since SVM was born for binary classifications, to apply it in the

multi-category analysis is necessary to create a multilevel SVM. There are basically two approaches.



**Figure 32.** Optimum separation plane (hyperplane) and support vectors data that define it. (Salah, 2017b).

The first, called one-against-the-rest or one-against-all (OAA), consists of creating a SVM classifier tree, the first distinguish in class 1 and “all the rest”. All the rest in then input dataset for class 2 and so on. This method is largely applied, but it is sensitive to an unbalanced training dataset (Richards, 2013; Salah, 2017b). The second approach consists of using several binary classifiers in parallel. All the possible combinations between the classes are analyzed. All the classifiers classify each pixel/object, and it is assigned to the class with major classification in favor. This part constitutes the logic decision rule. This method is defined as one-against-one (OAO) (Figure 33). It requires higher computational time and power since it runs many binary classifiers in parallel (Richards, 2013; Salah, 2017b). Apparently, the results of OAA and OAO are very similar (Salah, 2017b).



**Figure 33.** Example of a simple SVM decision tree (a) and a multiclass decision using SVM classifiers in parallel with final decision logic (b). (Richards, 2013).

### *Artificial Neural Networks (ANN)*

Artificial Neural Networks are non-parametric classification systems that are conceptualized as human brains. Their structure is composed of several axons (neurons) interconnected by synapses, like animals' brains. Besides the human-like structure, ANNs are compared to the human brains also for their functioning. Indeed, ANN are considered a form of artificial intelligence that simulates some functions of the human brain to associate the correct meaningful labels to image pixels (Maxwell et al., 2018; Salah, 2017b; Talukdar et al., 2020). The neurons are processing units organized in layers. Each neuron is connected to the neurons of adjacent layers, and these connections are weighted. The weights on the connections, combined with the typically non-linear activation function that further modifies values at each neuron, determine how input values are assigned to values on the output nodes. The transfer of information between neurons through the weighted connection is called a forward connection (Talukdar et al., 2020). A peculiar characteristic of ANN is the presence of hidden layers in the network that increases the potential for describing very complex class delineation (Maxwell et al., 2018). An ANN has minimum input and output layers, a neuron for each input variable, and a neuron for each output class (Maxwell et al., 2018). During the training, the ANNs learn the regular structure of training data and, through interactive guessing and adjusting of the connection weights, define the final network (classification model) (Maxwell et al., 2018).

Several ANN algorithms for remotely sensed images classification exist (Salah, 2017b). Some of the most common in Land Cover classification are Multi-layer perceptron (MLP), Fuzzy ArtMap classification, Self-Organized feature Map, and



Radial Basis Function Network (Salah, 2017b). It is recognized that ANN are generally very slow to train, they need a large training dataset, and they are particularly prone to overfitting. Additionally, there are many user-determined parameters to specify (Maxwell et al., 2018). Their use has recently spread in parallel with the increment of computational power and data storage of computers. For this reason, few remote sensing classification software have ANNs algorithms implemented.

### *Random forest*

The Random Forest is a supervised non-parametric ensemble classifier. Ensemble classifiers have become quite popular in the last years (Belgiu and Drăguț, 2016). They consist of many algorithms, or a single algorithm, that operate on the same dataset to produce individual, sometimes competing, classification of a single pixel. The results of these classifications are fed to a final decision maker, or chairmen, for the assignment of the final label to the pixel (Belgiu and Drăguț, 2016; Gislason et al., 2006; Richards, 2013). The ensemble classifiers are based on many supervised classifiers trained using bagging or boosting approaches (Belgiu and Drăguț, 2016; Richards, 2013).

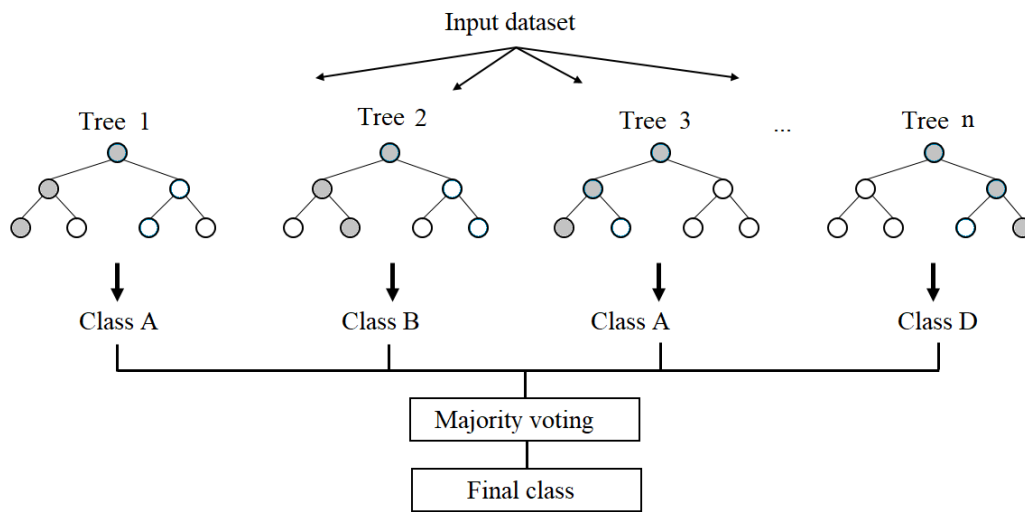
The bagging training approach (also known as the Bootstrap AGGregation approach) works on randomly chosen subsets of the training dataset. This process is called bootstrapping. The training dataset is sub-grouped into several different datasets, each containing  $n$  training pixels/objects. The  $n$  pixels/objects are chosen randomly from the entire training dataset, with replacement. This means that the same pixel could appear more than once among the  $n$  chosen. Each of the sub-groups to train a classifier. The results of the individual classifiers are then combined by voting (Richards, 2013).

The boosting approach, which is also called Adaptive Boosting or Adaboost, consists of several classifiers that are trained sequentially. After the first training, the training pixels are classified and the ones that are found to be in error are trained again by the second classifier, and so on. The final label is allocated to a pixel/object based on the outputs of all the classifiers (Richards, 2013).

Bagging and boosting methods have been proven to improve the goodness of the Land Cover classification compared to single classifiers, and generally, boosting provides better results than bagging (Belgiu and Drăguț, 2016). Nevertheless, the boosting approach requires consistent computational power, it is prone to overfitting if there are insufficient training samples, and it is sensitive to noisy training dataset and outliers (Belgiu and Drăguț, 2016; Gislason et al., 2006). In contrast, the bagging approach reduces the classification variance, but they have

little effect on the classification bias. The ensemble classifiers are more stable and robust to noise in the training data (DeFries and Chan, 2000). Random Forest is an ensemble classifier composed of several CART classifiers trained with a bagging approach and was introduced by (Breiman, 2001). Since it is composed of CART classifiers, it can be applied for regressions and classifications both. It is called random forest because it comprises several decision trees (CART) that are random in their construction (Belgiu and Drăguț, 2016; Richards, 2013). The Random Forest uses around two-thirds of the training dataset to train the model and the remaining one third is used for the internal cross-validation of the model's performance (Belgiu and Drăguț, 2016; Breiman, 2001). The two-third of the sample is defined as an in-bag dataset or in-bag samples, and the one-third for the cross-validation is called out-of-bag (OOB) samples. The decision trees are built according to the parameters identified by the analyst and without pruning. The analyst defines the number of trees and the number of features needed to split a node. In this way, the random forest algorithm creates trees that have high variance and low bias (Breiman, 2001).

The final decision-maker of the classification consists of the modal logic of the class assignment probabilities calculated by all produced trees (Belgiu and Drăguț, 2016; Richards, 2013), (Figure 34). The Random Forest's decision trees need to be uncorrelated to be effective, and this is ensured by the bagging approach (Breiman, 2001; Richards, 2013). The number of trees (Ntrees) and the minimum number of nodes to split the tree (Nnodes) are the only two parameters that the analyst needs to set for the Random Forest classifiers. The review about the Random Forest in Land Cover classification of (Belgiu and Drăguț, 2016) highlights that the goodness of the classification is less sensitive to the number of trees than to the minimum number of features parameter. Indeed, the number of trees is generally set as larger as possible because there is no overfitting risk. In Land Cover classification, the Ntrees is generally set between 500 and 1000 to obtain reliable results. According to other research (Belgiu and Drăguț, 2016; Du et al., 2015; Topouzelis and Psyllos, 2012), the Random Forest can also be efficient with a lower value Ntrees. Some software packages (e.g. Image Processing Package in matlab©) allows the optimization of the number of trees parameter. Generally, the Ntrees parameter depends on the dataset to be classified. The minimum number of nodes necessary to split the tree is a relatively easier parameter to be defined, and it depends on the number of input features. (Gislason et al., 2006) suggest setting as Nnodes the number of input variables' root square value. Large values of Ntrees and Nnodes influence the computational time of Random Forest classifiers (Belgiu and Drăguț, 2016).



**Figure 34.** Structure of Random Forest classifier. It is composed of  $n$  trees with a different number of nodes. Each tree defines a class for each element to be classified, and the most frequent (majority voting) is the final class assigned to the element. Modified from Venkata Jagannath, CC BY-SA 4.0

An additional interesting aspect of the Random Forest classifier is the possibility of evaluating the importance of the features in the classification (Breiman, 2001; Grömping, 2009). This parameter indicated the role of each feature within the classification model. In this way, low-importance variables or the ones that introduce noise can be removed from the classification.

Also, a few parameters to set good accuracy values and the ability to deal with small training samples are other causes behind the method's recent popularity (Biau and Scornet, 2016). It has been successfully applied in various fields. The Random Forest algorithm is the most successful general-purpose algorithm in modern times (Bowles, 2012).

Various studies have been realized in the theoretical aspects of Random Forest. Nevertheless, some difficulties emerged, which can be explained by the method's collage nature (Biau and Scornet, 2016). Indeed it is composed mainly of the bagging algorithm and the CART that are difficult to analyze with rigorous mathematics. According to Biau and Scornet, this is the reason why most of the theoretical studies on Random Forest have so far considered simplified versions of the original procedure. Nevertheless, Random Forest can estimate patterns that are more complex than classical ones, and they are still to be discovered, quantified, and mathematically described method (Biau and Scornet, 2016).

### 4.4.3. Machine Learning classifiers for Land Cover

Some of the most popular classifiers are presented in the previous paragraphs. Some of them, such as K-NN, use the information about the neighboring pixels to model the training dataset pattern. Others result from the application of several single classifiers, such as RF that uses a random subset of training data to construct multiple decision trees, or, in a certain way, the SVM classifier composed of several binary SVM classifiers. ANN builds multiple layers of nodes to pass input observations back and forth during the training until it reaches a stable condition. In the Land Cover analysis realm, which is the most effective classifier? Many authors have tried to answer this question. Excellent reviews for machine learning in Land Cover exist (Lary et al., 2016; Maxwell et al., 2018; Pandey et al., 2019; Richards, 2013; Salah, 2017b; Talukdar et al., 2020). Most of the literature suggests that machine learning performs better than traditional methods (Lu and Weng, 2007), and especially Random Forest and SVM proved the best accuracy values (Belgiu and Drăguț, 2016; Maxwell et al., 2018).

In general, these methods appear to produce higher overall accuracies compared to other machine learning classifiers such as single DT and k-NN. However, each classification may have a different answer to selected classifiers. The best algorithm may be case-specific. It depends on the selected classes, the quality of the training data, and the dataset to be classified (Lu and Weng, 2007; Pandey et al., 2019). There is currently no theory that can be used to predict how classifier performance may relate to these attributes. Thus, if possible, users should experiment with multiple classifiers to identify the best method. Generally, machine-learning methods, especially SVM, RF, and boosted DTs, have been more robust to large or complex feature spaces than parametric methods. SVM and RF have been found in many studies to be of value for classifying hyperspectral data. On the other hand, k-NN generally does not perform well in complex feature spaces (Belgiu and Drăguț, 2016; Maxwell et al., 2018).

According to other research (Pandey et al., 2019), the Random Forest performs equally well to SVM when all parameters are considered similar to both classifiers. However, SVM is more sensitive to the nature of the input features. (Ma et al., 2017b) analyzed 173 papers on object-based classification of Land Cover and observed that Random Forest provides the best performance in object-based classifications. Indeed, they notice that it has attracted significant attention in recent years, followed by SVM. Furthermore, they underline that k-NN is the most applied algorithm in object-based classification, despite appearing unsuitable for more extensive use in object-based classification (Ma et al., 2017b). According to the

analysis of (Belgiu and Drăguț, 2016), Random Forest outperforms in terms of classification accuracy DTs and ANN.

Nevertheless, its performance against other ensemble classifiers, such as Adaboost, is slightly lower. For all above-selected algorithms, the Random Forest is easy to define and requires less number of user-defined parameters as compared to other classifiers, and moreover, it outperforms others in terms of classification accuracy for the same set of parameters and training time (Belgiu and Drăguț, 2016; Pandey et al., 2019). Despite the better performance, ANN require a large training dataset. It has been discussed by (Biau and Scornet, 2016) the similarity between Random Forest and the deep network architectures since it allows the discrimination of classes in an extensive dataset. This can be one of the reasons behind the success of Random Forest's application on large-scale data. The connections between random Forests and Neural Networks are still unexamined (Biau and Scornet, 2016). The decision of the best classification algorithm depends on several factors, such as the type of classification, the nature of the input dataset, the information needed, the experience of the analyst, and the computational power and the time available. Nevertheless, the facility of application and availability of algorithms in classic classification software might influence the diffusion of certain algorithms that others. Table 15 is derived from (Maxwell et al., 2018)'s work and shows the software that has implemented machine learning algorithms.

**Table 15.** Machine learning algorithms are implemented in some of the most used image classification software by author's analysis in 2020.

Software		Algorithms					
		k-NN	ANN	DTs	Boosted DTs	RF	SVM
Geospatial software	ArcGIS 10.5/ArcPro 2					•	•
	eCognition Developer 9	•		•		•	•
	ENVI 5.4		•				•
	Erdas Imagine 2016						
	TerrSet/IDRI SI 18.3	•	•	•			
	QGIS 2.18	•	•	•	•	•	•
Statistical software	Matlab 9.3	•	•	•	•	•	•
	R 3.4	•	•	•	•	•	•

#### **4.4.4. Selection of the training samples for supervised classification**

The definition of the training samples has a fundamental role in supervised classification and can strongly influence the classification results since it feeds the classification model. The training samples are a set of statistics that describes the spectral response for each land cover class to be classified (Salah, 2017b). Four aspects regarding the nature of the training samples are fundamental for a good classification (Belgiu and Drăguț, 2016; Lu and Weng, 2007; Salah, 2017b):

- i. Training dataset and the validation dataset are statistically independent;
- ii. Training samples are class balanced;
- iii. Training samples are representative of the selected classes;
- iv. Training samples are large enough to accommodate the increasing number of data dimensions.

A sufficient number of training samples and their representativeness are critical for image classifications (Lu and Weng, 2007; Ma et al., 2017b). The creation of the training dataset is a time consuming, expensive, and subjective (Belgiu and Drăguț, 2016). Namely, to generate the training samples, the analyst has to know the study area, he/she needs to have field experience with the landscape (i.e., Land Cover), and he/she should be familiar with the particular problem the study is addressing (Lu and Weng, 2007). The analyst practically identifies a certain number of pixels/objects (can be grouped in polygons or single points) for each class. In the past years, the training samples were collected from fieldwork. However, this method has been abandoned for large-scale classifications, and nowadays, training samples are collected from visual interpretation of aerial images or extracted from already existing Land Cover maps. The number of training samples selected for each class can influence the classification's goodness, especially with some classifiers such as Random Forest (Belgiu and Drăguț, 2016). The exact number of training pixels required depends not only on the type of classifiers but also on the number of classes, the features, and the image's size to be classified. The training dataset has to be large enough to provide precise information regarding the characteristics of each class. Namely, it should include a sufficient number of pixels to estimate each class's spectral characteristics reliably.

Nevertheless, the training samples should not be too large because large datasets may increase the possibility of including outliers (pixels/objects that do not represent the target class). As a general guideline, the analyst should select at least 100 pixels for each class (Lu and Weng, 2007), and the optimum size of training

samples depends on the heterogeneity of each landscape (i.e., area) and each class legend. Thus, each analyst should develop his/her own guidelines based on experience acquired in specific circumstances (Lu and Weng, 2007). This view is shared by (Lu and Weng, 2007), who wrote that:

*The selection of training samples must consider the spatial resolution of the remote-sensing data being used, availability of ground reference data, and the complexity of landscapes in the study area.*

Other authors (Kavzoglu and Mather, 2003) propose a different approach for defining the training sample size that depends on the number of input features. It should range between  $[30 * N_i * (N_i + 1)]$  and  $[60 * N_i * (N_i + 1)]$ .

$N_i$  is the number of input features (Kavzoglu and Mather, 2003; Salah, 2017b). Similarly, (Richards, 2013) identifies the needed number of training samples in the minimum of  $10N_i$  training pixels per spectral class is recommended, with as many as  $100N_i$  per class. Nevertheless, he underlines the difficulty of reaching such values of training samples in large  $N_i$  such as hyperspectral datasets.

It is essential to underline that the above methods were born for the Maximum Likelihood classifier, a parametric algorithm based on the classification of the covariance matrix and, therefore, may require more training samples non-parametric methods. If the training sample is small in number, or data quality is uncertain, an algorithm that is robust to these issues should be used, such as ensemble Decision Trees (DT) methods (e.g., Random Forest or boosted DTs) (Maxwell et al., 2018).

Besides the number of training pixels, the location and the distribution of the training samples within the scene may affect the classification (Campbell and Wynne, 2011). Indeed, the training samples collected in contiguous blocks tend to underestimate the variability within each class and overestimate categories' distinctness (Campbell and Wynne, 2011). The sample pixels should be distributed throughout the image to provide a basis for the representation of the diversity present within the scene. The training pixels must be placed away from the edges of different land covers, but at the same time, they should also be ensured the representation of each spectral subclass. It is also proven that it is generally better to use a large number of small training fields rather than a few broad areas (Campbell and Wynne, 2011).

Different strategies for the collection of the training sample exist. The analyst should decide if the training samples are constituted by single pixel (point-based classification) or polygons (area-based classification). It is worth highlight that in

object base classifications, the training dataset needs to be composed of objects, thus polygons. When the OBIA classification is point-based, the polygons in which the training points lay are used as samples. Differently, in pixel-based classification, the training pixels can be isolated or grouped in homogeneous areas. In both cases, the classifier will merge the information regarding the pixels on class basis.

(Ma et al., 2017b) carried out a study on the relation of the number of training samples, their nature (points or polygons), and OBIA classifications' accuracy. They observed that in general, with an increase in the size of training samples, the classification accuracy increases accordingly, even if this positive correlation between size and accuracy is very weak, especially in the point-based classification that detects a very poor increment of the accuracy. Point-based training samples may not be able to represent each class correctly. On the other hand, area-based training samples can include outliers, especially in high spectral variability classes. The proportion of pixels per class is another aspect of the classification that needs to be taken into account when creating the sample dataset. The pixels per class can be random sampling, the number of samples per class can be proportional to the expected covering area, or each class can have an equal number of samples. Therefore, it is essential to evaluate the sensitivity of the classification to sampling design and imbalanced training samples. This aspect assumes more importance for some algorithms than others, such as Random Forest (RF). RF classifier fails to cope with imbalanced training data and favors the most representative class (Belgiu and Drăguț, 2016).

The most common methodology for creating the training samples is the manual detection and creation of a single sample by the analyst. Recently some other application has been used, such as simple random sampling and stratified random sampling. The single random sampling algorithm randomly locates a user-defined number of pixels within the study area. The analyst can analyze each of them and assign the proper class. The stratified random sampling algorithms randomly locate a user-defined number of pixels within the given classes. This allows the analyst to use existing land cover maps as a basemap for the training sample creation (Ma et al., 2017b).

The feature space can be simplified using feature extraction or feature selection. Unfortunately, these techniques are not commonly implemented into commercial remote-sensing software packages, so statistical or data analysis software may be required. Methods of feature selection based upon the Random Forest algorithm have been shown to be promising.



## **4.5. Accuracy assessment methodologies and measures**

After the classification, its accuracy needs to be assessed. Accuracy assessment is necessary to understand the goodness and allow the analyst to evaluate the effectiveness of the results of the land cover map for the intended applications (Richards, 2013; Salah, 2017b). There are several measures for expressing the accuracy of classification (Richards, 2013). The accuracy assessment generally includes three essential components: the creation of test samples, detection of classification's response to the test, and estimation and analysis procedures. The samples are randomly selected and generated similarly to the training samples used to train a classifier in the first instance. In most cases, the analyst labels as many pixels/objects as practicable and then uses a subset for training and another subset for assessing the accuracy of the final product (Richards, 2013).

As for selecting the training sample, identifying a suitable test sampling strategy is one of the most critical steps (Lu and Weng, 2007). Indeed, training samples and test samples can be selected in the same way. Polygons or points can constitute them. The influence of the test samples' nature on the classification accuracy can be attributed to the ones of the training samples. Different from training sample identification, significant accuracy assessment needs a lower number of samples. Unfortunately, very few studies have explored candidate samples' labeling during supervised object-based image classification to date. Moreover, the labeling process is not clearly stated in numerous studies on supervised classification. Because it was already explicitly demonstrated that accuracy performance benefits more from homogeneous objects (Li et al., 2016), which signifies when the area-based method is used in accuracy assessment, the more homogeneous objects selected as training samples or test samples, the higher the classification accuracies.

Many sources of errors can affect the classification result. Before implementing a classification accuracy assessment, one needs to know them. The error can derive from the classifier errors, the registration of the images, the low quality of training, and/or interpretation errors (Salah, 2017b). They may lead to uncertainties and influence the classification accuracy, as well as the estimated area and distribution of land-cover classes (Salah, 2017b). When analyzing a classification's accuracy, it is generally assumed that the errors descend from the classification (Lu and Weng, 2007). The accuracy assessment is based on comparing the results of the classification and the reference (or test) samples. The most applied accuracy assessment of land cover classification is the error matrix (Campbell and Wynne, 2011; DeFries and Chan, 2000; Long et al., 2013; Lu and Weng, 2007; Richards,

2013; Salah, 2017b). The error matrix is the base for many accuracy measures such as overall accuracy, producer's accuracy, user's accuracy. In OBIA classifications of Land Cover, the goodness of the segmentation is an additional source of error. As presented in paragraph 4.2, page 51, the segmentation process is a key step of the OBIA approach and strongly influences the final classification. For this reason, its goodness needs to be assessed too. In fact, the test samples affect the assessment of classification accuracy performance because (Ma et al., 2017b):

- I. The actual interpreted image layer objects cannot fully coincide with the segmentation objects;
- II. Segmentation objects consist of mixed land cover types.

Besides the spread application of object-based classification technique, it still does not exist a shared and well-established methodology for assessing segmentation. A briefs review of the existing methods for the segmentation assessment is presented in paragraph 4.5.2, page 90.

#### **4.5.1. Error matrix and its derived measures**

Regardless of the nature of the reference dataset (i.e., test samples), it is common to express the results in an error matrix that lists the reference data classes by column and the classes indicated on the thematic map by row. It identifies the overall errors for each class and the misclassifications (due to confusion between categories) by class. Other important accuracy assessment elements, such as overall accuracy, omission error, commission error, and kappa coefficient, can be derived from the error matrix. The error matrix is an  $n \times n$  matrix where  $n$  is the number of classes in the classification. Conventionally, the existing samples classes on the map are indicated in the rows, and columns contain the same  $n$  categories from the reference data (Figure 35). Here values in the matrix represent numbers of pixels for which the analyst has been able to compare the evaluated and reference images. The matrix cells indicate the samples in common between reference sample classes and classes from the resulting classification. The diagonal values represent the correctly classified test samples. Thus, the best-case scenario is when all the values outside the diagonal are equal to zero (or very small), which indicates a perfect classification. The column sums in the error matrix represent the number of reference samples available per class, and the row sums represent the total number of samples labeled by the classifier as coming from a particular class. These values indicate the errors of omission and errors of commission. The omission errors are the pixels that the classifier has failed to recognize, and the classifier label is

different from the reference label. The commission errors correspond to those samples belonging to other reference classes that the classifier has placed in the class of interest. Some of the error matrix measures are the overall accuracy, producer's accuracy, user's accuracy, k coefficient, and f1 score.

The overall accuracy is the most applied approach for the evaluation of the goodness assessment of classification. It is calculated as (equation 2):

$$OA = \frac{CC}{RS} \quad [2]$$

Where  $OA$  is the overall accuracy (often expressed as a percentage),  $CC$  is the total number of correctly classified samples, and  $RS$  is the total number of reference samples. The level of agreement between the classified dataset and test dataset can be measured in 5 classes, poor or very poor, fair, good, very good, and excellent, corresponding to the values lower than 0.4, from 0.4 to 0.55, from 0.55 to 0.70, from 0.70 to 0.85, and higher than 0.85, respectively, between images and ground reality (Talukdar et al., 2020).

		Reference data				
		Class 1	Class 2	Class 3	Class 4	Total (omission)
Classified data	Class 1	$X_{1,1}$	$X_{1,2}$	$X_{1,3}$	$X_{1,4}$	$X_{1+}$
	Class 2	$X_{2,1}$	$X_{2,2}$	$X_{2,3}$	$X_{2,4}$	$X_{2+}$
	Class 3	$X_{3,1}$	$X_{3,2}$	$X_{3,3}$	$X_{3,4}$	$X_{3+}$
	Class 4	$X_{4,1}$	$X_{4,2}$	$X_{4,3}$	$X_{4,4}$	$X_{4+}$
	Total (commission)	$X_{+1}$	$X_{+2}$	$X_{+3}$	$X_{+4}$	

**Figure 35.** Example of error matrix. The elements on the diagonal are the correctly classified samples.

The producer's accuracy ( $PA$ ), equation 3, is the number of correctly classified samples ( $CC$ ) of a particular category ( $m$ ) divided by the total number of reference samples for that category ( $RS_m$ ).

$$PA = \frac{CC_m}{RS_m} \quad [3]$$

It is a measure of the error of omission (Story and Congalton, 1986). The user's accuracy ( $UA$ ) is the number of correctly classified samples ( $CC$ ) of a particular category ( $m$ ) divided by the total number of reference samples being classified as that category (including the misclassified) ( $RS$ ). It measures the error of commission (equation 4).

$$UA = \frac{CC_m}{RC_m} \quad [4]$$

The K measure (kappa) is the difference between the observed agreement between two maps (as reported by the diagonal entries in the error matrix) and the agreement that might be attained solely by chance matching of the two maps, equation 5. Not all agreements can be attributed to the success of the classification.

$$k = \frac{N \sum_{i=1}^r X_{ii} - \sum_{i=1}^r (X_{i+} * X_{+i})}{N^2 - \sum_{i=1}^r (X_{i+} * X_{+i})} \quad [5]$$

Where  $r$  is the number of rows in the error matrix;  $X_{ii}$  is the number of combinations along the diagonal;  $X_{i+}$  is the total observations in row  $I$ ;  $X_{+i}$  is the total observations in column  $I$ ; and  $N$  is the total number of cells. Kappa analysis is recognized as a powerful method for analyzing a single error matrix and for comparing the differences between various error matrices (Campbell and Wynne, 2011; Lu and Weng, 2007; Salah, 2017b)

The relation between  $UA$  and  $PA$  is described by the F1 score [6]:

$$F1 = \frac{2 \times PA \times UA}{PA + UA} \quad [6]$$

Previous literature has defined the meanings and provided computation methods for these elements (Lu and Weng, 2007). The assessment of the classification can be realized using as test sample the total number of pixels present in the scene. This approach is a point-by-point basis accuracy assessment and allows one to determine exactly how each of the validation samples is represented in the classification. The validation samples and the map must be well co-registered to one another. Registration errors will appear as errors in classification, so registration problems

will create errors in accuracy assessment. For this approach, the reference sample is a Land Cover map.

#### **4.5.2. Measures for the assessment of the segmentation process of object-based classifications**

In object-based high-resolution remote-sensing image classification, researchers are more inclined to view the object as an individual point. Thus the classification of this object is either correct or incorrect (Ma et al., 2017). However, its classification accuracy increased with increasing scale, which is not reasonable over large scales because an increase in the number of mixed objects may reduce classification accuracy. The area-based validation method essentially assesses classification accuracy based on the scope and spatial distribution of segmentation objects (Ma et al., 2017). The main issue is that the accuracy assessment unit is no longer a regular pixel unit, and each object is a geographical object of differing sizes (Ma et al., 2017). The literature is rich in methodologies for evaluating the goodness of segmentation and extraction of specific objects from imagery (Clinton et al., 2010). Nevertheless, a shared and accepted methodology for the accuracy assessment does not exist (Persello and Bruzzone, 2010). Besides this, the methods applied are quite similar to each other, and generally, as for the pixel-based classification, they are based on the comparison between manually digitalized reference objects and the segmented objects (Clinton et al., 2010; Hussin et al., 2014; Ke and Quackenbush, 2011; Persello and Bruzzone, 2010; Radoux and Defourny, 2007; Yurtseven et al., 2019). The most common validation methodologies can be distinguished in visual evaluations and quantitative measures. The visual evaluations are based on comparing reference objects to the segmented ones and their attribution to the match or non-match categories by the operator. The omission and commission errors are then calculated (Ke and Quackenbush, 2011; Mohan et al., 2017; Qiu et al., 2020; Wolf and Heipke, 2007). The quantitative measures focus on comparing the reference dataset and the segmentation results based on specific metrics. The perimeter, the area, and the distance between centroids of the objects are some of the most calculated metrics for the goodness of the segmentation assessment (Clinton et al., 2010; Hussin et al., 2014; Persello and Bruzzone, 2010; Yurtseven et al., 2019). Generally, the evaluation of the metrics is performed by applying normalized indices (Clinton et al., 2010; Hussin et al., 2014; Persello and Bruzzone, 2010; Yurtseven et al., 2019) or by calculating the Root Mean Square Error (RMSE) (Hussin et al., 2014; Ke and Quackenbush, 2011; Yurtseven et al., 2019). The normalized indices can provide a value representing the goodness of the segmentation that can be easily compared to

other segmentation. The quantitative methods are almost entirely applied only to evaluate satellite imagery segmentation of heterogeneous land cover scenes (Talukdar et al., 2020). In this work, VHR images' segmentation was assessed through quantitative and qualitative methods; see paragraph 7.1, page 135, and paragraph 8.3, page 235.

## 4.6. Lesson learned

This chapter intends to analyze the workflow for the analysis and the generation of Land Cover maps, from collecting the raw data to the generation of the final maps. Some of the paragraphs in this chapter treats only a small part of comprehensive arguments that, in some cases, constitute an entirely separate field of research. Hence, this chapter does not aim to consider each aspect of Land Cover analysis classifications deeply, but its goal is to consider the entire classification as a whole in a relevant literature framework. With this aim, the literature review emerged that the non-parametric supervised classification algorithms (i.e., machine learning) are the most used and studied for the Land Cover Classification. Specifically, machine learning dominates the LC scene for the last ten years. In summary, some considerations are proposed below:

- I. High spatial resolution remote-sensing imagery remains the most common input data for supervised land cover classification, and the dominant image resolutions range between 0–2 m. Generally, data are spaceborne-collected. Little work on higher resolution derived from UAV exists.
- II. In supervised classifications, the sample size and quality of training data significantly impact classification accuracy. Generally, it is best to obtain many high-quality training samples that fully characterize the target classes. However, there are practical limits to the collection of many and error-free training samples. Wheatear the training dataset is small in samples and/or data quality is uncertain, an algorithm that is robust to these issues should be used, such as ensemble DT methods (e.g., RF or boosted DTs).
- III. Machine-learning classifiers have several parameters that should be optimized.
- IV. Some algorithms have been reported to be robust to parameter settings, such as RF, it outperforms parametric classifiers, such as Maximum Likelihood, even without optimization. Selecting many trees (e.g., 500) appears to

produce a classification accuracy close to what can be achieved through optimization.

- V. Additional output information generated by some classifiers may be useful. For example, RF provides an estimation of variable importance, useful information for the feature selection process. RF attracted significant attention in recent years (followed by SVM).
- VI. Furthermore, aNN provides excellent results in Land Cover classification, but it requires vast training datasets. Unexpectedly, aNN appears less suitable for more extensive use in object-based classification.
- VII. Currently, implementations of machine learning in commercial remote-sensing software packages is limited. It is more frequent in statistical or data analysis software. Besides, the commercial implementations do not facilitate automated tuning, feature selection, training data balancing, or comparison of algorithms.
- VIII. Feature selection is a fundamental step, especially for high-resolution classification. Texture analysis has been proven to improve the classification accuracy and discriminants of built-up and soil areas.
- IX. Concerning segmentation algorithms, the multi-resolution segmentation technique is the most popular. A negative correlation exists between the optimal segmentation scale and the spatial resolution of imagery.
- X. Classification accuracy can be affected by training data. Generally, overall accuracy may not decrease significantly due to imbalance, though the user's and producer's class accuracies of the rare classes can be significantly affected. Thus, it is important to consider training data imbalances, especially if there is a need to map rare classes with accuracy.
- XI. A negative correlation exists between overall classification accuracy and the number of classes defined.

# Chapter 5

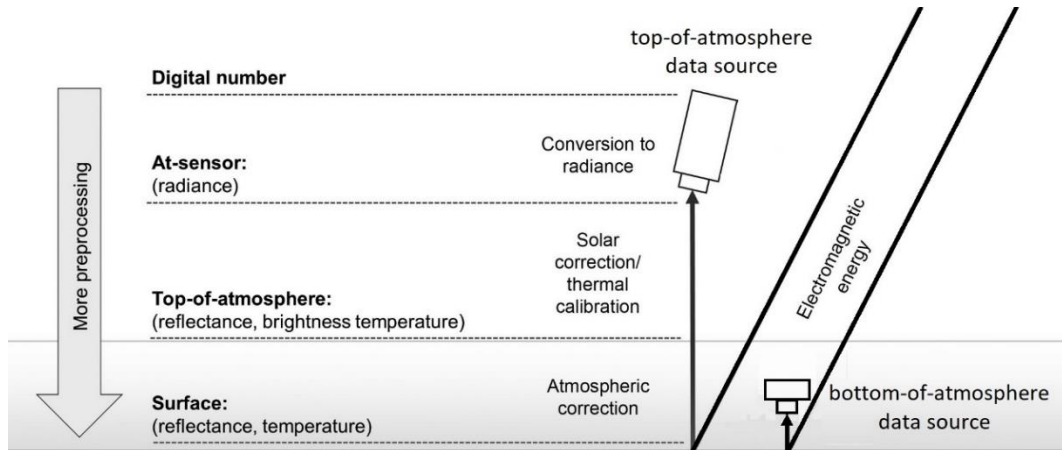
## Pre-processing of images

The remotely sensed input dataset needs to be treated and made suitable for the classification process to obtain reliable results. This step is fundamental, and it is realized before the selection of the classification system. Image pre-processing deals with sensor characteristics and atmospheric conditions and includes many operations such as georeferencing, geometric rectification, radiometric calibration, and atmospheric and topographic corrections. The number and the nature of operations needed in the pre-processing stage vary according to the type of use sensor and raw data type. For the purpose of this thesis, the first distinction needs to be made between *top-of-atmosphere*-sourced data, such as satellite optical imagery, and *bottom-of-atmosphere*-sourced data, such as Unmanned Aerial Vehicles (UAV) and airplanes imagery. The raw data format and the atmospheric effect on the data are the main differences between the two imagery types. Indeed, satellite imagery is generally provided in the form of a georeferenced orthophoto that needs to be cleaned from the distortions caused by the atmosphere and the topography. Thus, the dataset provided to the analyst is already partially pre-processed.

On the other hand, the top-of-atmosphere imagery needs to be entirely generated or combine single pictures in georeferenced orthophoto. Once the orthophoto is correctly created, it needs to be radiometrically corrected. The UAV data are not influenced by the atmosphere effect as much as the satellite data because they collect data in the proximity of the Bottom Of the Atmosphere (BOA), and consequentially the layers of the atmosphere do not interfere. The next paragraph will explore the steps required to prepare UAV- and the satellite-



generated imagery to the classification core (algorithm application). Paragraph 5.1 treats the steps required for the Satellite imagery pre-processing, while paragraph 3 explores the workflow for the pre-processing of UAV datasets.

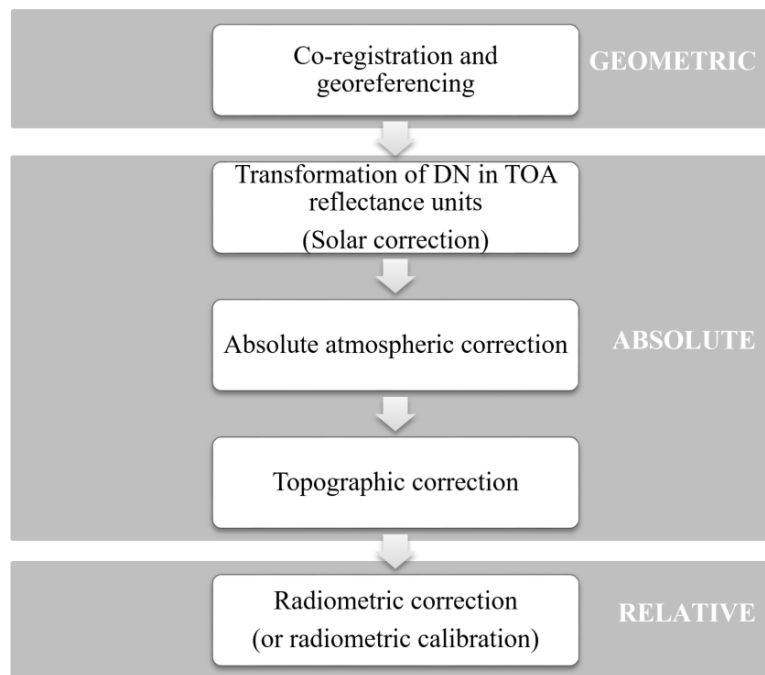


**Figure 36.** Simplified scheme of needed data corrections and calibrations due to the atmosphere. Satellite-mounted sensors collect data in the form of radiance that needs to be transformed into reflectance at the surface (or bottom-of-atmosphere). The UAV-mounted sensor is not subjected to atmosphere distortions because they are close to the Earth’s surface. Modified from (Young et al., 2017).

## 5.1. Satellite optical imagery

Images acquired from satellites are characterized by distortions caused by the effects of the sensor, the light, the atmosphere, and the topography of the scene. Many pre-processing steps are needed to minimize or delete such distortions. Some of them are compulsory, and they need to be realized in a specific order. The general workflow is proposed in Figure 37.

The requirement for a particular step of the workflow depends on the sensor type but also on the final application of the dataset. For example, if a single epoch classification is performed, the atmospheric corrections may not be required (Hurni et al., 2017; Young et al., 2017). If the study area includes mountainous regions, a topographic correction becomes necessary. The entire workflow for the preparation of satellite images is fundamental and composed of many specific steps. The Sentinel (ESA, 2019) and Landsat (USDG, 2020) user guides are suggested for deep analysis. Since satellite data providers, such as NASA and ESA, make available data partially correct the decompacting and conversion of data, denoise pixel-response correction, and, generally, all those specific actions realized before the geometric calibration (ESA, 2019) are not considered in this pre-processing overview.



**Figure 37.** Potential workflow for the correction of the satellite images. Not all the steps are always necessary. The figure is adapted from the work of Young et al. (2017).

### 5.1.1. Geometric correction

The processes of georeferencing (alignment of imagery to its correct geographic location within a given and specific reference frame) and ortho-rectifying (correction for the effects of relief and view direction on pixel location) are the components of the geometric correction necessary to ensure the exact positioning of an image. The georeferencing involves the resampling of the image and the use of know-location points on the Earth's surface, with sub-pixel accuracy. These Ground Control Points (GCPs) are used to project the image into the correct geographic location. The products follow slightly different georeferencing process according to the belonging Earth Observation mission. For example, Sentinel 2, the Earth Observation satellite mission of the European Space Agency, first compute the tile's monolithic geometry and then resample each image according to it. The bands are then co-registered using tie points identified within the tiles (ESA, 2019).

In contrast, Landsat uses GCPs for the definition of the parameters of polynomial transformation function to correct the image and result in a 'map-accurate' dataset (Young et al., 2017). The ortho-rectification step involves the correction of local topography using a Digital Elevation Model (DEM) to further

enhance the image geometry by accounting for the significant spatial distortion caused by relief displacement. Its application in the study area was of particular importance because of the high incidence of varied topography.

### 5.1.2. Absolute correction

The Absolute radiometric correction refers to a collection of preprocessing steps that account for sensor, solar, atmospheric, and topographic distortions. The absolute correction is meant to obtain true and comparable values of the scenes, although these values are still approximations (Young et al., 2017). The image's absolute corrected can be compared to images that have undergone the same level of processing. Indeed, Digital Numbers (DN) cannot be used to compare spectral values across time due to differences between sensors and single sensor degradation (Young et al., 2017). Thus, the first step of absolute radiometric correction transforms the Digital Numbers (DN) in the Top Of Atmosphere (TOA) reflectance units. This aspect is fundamental when working with multi-temporal and multi-tile datasets because it can minimize the variations between the images due to sensor differences, the Earth-sun distance, and the solar zenith angle (Hurni et al., 2017). The transformation of DN to TOA radiance can be obtained from the application of equations 7 and 8.

$$L_{\lambda} = Gain * DN + Offset \quad [7]$$

Where  $L_{\lambda}$  is the spectral radiance as function of spectral bandwidth ( $\lambda$ ); DN is the Digital Number value recorded in a single pixel, Gain is equal to  $(L_{\max} - L_{\min}) / \text{maximum DN}$ ; the Offset is equal to  $L_{\min}$  that is the lowest radiance measured by the sensor in  $\text{mWcm}^{-2}\text{sr}^{-1}$ , and  $L_{\max}$  is the radiance measured at sensor saturation in  $\text{mWcm}^{-2}\text{sr}^{-1}$ .

$$\rho_{\lambda} = \frac{\pi d^2 L_{\lambda}}{E_{0\lambda} \cos \theta_s} \quad [8]$$

Where:  $\rho_{\lambda}$  is the Top Of Atmosphere (TOA) reflectance as a function of bandwidth;  $d$  is the Earth-sun distance correction;  $L_{\lambda}$  is the spectral radiance;  $E_{0\lambda}$  is the atmospheric irradiance and  $\theta_s$  is the solar zenith angle. These data can be obtained from the sensor information and as supplementary data from the image provider.

### 5.1.3. Absolute atmospheric correction

When the TOA reflectance data are georeferenced, orthorectified, with co-registered bands, and radiometrically calibrated, their single-image analysis provides reliable results. Nevertheless, these data still suffer from the effect of the atmosphere's scattering: molecules of water vapor, fog, desert dust, air pollutants, and other particulates are atmospheric components that may alter the satellite imagery reflectance due to their different scatter characteristics and absorption capacity. These effects are multiplicative and additive, and they differ horizontally and vertically and are also band-dependent (Bruce et al., 2006). Thus, the atmospheric correction is considered fundamental in multi-temporal analysis and mosaic of images (Hadjimitsis et al., 2004; Lantzanakis et al., 2017; Martins et al., 2017; Sola et al., 2018). The atmospheric correction removes the scattering effect of the Earth's atmosphere, and it can be based on Radiative Transfer Models or Image-Based Correction Techniques (Hadjimitsis et al., 2004; Lantzanakis et al., 2017; Martins et al., 2017). On the one hand, the Radiative transfer models (also called physical-based models) (Lantzanakis et al., 2017) are specific mathematical models that consider external information, which is independent of the image, such as the latitude, season, and atmospheric conditions, for the removal of the scattering effect of the atmosphere. On the other hand, the image-based models estimate the atmosphere scattering using information and data derived within the image (Martins et al., 2017).

Radiative transfer models use as input parameters for atmospheric modeling independent data obtained from historical data, standard or meteorological data, and also field measurements. The models that require *in situ* measurements for retrieving the spectral properties of ground samples during the satellite overpass are resource-consuming and thus used only in major projects (Hadjimitsis et al., 2004). Nevertheless, when *in situ* data cannot be obtained from ground measurement, aircraft, UAVs, and other satellites can be used. During the last 40 years, many radiative transfer models have been developed. Some examples are: 6S model that it is based on the method of successive orders of scatterings approximations (Vermote and Vermeulen, 1999); ATCOR-2 that includes topographic corrections (Richter, 1990); SMAC (Simplified Method for Atmospheric Correction) model that is largely derived from the 6S model (Rahman and Dedieu, 1994); DART based on the discrete ordinate method (Gastellu-Etchegorry et al., 2004); FLAASH (Fast Line-of-sight Atmospheric Analysis of Spectral Hypercubes) based on MODTRAN 4 Radiative Transfer Code (Anderson et al., 2002). Some of these models also include additional features such

as spectral smoothing, topographic correction, and adjacency effect correction (Gao et al., 2006). The most applied Radiative Transfer Models for Sentinel 2 is SEN2COR (ESA, 2019; Sola et al., 2018; Young et al., 2017), incorporated in the Sentinel-2 processing toolbox. The Radiative Transfer Models are considered more accurate than the image-based corrections and, therefore, more applied (Bruce et al., 2006). However, Radiative Transfer Models pre-processing steps are time-consuming, imperfectly address the artifacts to be removed, and can introduce additional sources of error (Young et al., 2017).

The Image-based models for atmospheric corrections use data derived from statistical analyses of the raw pixel data. Most of these models are based on Darkest Pixel (DP) method. The darkest Pixel method consists of subtracting the minimum DN value in each band from all the other DNs in that band. It provides a reasonable correction (Hadjimitsis et al., 2004a), and it is based on the assumption that most of the signal reaching a sensor from a dark object is contributed by the atmosphere at visible wavelengths. If the radiance at the sensor ( $L_{\lambda\text{sensor}}$ ) of any objects is the sum of atmospheric distortions ( $atm$ ) and the radiometric response of the object surface ( $L_{\lambda}$ ) and dark objects radiance at the sensor is approximately null, then the radiance values at the sensor of dark objects must represent the atmospheric component, equation 9.

$$L_{\lambda\text{sensor}} = L_{\lambda} + atm \quad [9]$$

Therefore, in the Darkest Pixel approach, the pixels from dark targets are considered indicators of the amount of upwelling path radiance in a specific band (Hadjimitsis et al., 2010). The most widespread image-based techniques are the Darkest Object Subtraction or Histogram Minimum method described above (Chavez, 1988). Other methods based on Chavez's work exist, such as the DDV (Dense Dark Vegetation) (Kaufman and Sendra, 1988) and the MDDV (Modified Dense Dark Vegetation) (Song et al., 2001) techniques.

(Song et al., 2001) found that the best overall results with respect to their impacts on image classification and change detection accuracies were achieved by using the more straightforward Dark Object Subtraction method (Chavez, 1988), rather than the more complex atmospheric corrections that combine both atmospheric models and the dark object concept (Song et al., 2001). They concluded that simple atmospheric correction algorithms are recommended for applications in which surface reflectance is not required. Similarly, (Hadjimitsis et al., 2010) have found that the Dark Object Subtraction technique seems to be the

most efficient in visible and near infrared and short-wave infrared spectral areas. The Radiative transfer often requires ancillary data about atmospheric conditions at the time of image collection and can introduce additional errors (Bruce et al., 2006). Moreover, many authors underline that atmospheric correction is not always needed (Bruce et al., 2006; Hurni et al., 2017; Lu and Weng, 2007; Song et al., 2001; Young et al., 2017). Indeed, the atmospheric correction is compulsory only when the dataset is heterogeneous, for example, when it is composed of images collected by different sensors (integration of satellite-satellite, but also satellite-UAV and satellite-spectrometers) or collected by one sensor at different time, and thus atmospheric, conditions. Also, datasets composed of more than one footprint should go through the atmospheric correction process (Hurni et al., 2017). The atmospheric correction of heterogeneous datasets analyzes the same domain (i.e., classification samples collected on one image may be applied to another image) (Young et al., 2017).

#### **5.1.4. Topographic correction**

In mountains and hills, the changes of the illumination conditions caused by the sun position, the slope, and the aspect, can result in variations of the reflectance in the same land cover type. For example, the same types of forest placed in different mountainsides can have different reflectance values between the sunlit and shaded slopes. Consequently, the classifier might assign the sides of a mountain to different LC classes even if they have the same Land Cover. The reason behind the need for topographic corrections is to vary the reflectance of sloped areas derived by the inclination of the terrain and the sun elevation and flat their reflectance (Poortinga et al., 2019; Shepherd and Dymond, 2010), namely approximate reflectance values of sloped areas to the ones that would be recorded over a flat surface (Figure 38). Different approaches for the topographic illumination correction exist, and they can be classified into three categories:

- I. Empirical methods
- II. Physical methods
- III. Semi-empirical methods

The simplest methods are empirical topographic corrections, which uses only image-derived information. For example, the image is corrected through the calculation of band ratios. These methods are based on the assumption that radiance values distortion due to topography is proportional in all spectral intervals. They are easily implemented; however, these methods are rarely applied because they

lead to the loss of spectral resolution and, consequentially, to the loss of classification accuracy (Sola et al., 2018).

The physical methods do not derive any information from the image, but they model the full radiance path through the atmosphere to the target object and backward (Sola et al., 2018). These methods do not consider the diffusive effect of the atmosphere, which influences the radiance and increases along with the slope and vegetation presence. The topography and the is not considered either. These physical methods lead to the overcorrection of steep and vegetated areas (Hurni et al., 2017). The semi-empirical models are midway between empirical and physical models. They consider the topography of the area by introducing the Digital Elevation Model (DEM) information. The DEM, which can be a DSM or a DTM according to the needs of the work, is used to simulate the illumination conditions by deriving correction parameters through a linear regression between each image band and the illumination condition at the time of the image acquisition (IL or (*is*)). The semi-empirical methods outperform the other methods in the majority of studies, although they are computational expensive (Sola et al., 2018).



**Figure 38.** Shadow's effect depending on sun elevation and position. From <https://www.youtube.com/watch?v=LgZbhogv9Q8>. The proposed example regards some trees, but the same effects exist over hills and mountains.

The most applied algorithms are the Cosine Correction, the C-correction, and the Minnaert correction that considers non-Lambertian behavior of vegetated surfaces. The Sun-Canopy-Sensor-correction (SCS-correction) has been developed specifically for removing topographic effects in Landsat TM images of forested areas. A clear and concise overview of these methods is provided by (Soenen et al., 2005), and some of the most applied correction methods are described in Table 16.

For this thesis, only the SCS+C correction is analyzed in detail. The cause of the overcorrection in the SCS model is similar to that of the cosine correction.

**Table 16.** Some examples of most applied topographic correction methods and coefficients. The table shows the name, the type of correction, and a brief description.

Methods	Category	Notes
Cosine Correction	Physical correction	Takes into account the solar zenith angle but not the diffuse solar irradiance
Minnaert Correction	Physical correction	It considers the type of reflection of surfaces. the Minnaert constant will range from 0 (specular reflector) to 1 (Lambertian surface).
Sun-Canopy-Sensor-correction (SCS)	Physical correction	The SCS correction improves on the cosine correction by normalizing the illuminated canopy area. It overcorrects the image
C-Correction	Semi-empirical correction	Addition of a semi-empirical moderator (C) to the cosine correction. A linear relationship exists between the reflectance and the incidence angle based on an examination of image data.
Sun-Canopy-Sensor-correction + C	Semi-empirical correction	Combination of the SCS physical correction with the C semi-empirical moderator

As the angle of incidence approaches 90°, the correction factor becomes excessively large. In the C-correction, parameter C has a moderating influence on the cosine correction by emulating the effect of diffuse sky illumination, and it is derived from the Minnaert and C-correction by (Teillet et al., 1982). The SCS+C correction is calculated as follow (equation 10):

$$L_N = \frac{\cos\alpha \cdot \cos\theta + C}{\cos i + C} \quad [10]$$

Where  $L_N$  is the normalized radiance,  $\alpha$  is the terrain slope derived from the DEM,  $\theta$  is the solar Zenit angle,  $i$  is the incidence angle (defined as the angle



between the normal to the pixel surface and the solar zenith direction).  $C$  is the semi-empirical correction factor, from Teillier theory (Teillet et al., 1982), which is based on the assumption that a linear relationship between the radiance and the cosine of the incidence angle exist (equation 11):

$$L = a + b \cos i \quad [11]$$

Thus he calculated  $C$  as the ration between  $a$  and  $b$ , (equation 12):

$$C = \frac{a}{b} \quad [12]$$

This correction approach has been proven to outperform SCS topographic methods, providing good results, especially in sloped forested areas (Soenen et al., 2005).

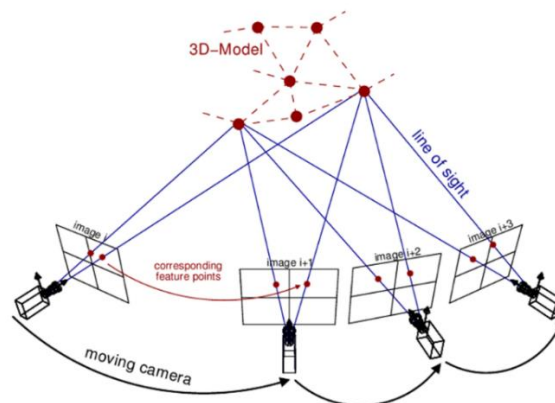
Usually, corrections for atmospheric and topographic effects are applied sequentially and independently. In addition to error propagation issues, sequential processing does not reflect the physical interactions between these effects, because all these effects are inter-related, it is not possible to correct for each effect without making simplifying assumptions about the others or using an explicit physically-based approach (Laurent et al., 2011).

Satellite imagery is often interested by cloud cover on the scene. Two solutions are commonly used for cloud removal in multi-temporal images. One method is to replace the cloudy temporal data with data from images without clouds or snow taken in the same season but in different years. As a result, most land cover products are mapped at intervals of 5 or 10 years, which significantly reduces “currency”. The other method entails filling cloudy locations using per-pixel temporal compositing procedures via adjacent temporal interpolation, a time-series curve filter, or inversion of  $n$ -day observations to estimate reflectance based on the bidirectional reflectance distribution function. These methods do not increase information content but may introduce gross errors, mainly when continuous temporal data are unavailable. It is worth noting that, because of the low temporal frequency of the Landsat satellite, the data obtained are rarely completely cloudless, and most images contain cloud cover. When cloud coverage reaches a threshold such as 30%, the temporal image is deemed unusable, and the remaining 70% of the image will also be discarded. In other words, for a given satellite time series,

the temporal dimension of each pixel might not be the same, despite using the same period. Therefore, only methods that work with unequal time series will fully exploit the available data (Zhai et al., 2018).

## 5.2. UAV-derived imagery: SfM for orthophoto generation

UAV-derived images are elaborated to generate a 3D model of the object of the study. This elaboration is realized through the application of photogrammetric techniques. In recent years, the Structure from Motion (SfM) technique has become very popular within photogrammetric techniques and has quickly reached the consolidated traditional digital photogrammetric techniques. SfM is a computer vision technique that allows users to transform 2D data into 3D data. Mainly, SfM aims to recover the structure of the scene (i.e., 3D coordinates of object points, and the camera motion, i.e., the exterior orientation (position and attitude) of the images) starting from multiple images of a stationary scene (Figure 39). Similar to classic stereo-photogrammetry, SfM uses images acquired from multiple points of view to return the three-dimensional geometry of an object (Fonstad et al., 2013; Iglhaut et al., 2019). Traditional photogrammetry methods are based on the similarity to the human binocular vision. Indeed, as human eyes can perceive the depth, traditional photogrammetry methods perceive it by knowing the relative position of two points of view. The depth, or 3D features, can be perceived from a single observing point, too, if the observer, or the object, is moving (Iglhaut et al., 2019).



**Figure 39.** Structure from Motion technique. The acquisition of moving (black cameras) to get data from a static object (red dots) creates a 3D model (Iglhaut et al., 2019).

SfM relies on these two pillars: i) depth can be perceived from binocular vision and, ii) depth can be perceived by changing the vision of an object moving or observed from a moving point. The main differences between SfM and traditional photogrammetry are three:

**i) Approach of the image matching algorithms.**

Traditional photogrammetric methods typically rely on strips of overlapping images acquired in parallel flight lines. SfM algorithms automatically identify and match the conjugate features (physical features present in many images) of the images regardless of the changes in the scale (i.e., resolution), the point of view, and orientation. Clearly, in SfM, each physical point on the resulting object must be present in multiple images as per traditional photogrammetry. This is a significant advancement compared to traditional photogrammetry techniques because it allows the 3D reconstruction and unorderedly positioned acquisitions.

**ii) In SfM, camera positions or ground control points are not compulsory for 3D reconstruction, although they can be calculated.**

Another difference between SfM and traditional photogrammetry is the point in the workflow at which the results are georeferenced. In traditional digital photogrammetry, the collinearity equations, which identify the relationship between three-dimensional features and their projections into two-dimensional images (Iglhaut et al., 2019; Snavely, 2008), are solved *after* the user identifies and inputs Ground Control Points (GCPs) and/or the positions and orientations of the camera. While in SfM, the collinearity equations are solved *before* the introduction of GCPs. The Ground Control Points are points of known coordinates and position. Indeed, the SfM technique can solve the collinearity equations in an arbitrarily scaled coordinate system thanks to the large number of conjugate points identified during the automated image matching phase (Iglhaut et al., 2019; Snavely, 2008). In SfM, a massive number of conjugate points are automatically generated. A disadvantage of this procedure is the potential introduction of errors that became systematic and underestimated the deformations.

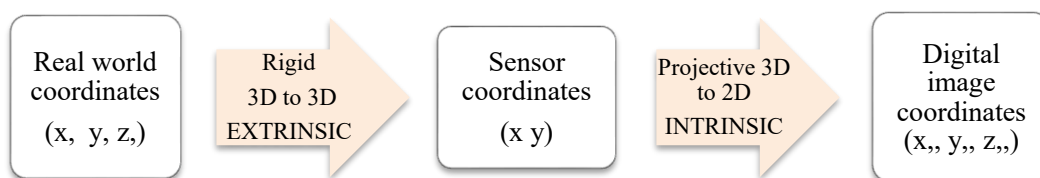
**iii) Camera calibration can be refined during the process.**

The large number of conjugate points identified during the automated image matching phase allows a full camera calibration. This SfM phase results in a relative point cloud of X, Y, and Z positions, which is not registered in a local reference system (nor in any real-world coordinate system). At this point, the analyst can introduce GCPs and the camera positions to register the point cloud to a specific

coordinate system. This transformation is linear and rigid and results in a point-cloud suitable for mapping applications.

Cameras' geometric calibration is a fundamental step for the 3D reconstruction of a real-world scene since it allows the identification of the camera's location within the scene. Moreover, the cameras' geometric calibration allows for the correction of lens distortion and the measure of the size of an object in real-world units. These applications are used not only for 3D reconstruction but also in machine vision, robotics, and navigation systems. The geometric calibration identifies the correction parameters of a camera's lens by applying specific equations that relate the coordinate systems of the camera's picture, the real world, and the camera's sensor, Figure 40 and Figure 41 (Forsyth and Ponce, 2012).

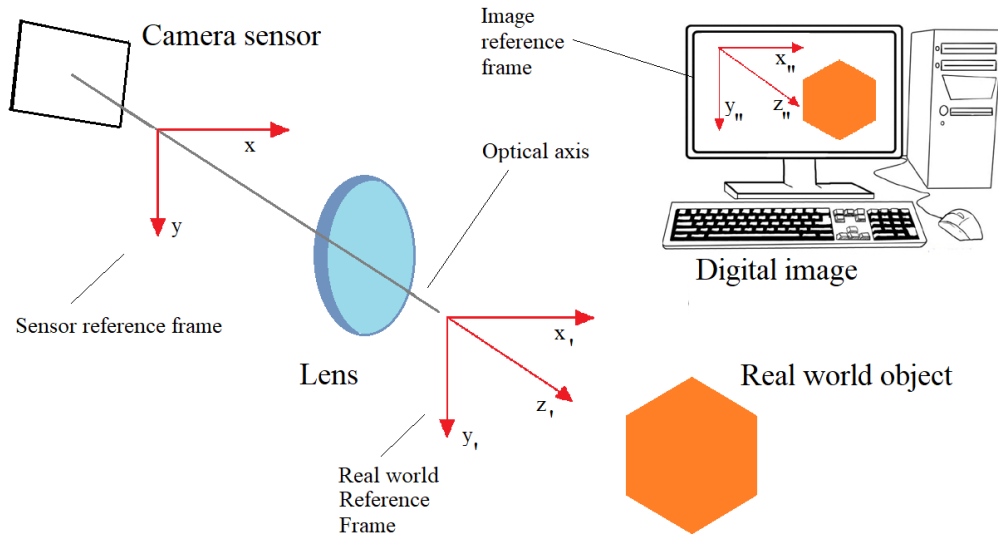
A known-measure object in the real-world is needed to estimate the geometric correction parameters. Several images are needed for such an object, and using the correspondence between the measured object and the digital image, it is possible to estimate the camera parameters. Camera parameters include the intrinsics, extrinsic, and distortion coefficients. The intrinsic parameters refer to the camera coordinates' projective transformation into sensors coordinates, and it includes the focal length, the skew coefficient, and the optical center. The extrinsic parameters regard the rigid transformation of the real world coordinates into camera coordinates. They are the Rotation (R), the Translation (t), and the optical center of the camera, which is the origin of the camera's coordinate system (Forsyth and Ponce, 2012).



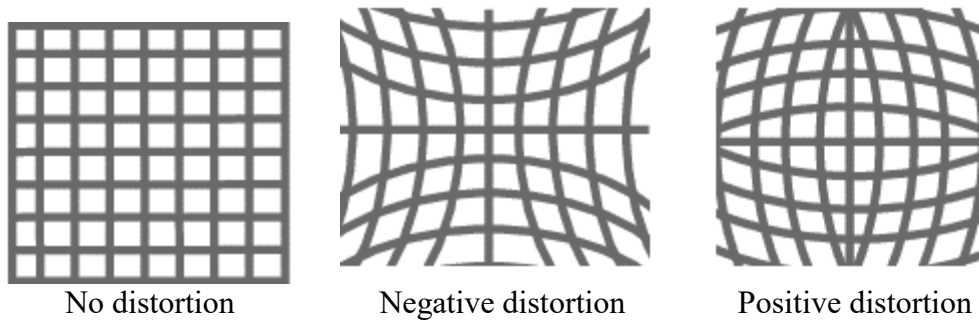
**Figure 40.** Geometric calibration workflow.

To accurately represent a camera, it is also necessary to consider the radial and tangential lens distortions. The radial distortion can be positive or negative and depends on the distribution of light rays on the lens, while when the lens and the image are not parallel, there is a tangential distortion (Figure 42). Radial distortion of the lens is expressed by  $K_1$ ,  $K_2$ , and  $K_3$  coefficients. Tangential distortion of the lens is expressed as  $p_1$  and  $p_2$  coefficients. The estimated focal length is expressed in millimeters. The principal point (i.e., the optical center of the camera) is in pixels. The mean reprojection error is an extrinsic parameter representing the average

Euclidean distance between reprojected and detected points and is expressed in pixel. SfM automatically solves the camera calibration, using the matching points detected in the automated image matching phase.



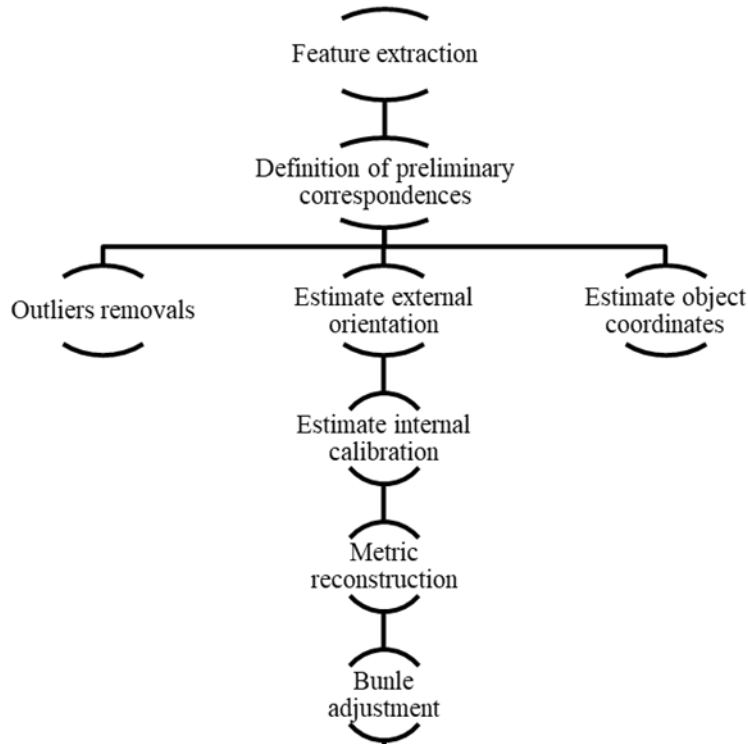
**Figure 41.** Camera calibration defines the relation between the sensor, real-world, and image reference frames and calculates the camera's intrinsic and extrinsic parameters.



**Figure 42.** Example of the effects of positive and negative radial distortions on an image. Adapted from <https://it.mathworks.com>.

These three main differences between SfM and traditional photogrammetry are some of the reasons behind the quick-increasing popularity of SfM. Particularly, SfM is appreciated for its ability to extract 3D information from unordered and heterogeneous images, such as video sequences, pictures of smartphones, and standard cameras. Usually, the SfM term indicates the entire workflow of transition

from 2D images to 3D models. Although precise, SfM refers exclusively to the bundle adjustment, which is only a specific step in the workflow (Figure 43).



**Figure 43.** Structure from Motion processing steps, (Wu et al., 2012).

Incremental steps carry out the 3D model generation. First, the key-points are extracted from the images based on contrast and texture-related rules. The process is initialized by computing the epipolar geometry between two images and calculating the projection matrices and the fundamental matrix (Hartley and Zisserman, 2003). The key-points were identified in all input images and then matched across different images. Before the final match, eventual outliers are eliminated to improve the coherence and the stability of the future matching to this purpose, robust estimation algorithms, such as the RANdom SAmple Consensus (RANSAC) paradigm (Fischler and Bolles, 1981; Raguram et al., 2008) are used.

If there is a sufficient number of matched key-points, SfM performs the bundle adjustment (Agarwal et al., 2010; Snavely, 2008; Triggs et al., 2000; Wu et al., 2012, 2011). It is a non-linear least-square optimization algorithm that minimizes the re-projection error caused by measurement noise. Specifically, it is solved using sequences of randomly selected matched key-points and parameters from the cameras along with a non-linear refinement. Besides containing the error accumulation, the bundle adjustment computes the camera parameters and

generates the sparse point cloud. Usually, after the bundle adjustment, the sparse point cloud is scaled and georeferenced based on GCPs and/or the data from navigation devices mounted on the camera or its platform, unless the initial extrinsic parameters were not provided (e.g., the coordinates of the acquisition center).

The georeferenced sparse point cloud is then densified. Specific algorithms, such as Multi-View Stereo MVS, are used in a subsequent step to densify the point cloud. Contrary to SfM, MVS aims to extract as much information from all the pixels of the input images and not only from a subset of the images. Several MVS algorithms exist, although they are not fundamental for the understanding of this work. For additional information, (Seitz et al., 2006)'s work is suggested. The whole process of 3D model generation is also called SfM-MVS. A dense point cloud characterized by spectral information extracted from the input images is the SfM-MVS workflow's output (Figure 44).

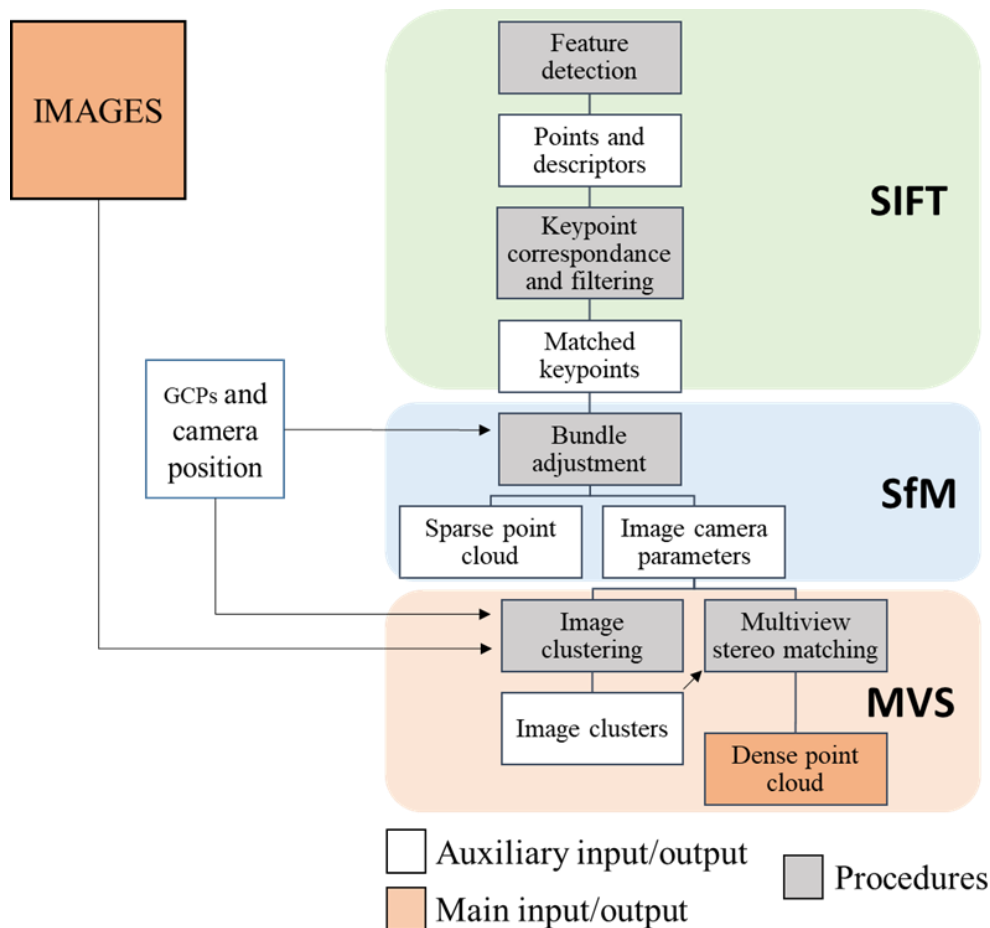


Figure 44. SfM-MVS workflow for the generation of the Dense Point Cloud, (Seitz et al., 2006)

In aerial surveys, the following step involves the 2D information extraction from the 3D model. Particularly, it is derived from the Digital Surface Model (DSM) due to the mesh-grid generator, namely the 2D grid containing the elevation information of the dense cloud's points. Eventual outliers points need to be filtered by some appropriate algorithms interpolated to substitute the outliers' values. Most commercial SfM-MVS software provides the users with classification tools to classify ground points and extrapolate DTM.

Similarly, through the rasterization of the model, it is possible to extract the orthomosaic. Technically, the orthomosaic is a series of individual photos that are programmatically matched up to form a new composite image, consisting of all the smaller ones. In the final mosaic image, each source image contributes data to a small region (Mills and McLeod, 2013). Additionally, image metrics like radiance/reflectance values and texture may be extracted.

SfM photogrammetry is firmly dependant on the quality of the input images. To obtain a reliable input dataset, some basic rules and expedient should be followed (paragraph 3.1.3, page 29). Today, many software for the SfM-MVS workflow exist. Table 17 sums up the most frequent and their main characteristics.

**Table 17.** Most popular software for SfM-MVS workflow. The type (meant as aerial or terrestrial), the file output format, the operating system, and the price are analyzed. The pricing should be interpreted carefully. It refers to single-user license in April 2020. Source: <https://all3dp.com/>

Name	Type	Output File Formats	Operating System	Price
COLMAP	Aerial, Terrestrial	ply, vrml	Windows, macOS, Linux	Free
Meshroom	Aerial, Terrestrial	abc, obj	Windows, Linux	Free
MicMac	Aerial, Terrestrial	geotiff, ply, xml	Windows, macOS, Linux	Free
Multi-View Environment	Aerial, Terrestrial	MVE	Windows, macOS	Free
OpenMVG	Aerial, Terrestrial	Ply	Linux, Windows, MacOS	Free
Regard3D	Aerial, Terrestrial	obj, ply	Windows, macOS, Linux	Free
Continue in the following page (1)				



VisualSFM	Aerial, Terrestrial	Ply	Windows, macOS, Linux	Free
3DF Zephyr	Aerial, Terrestrial	ply, obj, fbx, pdf 3D, u3d, dae, pts, ptx, xyz, txt, las, e57	Windows	Limited free version and paid version from €149+tax
Autodesk ReCap	Aerial, Terrestrial	asc, cl3, clr, e57, fls, fws, isproj, las, pcg, ptg, pts, ptx, rds, txt, xyb, xyz, zfs, zfprj	Windows	€40/month
Agisoft Metashape	Aerial, Terrestrial	Fbx	Windows, macOS, Linux	From €179
Bentley ContextCapture	Aerial, Terrestrial	3ms, 3sm, kml, dae, fbx, obj, dae, stl	Windows	On request
Correlator3D	Aerial	.asc, geotiff, .las	Windows	€250/month
DatuSurvey	Aerial, Terrestrial	ENH, NEH, DXF, PLY, PDF, LAS, PNG, GTIFF	Windows	€350/month
DroneDeploy	Aerial	dxs, GeoTIFF, las, obj, xyz	Windows, macOS, Android, iOS	€149/month or €99/month when billed annually
Elcovision 10	Aerial, Terrestrial	All currently known image formats	Windows	On request
iWitnessPRO	Aerial, Terrestrial	TXT, CSV, PTS, LAS, PLY, DXF, KML	Windows	€2,495
IMAGINE Photogrammetry	Aerial	img, igg, ovr, l, noaa, rpf, ddf, dem, til, dt2, ecrg, hdr, xml, ecw, url, ant, dig, alg, ers, gis, ...	Windows	On request
LiMapper	Aerial, Terrestrial	PLY, OBJ, LAS		On request
Photomodeler	Aerial, Terrestrial	3ds, 3dm, dxf, igs, kml, kmz, las, ma, ms, obj, pts, byu, facet, iv, ply, stl, txt, wrl	Windows	One time fee of €995 €49/month
Pix4D	Aerial	obj, fix, dxf, las, las, kml, tif, osgb, slpk, shp	Windows, macOS, Android, iOS	€260/month or €217/year
Continue in the following page (2)				

RealityCapture	Aerial, Terrestrial	jpg, png, XYZ, XYZRGB, tiff, bmp, dib, rle, jpeg, jpe, jfif, exif, exr, tif, wdp, jxr, dds, KML, KMZ, obj, ply, partlist, fbx, dxf, dae, bvh, htr, trc, asf, amc, c3d, aoa, mcd, wmv, mp4	Windows	From €33/ months
SOCET GXP	Aerial		Windows	On request
Trimble Inpho	Aerial, Terrestrial		Windows	On request
WebODM	Aerial	GeoTIFF, png, las, obj	Windows, macOS	From €57

# Chapter 6

## Study areas and materials

The present work considers two cases study: the villages along the Sirba River in Sub-Saharan areas and the protection forests of Alpine Arch. Both cases are the object of study of specific projects on natural hazard risk prevention, the areas along the Sirba River for the prevention against flood hazard, and the Alpine forest as a mitigation entity of rock falls. Besides having the susceptibility to natural hazards in common, both areas can be considered complex landscapes and difficult-to-map areas. The choice of these two case study is ascribable to these three common aspects:

- I. Critical areas to classify for their landscape complexity, remoteness, and difficult gathering of *in situ* data;
- II. Natural hazards-prone zones;
- III. Significant differences in the case studies to test the applicability of the proposed methodology for the LC atlas generation.

Paragraphs 6.1 and 6.2 of this chapter describes the main aspects of the case study.

### **6.1. Study area A, protection forests of Alpine arch: ROCKTHEALPS project**

Forests provide us with many services, so-called ecosystemic services, and the regulation of hydrogeology cycle and slope stability. This service is vital in mountainous areas where forest stands have a mitigation effect on slope-related

phenomena (i.e., rockfall avalanches, landslides). In this context, the stands' structure is a crucial parameter in defining forests' protection function against natural hazards (Maier et al., 2008). Forest protection and management benefit from a complete knowledge of trees' shape and distribution in forest stands. In this scenario, the EU Gothenburg priorities (Priority 2 2015) focus on the effective management of forest ecosystems and risk prevention, as well as the protection and preservation of forest ecosystems. Many national and European projects aim to contribute to the future sustainable development of the environment and land use. One of these is ROCKTHEALPS project, which studies the protection forest of the Alpine Arch in the function of rockfall hazard. Even if the international scientific community broadly recognizes the role of forest stands in rockfall-related risk mitigation, the information regarding single events is still scarce.

In most cases, historical records do not exist or are approximate. The test area is studied within ROCKTHEALPS (RTA) project. Its goal is to develop an innovative common regional rockfall model considering protection effects of forests and derived information for producing the first Alpine Space wide harmonized map of rockfall risk and protection forests. The areas showing high vulnerability to rockfalls are the object of the study. The methodology proposed in this work easily fits the needs of ROCKTHEALPS. A forest in Northern Italy was monitored and classified to provide data (i. High-resolution, ii. Multi-layered, iii. Multi-temporal) to evaluate the barrier effect of woods in rockfall processes using UAV. ROCKTHEALPS project is interested in different sites places all over the Alps. In this work, only the site of Cesana Torinese (Italy) was considered for the analysis (44°56'46.1"N 6°46'29.5"E). The test study is a coniferous forest (Figure 45). It is dominated by Silver fir (*Abies alba* Mill.), Norway spruce (*Picea abies* (L.) H. Karsten), and European larch (*Larix decidua* Mill.). Scots pines (*Pinus sylvestris* L.), and Swiss pines (*Pinus cembra* L.) are sporadically present. The study area extends approximately 38 hectares over a high-sloped mountainous area with North exposure. The steep mountainsides make the area particularly prone to rockfall and avalanches.

Despite the extreme condition of the study phenomena, comprehensive knowledge of the territory is required, for example, by adopting geomatics techniques and innovative cartographic products. To this purpose, aerial surveys using UAVs have increased for monitoring applications (Banu et al., 2016; Berie and Burud, 2018; Paneque-Gálvez et al., 2014; Tang and Shao, 2015; Torresan et al., 2017; Vepakomma et al., 2015). Successful implementation of drones in forestry depends on UAV's following features: flexibility of use in flight planning, low cost, reliability and autonomy, and capacity to produce high-resolution data (Torresan et

al., 2017). UAV can have many benefits in surveying and monitoring the protection forest to maintain and regenerate the barrier effect of forests.

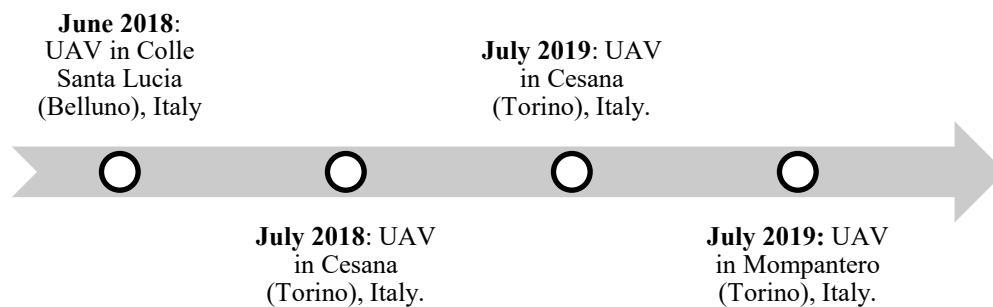


**Figure 45.** The study area in Cesana Torinese

The remote sensing techniques UAV offers a versatile opportunity to improve forest mapping and monitoring regarding natural hazards (Giordan et al., 2017). Remote sensing techniques face various challenges in mountainous regions. The complex terrain limits the availability of observations. In narrow elevation zones of mountainous areas, mountainside can be permanently shadowed (Dietz et al., 2018). Moreover, the snow cover prevents the classification in the winter months. High-peaked areas are prone to frequent orographic rains and clouds, which mechanisms are influenced by the terrain (Houze, 2012). These conditions lower the possibility of accurate classifications. Mountainous forests are particularly susceptible to the shadows' effect within the crowns. In fact, it has been proven that forest stand maps of less-rugged or flat terrain are generally more accurate (Dorren et al., 2003). One of the reasons for this is that both land cover and topography determine the spectral values in remote sensing imagery, especially in steep or high relief energy areas. Substantial variability in the reflectance from canopies of similar forests and direct shadows as well as cast shadows are indissoluble results of the topography in such areas, which complicate the classification. Data gathering in the field is time consuming due to the difficulty of the terrain morphology (i.e., steep slopes) and road access. Operators can be exposed to several risks during the field survey; Personal protective equipment (PPE) is always required during the surveys. A substantial limitation is presented by the tree canopy, which excludes

GPS signals and impedes the use of aerial imagery to study the undergrowth. Combining these factors makes the generation of the land cover maps of mountainous areas particularly challenging and generally recognized as fairly-low accurate (Dorren et al., 2003; Itten and Meyer, 1993).

A land cover high thematic resolution analysis of the land cover was performed starting from aerial images. Specifically, the single tree crowns were segmented to measure the main parameters needed to define the forest's protective effect from rockfall risk. Since June 218 four land surveys have been carried out.

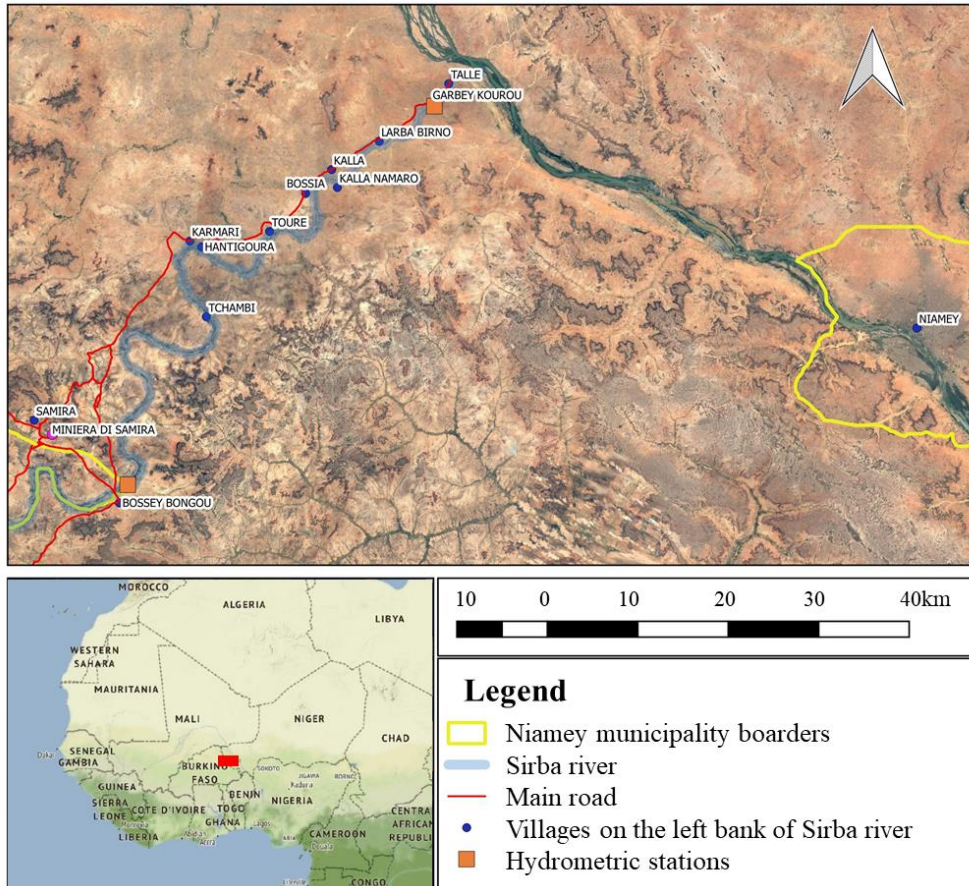


**Figure 46.** Timeline of land surveys in the Alps region.

## **6.2. Study area B, Sub-Saharan areas along Sirba River: ANADIA 2.0 project**

Over three-fourths of the Sahara has an annual average rainfall of less than 100 mm, and one-fourth has less than 20 mm. In these areas, local enhancements of temperature and heavy rains occasionally occur (Warner, 2004) owing to the sudden change of weather patterns that brings more extreme weather events, of which, flash floods of the dry valleys are the most devastating (Moawad et al., 2016). Floods in the Sahara are often characterized by deep, fast-flowing water, which, combined with the short time available to respond, increases the risk to people and property (Sene, 2013). In the last decades, it has been recorded evidence of an increasing number of massive rainfall events over the West Sahel (Bigi et al., 2018; Oguntunde et al., 2018). The climatic conditions of the Sahelian zone of the Niger basin is not an exception. It fits the changing climate pattern of Sahel. Catastrophic flooding has become an increasing threat during the last decades, leading to more than ten million people affected since 2000 (Aich et al., 2016). Sirba River, a tributary of Niger River, crosses Burkina Faso and Niger (Figure 47).

Its basin is prone to floods, and villages along the river are vulnerable to life and economic losses (Massazza et al., 2019, 2018; Tamagnone et al., 2019).



**Figure 47.** Sirba River in Niger country

Along the Nigerienne branch of Sirba (about 100 km length), the only existing route connecting the upstream villages to the capital (Niamey) is often flooded and getting complicated by the people during the rainy season’s movement. The Sirba basin is 39138 km<sup>2</sup>, and direct monitoring is almost impossible due to the vastness of the area, the difficult climatic conditions, and the lack of a developed road network. In this area, the need for climatic planning and the development of adaptation strategies to climate change at the local level is not negligible (Tiepolo et al., 2018). Despite this undeniable need, there is no appropriate risk mapping of the area; indeed, subnational risk mapping lacks detail (Tiepolo et al., 2018). The Sirba basin in Niger territory is the study area of the ANADIA 2 project. The Italian Agency for Development and Cooperation (AICS) funds it (Massazza et al., 2019).

It aims to create an Early Warning System to face climate change effects in Sirba River Basin<sup>2</sup>, enhance local technicians' knowledge regarding floods forecasting, and create an adaptation strategy planform two villages along the Sirba River. The data gathered and the information provided by this research will be directly involved in ANADIA 2.0, by feeding the adaptation strategy plan and investigating the cause-effect relation of floods. The villages of Larba Birno and Touré are interested in adaptation planning strategy, and they will be the object of Very High-Resolution Unmanned Aerial Vehicles (VHR-UAV) analysis. The difficulty of land cover mapping of this area is due to the high spectral homogeneity of cover types. One of the most significant problems in the remote sensing of Sub-Saharan regions is that reflectance from soil and rock during the dry season is often much greater than that of the sparse vegetation making it difficult to separate the vegetation. Some of the specific problems involved with remote sensing of arid vegetation include multiple scattering of light (nonlinear mixing) between vegetation and soil (Huete, 1988). Moreover, it is hard to separate built-up areas from the soil even from VHR imagery. Most of the buildings along the Sirba River are made of locally produced brick. This production is realized using clays from the Sirba riverbed and the buildings are not plastered (Figure 48).



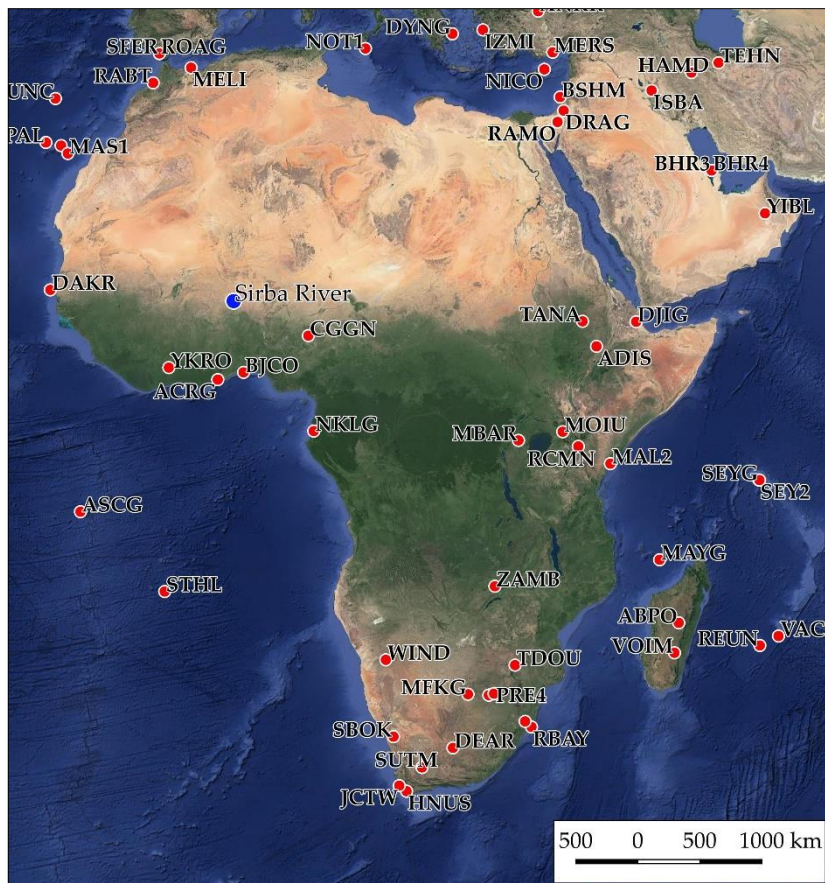
**Figure 48.** Example of local architecture. Aerial view.

---

<sup>2</sup> The transboundary basin of Sirba river lies between the countries of Burkina Faso and Niger in the centre of the Sahel strip. It is a sparsely populated area whose inhabitants are dedicated to food and farming activities.



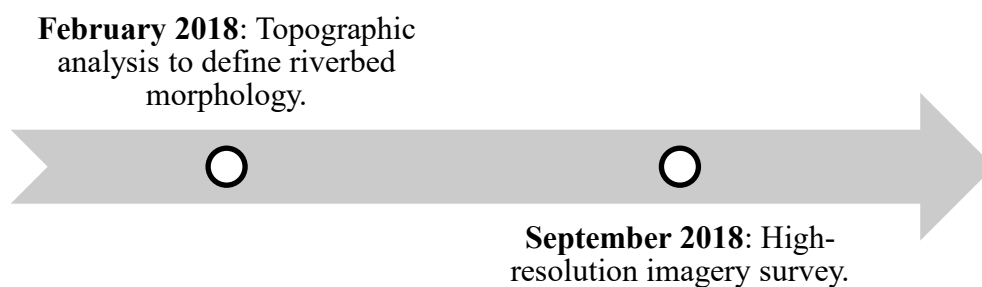
The main road and the streets of the villages are unpaved. As a consequence, the spectral response of buildings is the same as roads and bare soil. The strong seasonality adds further complexity to the classification as the frequent cloud cover during the rainy season and sand presence in the air may alter the sensed data's spectral value. From the geodetic point of view, the Sirba River area is disadvantaged. A dense network of permanent stations is not available to process GNSS data (Kim et al., 2014). Despite today CORSs covering most of the world's countries, some areas are still not included in the network, such as some sub-Saharan countries and the Sirba basin (Figure 49). Indeed, the lack of CORS and known coordinates points is quite a frequent condition in sub-Saharan rural areas, strongly affecting topographic surveys. Indeed, there is poor access to general services (e.g., electricity, computers) and few people with enough expertise to use



**Figure 49.** CORS in Africa continent. The dots indicate the stations that provided raw observations to the International GNSS Service (IGS) in the last ten days. The map is daily updated. This image is referred to the 17 January 2020. Source: International GNSS Service (IGS).

GNSS software. These unfavorable conditions can be exacerbated by emergencies, like during (or immediately after) natural hazards.

This research tries to overcome the criticalities of LC mapping in the Sirba basin by using low-cost geomatics. Specifically, a Digital Terrain Model and a Digital Surface Model were created. Potentially flooded areas were mapped using images collected via UAVs using low-cost optical sensors and via VHR satellite. On the same data, LC classification was performed. The case study required two land surveys in 2018, Figure 50.



**Figure 50.** Land surveys in the Tillaberi region.

Multiband imagery was collected by RGN (Red-Green-NIR), and RGB (Red-Green-Blue) sensors mounted on UAV systems. The imagery was used for the creation of multiband orthophotos for the detection of waterlogging.

### **6.3. Tools and Hardware**

The tools are intended as the optical sensors used for the data collection. They are presented in the next sections grouped according to the platform they are integrated into: Unmanned Aerial Vehicles and Satellites. As previously mentioned, both commercial and non-commercial solutions were used for the collection of UAV datasets. The performances and the functioning of non-commercial sensors were tested in the laboratory before the field application.

#### **6.3.1. Hardware: UAV-mounted optical sensors**

The optical sensors employed in this thesis are RGB and NIR sensors embedded in fixed-wing UAVs. Optical sensors mounted on UAVs can have two types of relationships with the drone. It can be direct, in which the sensor communicates directly with the drone. In this case, the photo shooting is optimized, and the

pictures are taken according to the flight speed and the UAV position using a trigger concerning the mission plan. In this type of relation, usually, the power is provided to the sensor by the drone. Although the optical sensor on-board can be independent of the UAV: the power supply can be an extra battery independent from the UAV system and the frequency of shooting set by the pilot before the flight. In this case, the planning phase needs further caution to find the perfect shooting parameters for the selected flight.

For this thesis, both types of relations were used for different sensors. Two RGB mass-market sensors were employed (S.O.D.A. and Sony ILCE-5100), one mass-market NIR sensor (Canon S110) and a low-cost *ad hoc* created NIR sensor (Raspberry Pi camera). The next paragraphs will briefly describe the characteristics of the mass-market sensors and the functioning and calibrations realized of the Raspberry Pi camera.

### *Mass-market cameras*

#### *S.O.D.A.*

The Sensor Optimized for Drone Applications (S.O.D.A.) is a camera commercialized by Sensefly<sup>3</sup>, which is embeddable on eBee and eBee Plus drones. It has a global shutter, and it collects 3-band (Red, Green, Blue) imagery simultaneously on a single CMOS sensor. The S.O.D.A. has a lens with focal length of 10.6 mm and a 20 MP (5472 x 3648) RGB sensor (13.2×8.8 mm).

#### *Sony ILCE-5100*

The Sony ILCE-5100 is a mass-market mirrorless RGB digital camera. It is also broadly used for non-photogrammetric purposes. It has an APS-C type Exmor CMOS sensor to collect three-band imagery. It has a 24 MP resolution and 1.5x multifocal length.

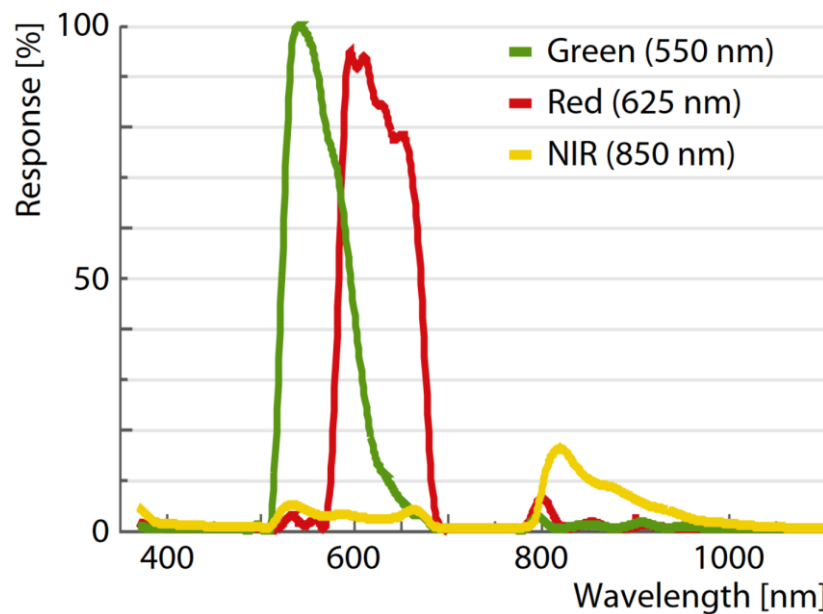
#### *Canon S110*

The Canon Powershot S110 NIR is an RGN (Red Green NIR) camera sensor created to be mounted on eBee drones. It can directly communicate with the drone. The Canon S110 has a resolution of 12.1MP (4000x3000) and a focal length of 5.2 mm. It has a modified filter that acquires the NIR in place of the blue band. The central wavelengths of the bands are 500 nm (Green), 625 nm (Red), and 850 nm

---

<sup>3</sup> <https://www.sensefly.com/>

(NIR), but all bands partially overlap across the range 350 and 1150 nm (Figure 51).



**Figure 51.** Spectral response of Canon Powershot S110 NIR. Since the NIR filter was removed, the NIR channel is broad and encompasses the visible electromagnetic spectrum. Source: Sensefly

### *Raspberry Pi camera*

To pursue the principle of low-cost sensors, it was developed a multispectral, UAV-mountable sensor using a Raspberry System (Raspberry Pi 3) and two Raspberry cameras. The sensor collects information from the visible and infra-red range of the electromagnetic spectrum (Belcore et al., 2019b; Piras et al., 2019).

The Raspberry Pi 3 is a personal computer board with a Linux-based operating system installed. Users can integrate any hardware. It is cheap, and its commercialization aims to encourage young people to learn to program (Agrawal and Singhal, 2015). Although initially developed to increase interest in software engineering, it has soon become accepted as a programmable control unit in many different applications (Sobota et al., 2013). Indeed, it can connect to numerous external accessories (Foundation Raspberry, 2019), including optical cameras. Many camera modules for Raspberry are available. Among others, some sensors can collect InfraRed light. The Raspberry device developed for photogrammetric purposes (Figure 52) is composed of i) a central Raspberry Pi 3 board; ii) a 3.5 inches touch screen; iii) a multiplexer chip; iv) a Raspberry Pi 3 V.2 camera; v) a Raspberry Pi 3 V.2 NoIR camera; vi) a 5v power bank (Table 18).



**Figure 52.** Raspberry-based device used in this study

The device's size was 85mmx56mmx32mm, the final weight (battery included) was 300 g, and it cost around 100€. The Raspberry Pi was coded to shoot and save pictures automatically from both cameras at a given frequency.

**Table 18.** Components of the Raspberry-based device

<b>Component</b>	<b>Description</b>
Central Raspberry Pi board	Raspberry PI 3 Model B+
3.5 inches touch-screen	Standard touchscreen connected (and powered) to the Central board
Multiplexer chip	Component that allows the use of two cameras on the same Raspberry board
Raspberry Pi 3 V2	8MPx camera, RGB, 3g, Sony IMX219
Raspberry Pi 3 V2 NoIR	8MPx camera, NoIR-GB, 3g, Sony IMX219

The Raspberry Pi 3 cameras v2 employed were a regular RGB Pi 3 camera v2 (Red, Green, Blue) and a NoIR Pi 3 camera v2 (NoIR-RGB). The RGB and NIR cameras did not work simultaneously, but with a 0,1-second delay between them, which was considered negligible for UAV's flights' speed. Additionally, the data's resolution was reduced to 5 MP to allow the device to store the pictures at 1Hz frequency correctly.

Since camera calibration is fundamental for any metric reconstruction from images (Nex and Remondino, 2014), the NoIR camera module was tested in the laboratory. (Pagnutti et al., 2017) realized an in-depth study on the Raspberry Pi 3 v2 RGB camera. Considering the already existing study regarding the RGB Raspberry sensor, the calibrations were realized only on the NoIR Camera Module.

Specifically, the geometric calibration, the dark frame assessment, and the radiometric tests were performed.

### *Geometric Calibration*

The geometric calibration allows identifying the coefficient of geometrical image distortion. The lens' flaw usually causes distortion, and it is around some millimeters (see paragraph 5.1.1, page 95). it is necessary to take pictures of several known-size objects and check the ratio between them in the pictures to perform such analysis. Using specific algorithms is then possible to extract the distortion coefficient based on the difference between real world measures and picture measures.

The Raspberry Pi NoIR camera was geometrically calibrated using a known size chessboard (Figure 53). Twenty pictures were taken from different angulations. The camera's distortion was then estimated using MATLAB camera calibration tool (MATLAB, Computer Vision Toolbox™). Table 19 shows the results and, for each parameter, shows the  $\sigma$  (standard error) value on x and y components that represents the uncertainty of the estimated parameters.

**Table 19.** Geometric calibration results

	x	y	x-error	y-error
Radial distortion	0.1913	-0.3323	0.0093	0.0363
Tangential distortion	-0.0026	-0.0113	0.0013	0.0015
Estimated focal length [mm]	2.28	2.29	0.0033	0.0039
Principal point [pixel]	1233	969	6.301	5.991
Mean reprojection error [pixel]	0.663			



**Figure 53.** Known-size chessboard used for the geometric calibration

The errors have the same unit of measure on the corresponding parameter and are expressed for both x and y components.  $\sigma$  can be used to calculate confidence intervals.

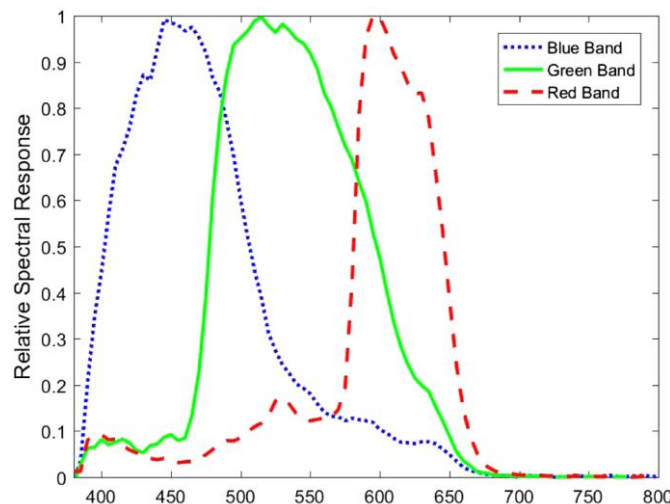
#### *Dark frame knowledge*

The dark frame assessment identifies the background noise of the sensors. It is based on the assumption that in total-dark conditions, the DN values should be zero. A picture in the dark condition and the DN values registered are considered correction values for the acquisition in normal-light conditions. Since the dark noise is ISO- and temperature-dependent, this passage must be done for each ISO setting and constant temperature.

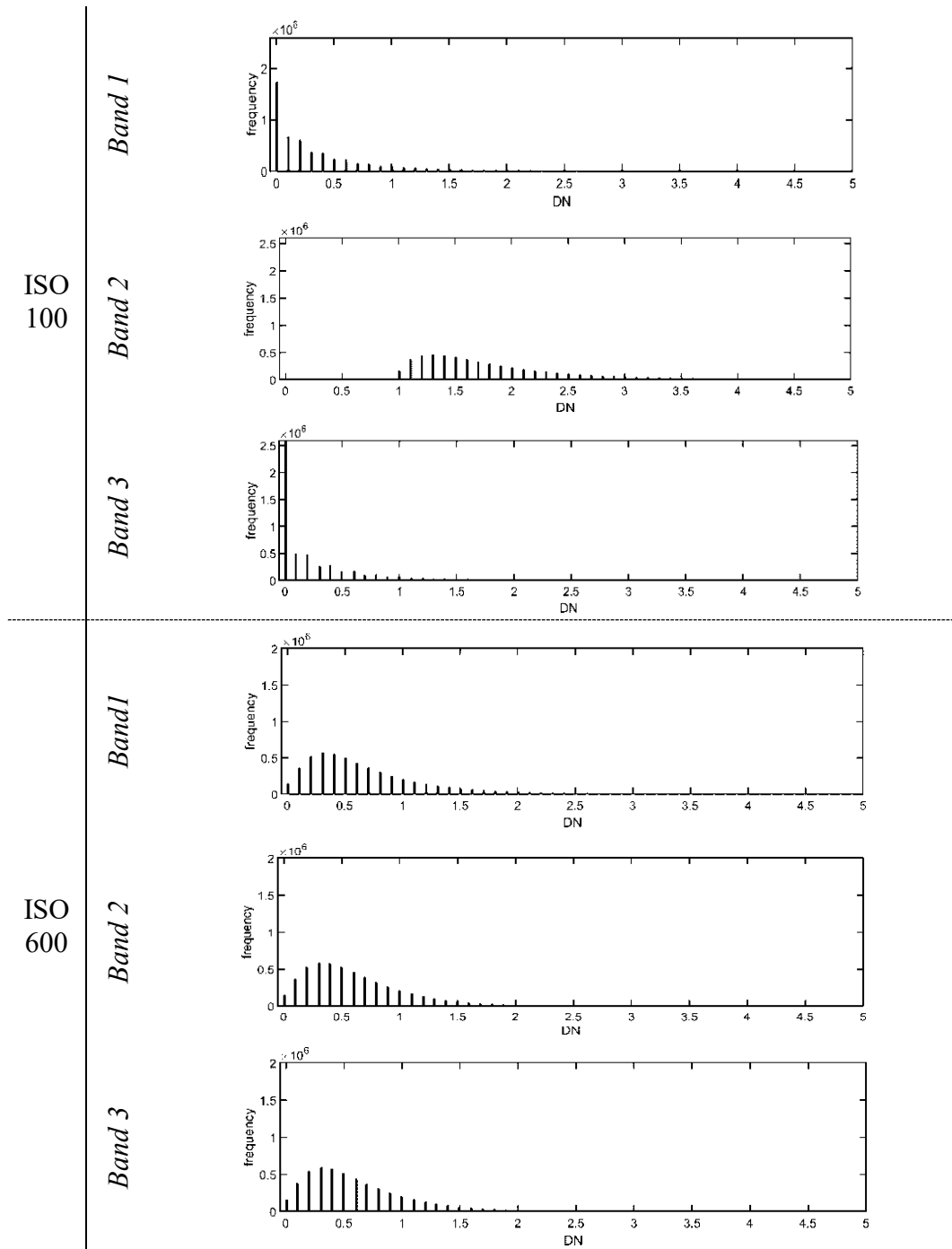
The test was performed in stable conditions of temperature (indoor, 21°C). The sensor was covered with a black stopper, and 50 pictures were captured at different ISO (100, 200, 300, 300, 500, and 600) and constant exposure of 5ms. It was noticed that the first three pictures acquired were overexposed, thus discarded. The DNs of each band were spatially averaged. The results are three matrices (NoIR channel dark frame; green channel dark frame; blue channel dark frame) for each ISO setting. As expected, the dark frame is ISO dependant: its values increase for higher ISO (Figure 55). Table 20 reports DN distributions' histogram for the dark frame assessment for ISO 100 and ISO 600.

#### *Spectral response*

Pagnutti et al. (2017) realize a study on the Raspberry Pi 3 v2 camera identifying its bands' spectral resolution (Figure 54). As far as we know, there are no studies on the spectral response of the Raspberry NoIR.



**Figure 54.** Raspberry Pi camera spectral response. Source: Pagnutti et al.,2017



**Figure 55.** Histograms of frequency for the DN of dark frame assessment at 100 ISO (for Band 1, 2 and 3) and 600 ISO (for Band 1, 2 and 3).

The producer does not reveal information in its regard, but the NoIR camera is a “standard” Raspberry PI camera without the IR filter (RaspberryFoundation, 2019). This means that the camera can detect InfraRed light, but it is unknown



which part of the electromagnetic spectrum. A clue regarding the sensor derives' radiometric resolution derives from the work of (Hobbs et al., 2016). They created a spectrometer using a Raspberry Pi NoIR, and it is sensible between 315 nm and 775 nm. This includes part of the Near-InfraRed spectrum. NoIR data were checked against one of a hyperspectral camera, Sonap Rikola, to define the device's spectral resolution better. Ten pictures of a calibration target and a plant were captured with the Raspberry and the hyperspectral sensor simultaneously. The data were spatially averaged and dark frame subtracted. The hyperspectral camera cannot detect values below 500nm (Blue) of the spectrum. Consequentially the blue band of the Raspberry was not taken into consideration. Thirteen bands between 630 nm and 900 nm were acquired (amplitude of bands of 20 nm). The spectral signatures of sample pixels from the scene were extracted. The reflectance values of the green channel of Raspberry (i.e., 550nm) were subtracted to the one of the hyperspectral, showing a constant difference for the sample pixels (Table 21).

**Table 20.** Dark frame assessment per band for different ISO settings.

<b>ISO</b>	<b>Band</b>	<b>Min DN</b>	<b>Max DN</b>	<b>Mean DN</b>	<b>Median DN</b>	<b>STDev</b>
100	1	0.00	32.60	0.33	0.20	0.13
	2	0.70	35.90	1.81	1.60	0.17
	3	0.00	32.30	0.25	0.00	0.13
200	1	0.00	30.80	0.01	0.00	0.03
	2	0.00	31.00	0.08	0.00	0.05
	3	0.00	30.00	0.01	0.00	0.03
300	1	0.00	19.60	0.03	0.00	0.06
	2	0.00	19.30	0.03	0.00	0.06
	3	0.00	19.90	0.03	0.00	0.05
400	1	0.00	33.60	0.23	0.10	0.09
	2	0.00	25.00	0.23	0.20	0.08
	3	0.00	22.60	0.23	0.15	0.08
500	1	0.00	50.00	0.58	0.30	0.13
	2	0.00	33.30	0.36	0.30	0.10
	3	0.00	35.20	0.33	0.30	0.11
600	1	0.00	35.80	0.66	0.50	0.15
	2	0.00	32.90	0.60	0.50	0.11
	3	0.00	36.80	0.61	0.50	0.12

The values of the NoIR channel of Raspberry were subtracted to the ones of each hyperspectral band between the 630nm and 900nm. Then the differences were compared to evaluate constant distances between the spectral values. Apparently, there are no correlations with any band of the hyperspectral. In both the Green and NoIR band, the reflectance values of the black panel are very close. The remaining panels show small differences for the bands of 680nm and 700nm, although the white panel values are very close. There are no significant results from the comparison.

**Table 21.** Distances between Raspberry reflectance values of the green band and Hyperspectral ones. The data are referred to as sample pixels of the calibration panels.

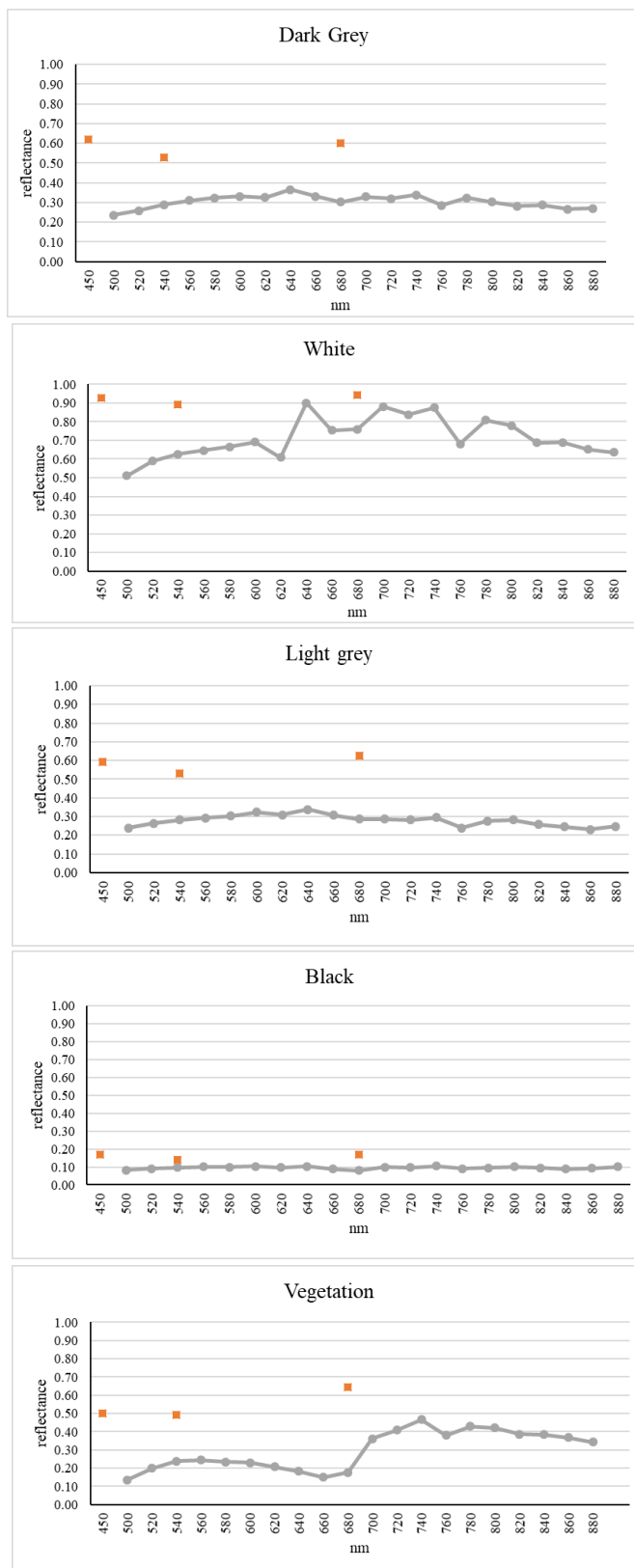
<b>Raspberry NoIR and hyperspectral reflectance difference on Green band (550nm)</b>				
Dark Grey	White	Light Grey	Black	Vegetation
0.23	0.26	0.25	0.03	0.25



**Figure 56.** Picture of the calibration scene taken by the NoIR camera. On the left, the calibration target comprises four panels (white, light grey, dark grey, and black). On the right side of the picture, a plant. At the bottom of the picture is visible, the irradiance sensor of the hyperspectral.

Table 22 shows a comparison between the spectral signatures (Figure 57). The laboratory tests show that Raspberry Pi-based sensors are affordable and trustworthy multiband (NoIR-RGB) alternatives to commercial radiometric sensors. The possibility of coding and personally designing the device adds further potentialities, such as the sensor's connection with the UAV system. The coding broadens the application prospects of this low-cost sensor, making it adaptable to several unmanned vehicles. Nevertheless, the uncertain radiometric resolution is a limit to the employment of the sensor in scientific fields.

**Figure 57.** Plots of spectral signatures on the SONAP (grey dots) and the Raspberry NoIR (orange squares). The wavelength is on the x-axis, while the reflectance (0-1 scale) on the y-axis.



**Table 22.** Difference between the Band NoIR of the raspberry NoIR and one of the hyperspectral bands between 630nm and 880nm ion the 5 sample points selected for the comparison.

<b>Bands</b>	<b>Dark Grey</b>	<b>White</b>	<b>Light Grey</b>	<b>Black</b>	<b>Vegetation</b>
630nm	0.25	0.03	0.25	0.07	0.36
660nm	0.29	0.17	0.29	0.08	0.39
680nm	0.32	0.17	0.31	0.09	0.37
700nm	0.29	0.03	0.31	0.07	0.28
720nm	0.30	0.09	0.31	0.07	0.23
730nm	0.28	0.05	0.30	0.06	0.18
760nm	0.33	0.23	0.35	0.08	0.26
780nm	0.30	0.12	0.32	0.07	0.21
800nm	0.32	0.15	0.31	0.07	0.22
820nm	0.33	0.23	0.33	0.07	0.26
830nm	0.33	0.23	0.35	0.08	0.26
860nm	0.35	0.27	0.36	0.08	0.28
880nm	0.35	0.29	0.33	0.07	0.30

We can presume that the NoIR camera is sensitive to the Near InfraRed light from this study and the literature. This is partially confirmed by validating the data collected in the field, which provides reasonable results. This specific sensor was applied for data collection in South-west Niger.

### **6.3.2. Satellite sensors**

#### *Sentinel-2*

Sentinel-2 is an Earth observation mission of the European Space Agency (ESA). It comprises a constellation of two polar-orbiting satellites that aims to:

1. Systematic global acquisitions of high-resolution, multispectral images allied to a high revisit frequency;
2. Continuity of multi-spectral imagery provided by other satellite Earth observation programmes ( such as the SPOT series of satellites and the USGS LANDSAT Thematic Mapper instrument);
3. Observation data for the next generation of operational products, such as land-cover maps, land-change detection maps, and geophysical variables.

The satellites (Sentinel-2A and Sentinel-2B) are placed in the same sun-synchronous orbit, phased at 180° to each other. They have a wide swath width (290

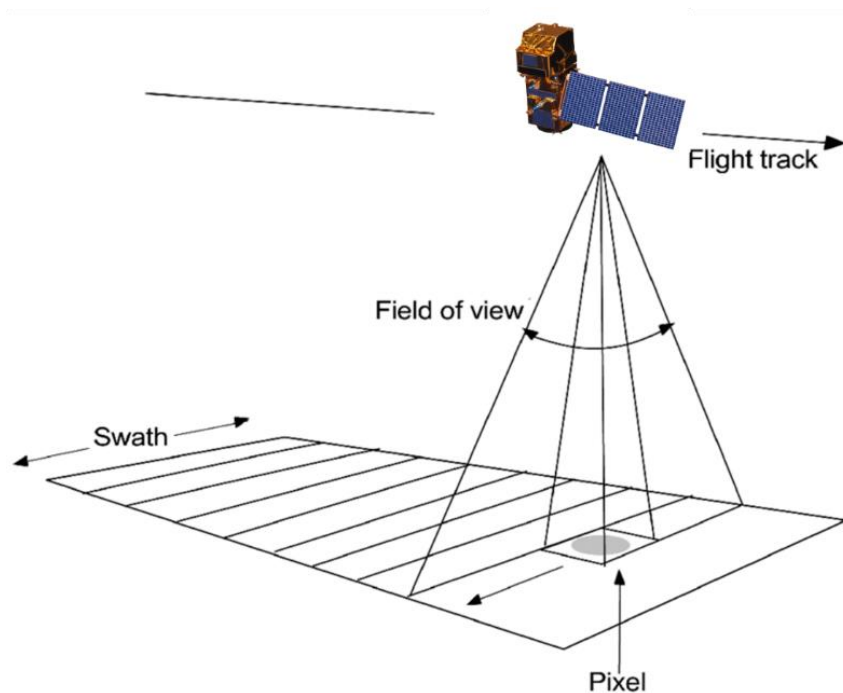
km) and high revisit time (ESA, 2019). Namely, each satellite has ten days of revisiting time at the equator. Since Sentinel-2A and Sentinel-2B are phased, data of a specific point on Earth are available every five days (with cloud-free conditions). This corresponds to in 2-3 days at mid-latitudes. The data acquisition is limited between latitudes 56° south and 84° north.

SENTINEL-2 carries an optical instrument, MultiSpectral Instrument (MSI), that samples 13 bands: four bands at 10 m, six bands at 20 m, and three bands at 60 m spatial resolution (Table 23).

**Table 23.** Spatial resolution and bandwidth of Sentinel-2A (S2A) and Sentinel-2B (S2B).

Band	S2A		S2B		Spatial resolution
	Central wavelength (nm)	Bandwidth (nm)	Central wavelength (nm)	Bandwidth (nm)	
1	442.7	21	442.2	21	60
2	492.4	66	492.1	66	10
3	559.8	36	559.0	36	10
4	664.6	31	664.9	31	10
5	704.1	15	703.8	16	20
6	740.5	15	739.1	15	20
7	782.8	20	779.7	20	20
8	832.8	106	832.9	106	10
8a	864.7	21	864.0	22	20
9	945.1	20	943.2	21	60
10	1373.5	31	1376.9	30	60
11	1613.7	91	1610.4	94	20
12	2202.4	175	2185.7	185	20

MSI is a pushbroom sensor that collects rows of data (i.e., several pixels' projections on the ground) across the orbital swath and utilizes the forward motion of the spacecraft along the path of the orbit to provide new rows for acquisition (Figure 58). In particular, in the MSI, the light reflected by the Earth is collected by a three-mirror (M1, M2, and M3) telescope and focused on two Focal Plane Assemblies: the visible and NIR spectrum and one for the three SWIR spectrum. To achieve the required 290 km swath width, both the Focal Plane Assemblies are composed of 12 detectors, spaced in two horizontal rows.



**Figure 58.** Pushbroom sensor functioning. Modified from <http://fao.org>

The commercial products of Sentinel-2 are TIFF images representing a 100kmx100km of Earth's surface. ESA distributes them with two possible processing levels: Level-1C is the Top-Of-Atmosphere reflectance in cartographic geometry and level-2A Bottom-Of-Atmosphere reflectance in cartographic geometry. Level-1C imagery is the geometric and absolute calibration object, while Level-2A is also radiometrically calibrated (paragraph 5.1, page 94). The data can be downloaded by the Sentinel-2 toolbox, the Copernicus project platform Sci-Hub, and after a couple of days from Copernicus and ESA. They can be download also from other services such as Google Earth Engine.

## 6.4. Tools for data processing

Software, platforms and online services were used to pre-process, classify, and validate this work. The choice of the tools was accurately selected based on the cost, the source code's openness, and the performances. The selection of some tools required specific effectiveness tests and analysis, namely the Canadian PPP service. In the following sections will be presented the main tools used divided according to their functions: *Image processing and classification*, *Structure from Motion*, and *GNSS-PPP*.

### **6.4.1. Image processing and classification**

#### ***Google Earth Engine***

GEE is a web-based platform for geospatial analysis launched in 2010, and it is free for research and education purposes (Gorelick et al., 2017; Kumar and Mutanga, 2018). The GEE data catalog comprises continuously updated geospatial datasets provided by different national and international programs, such as NASA and ESA (Hu et al., 2018; Kumar and Mutanga, 2018; Shelestov et al., 2017; Sidhu et al., 2018). The datasets included some already elaborated satellite data. GEE's real innovation is the possibility of interacting with massive datasets and computing basic geospatial analysis directly on GEE servers through JavaScript/Python-based API (GEE API) (Goldblatt et al., 2017; Google Earth Engine, 2020). GEE makes available the imagery captured by Sentinel 2. Sentinel 2 is a mission of the European Space Agency (ESA), and it is composed of twins satellites (Sentinel-2A and Sentinel-2B) that carry multispectral optical sensors. The significant limits were detected in the memory available for single users, the inadequate information regarding the available functions, and the lack of some useful functions (like layers importance). Nevertheless, it is a relatively young service that is continuously enriched with new functions and features, and our analysis was quite ambitious from the computational point of view.

#### ***Orfeo toolbox***

Orfeo ToolBox (OTB)<sup>4</sup> is a FOSS project for state-of-the-art remote sensing. OTB's goal is to provide users with remote sensing tools that can deal with large datasets from resource-limited PC. The initial project was funded in 2006 by the French space agency. It is developed to process high resolution optical, multispectral, and radar images. It can process data at the terabyte scale. OTB provides users with a wide variety of optical imagery applications, from ortho-rectification or pan-sharpening to object-oriented classification. The OTB's algorithms are accessible from the GIS platforms, such as Qgis.

#### ***eCognition Developer***

eCognition Developer is proprietary software for object-based image analysis. It is based on the Cognition Network Technology analysis method that extracts information from images using a hierarchy of groups of pixels (i.e., object-oriented approach). eCognition was launched in 2000, and today its use for geospatial

---

<sup>4</sup> <https://www.orfeo-toolbox.org/>

analysis is consolidated in several fields. Table 24 shows a brief analysis of the software's usability and effectiveness in this thesis, according to the author's experience.

**Table 24.** Author's experience over the image processing software used in this work.

<b>Software</b>	<b>Usability</b>	<b>Power</b>	<b>Notes</b>
Google Earth Engine	<ul style="list-style-type: none"> <li>• Basic coding knowledge compulsory;</li> <li>• Many algorithms, but little control over the parameters;</li> <li>• Little memory allocated for the user (out of memory error) for large VHR datasets;</li> </ul>	<ul style="list-style-type: none"> <li>• Fast computing of very large dataset;</li> <li>• Computing is user's machine-independent, since on cloud;</li> <li>• Long time to download the results;</li> </ul>	Working with GEE has been extremely time-consuming for the limitation of memory consumption over Google servers and the impossibility of communication between the GEE asset and the GEE visual editor (no direct edits of the files imported from non-GEE-environment).
Orfeo toolbox	<ul style="list-style-type: none"> <li>• Can be used as stand-alone software or as add-on of Qgis;</li> <li>• Many algorithms and parameters that the user can easily control;</li> <li>• Few segmentation algorithms, with little control of the user;</li> </ul>	<ul style="list-style-type: none"> <li>• Fast computing, although depending on PC specification;</li> <li>• Batch process possible;</li> </ul>	Extremely performant and easy to use. I detected some bugs in the Qgis (version 3.4) add-on. It is better to use it as a stand-alone (with graphical interface).
Ecognition	<ul style="list-style-type: none"> <li>• User-friendly;</li> <li>• Good visualization and control over segmentation algorithms;</li> </ul>	<ul style="list-style-type: none"> <li>• Long time requirements for computing, but the possibility of realizing the analysis on sample area;</li> </ul>	The interface is straightforward to use, and the user has much control over the segmentation results. Nevertheless, most of the algorithms seem to be black boxes. It is hard to manage large amounts of data.



## **6.4.2. Structure from Motion**

### ***Metashape***

Agisoft Metashape (the previous version was called Agisoft Photoscan) is stand-alone proprietary software that performs SfM-MVS photogrammetric processing. It allows processing images from RGB and multispectral cameras, including multi-camera systems. Besides the production of georeferenced true orthomosaics and DEMs, it also proposed post-processing features, such as algorithms for shadows and texture artifacts removals and radiometric indices' computation. It can also work with satellite imagery and LiDAR data. An additional benefit of Agisoft Metashape is the out-of-core implementation that reduced the memory consumption fastening the SfM process.

## **6.4.3. GNSS post-processing Service**

### ***CSRS-PPP***

Operative since 2003, the CSRS-PPP is an online free tool provided by the Canadian government (Mireault et al., 2008). It calculates with high accuracy the positions of the information collected by GNSS receivers based on the RINEX files (Natural Resources Canada, 2016). The CSRS-PPP uses GNSS ephemerids to produce absolute constant accuracy coordinates, meaning using accuracy values that do not depend on the position in the globe in which they have been collected or on the distance between GNSS receiver and CORS. The position is as much accurate as long in the acquisition session. The CSRS-PPP uses ephemerids of three types, Final, Rapid, and Ultra Rapid.

# Chapter 7

## Case study A: Alpine Arch forest

The Alpine case study is located in Cesana Torinese (TO, Italy) and analyzed a rockfall-prone area. In this framework, two classifications were realized, which differ in thematic detail and the data sources. Table 25 summarizes the characteristics of the three classifications in the Alpine arch environment.

**Table 25.** Classifications that interest the Alpine arch area.

<b>NO.</b>	<b>Classification</b>	<b>Temporal</b>	<b>Spatial</b>	<b>Thematic</b>	<b>Reference publication</b>
i	UAV-ITD	Low	Very High	High	(Belcore et al., 2020)
ii	SAT-LC	High	Medium	Low	(Belcore et al., 2020)

### 7.1. UAV- ITD

UAV application in forestry inventory and, more generally, in the extraction of the primary forest parameters (e.g., forest stand density, crowns widths, basal area, average diameter at breast height, height) is well established. The structural information of forest stands is vital for silviculture and forestry inventories. The tree crowns' accurate detection is necessary to estimate the dendrometric attributes of forest stands, such as the tree position, the stem diameter, height, crown extension, and volume (Magnard et al., 2016; Qiu et al., 2020; Sačkov et al., 2014). Besides, these forest parameters can be valuable ecological indicators, which determine, among others, the carbon sequestration, the shading, the risk of wind-

breakage, and the tree growth (Panagiotidis et al., 2017). The determination of these parameters is performed at the individual tree level and requires information about single trees.

### **7.1.1. Class identification**

Up to this time, many approaches have been proposed for Individual Tree Detection (ITD) via remote sensing. Generally, they are based on Digital Elevation Models (DEM) that can be generated from LiDAR acquisitions (Bottai et al., 2013; Dong et al., 2020; Moe et al., 2020; Sačkov et al., 2014; Wang et al., 2019; Yao et al., 2012; Zaforemska et al., 2019) or Structure from Motion (SfM) (Abdullah S et al., 2019; Grznárová et al., 2019; Moe et al., 2020; Mohan et al., 2017; Panagiotidis et al., 2017). SfM uses optical images acquired from multiple perspectives to recreate the three-dimensional geometry of an object (Fonstad et al., 2013; Iglhaut et al., 2019). The 3D model generation is carried out by incremental steps. See paragraph 3, page 103, for more information about the SfM process.

Regardless of the data source, some 2D ITD methodologies include the computation of the Canopy Height Model (CHM) to detect and delineate tree crowns (Mohan et al., 2017; Vastaranta et al., 2012). First, the local maxima of the CHM are computed to detect treetops (Mohan et al., 2017; Vastaranta et al., 2012), and then, the crowns are delineated using image-processing and segmentation algorithms (Bottai et al., 2013; Dong et al., 2020; Ke and Quackenbush, 2011; Wang et al., 2019). The most common technique for delineating crowns consists of the watershed segmentation using as input seeds the local maxima. Segmentation works on contiguous pixels grouped based on similar Digital Numbers (DN) values (De Luca et al., 2019; Dong et al., 2020; Torres-Sánchez et al., 2015; Wang et al., 2019). When the local maxima are identified, they are used as input seeds or starting points for the segments' generation. Many other 2D ITD spectral information methodologies have been explored, but unlike the others, these procedures mainly work on the segmentation based on brightness levels (Bottai et al., 2013; Panagiotidis et al., 2017; Pouliot et al., 2002; Sačkov et al., 2014; Vastaranta et al., 2012; Wolf and Heipke, 2007). They consider the brightest pixel in a neighborhood as the tree crown apex and identify the tree crown perimeters using dark-pixel and valley-following approaches. Most of the ITD techniques depend on CHM generation methods that may affect trees' crowns delineation (Dong et al., 2020; Mielcarek et al., 2018). CHM is calculated as the difference between the Digital Surface Model (DSM) and the Digital Terrain Model (DTM). Thus, a good DTM is a fundamental prerequisite for CHM's accurate characterization (Moe et al., 2020).

When the DTM of a forest stand is interpolated from LiDAR or photogrammetric point clouds, their accuracy is strongly influenced by the forest stand's density, meaning the number of ground points identified by the sensor (Moe et al., 2020). Indeed, the CHM-based methods for ITD assume that local maxima analysis detects treetops. However, in structurally complex forest stands and steep slope areas, the results should be carefully interpreted (Panagiotidis et al., 2017). In this framework, LiDAR data is much more accurate (Mohan et al., 2017) than the SfM-based approaches since LiDAR can penetrate tree crowns and obtain terrain information by reaching the ground (Pearse et al., 2018). Because of that, and the commercialization of light-weighted sensors that can be mounted on UAVs, the most recent applications of ITD methodologies work on 3D datasets acquired with Aerial Laser Scanners (ALS) (Mohan et al., 2017; Wang et al., 2019; Yao et al., 2012). Besides generating more accurate point clouds, LiDAR technologies are more expensive than optical ones (Pearse et al., 2018; Vastaranta et al., 2012). Even if some countries, such as Norway, Sweden, and Canada, use LiDAR technology for national forest inventories, several annual acquisitions at local and regional scales are generally cost-prohibitive (Pearse et al., 2018). Therefore, many countries are not in the economic position to rely on LiDAR technologies. Generally, SfM-derived data for forestry inventories are more cost-effective than LiDAR data and can cost about one-half to one-third of LiDAR data (White et al., 2013).

Moreover, LiDAR sensors are heavier than multispectral cameras and need to be mounted on UAVs with higher payload capacity. Besides being more expensive, larger UAVs with heavy payloads may require additional training and licensing (most UAV license national systems are based on Maximum Take-Off Weight, MTOW, categories). LiDAR also requires high data storage structures (Vastaranta et al., 2012) and powerful computational techniques to obtain accurate results (Mohan et al., 2017). The LiDAR data do not provide the users with the spectral information, although some models have a camera integrated into the acquisition systems. Table 26 provides an advantages and disadvantages analysis of the optical and LiDAR systems focused on UAV data acquisition for ITD. The ITD approaches based on UAV aerial images turn to be a cost-effective and valid alternative to LiDAR. They provide users with good accurate data with little usage of resources. Several studies have been carried out on the accuracy of ITD from UAV-derived information. Some methods identify the tree crowns from the brightness values of visible and infrared images (Pouliot et al., 2002; Wolf and Heipke, 2007), some more recent ones work on multiscale filtering, segmentation of imagery, and math

morphology algorithms (Qiu et al., 2020) to define tree crowns (Abdullah S et al., 2019; Ke and Quackenbush, 2011; Maschler et al., 2018).

**Table 26.** UAV and LiDAR systems' advantages and disadvantages for the acquisition of data in forested areas with UAV for the Individual Tree crown Detection (ITD) from literature and authors' personal experience.

	<b>Advantages</b>	<b>Disadvantages</b>
Optical	<p>Low-costing (Pearse et al., 2018; Vastaranta et al., 2012);</p> <p>No advanced-trained personnel needed;</p> <p>Provides multispectral information (Campbell and Wynne, 2011);</p> <p>Requires medium data storage structures;</p>	<p>Incapable to penetrate tree crowns;</p> <p>Inaccurate DTM in case of high-density stands (Mohan et al., 2017);</p> <p>Sensitive to varying illumination conditions (Iglhaut et al., 2019);</p> <p>Incapable of collecting data of trunks (2D-nadir information only) (Moe et al., 2020).(Moe et al., 2020);</p> <p>Requires powerful computational technology;</p>
LiDAR	<p>High accurate (Mohan et al., 2017);</p> <p>Penetrates tree crowns (Moe et al., 2020; Pearse et al., 2018);</p> <p>Provides trunks and lower forest strata information (Moe et al., 2020).</p>	<p>Expensive (Moe et al., 2020; Pearse et al., 2018; Vastaranta et al., 2012);</p> <p>Requires UAV systems with high MTOW capability;</p> <p>No multispectral information available (Campbell and Wynne, 2011) ;</p> <p>Requires high data storage structures (Vastaranta et al., 2012);</p> <p>Powerful computational technology needed (Mohan et al., 2017).</p>

These methods usually have complex segmentation workflows and require image filters, such as Laplacian filters, Gaussian filters, and math morphology algorithms. Complex segmentation processes are necessary because UAV optical imagery of forested areas is frequently affected by shadows, slope-derived distortions, and low contrast (Dorren et al., 2003; Itten and Meyer, 1993). These aspects, which are enhanced by the high spectral variability of VHR imagery, make the segmentation difficult. VHR images represent a challenge for segmentation and classification because, unlike in lower resolution images, single pixels no longer capture the classification targets' characteristics (Torres-Sánchez et al., 2015). Image-based methodologies for ITD, even if efficient, usually require several steps. Therefore high computational time is needed. This is one of the reasons why CHM-based methods have partially overcome the image-based processes for ITD.

Nevertheless, when CHM is not accurate enough or too expensive, such as structural complex stands, image processing methods that do not require CHM

exist, and they can be a valuable alternative to CHM-based methods. Indeed, image-based segmentation techniques can provide good accuracy results, especially when a textural analysis is applied (Blaschke, 2010; Lewiński et al., 2015). A shared methodology of texture analysis for segmentation (and classification) is based on the Gray Level Co-occurrence Matrix (GLCM) according to the Haralick measures (Haralick et al., 1973). For the images of complex structures, some researchers proposed to use segmentation algorithms based on fractal and multifractal analysis (Stojić et al., 2006a; Véhel and Mignot, 1994; Voorons et al., 2003). It is worth reminding here that a fractal is a rough or fragmented geometrical object that can be subdivided into parts, each of which is (at least approximately) a reduced-size copy of the whole object (Mandelbrot, 1982). Fractals are described by one quantitative number – a fractal dimension, for computation of which various methods have been proposed (see, e.g. (Sun et al., 2006)), but generally, it can be treated as information about the considered objects' measure of complexity and self-similarity.

Fractal dimension has been used together with other features for image texture description and segmentation, e.g., (Keller et al., 1989), see paragraph 4.3.1, page 56. The fractal dimension has also been utilized in the forestry and classification fields. For instance, an interesting description of fractals in forest science can be found in (Lorimer et al., 1994). (Zeide and Pfeifer, 1991) showed that tree crowns' fractal dimension could be useful in crown classification and foliage distribution within a single tree crown analysis. Similarly, (Mandelbrot, 1982) suggested applying fractals to modeling trees and analyzing their structure. A comprehensive review of the application of fractal description in forest science can be found in (Lorimer et al., 1994).

At the beginning of the multifractal image analysis, a measure is assigned to of the image and in the next steps, the measure regularity of this measure is analyzed as the information on the image complexity/inhomogeneity. It is worth to underline that various measures defined based on pixel intensities can be applied (Stojić et al., 2006a; Turner et al., 1998; Véhel and Mignot, 1994). The local (pointwise) degree of regularity of a given measure is described by so-called Hölder exponent values that strongly depend on the actual position on the image and identify points that differ from the background (Stojić et al., 2006a). On the other hand, the distribution of Hölder exponents on the image is summarized in the form of the so-called multifractal spectrum treated as the global characteristic of a measure regularity (image complexity/inhomogeneity) (Stojić et al., 2006a; Véhel and Mignot, 1994). Global multifractal characteristics have already been applied to VHR optical data (Jenerowicz et al., 2019; Wawrzaszek et al., 2014), mostly to

distinguish between different land cover types. One can also find their application in the context of the study of forest cover, such as in (Danila et al., 2019) 's work, or to perform the segmentation of plants' diseases images (Wang et al., 2013).

On the other hand, the local multifractal description by using Hölder exponents has rarely been used, mainly to perform segmentation of medical data (Stojić et al., 2006a; Véhel and Mignot, 1994), or in the change detection aspects of satellite images (Aleksandrowicz et al., 2016; Véhel and Mignot, 1994). Anyway, the results obtained in papers (Aleksandrowicz et al., 2016; Stojić et al., 2006a; Véhel and Mignot, 1994) suggested the usefulness of the Hölder exponent in the context of image content description. In particular, the authors of these studies underlined the fuller description of complex shapes, heterogeneous measures, and structures typical for satellite remote sensing. It is worth mentioning that to the best of our knowledge. The Hölder exponent parameter has not been determined both for VHR UAV-derived imagery yet and in the context of the forest analysis. Therefore, in this study, we focus on determining the local Hölder exponent connected with multifractal theory and using it to segmentation single tree crowns from VHR UAV-derived imagery. More precisely, we propose to apply this quantitative descriptor as the unique input for the efficient identification of single tree crowns using only a cycle of the multiresolution segmentation algorithm (Ke and Quackenbush, 2011; Mohan et al., 2017; Qiu et al., 2020; Wolf and Heipke, 2007).

### **7.1.2. Data collection and pre-processing**

UAV technology was used in this research to generate photogrammetric products to be used as input data for the segmentation of single tree crowns using multifractal analysis.

#### ***Orthomosaic generation***

The UAV system used was chosen to consider the characteristics of the study area, regarding the topography, and the environmental conditions that could affect the execution of flights, the resolution of the products to be generated and the sensors to be integrated. Besides the radiometric information regarding the visible part of the electromagnetic spectrum (Red, Green, Blue), the Near InfraRed (NIR) part was necessary. Indeed, NIR information can enhance vegetation in the image-processing phase, and, generally, NIR information helps distinguish shadows from dark objects, which have higher reflectance in the NIR. Due to the large area involved in this application and the steep terrain, with an elevation difference of about 400 m, we used a commercial fixed-wings solution, an eBee Plus made by senseFly. The eBee has a payload of up to 0.3 kg, a flight autonomy of 59 minutes,

and it can reach a cruise speed of 40-110 km/h. Moreover, it does not require expert users because take-off and landing are entirely automatic, thanks to the built-in GNSS receiver.

Two different camera devices were employed for the collection of the RGB and NIR electromagnetic spectrum. To perform the RGB flight, the eBee Plus was equipped with the RGB senseFly S.O.D.A. digital camera (paragraph 6.3.1, page 119). A fixed number of frames per second equal to 0.25 fps (4 Hz frequency) was automatically acquired by the camera using a shutter cable. The flight with the eBee was planned using the eMotion software considering a photogrammetric overlap between images of 80% in the lateral and longitudinal direction, an altitude of 220 m, a speed of 9 m/s, and an average ground resolution of 5 cm.

Due to the extension of the area and the significant difference in the height of the terrain, which could have adversely affected the battery's autonomy, not allowing the flight to end, it was decided to survey the area through two distinct flights (Table 28). The flights were planned using as a base a Digital Surface Model (DSM) of the area from which the flight height was fixed. Given the steep terrain, the flight plan was created so that the flight path's survey lines would be parallel to the contour lines of similar elevation and then at a constant height. In order to acquire NIR images, we used a commercial camera, the Canon S110 NIR (paragraph 6.3.1, page 119). Taking into account the characteristics of the camera sensor, the flight was performed with the eBee at a height of 220 m and a speed of 11 m/s, in order to guarantee an image overlap of 80% on both directions and an average ground sample distance (GSD) of about 6 cm. **Table 27** recaps the characteristics of the sensors and **Table 28** shows the characteristics of the photogrammetric flights. The data acquisition is a crucial step of the photogrammetric process since the quality of the final result depends on it. The data acquisition phase includes flights, but, if necessary, the measurement of Ground Control Points (GCPs), for the point clouds georeferencing, and of Check Points (CPs) for the evaluation of the accuracy of the final results. To this purpose, before performing flights, 20 colored markers of size 40 x 40 cm were placed within the study area. Fourteen of them were used as GCPs during the data processing phase, while six markers were employed as CPs for the validation of the model (Figure 59). The position of the GCPs and CPs was acquired through a GNSS (Global Navigation Satellite System) receiver using a Real-Time Kinematic (RTK) (with GSM connection for real-time correction) approach, considering a session length of about 10 seconds for each point. The points' coordinates were estimated with fixed-phase ambiguities. The centimeter-level accuracy ( $\cong 3$  cm) ensured a high level of precision for the georeferencing process.

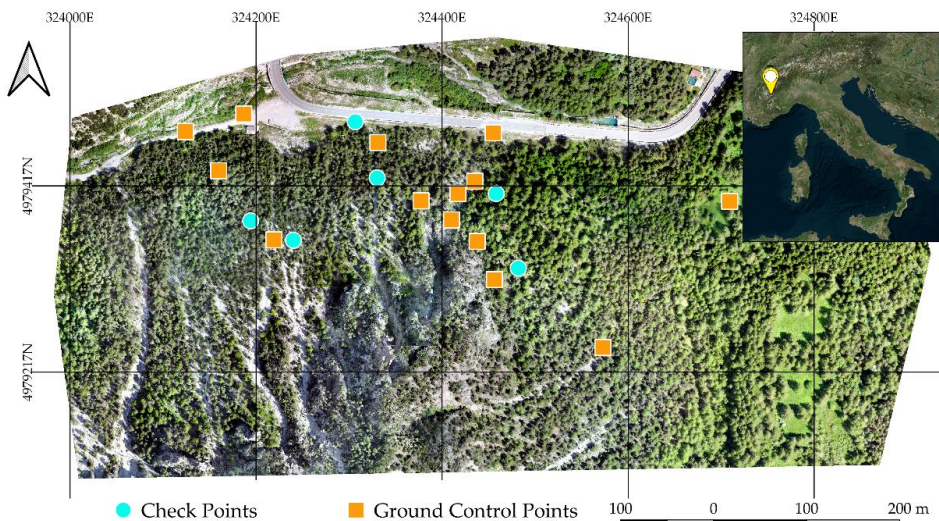


**Table 27.** Characteristics of the sensors of the flights

Characteristics	RGB senseFly S.O.D.A	Canon S110 NIR
Resolution	20 MP	12.1 MP
Bands sensor	RGB	RGN
focal length	10.6 mm	5.2 mm
Shutter frequency	4 Hz	1 Hz
Sensor size	13.2×8.8 mm	7.53×5.64 mm
Lateral overlap	80%	80%
Longitudinal overlap	80%	80%
Number of flights	2	1
Average duration of flight	15 minutes	19 minutes
Height of flight from the ground	220 m	220 m
GSD	5 cm/pixel	6 cm/pixel

**Table 28.** Characteristics of the three flight plans (Num. = Number).

	S.O.D.A. _ I <sup>st</sup> flight	S.O.D.A. _ II <sup>nd</sup> flight	Canon S110 NIR
Area [ha]	60	40	76.4
Num. of images	221	137	176
Camera orientation	Nadir	Nadir	Nadir



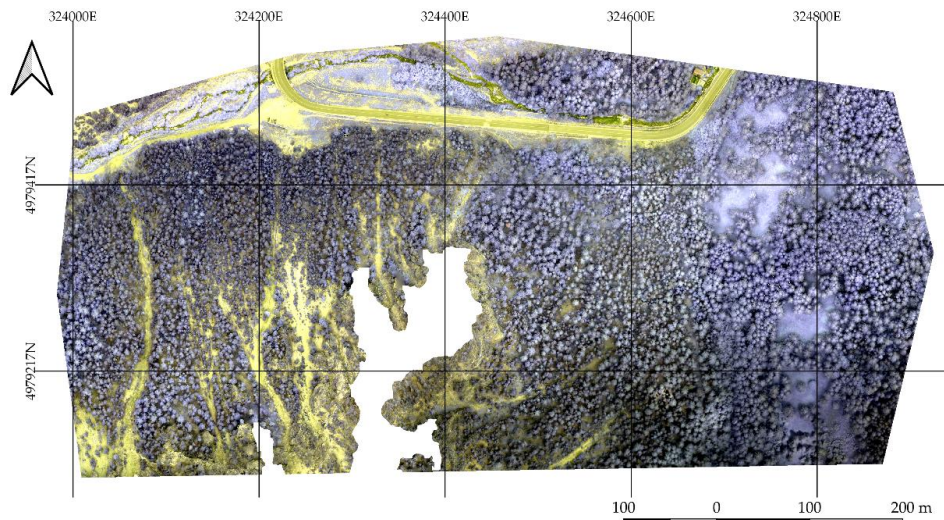
**Figure 59.** The study area in Cesana Torinese. The light blue circles are the CPs and the orange squares are the GCPs.

The aerial image acquisitions aimed to produce the RGB and RGN (Red, Green, NIR) orthomosaics. All the UAV data were post-processed through the SfM approach (Turner et al., 2012). These algorithms, which are now implemented in several commercial software, allow to rapidly and accurately align the images, compute a three-dimensional dense point cloud, and then reconstruct a textured mesh of the object of study. In this case study, the photogrammetric process was carried out using the AMP (Agisoft Metashape Professional) commercial solution (see 6.4.2, page 134 for more information regarding AMP).

The RGB datasets, acquired in two different flights, were processed together in the same project. A specific project was then dedicated to the processing of the RGN images. Nadiral images, in both projects, were aligned together, setting up the “high” level of accuracy of AMP, removing any limit on the key and tie points number. Subsequently, the measured GCPs and CPs were collimated in all the images, obtaining a 3D georeferenced model of known accuracy, as shown in Table 29. The Root Mean Square Error express the accuracy, as per equation 13.

$$RMSE (m) = \sqrt{\frac{\sum_{i=1}^n (R_i - S_i)^2}{n}}, \quad [13]$$

Where the  $R_i$  is the reference (check points measured coordinates) and  $S_i$  is the same point measure from the orthomosaic (check points measured points from the orthomosaic). The 3D dense point clouds were produced using a “high” level of details to obtain products suitable for medium/large-scale representations (1:500) and an “aggressive” depth filtering in order to remove the noise due to the presence of dense vegetation. The next step involved the generation of a “high” quality level mesh, from which we were able to generate the DSM of the study area. The UAV image data processing results were two orthomosaics in the RGB (Figure 59) and RGN (Figure 60) channels of the area of interest in the WGS84 – UTM 32N coordinates system. According to the model's accuracy, the orthomosaics were produced with a resolution of 10 cm, setting the “mosaic” blending mode option in AMP. The borders of the orthomosaics were cut out from the study area to avoid distortion of the images and get a regular shape.



**Figure 60.** Resulting RGN orthomosaic.

**Table 29.** Estimated residuals on the GCPs and CPs and characteristics of the obtained dense point clouds (where N = Number and RMSE=Root Mean Square Error).

Input dataset	Data resolution [pixel]	N. of images	RMSE on GCPs [m]			RMSE on CPs [m]			N. of points (dense cloud)
			x	y	z	x	y	z	
RGB	5472×3648	358	0.026	0.050	0.048	0.052	0.039	0.029	35144184
RGN	4048 × 3048	176	0.045	0.061	0.053	0.018	0.051	0.080	27624422

Comparing the two orthomosaics obtained, it can be observed that the product in the RGN channels is incomplete concerning the central part of the study area. It was impossible to align the RGN images related to this portion of the area, probably due to the considerable difference in altitude of the terrain, due to an almost vertical rock wall. However, the vegetation present in this area was relatively low and sparse, and, therefore, this does not affect the application of the algorithms described below. Finally, in addition to the two products already described, it was possible to generate the DTM of the area, using the dense point cloud as input data. Due to the complex terrain orography and the presence of dense vegetation, a semi-automatic approach was chosen. In a first step, the points belonging to the ground were classified with a specific AMP algorithm by setting the maximum angle equal to 45 (i.e., the maximum angle between the terrain model and the line to connect a point with a point from a ground class). Subsequently, the classification was optimized manually to replace the points not correctly classified by the software.

Exploiting the ground's identified points, it was, therefore, possible to generate the DTM with a resolution of 10 cm.

### *Features extractions*

This analysis focused on the local description of VHR UAV-derived imagery using parameters related to multifractal formalism. More precisely, we determined the singularity strength  $\alpha$  (known as the Hölder exponent), which depends on the pixel's actual position in the structure (i.e., the single-band image) and makes possible to describe the local degree of regularity of the measure around the pixel (Aleksandrowicz et al., 2016; Stojić et al., 2006b). The procedure used to calculate the Hölder exponent  $\alpha$  is graphically presented in Figure 61 and briefly summarized below.

For each pixel  $(m, n)$  of the NIR channel, we considered a square neighborhood of size  $\varepsilon_i = 2i - 1$ ,  $i = 1, 2, \dots, j$ , where  $j$  denotes the total number of squares, while  $\varepsilon_i$  is the size of a region centered on the pixel  $(m, n)$ . In this notation,  $\varepsilon_i = 1$  denotes a square, which contains only a single pixel,  $\varepsilon_i = 3$  represents a square of size  $3 \times 3$  containing pixel's neighbors, while  $\varepsilon_i = 5$  is a square of size  $5 \times 5$ , etc. It is worth to stress that during the computation of  $\alpha(m, n)$  various sizes of pixel neighborhoods  $j$  as well shapes can be applied, allowing to describe localized or more widespread singularities. Here, we consider cases where the maximum neighborhood (maximum square size) of a pixel is  $5 \times 5$  ( $j = 3$ ). The next important aspect of Hölder exponent determination stated the use of various capacity measures ( $\mu$ ), which emphasizes various effects on the image (Jenerowicz et al., 2019; Stojić et al., 2006a). In the frame of this work, based on the initial tests we applied the following type of capacity, equation 14:

$$\mu_i^{ISO}(m, n) = \text{card}\{(k, l) | g(m, n) \equiv g(k, l), (k, l) \in \Omega_i\}, \quad [14]$$

where  $m, n$  denotes the pixel position,  $g(k, l)$  is a gray-scale intensity at point  $(k, l)$ ,  $\Omega_i$  is the set of all pixels  $(k, l)$  in the  $i$ th square. Capacity measure ISO (Eq. 1) gives the number of pixels in the considered neighborhood, which have the same values as centered pixel  $(m, n)$ . A more detailed discussion about the used measures can be found in (Stojić et al., 2006a; Turner et al., 1998; Véhel and Mignot, 1994).

After calculation of capacity  $\mu_i^{ISO}$ , in the pixel neighborhood  $\varepsilon_i$ , the discrete set of coarse Hölder exponents has been determined:

$$\alpha_i(m, n) = \frac{\log(\mu_i^{ISO}(m, n))}{\log \varepsilon_i}, \quad [15]$$

Finally, the limiting value of the Hölder exponent for each pixel from the NIR channel has been estimated using the formula:

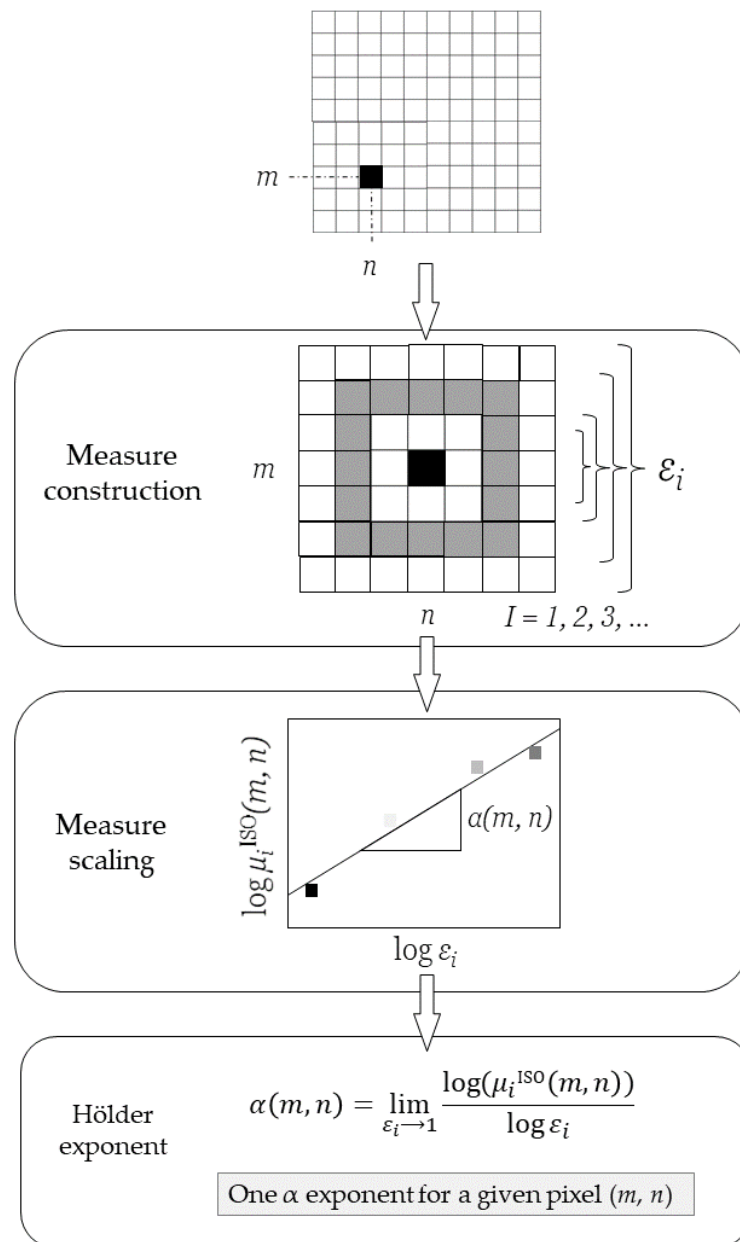
$$\alpha(m, n) = \lim_{\varepsilon_i \rightarrow 1} \frac{\log(\mu_i^{ISO}(m, n))}{\log \varepsilon_i}, \quad [16]$$

as the slope of the linear regression through points on a log-log plot, where  $\log \varepsilon_i$  is plotted on the x-axis, and  $\log \mu_i^{ISO}(m, n)$  on the y-axis, as shown in the middle section of Figure 61 (Aleksandrowicz et al., 2016). In the final step of the analysis, a two-dimensional ' $\alpha$ -image', which collects Hölder exponents, is calculated. As we underlined in the Introduction, next to the local Hölder exponent, the multifractal description also enables to analyze the global distribution of the regularity in a whole scene and to summarize it in the form of the multifractal spectrum, see, e.g. (Stojić et al., 2006a). However, the usefulness of this function in the context of tree detection will be the topic of separate analysis.

### 7.1.3. Methods

#### *Segmentation*

In the further analysis steps, the Hölder exponent layer ( $\alpha$ -image) determined using ISO capacity has been used as the base raster for the ITD through the segmentation process. First, it was smoothed with a simple average filter to remove small variations on the crown surface. The degree of smoothness was defined by the size of the filter (3x3). The segmentation was realized with eCognition Developer software. Two steps accomplished the crown extraction. In the first step, the high-fractality pixels were separated from the low-fractaly ones using a multi-threshold algorithm applied to the Hölder exponent layer calculated on the InfraRed band. It was necessary to find the threshold value that represented the breakpoint between tree crowns and other elements. Table 30 shows the adopted parameters. The threshold parameters were selected to satisfy the spectral difference between crowns and other elements, and they are designed to consider overexposed areas.



**Figure 61.** The procedure used to calculate the Hölder exponent  $\alpha$ , adapted from Figure 1b in (Aleksandrowicz et al., 2016)

The second step consists of selecting single crowns applying a multiresolution segmentation algorithm (Table 30). The segments' borders were redefined by growing them of 1 pixel and the objects with an area less than 80 pixels were considered outliers and removed.

**Table 30.** Algorithms, parameters, and computational time are used for the segmentation. The input band is the Hölder exponent image.

Algorithm	Parameters	values	Computing time	Notes
Contrast split segmentation	Minimum threshold	0.4	5' 42''	
	Maximum threshold	1		
	Step size	5		
	Stepping type	Add		
	Class for bright objects	Other		
	Class for dark objects	Trees		
Multiresolution segmentation	Scale parameter	11	5' 31''	Only on Trees class
	Shape	0.05		
	Compactness	0.5		
Chessboard segmentation	Object size	3	12''	Only on Other class
Assign class	Use class	Temporary class	5''	Only on Other class
	condition	Border to Trees >0px		
Grow region	Candidate classes	Temporary class	6''	Only on Trees class
Remove object	Condition	Area < 80Px	<0,001''	Only on Trees class

### ***Validation***

The literature is rich in methodologies for evaluating the goodness of segmentation and extraction of specific objects from imagery (Clinton et al., 2010). Nevertheless, as far as we know, a shared and accepted methodology for the accuracy assessment does not exist (Persello and Bruzzone, 2010). Besides this, the methods applied are quite similar to each other, and generally, they are based on the comparison between manually digitalized reference objects and the segmented objects (Clinton et al., 2010; Hussin et al., 2014; Ke and Quackenbush, 2011; Persello and Bruzzone, 2010; Radoux and Defourny, 2007; Yurtseven et al., 2019). The most common validation methodologies can be distinguished in visual evaluations and quantitative measures. The visual evaluations are based on

comparing reference objects to the segmented ones and their attribution to the match or non-match categories by the operator. The omission and commission errors are then calculated (Ke and Quackenbush, 2011; Mohan et al., 2017; Qiu et al., 2020; Wolf and Heipke, 2007). The quantitative measures focus on comparing the reference dataset and the segmentation results based on specific metrics. The perimeter, the area, and the distance between centroids of the objects are some of the most calculated metrics for the goodness of the segmentation assessment (Clinton et al., 2010; Hussin et al., 2014; Persello and Bruzzone, 2010; Yurtseven et al., 2019). Generally, the evaluation of the metrics is performed by applying normalized indices (Clinton et al., 2010; Hussin et al., 2014; Persello and Bruzzone, 2010; Yurtseven et al., 2019) or by calculating the Root Mean Square Error (RMSE) (Hussin et al., 2014; Ke and Quackenbush, 2011; Yurtseven et al., 2019). The normalized indices can provide a value representing the goodness of the segmentation that can be easily compared to other segmentation. The quantitative methods are almost wholly applied only to evaluate the segmentation of satellite imagery of heterogeneous land cover scenes. As far as we know, few applications have been realized in the ITD context.

The accuracy was evaluated in terms of correspondence between the reference crowns and the segmented ones. The evaluation methodology translates specific pixel-based accuracy measures (user's and producer's accuracy and F1 score) in object-based measures. Particularly, the producer's accuracy (PA) and the user's accuracy (UA) are calculated using the following equations:

$$PA = \frac{M}{RC}, \quad [17]$$

$$UA = \frac{M}{DC}, \quad [18]$$

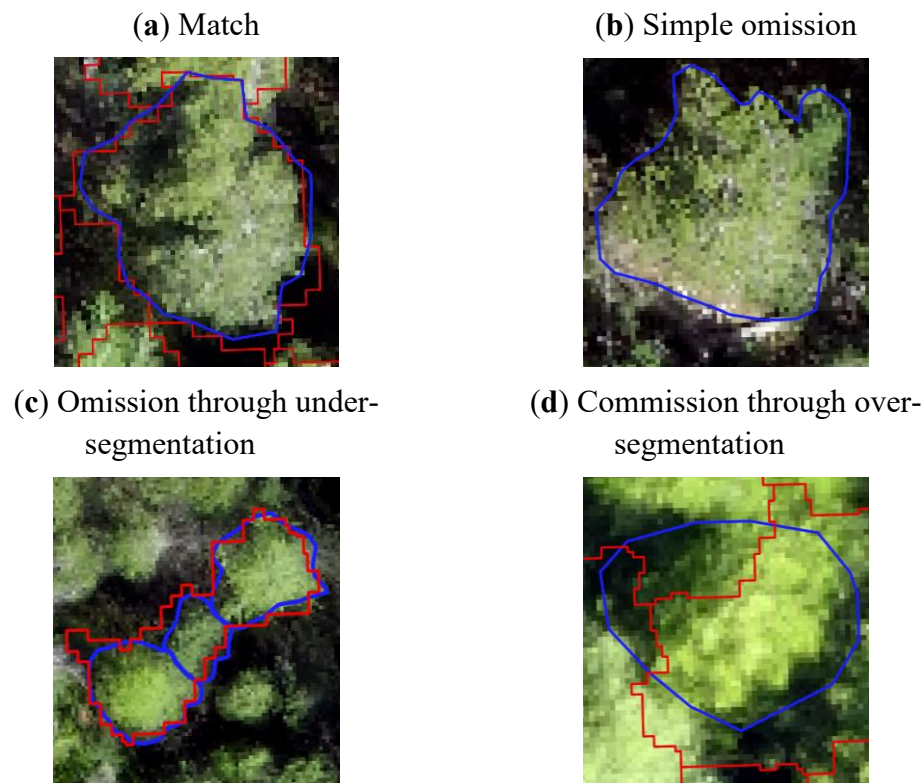
where PA is Producer's accuracy, UA is User's accuracy, M the number of matching crowns, RC is the number of reference crowns, and DC the number of defined crowns. The relation between UA and PA is described by F1 score, from the equation:

$$F1 = \frac{2 \times PA \times UA}{PA + UA}. \quad [19]$$

The situation shown in Figure 62a was considered as matching crowns (M), while the relations of reference and segmented crowns in Figure 62b, Figure 62c,



and Figure 62d were considered as non-matching crowns. The segmented crowns were counted based on their overlap with the reference crowns. For example, the segmented crowns in Figure 62b are zero, in Figure 62c is one, and in Figure 62d are three. Even if significant, these measures provide a partial view of the goodness of the segmentation. The Omission and Commission errors can describe more precisely the goodness of the segmentation. As illustrated by (Ke and Quackenbush, 2011), we took into consideration four possible cases of the relation between the reference dataset and the segmented one: i) Match, ii) Simple omission, iii) Omission through under-segmentation, and iv) Commission through over-segmentation, (Figure 62).



**Figure 62.** Possible cases of the relation between reference crowns (blue border) and segmented crowns (red border)

It is based on the works of (Persello and Bruzzone, 2010), (Clinton et al., 2010), and (Yurtseven et al., 2019). The areal difference, the perimeter, the centroid's distance, the Under-segmentation index, the Over-segmentation index, and the Completeness index are the evaluated metrics. The Root Mean Square Error (RMSE) was calculated for the area and the perimeter.

The areal distance is the most common metric used as an indicator of segmentation goodness. It was calculated for reference objects and the segmented objects. In the case of over-segmentation, the reference area was compared to the sum of the segmented objects in the reference tree's correspondence.

The perimeter measures the length of the object borders. In the case of more than one crown corresponding to the reference, the segmented perimeter was calculated as the sum of the perimeters on every object composing the crown in the exam. With this approach, over-segmented objects have high RMSE values. It is worth mentioning that the perimeter metrics results should be considered with caution. Indeed the values can vary according to the shape and the number of tree branches considered.

The centroid distance represents the Euclidean distance between the gravitational centers of two shapes. The Euclidean distance between the centroids is calculated as the RMSE (Yurtseven et al., 2019); thus, it can be considered as the indicator of an error on the distance between gravitational centers. In the case of more than one crown corresponds to the reference, the centroid distance was calculated between the reference crown and the closer centroid.

The RMSE of perimeter and area were calculated with equation 13, where  $R_i$  is the value of metric  $m$  of the reference crown, and  $S_i$  is the metric  $m$  for the segmented crown. Four indicators for the evaluation of the goodness of the segmentation were applied. For each reference tree were evaluated the Over segmentation index (OS), the under-segmentation index (US), the Intersection over Union index (J), and the Completeness (D).

The OS and US were proposed by Clinton et al. (2010) and Persello (2010) (Clinton et al., 2010; Persello and Bruzzone, 2010). Their estimations are based on the relation between the segmented (S) area and reference objects (R). The following equations describe OS and US:

$$OS = 1 - \frac{|R_i \cap S_i|}{|R_i|}, \quad [20]$$

$$US = 1 - \frac{|R_i \cap S_i|}{|S_i|}, \quad [21]$$

where  $R_i \cap S_i$  is the overlapping area between the reference crown ( $R_i$ ) and the segmented crown ( $S_i$ ) of object  $i$ . The indices describe a perfect match with a value of 0, while values that approach 1 indicate disagreements between the reference and the segmented object and, respectively, under-segmentation for the US and over-

segmentation for OS. The OS and US indices were considered the maximum, minimum, median, and average values.

The Intersection Over Union (J), also known as the Jaccard index, also quantifies the false positives within the segmentation, and it is calculated as the ratio between the overlapping area and the union area

$$J = \frac{|R_i \cap S_i|}{|R_i \cup S_i|} \quad [22]$$

It is worth to stress that when J is equal to 1 there is a perfect segmentation.

Finally, the completeness of the segmentation was evaluated through the Completeness index (D) (Clinton et al., 2010), calculated as the distance between the OS and the US, as follows:

$$D = \sqrt{\frac{OS_i^2 + US_i^2}{2}} \quad [23]$$

The Completeness index D should be interpreted as the closeness to an ideal segmentation result concerning the reference set. When D index is close to 0, it indicates a perfect segmentation.

### ***Comparison with segmentation methodologies based on spectral, textural, and elevation information***

The results were checked against four different segmentations based on the elaboration of spectral, textural, and elevation information to evaluate the Hölder exponent segmentation's goodness. Namely, were used as terms of comparison: i) original spectral bands (Red, Green, NIR), ii) Normalized Difference Vegetation Index; iii) Haralick's Sum Variance measure from GLCM (Haralick et al., 1973), iv) the CHM, and v) a multi-sourced approach that considers both the CHM and the sum variance. This validation aimed to evaluate on equal terms the performances for ITD of Hölder exponent against other more common input data. Thus, the ITD from each of these measures was performed using the same ruleset applied for the Hölder exponent, but tuning the input parameters to achieve the best possible results. Basically, they were realized using Contrast split and Multi-resolution segmentation algorithms with minor differences in the sequence to improve the final segmentation. Appendix A recaps the applied rules and parameters of each segmentation. As mentioned in the introduction, the CHM was calculated as the difference between the Digital Surface Model (DSM) and the Digital Terrain Model (DTM). The treetops' location was then calculated by applying the Local Maxima

algorithm and used in the multi-sourced segmentation. The NDVI, the Sum Variance GLCM measure, the CHM, and the local maxima were calculated using Quantum GIS. The selection of Sum Variance among all the GLCM existing measures is based on the visual evaluation.

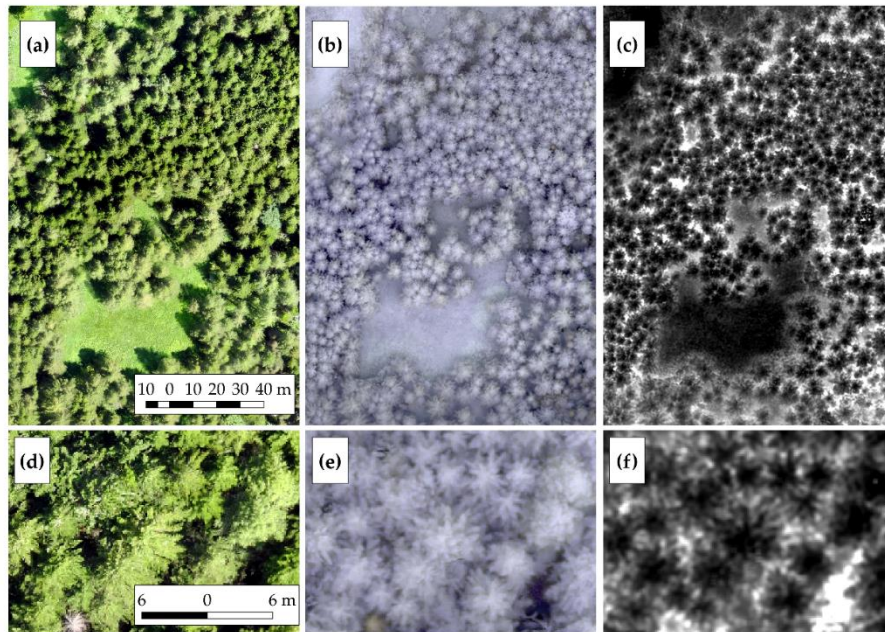
#### **7.1.4. Results**

Results of the Hölder exponent analysis and the Individual Tree Crown definition in Figure 63c and Figure 63f show the result in a sample area of Hölder exponents  $\alpha$ . It is apparent that the contrast between the tree crowns and other elements of the background. The top of the trees (black in Figure 63c and Figure 63f) have lower DN values than the lower branches (grey in Figure 63c and Figure 63f), which is generally lower than 0.2. The screens have the DN close to 0.3, while shaded areas vary from 0.4 to 1 (white areas in Figure 63c and Figure 63f). From the visual comparison of Figure 63 (e) and Figure 63 (f), we can see that the Hölder exponent reduces the DN variability of tree crowns and enhances the contrast between crowns and shaded areas. This aspect facilitated the segmentation process. The entire segmentation process was realized in about 13 minutes.

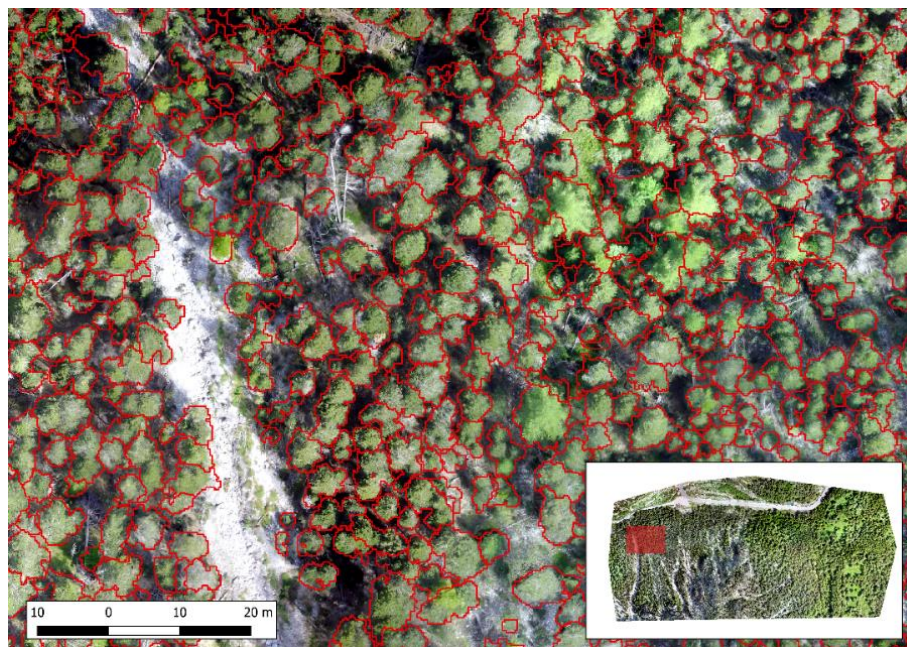
Table 31 shows the computational time for each applied algorithm and the graphic restitution of their results. The final segmented objects were 9215 with an average area of 21 m<sup>2</sup> and an average perimeter of 18 m. Figure 64 provides a sample of the segmentation result. From a very first visual evaluation appears that most of the crowns were detected. Some smaller crowns neighboring the scree appear slightly over-grown.

##### ***Results of validation***

The visual assessment of the segmentation provides positive results. Indeed only 3 crowns out of 200 references were not detected (simple omissions). Table 32 summarizes the results of the visual assessment of Hölder exponent segmentation (and of the validation datasets). Even if the simple omissions are rare, the ones through under-segmentation (OUS) are 27. The results underline the process tends to under-segmenting. Although the PA is slightly better than the UA, it reaches 79% against 69% of UA, while commission errors are much lower (only 13 out of 200). These affect the F1 score, which despite the OUS, reach an acceptable value (73%).


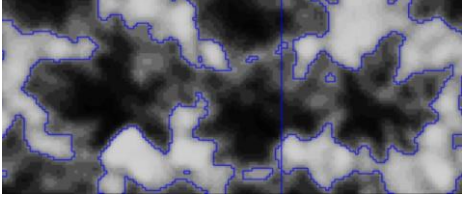
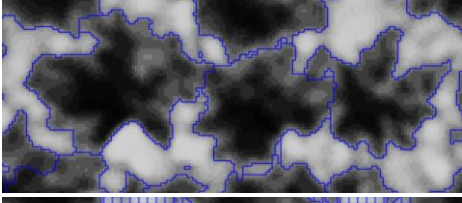
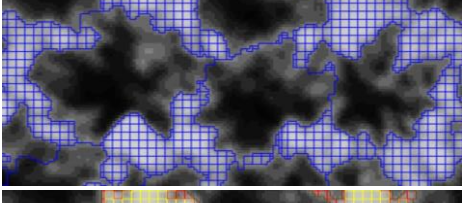
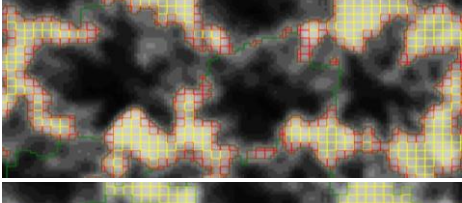
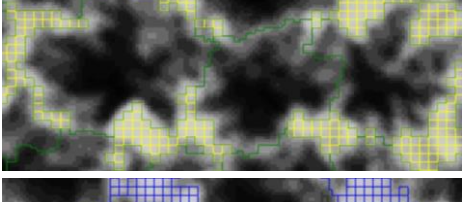
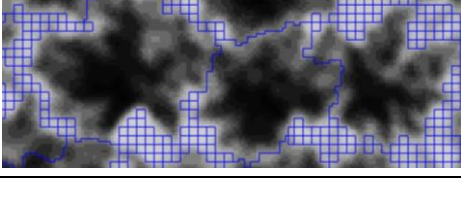


**Figure 63.** (a) and (d) Details of RGB dataset; (b) and (e) Detail of RGN dataset of the same area presented in (a) and (d); (c) and (f) Map of the Hölder exponents determined for the area presented in (a) and (d). The Hölder exponent layer restitution is in greyscale visualization, where 0 is black, and 1 is white. The shadows are mitigated, and the single crowns are easily identified as well as the grassland that are large areas of low DNs.



**Figure 64.** Detail of the delineation of single crowns (red border) on RGB orthomosaic. The red square in the bottom-right corner indicates the sample area's location within the entire study area.

**Table 31.** Computational time Graphic restitution of each step (algorithm) of the segmentation process. Figures in blue have no classification. The class *Trees* is green; the class *Other* is yellow, the class *Temporary* is red.

Algorithm	Computing time	Visual restitution
Starting image	/	
Contrast split segmentation	5' 42''	
Multiresolution segmentation	5' 31''	
Chessboard segmentation	12''	
Assign class	5''	
Grow region	6''	
Remove object	<0,001''	

**Table 32.** Results from the Visual evaluation of the Hölder exponent segmentation.

Validation of ITD	Hölder	Spectral	NDVI	Texture	CHM	Multi-Sourced
No. References	200	200	200	200	200	200
No. Segmented	228	289	529	248	247	330
Matches	157	85	39	64	57	68
Simple omission	3	1	9	3	38	8
Omission through under-segmentation	27	59	9	45	70	56
Commission through over-segmentation	13	55	143	88	35	68
Producer's accuracy	0.785	0.425	0.195	0.320	0.285	0.340
User's accuracy	0.689	0.294	0.074	0.258	0.231	0.206
F1-score	0.734	0.348	0.107	0.286	0.255	0.257

The area-based analysis positively confirms the outcome. As Table 33 shows, the RMSE on the area represents only 14% of crowns' average dimension. It is 3 m<sup>2</sup> over 21 m<sup>2</sup> of average crown extension. The RMSE on the perimeter is almost 3 m over 18 m of the average perimeter, corresponding to 15%. This may be caused by the difficulties related to the definition of the reference tree, but also the non-appropriate threshold value selected for the contrast split algorithm.

**Table 33.** Root Mean Square Error, the Average and the % of an error on the Average, of the Perimeter, the Area, and the Compactness metrics of the Hölder exponent segmentation and the validation datasets

	Metric	RMSE	Average	RMSE/Average
Hölder	Area [m <sup>2</sup> ]	2.903	21.099	14%
	Perimeter[m]	2.727	17.972	15%
Spectral	Area [m <sup>2</sup> ]	4.367	21.299	21%
	Perimeter[m]	10.378	18.055	57%
NDVI	Area [m <sup>2</sup> ]	3.758	21.407	18%
	Perimeter[m]	6.590	18.130	36%
Texture	Area [m <sup>2</sup> ]	4.025	20.885	19%
	Perimeter[m]	5.574	17.863	31%
CHM	Area [m <sup>2</sup> ]	2.090	23.126	9%
	Perimeter[m]	5.961	18.982	31%
Multi-Sourced	Area [m <sup>2</sup> ]	3.432	21.772	16%
	Perimeter[m]	4.812	18.356	26%

Table 34 presents the summary statistics regarding the Over Segmentation (OS), Under Segmentation (US), Completeness (D), Intersection over Union (J)

indices, and the distance between centroids. The minimum, maximum, and average values for each index were computed. What stands out is the high values of Under Segmentation, which confirm the visual estimation results. The Completeness (D) and the Intersection over Union (J) indices show significant positive results that confirm the accuracy of the ITD. The median values of D and J are respectively 0.18 and 0.72. The mean distance between the centroids of the reference and segmented crowns is 83 cm, while the median distance is exceptionally 45 cm. This value is promising and indicates that the results are close to 4 pixel-error in crown localization.

**Table 34.** Summary statistics of the Over-segmentation index (OS), the Under-segmentation index (US), the Completeness index (D), the Jaccard index (J), and the Distance between centroids.

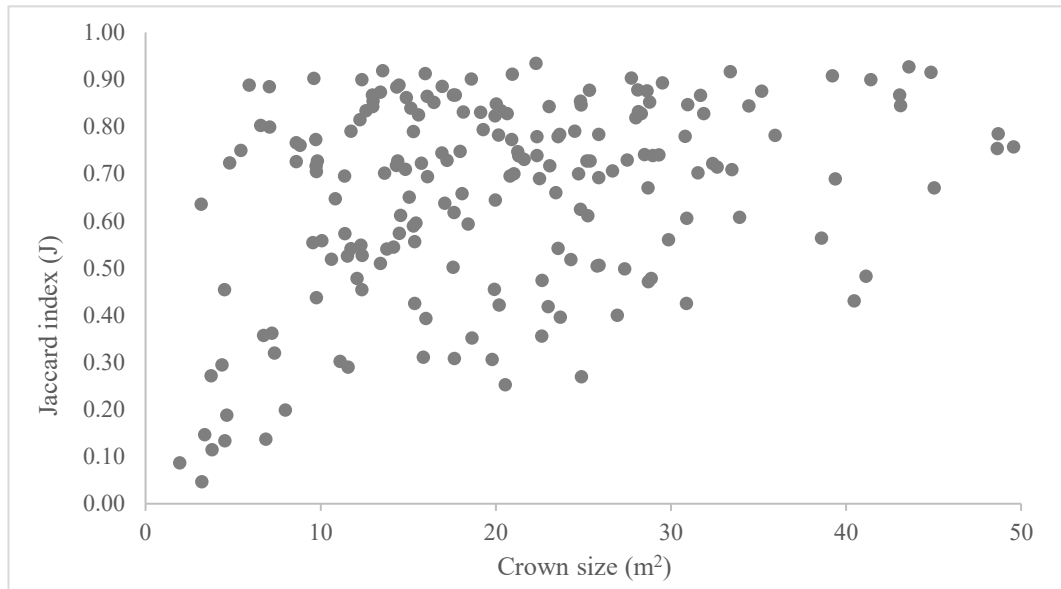
Parameter	OS	US	D	J	Centroids distance
daverage	0.084	0.284	0.227	0.661	0.830
min	0.000	0.002	0.037	0.047	0.021
max	0.533	0.953	0.674	0.935	4.077
median	0.056	0.214	0.181	0.718	0.458

Overall, the assessment pictures an optimistic scenario. The method used identifies the crowns' location (centroid distance is below 50 cm) as well as their extensions, with a segmentation mean error of 14% on the area. Figure 65 presents the median values of the Jaccard index plotted against the area of the reference crowns. It can be seen that the proposed method is very efficient on more massive crowns and prone to under-segmenting on smaller crowns. Indeed, the J index for the medium extension crowns (10-30 m<sup>2</sup>) is mostly above 0.5. The lowest values of J are recorded on tiny crowns (less than 5m<sup>2</sup>).

Concerning the comparison with the ITD based on spectral, textural, and elevation information, Table 32 and Table 33 respectively show the results from the visual evaluation and the RMSE for the other validation segmentation methodologies. Generally, the Hölder exponent performs better as an input feature for the segmentation ruleset. Regarding the visual assessments, at equal conditions, the results from the Hölder exponent outclassed the ones obtained from the other five validations datasets. For all methods, the producer's accuracy shows higher values. Indeed, the number of objects describing the reference dataset, in any case, is less than 228 (the number of segments from Hölder analysis). The segmentation generated from the spectral information has the highest F1 score within the validation datasets, although it is very far from the F1 score of Hölder exponent segmentation (0.734 of Hölder against the 0.348 of spectral bands). The CHM



methods show a larger number of Simple Omission, which might be attributable to the inaccuracies of photogrammetric DTM in areas with sloping.

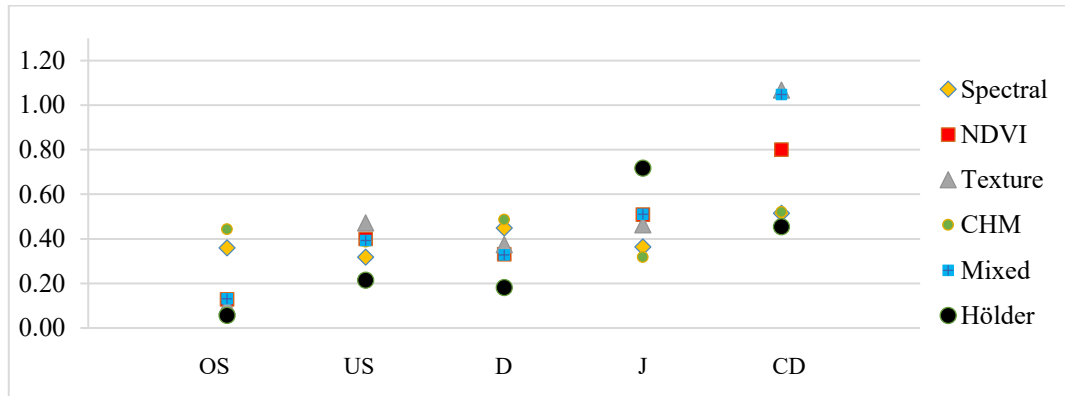


**Figure 65.** Distribution of the Jaccard index (y-axis) values according to the Crown size (x-axis)

The geometrical accuracy does not reflect the performance of the visual assessment. Indeed, even if quite-well performing in the F1 score, the spectral information does not provide an excellent geometrical match with the reference crowns, while the geometrical accuracy of the CHM method outperforms the Hölder exponent results. It is worth underlining that the CHM samples are only 162 reference objects due to the simply omitted crowns. Within the RMSE analysis, the multi-sourced approach's performances are the closest to the ones of the Hölder exponent.

Analyzing the indices' Median values in Figure 66, the Under-Segmentation (US) index does not reveal any significant difference between the Hölder exponent and other segmentation procedures. While on the Over-Segmentation (OS) analysis, we have similar values from Hölder, Sum Variance, and the NDVI. The mixed and the CHM approaches show the worst results in the completeness (D) and OS. The lowest value of the centroid distance is CHM. It appears that the results of the segmentation based on the NDVI and the multi-sourced inputs (CHM and Sum Variance textural analysis) are the closest to the ones of the Hölder exponent.

Nevertheless, no methods provided results as accurate as of the one of Hölder exponent by using the same simple segmentation.



**Figure 66.** The plot of the Over-segmentation index (OS), Under-Segmentation index (US), Completeness index (D), Jaccard index (J), and the distance between centroids (CD) calculated on the Hölder exponent dataset and the validation datasets (Spectral information, NDVI, Sum Variance textural information, CHM, and the mixed input data).

### 7.1.5. Discussion

The results of this very first application of multifractals analysis of UAV imagery for the identification of single tree crowns are promising. In a relatively short time (around 13 minutes), it was possible to analyze 38 hectares of forest using only one input layer. The Hölder exponent analysis results in a clear image of the single tree crowns (Figure 63). The pixels corresponding to the border of crowns present higher values of the Hölder exponent. This most probably led to the underestimation of the dimension of the crowns after the Contrast split segmentation. Nevertheless, growing the segmented objects of three pixels and smoothing them allowed us to limit such errors on most crowns.

The assessment of the classification reveals promising results. The visual evaluation suggests more than 73% of the F1 score, which is according to similar research. Indeed, the very recent application of (Qiu et al., 2020) reaches the accuracy of 76% in the VHR imagery segmentation but also higher than the Producer's and User's accuracy obtained by (Ke and Quackenbush, 2011). (Mohan et al., 2017; Vieira et al., 2019) 's works, respectively, reached 86% and 70% of the F1 score. It is worth mentioning that these comparisons should be interpreted with caution since many aspects can influence the goodness of the ITD. First, the high level of subjectivity affects visual evaluations. Secondly, the characteristics of the study areas have a dominant role in the results of the ITD. Indeed the illumination distortions due to the topography, the density, and the structure of the stand and the

dominant species, can influence the results (and the goodness) of the segmentation. To fairly compare the results, we should have at least similar case studies. Indeed the works mentioned above are realized in flat or low-sloped areas over different types of forest stands. The selected ruleset is an additional influencing factor: it must be underlined that the segmentation applied in this study is intentionally direct and can be further improved, especially in the refining phase.

As already mentioned, the visual evaluation is limited in the assessment of the goodness of the segmentation. Several other aspects regarding the shape and the size of the individual tree crowns can be considered. The results of the quantitative assessment are precise: the positions of the crowns, as well as their extension, are very well-identified. As evidence, the median value of the centroid distance is 45 cm. The area difference is not particularly relevant since the RMSE represents only 14% of the average crown area. Thanks to the smoothing process, there is an evident match between the segmented and reference objects' borders (the RMSE on the perimeter is almost 3 m). Although the validation indicates a good segmentation, it is essential to underline the difficulty of the manual segmentation of references: even for the human eyes, the identification of single trees is not immediate. This is a relatively common weakness of ITD (and more generally segmentation) researches. The RMSE of the perimeter has been calculated by Yurtseven et al. in their ITD research (Yurtseven et al., 2019). They obtain 6 m RMSE on the perimeter metric, even though they had the chance to identify the crowns on 1.2 cm/pixel RGB orthomosaic, as an additional demonstration of the subjectivity and complexity of the reference dataset identification. Compared to the existing works of ITD and segmentation, the Hölder exponent provides results perfectly in line with the literature.

The tendency of the proposed method to under-segmenting more than over-segmenting is evident also from the comparison of US (0.284) and OS indices (0.084). The Jaccard indicator is 72%, which results in line with other research, despite the high variability of the delineation of the reference dataset. (Hussin et al., 2014) applied the OS and US indicators to assessing tree segmentation using satellite imagery of 2 m resolution, and obtained comparable values for both under-segmentation and over-segmentation. Although in their work, they faced the opposite situation: over-segmentation errors are dominant in under segmentation ones. (Clinton et al., 2010; Persello and Bruzzone, 2010) obtained very similar OS and the US too, even though both studies are focused on the segmentation (and classification) of satellite imagery in urban areas. The 0.18 median value resulting from the D index mirrors the values in literature, and it is a relatively good result. The literature reports values between 0.31 and 0.42. Again, these metrics and

comparisons should be interpreted with caution since they are the results of segmentation from satellite imagery, and that does not include the extraction of single tree crowns. Finally, the Jaccard index, or Intersection over Union index, values vary between 0.05 and 0.95, with 0.72 as the median value.

On the same segmentation process, Hölder exponent segmentation results clearly outclass the others from spectral, textural, and CHM information. From this first application, it emerged that Hölder exponent can facilitate the ITD from UAV VHR imagery. Applying a basic segmentation process, we obtained satisfying results in line with the literature, but in a relatively short time and with one elevation-independent input layer only. With this approach, the ITD from optical imagery of densely forested areas might be more accurate than simple spectral and elevation-based analysis. Naturally, this work should not be interpreted as an attempt to discredit ITD from spectral and CHM dataset, but as an alternative and computational low-demanding solution to ITD.

The purpose of the current study was to determine the local Hölder exponent connected with multifractal theory and use it to describe VHR UAV optical imagery and the detection of individual single tree crowns. Although multifractals analysis has been applied in image processing in many different fields, from the medical to satellite remote sensing, their use on UAV imagery has not been confirmed. The high radiometric variability is typical of the VHR datasets that often introduced noise, reflected in imprecision in automatic segmentation and classifications. This aspect was reduced by the multifractal analysis and the single tree crowns clearly emerged. The Hölder exponent makes the segmentation easier and simply based on the threshold of the local contrast. The validation results are generally satisfying and in line with similar research realized on optical and LiDAR datasets. The main detected errors were classified as under-segmentation problems.

Unfortunately, as far as we know, little research on ITD applies quantitative methods similar to the ones we used to assess the segmentation. Indeed, a strong limit in the assessment of ITD is the subjectivity in the definition of the reference dataset. Nevertheless, the obtained results confirm the Hölder exponent applied to VHR imagery as a potentially powerful tool in the ITD. The analysis required a relatively short time and low computational power. Additionally, RGB and NIR sensors mounted on UAVs are systems that are becoming cheaper and easily operable. The present study lays the groundwork for future research into ITD from VHR optical imagery. Since this is its very first application, several aspects still need to be addressed and further investigated. Our focus area was characterized by the only presence of conifers, which crown present fractal patterns from a nadiral view. We might have very different results on broadleaves forests.

Moreover, we worked on Hölder exponent only and it would be interesting to explore additional measures in different forest types and try to work with different spatial resolutions, spectral bands and parameters.

Additionally, it may be worth testing different neighborhood sizes to calculate the Hölder exponent to verify its influence on the analysis. It is worth mentioning that multifractal descriptors can be applied in parallel with the DEM-based method by defining the treetops from the CHM and the delineation of the crown's boundary with segmentation from the multifractal analysis. This may help to ease up the process with an optical sensor on the Individual Tree Crowns detection. Among the others, some of the most interesting applications of the Hölder-ITD might be for the update of forestry inventories at the local scale and the multi-temporal monitoring of specific forest indicators (and parameters) related to the crown size. Additional application of this methodology might be on VHR satellite imagery. Several additional analyses and tests can still be conducted.

## 7.2. Satellite

During the last years, LC classification has taken significant steps forward: a wide range of free satellite medium-high optical imagery, specific classification algorithms, many processing platforms and machines with more and more high computational power are now available (Carrasco et al., 2019; Rizeei et al., 2016; Sidhu et al., 2018). Besides today's achievements, we still face some major constraints in LC classification, distinguished from environmental constraints and technical constraints (see paragraph 2.2, page 14). Among the technical constraints, the low temporal resolution of satellites is one of the most popular. However, it has been partially overcome by introducing medium-high resolution satellites that increase the free data available and make possible integrating the datasets from different acquisitions. However, data integration and high-spatial-resolution require managing a large amount of data and a large amount of storage and significant computing power and time (Carrasco et al., 2019). Managing satellite datasets requires considerable data storage capability, and the high spatial resolution further increases this requirement. Indeed, the antinomy between spatial resolution and computational power is another pervasive technical constraint. During the last few years, some geographic cloud computing platforms that allow the analysis and storage of geographic data were born. These services (such as Google Earth Engine) decrease the computational and storage limits of satellite data processing (Kumar and Mutanga, 2018). The atmospheric disturbance and the high seasonal variability are some of the leading environmental constraints in LC classification along with

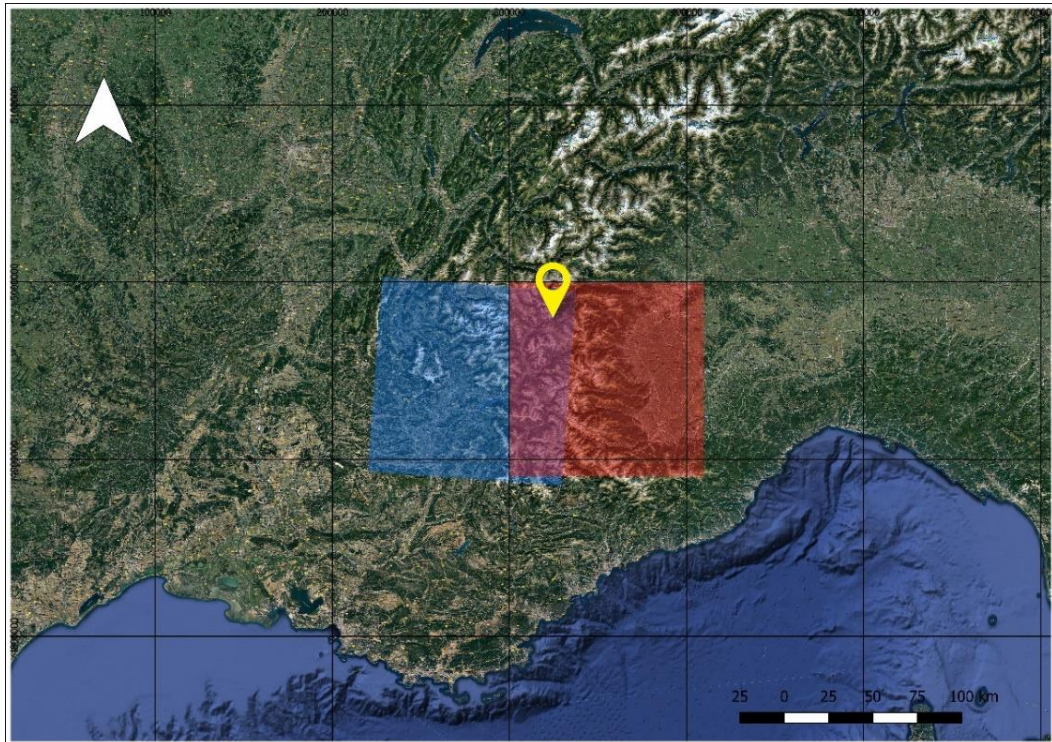
the topography variation. The topography strongly influences the spectral values in satellite imagery, especially in the case of steep areas. Indeed, the substantial variability in the reflectance and the spread shadows are the main effect of the topography on satellite imagery, which may complicate the classification (Dorren et al., 2003). This is particularly true in narrow valleys of mountainous areas, where some mountainside are permanently shadowed in winter months. The LC classification of mountainous areas is affected by other major environmental constraints due to climatic conditions. For example, the snow cover prevents the classification in the winter season, and the orographic rains and clouds, which mechanisms are influenced by the terrain (Houze, 2012), lower the possibility of accurate classifications. Combining these factors makes the generation of the land cover maps of mountainous areas, particularly challenging and generally recognized as fairly-low accurate (Dorren et al., 2003; Itten and Meyer, 1993).

In this paragraph, a specific methodology for the classification of the Land Cover in mountainous areas using Sentinel 2, 1C-level imagery is proposed. Several analyses and tests were carried out to pursue the best optimization for the entire classification process. The classification considers some specific high-altitude mountainous classes: clustered bare soil areas that are particularly prone to erosion; glaciers; and solid-rocky areas. The methodology tries to overcome the above-mentioned environmental limitations, and it consists of a pixel-based multi-epochs classification using a random forest algorithm. The analysis was performed in Google Earth Engine (GEE) environment because of its high computational speed and the large dataset of satellite imagery it makes readily available. Appendix B show the GEE code.

### **7.2.1. Data collection and pre-processing**

The images regarding the entire Sentinel-2 (both Sentinel-2A and Sentinel-2B) activity of sensing were filtered by location according to the extension of Cesana Torinese case study. The tiles must satisfy two parameters: the cloud cover percentage, which must be less than 10% over a single scene, and by the sensing period. Only images sensed during summertime (from June to August) were selected to minimize the effect of the shadows and avoid snow cover. Level 2A and Level 1C of processing were considered (see paragraph 6.3.2, page 129). The time-filter reduced the data available from level 2A (i.e., Sentinel-2 highest level of processing product that geometrically and atmospherically corrected): only ten images from level 2A satisfied the filter criteria against 29 images of level 1C. Therefore, to ensure a larger classification dataset, 1C level dataset was used (Table 35). It is worth mentioning that the study area is located in the overlapping area

between tile T31TGK and tile T32TLQ, as Figure 67 shows. Both tiles were considered for the analysis.



**Figure 67.** Tiles T31TGK (western tile, blue) and tile T32TLQ (eastern tile, red). The study area Cesana Torinese indicated by the yellow pointer lies in the overlap between T31TGK and T32TLQ.

### *Atmospheric correction*

The atmospheric correction of satellite imagery is considered fundamental in remote sensing applications, especially in multi-temporal analysis (Hadjimitsis et al., 2004; Lantzanakis et al., 2017; Martins et al., 2017; Sola et al., 2018). The atmospheric correction removes the scattering effect of the Earth's atmosphere and it can be based on Radiative Transfer Models (Specific mathematical models that consider latitude, season, and atmospheric conditions) or on Image-Based Correction Techniques (that estimate atmosphere scattering using information and data within the image) (Hadjimitsis et al., 2004; Lantzanakis et al., 2017; Martins et al., 2017). The existing atmospheric correction models are analyzed and described in paragraph 5.1, page 94.

**Table 35.** Sentinel 2 level 1C and 2A images of the classification dataset

	Tile	Year	No.	Sentinel Image Identification Code
2A LEVEL	K	2017	0	20170818T103021_20170818T103421_T31TGK
		2018	1	20180719T103019_20180719T103020_T31TGK
		2019	2	20190604T103029_20190604T103616_T31TGK
			3	20190719T103031_20190719T103715_T31TGK
			4	20190803T103029_20190803T103728_T31TGK
			5	20190808T103031_20190808T103026_T31TGK
	6	20190818T103031_20190818T103539_T31TGK		
	Q	2017	7	20170818T103021_20170818T103421_T32TLQ
		2018	8	320180719T103019_20180719T103020_T32TLQ
2019		9	20190803T103029_20190803T103728_T32TLQ	
1C LEVEL	K	2017	0	20170704T103019_20170704T103637_T31TGK
			1	20170714T103019_20170714T103022_T31TGK
			2	20170818T103021_20170818T103421_T31TGK
			3	20170823T103019_20170823T103018_T31TGK
		2018	4	20180619T103019_20180619T103559_T31TGK
			5	20180719T103019_20180719T103020_T31TGK
			6	20180719T103019_20180719T103820_T31TGK
			7	20180729T103019_20180729T103815_T31TGK
		8	20180828T103019_20180828T103013_T31TGK	
		2019	9	20190604T103029_20190604T103616_T31TGK
			10	20190629T103031_20190629T103537_T31TGK
			11	20190704T103029_20190704T103317_T31TGK
			12	20190714T103029_20190714T103635_T31TGK
			13	20190719T103031_20190719T103715_T31TGK
			14	20190729T103031_20190729T103230_T31TGK
		15	20190803T103029_20190803T103728_T31TGK	
		16	20190808T103031_20190808T103026_T31TGK	
	17	20190818T103031_20190818T103539_T31TGK		
	Q	2017	0	20170704T103019_20170704T103637_T32TLQ
			1	20170714T103019_20170714T103022_T32TLQ
			2	20170818T103021_20170818T103421_T32TLQ
			3	20170823T103019_20170823T103018_T32TLQ
		2018	4	20180619T103019_20180619T103559_T32TLQ
			5	20180704T103021_20180704T103023_T32TLQ
6			20180719T103019_20180719T103020_T32TLQ	
7	20180828T103019_20180828T103013_T32TLQ			
2019	8	20190604T103029_20190604T103616_T32TLQ		
	9	20190619T103031_20190619T103536_T32TLQ		
	10	20190704T103029_20190704T103317_T32TLQ		
	11	20190729T103031_20190729T103230_T32TLQ		
	12	20190803T103029_20190803T103728_T32TLQ		



Usually, the Radiative Transfer Models are more accurate and, therefore, more applied. For example, for producing atmospherically corrected imagery of Sentinel 2 (level-2A), ESA applies the Sen2Cor Radiative Transfer model. For the time being, there is no atmospheric correction model to be applied to Sentinel 2-level 1C implemented in GEE.

This means that Sentinel 2 at 1C processing level cannot be easily atmospherically corrected using Radiative Transfer Models in GEE environment. This is a severe limit to the performing of multi-temporal analysis. To overcome this limitation, in this work, the author applied a linear model for the atmospheric disturbance reduction: Dark Object Subtraction (DOS) (Chavez, 1988), which is recognized to perform similarly to radiative transfer models on homogeneous surfaces such as grass, water, and bare soil (Lantzanakis et al., 2017). DOS correction consists of subtracting the minimum value of the scene to the entire image. The application also considered the low values on each tile's borders, which are usually errors, and cut them off by applying a metric buffer on the edges of the image.

DOS methods are generally less accurate than Radiative transfer Models, mainly if applied to multi-temporal datasets because DOSs are sensitive to intense light and weather variations. However, the selected Alpine dataset is composed of imagery of a short time range, which has very similar weather and scene-illumination conditions. Thus, the DOS correction method should be accurate enough for this application. Moreover, its effects on the final results are expected to be weak because it classifies each epoch of the dataset separately. A significance analysis to evaluate DOS correction's suitability to this Land Cover classification was carried out. Specifically, the same images atmospherically corrected with two different methods (level 2A and the DOS-corrected) and the non-atmospherically corrected images (level 1C) were compared.

The sample for the significance analysis is composed of 1/5 of the entire images dataset. Namely, it constituted 2 tiles for each study year (2017, 2018, 2019) sensed in the same day, as Table 36 reports. All analyses were performed in Qgis and MATLAB environments in WGS84/32N, EPSG:32632 coordinate system. Tile K images were converted from WGS84/31N to WGS84/32N. Ten bands for each image (Table 37) were taken into consideration for the analysis. By using point sample tool plugin of Qgis 3.4.8, 213 points (randomly placed in same period scenes) were extracted from the three datasets: DOS-derived images, S2A images, and 1C images. Using Matlab, each analyzed DOS-corrected image was compared to the corresponding one of 1C and 2A correction.

**Table 36.** List of datasets used for the Dark Object Subtraction (DOS) accuracy evaluation.

Year	Id code	Name
2017	I4_2017_K	20170818T103021_20170818T103421_T31TGK
2017	I5_2017_Q	20170818T103021_20170818T103421_T32TLQ
2018	I16_2018_K	20180828T103019_20180828T103013_T31TGK
2018	I17_2018_Q	20180828T103019_20180828T103013_T32TLQ
2019	I28_2019_K	20190803T103029_20190803T103728_T31TGK
2019	I29_2019_Q	20190803T103029_20190803T103728_T32TLQ

**Table 37.** Bands of Sentinel-2 imagery considered in the DOS accuracy analysis.

Band	Wavelength (nm)	Channel name
2	490	Blue
3	560	Green
4	665	Red
5	705	Vegetation Red Edge
6	740	Vegetation Red Edge
7	783	Vegetation Red Edge
8	842	NIR
8A	865	Vegetation Red Edge
11	1610	SWIR
12	2190	SWIR

The following analysis of atmospheric corrections was performed

1. Difference ( $\Delta_{1C-EE}$ ) between 1C level ( $DN_{i,j}^{1C}$ ) and Earth Engine DOS ( $DN_{i,j}^{EE}$ ) for band  $n$  of test point ( $i,j$ )

$$\Delta_{1C-EE}(n) = DN_{i,j}^{1C} - DN_{i,j}^{EE} \quad [24]$$

2. Difference ( $\Delta_{1C-2A}$ ) between 1C level ( $DN_{i,j}^{1C}$ ) and DOS ( $DN_{i,j}^{2A}$ ) for band  $n$  of test point ( $i,j$ )

$$\Delta_{1C-2A}(n) = DN_{i,j}^{1C} - DN_{i,j}^{2A} \quad [25]$$

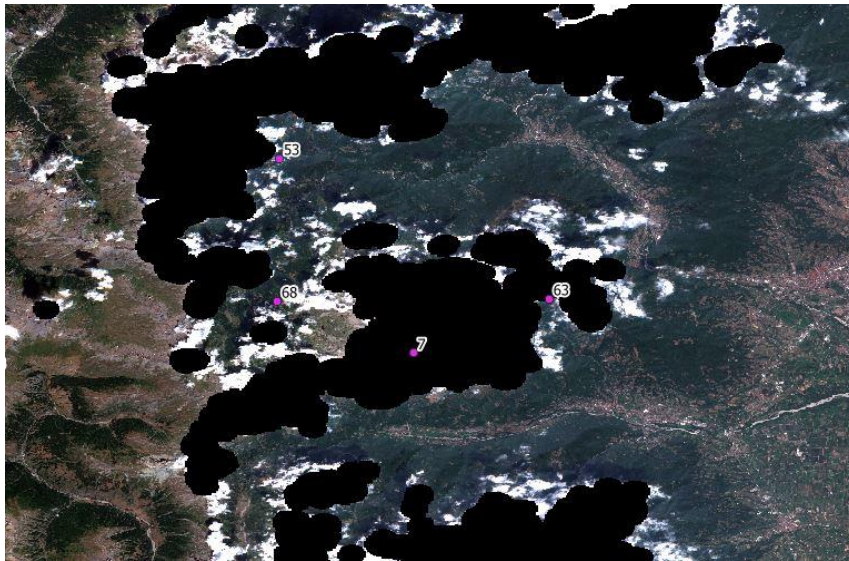
3. Difference ( $\Delta_{2A-EE}$ ) between 1C level ( $DN_{i,j}^{2A}$ ) and Earth Engine DOS ( $DN_{i,j}^{EE}$ ) for band  $n$  of test point ( $i,j$ )

$$\Delta_{2A-EE}(n) = DN_{i,j}^{2A} - DN_{i,j}^{EE} \quad [26]$$

4. Distribution, linear trend line, Root Mean Square Error (RMSE) and significance for each sample of points 1, 2, and 3, grouped by band  $n$ ;

5. Comparison of spectral signatures for each Corine Land Cover (CLC) class calculated for 2A, DOS, 1C.

The 0 values of DOS and 2A Digital Numbers were considered outliers since they record the null values of cloud masking. Furthermore, too bright pixels (Digital number over 1000) were considered outliers too because of not properly masked clouds (Figure 68).

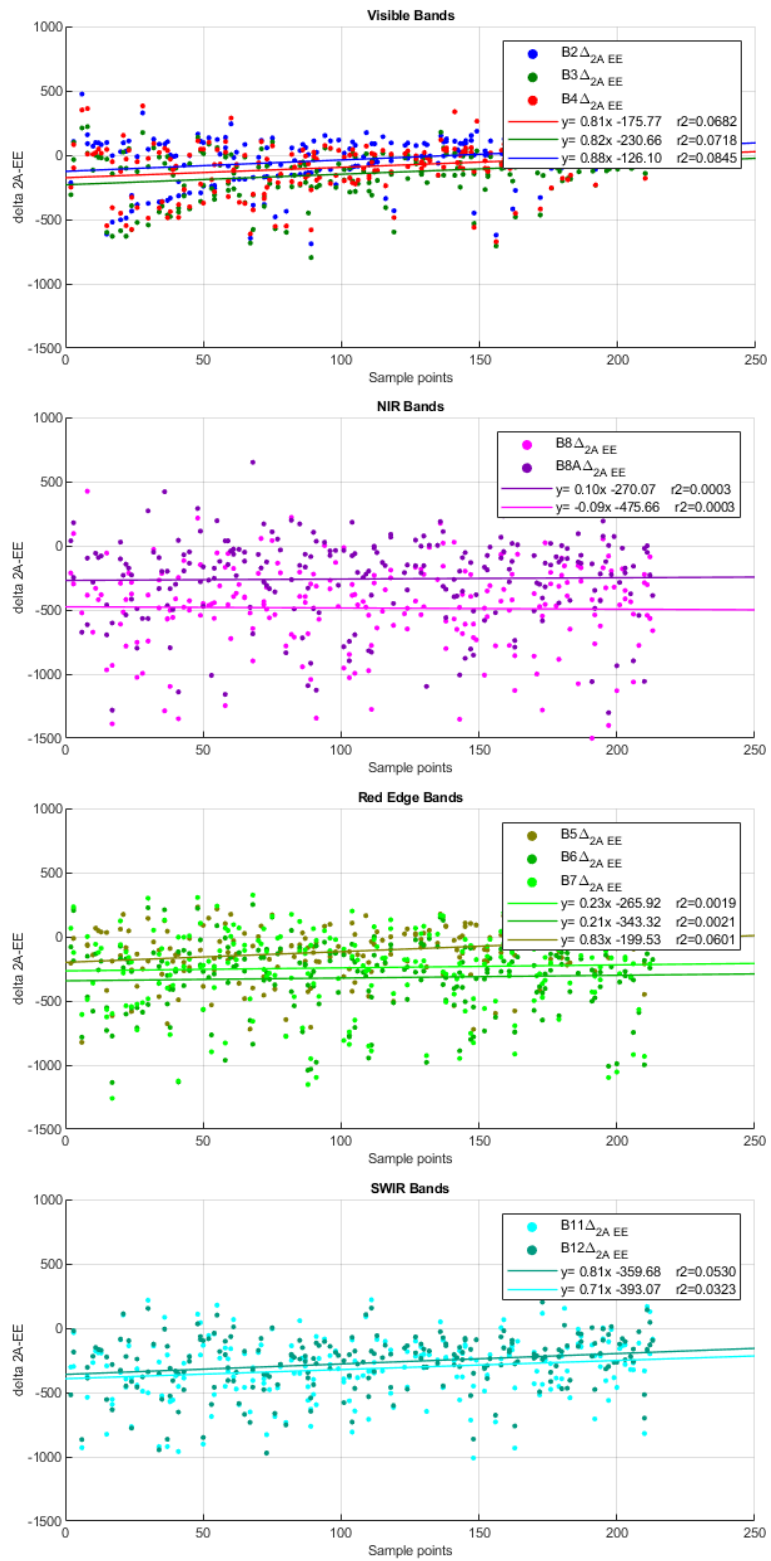


**Figure 68.** Example of outliers. The test points 7 and 63 are placed on the cloud-masked area (Digital Number 0), while point 68 is located on non-masked clouds due to the cloud-masking algorithm's inaccuracy, and it has Digital Number over 1000.

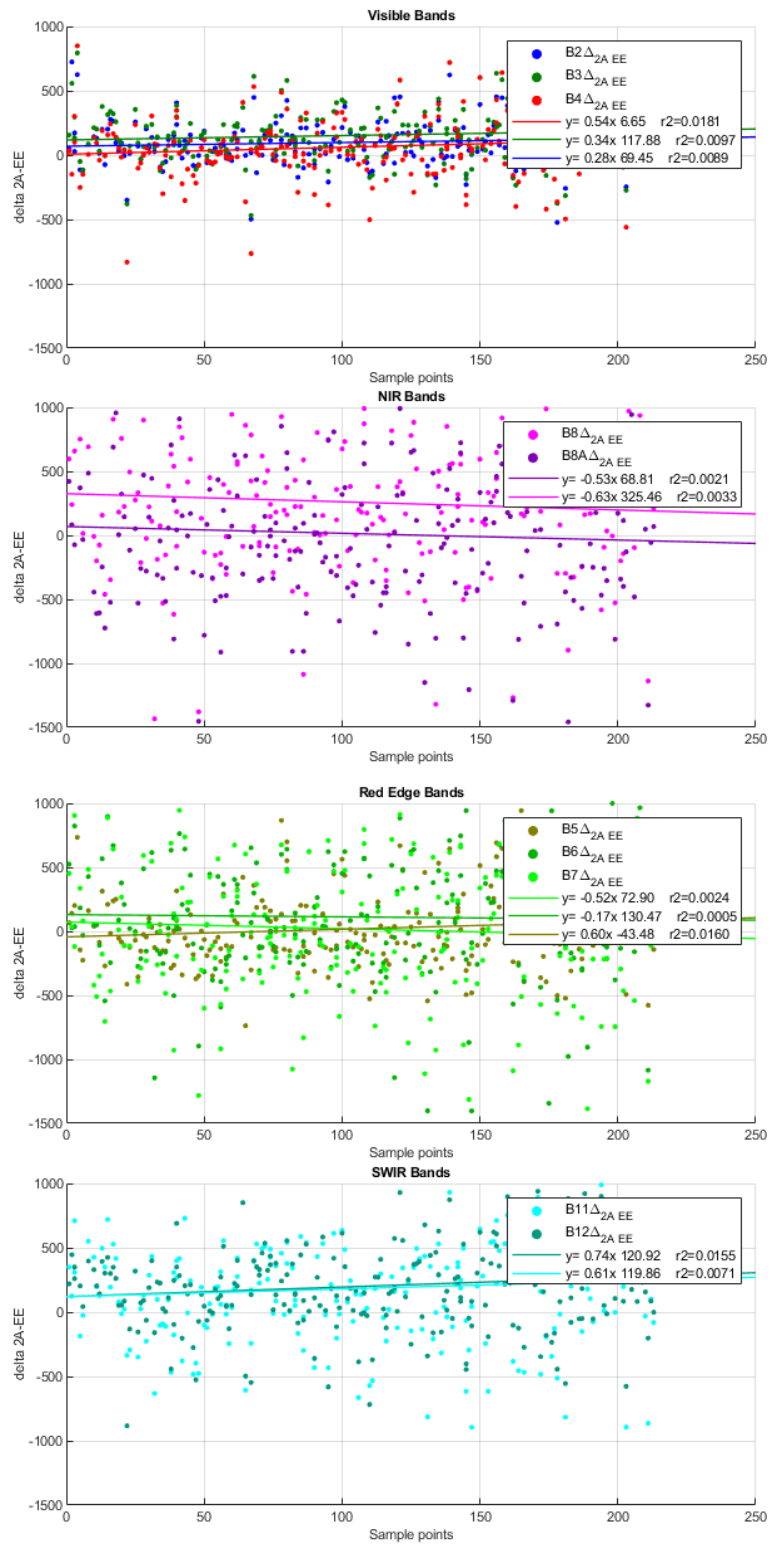
The distributions of the differences for points were plotted grouped by the spectral band. The trend lines and the dispersion of Earth Engine DOS (EE) and 2A datasets were calculated. Figure 69, Figure 70, and Figure 71 show the plots of  $\Delta_{2A-EE}(n)$  respectively for 2017, 2018 and 2019. Figure 72 shows the aggregated results. The distribution are represented in different graphs for the visible, red-edge, NIR, and SWIR bands. The  $r^2$  unadjusted was calculated for each distribution.

2017

**Figure 69.**  
 Graphs of  $\Delta_{2A-EE}$  of  
 2017. The  
 distributions are  
 represented in  
 different graphs for  
 the visible, red-edge,  
 NIR, and SWIR  
 bands.

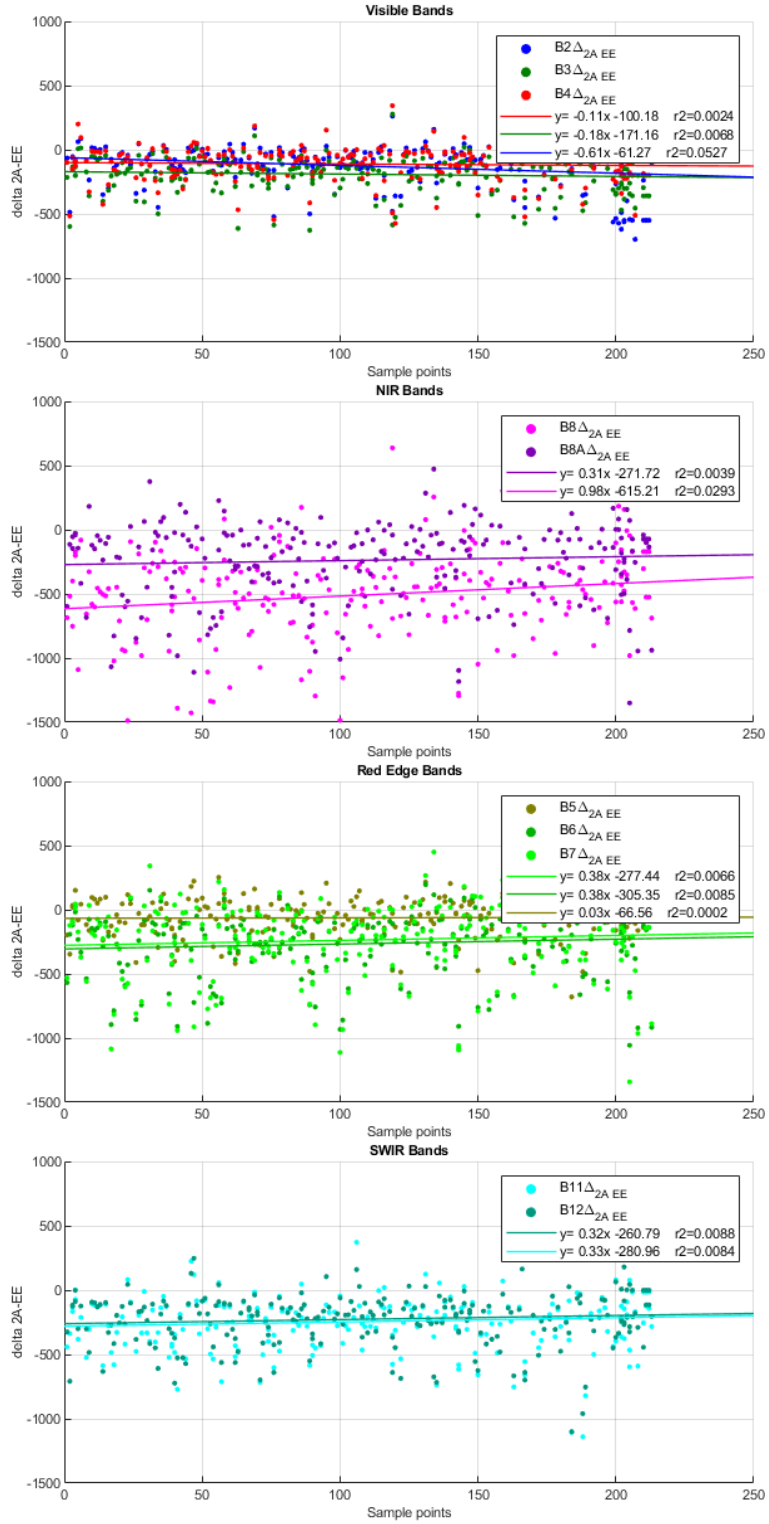


**Figure 70.** Graphs of  $\Delta_{2A-EE}$  of 2018. The distributions are represented in different graphs for the visible, red-edge, NIR, and SWIR bands.



2019

**Figure 71.**  
Graphs of  $\Delta_{2A-EE}$  of  
2019. The  
distributions are  
represented in  
different graphs for  
the visible, red-edge,  
NIR, and SWIR  
bands.



The c show high dispersion in all the samples, although, as clearly visible in Figure 72, it is particularly low in bands 6, 7, 8, and 8A. The marked difference between bands 6, 7, 8, and 8A also emerged from the visual comparison between 1c, 2a, and DOS spectral signatures (Figure 73).

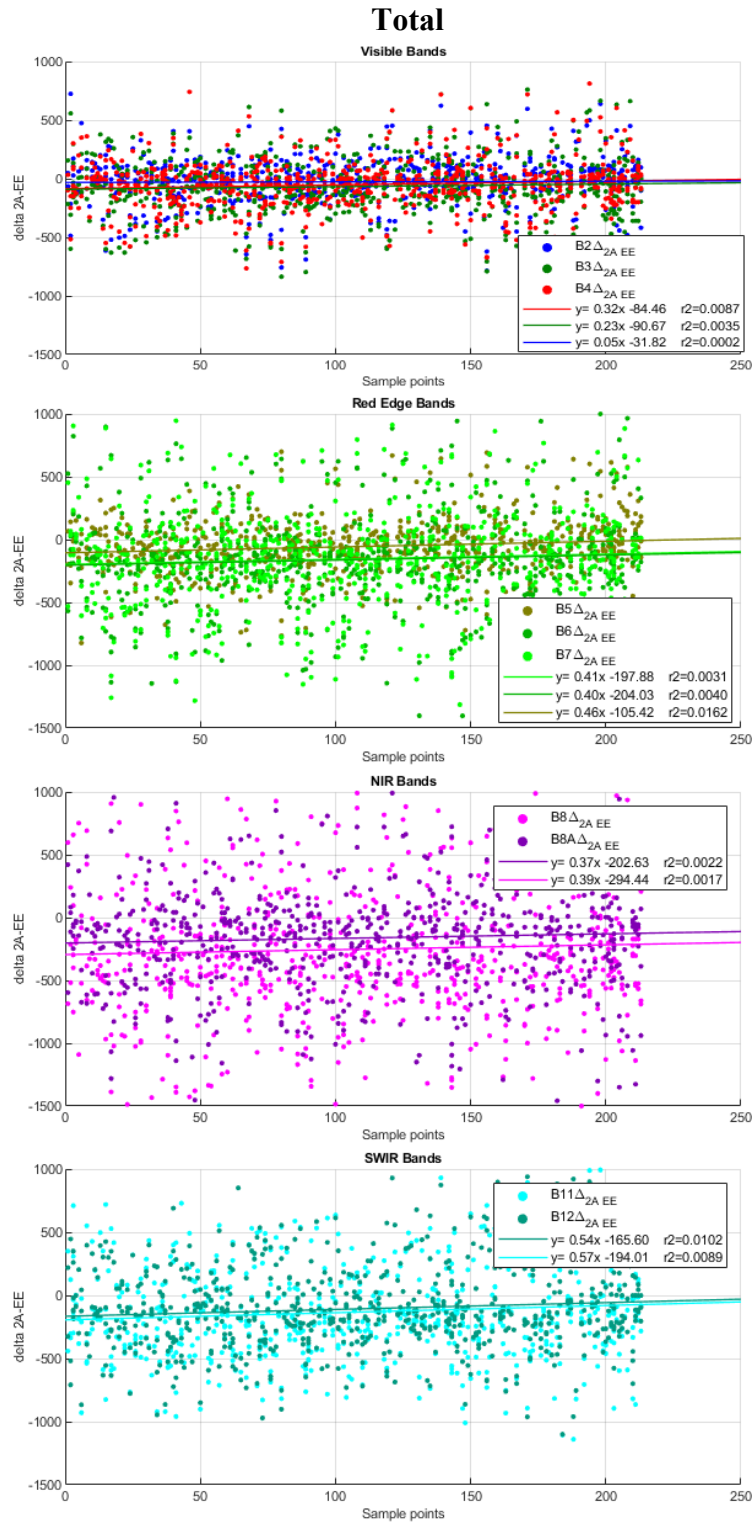
**Table 38.**  $r^2$  values for 2017, 2018, 2019 and aggregated (total) distributions of  $\Delta_{2A-EE}$ .

$r^2$	2017	2018	2019	total
B2	0.0845	0.0089	0.0527	0.0002
B3	0.0718	0.0097	0.0068	0.0035
B4	0.0682	0.0181	0.0024	0.0087
B5	0.0601	0.0160	0.0002	0.0162
B6	0.0021	0.0005	0.0085	0.0040
B7	0.0019	0.0024	0.0066	0.0031
B8	0.0003	0.0033	0.0293	0.0017
B8A	0.0003	0.0021	0.0039	0.0022
B11	0.0323	0.0071	0.0084	0.0089
B12	0.0530	0.0155	0.0088	0.0102

A great distance of DOS from other variables was detected in visible bands, especially in band 2 (Blue). The blue band is the most affected by atmosphere interferences. Other remarkable distances are shown in band (NIR) for 2A from 1C and DOS. The other bands have non-significant differences.

The final analysis was performed in the overlap area of Q and K tiles in the same sensing period to evaluate the correction methods' robustness and replicability. Thirty-five sample points were randomly located in the area of overlap of K and Q tiles. Reasonably, a general pixel with  $LAT, LON$  coordinates in K and Q tiles and sensed at the same time should have an approximately equal DN value, at least for 1C data values.

Unexpectedly, this is not true since some differences were recorded. In order to check the statistical significance of differences between the overlapping points in 1C, 2A, and DOS atmospheric corrections, was performed a Kolmogorov-Smirnov test on the visible and infrared bands (2, 3, 4, 8) that shows the highest differences between the two tiles (Figure 73).



**Figure 72.** Graphs of  $\Delta_{2A-EE}$  of 2017, 2018, and 2019. The distributions are represented in different graphs for the visible, red-edge, NIR, and SWIR bands.



The Kolmogorov-Smirnov test (K-S test) was selected because it is a non-parametric test applied on Gaussian and non-Gaussian distributions reliable also on a small dataset (like in this case, 35 observations for each band). The Null hypothesis was that *DN values from tile k* and *DN values from tile Q* are from the same continuous distribution (equation 27).

$$DN_{i,j}K \in f(DN) \text{ and } DN_{i,j}Q \in f(DN) \quad [27]$$

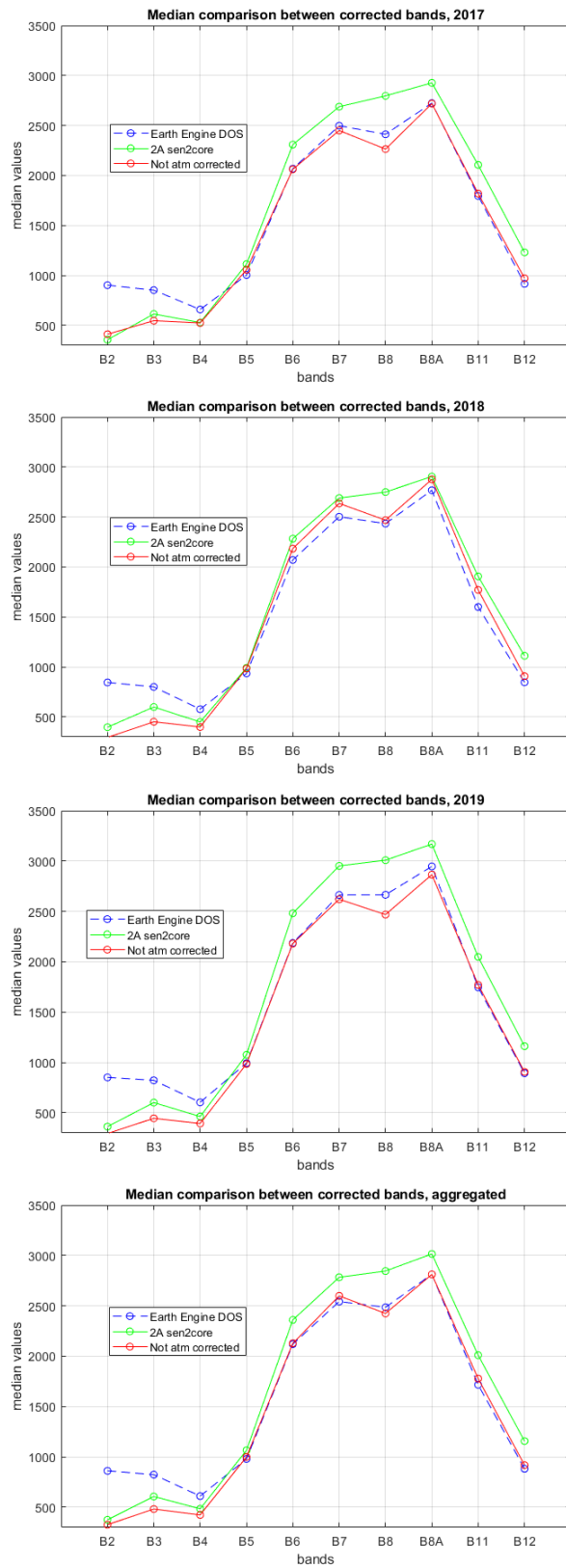
When the significance factor (h) is equal to 1, the null hypothesis is rejected, which means that DN values from tile k and DN values from tile Q are from *different* distributions (at a given alpha) and their difference is *significant*. Otherwise, when h is equal to 0, the rejection of the null hypothesis is failed, which means that DN values from tile k and DN values from tile Q are from the same distributions (at a given significance level, alpha), thus their difference is *not significant*. No significant difference was detected in any analyzed dataset: not in single year analysis nor total (all years aggregated) analysis (Table 39).

From the test performed, no remarkable differences were detected between the linear and energy transfer models. The main concerns may regard the blue band (2); indeed, it was not considered in the classification. The DOS application did not negatively affect the final results because the method we propose classifies each epoch of the dataset separately.

**Table 39.** Results of the Kolmogorov-Smirnov significance test carried out for the overlap area

	2017, alpha 0.005		2018, alpha 0.005		2019, alpha 0.005		Total, alpha 0.005	
	p	h	p	h	p	h	p	h
B1-1c	0.999	0	0.967	0	0.839	0	0.969	0
B2-1c	0.962	0	0.967	0	0.967	0	0.994	0
B3-1c	0.962	0	0.967	0	0.999	0	0.994	0
B7-1c	0.999	0	0.967	0	0.967	0	0.994	0
B1-ee	0.999	0	0.839	0	0.839	0	0.706	0
B2-ee	0.825	0	0.999	0	0.999	0	0.910	0
B3-ee	1.000	0	0.999	0	0.999	0	0.994	0
B7-ee	0.999	0	0.640	0	0.640	0	0.818	0
B1-2a	0.999	0	0.441	0	0.839	0	0.588	0
B2-2a	0.962	0	0.839	0	0.839	0	0.706	0
B3-2a	0.962	0	0.967	0	0.967	0	0.588	0
B7-2a	0.999	0	0.967	0	0.839	0	0.910	0

**Figure 73.** Spectral signature obtained by the median value of each point of vegetation (from CLC) of Earth Engine DOS, 2A and 1C datasets



### ***Topographic correction***

The topographic correction allows the variation in the reflectance derived by the terrain's inclination and the sun elevation (Poortinga et al., 2019; Shepherd and Dymond, 2010). This pre-processing phase is crucial in mountainous areas because of the steep mountainsides and the consequent alteration of reflectance values. The entire dataset was corrected by applying a semi-empirical correction. The code was initially implemented in GEE by Patrick Burns and Matt Macander and then adapted to the dataset. The correction is based on a semi-empirical method that takes into consideration not only the topography of the area (as for the empirical methods) but also the solar angle (both zenith and azimuth) (Shepherd and Dymond, 2010). The topographic correction is based on sun-canopy-sensor with a semi-empirical moderator (c) (SCSc) method (Poortinga et al., 2019; Soenen et al., 2005). A Digital Elevation Models (DEM) to detect the area's slopes and the solar position information (i.e., the sun inclination and sun irradiance) are the input data. These data are available from the satellite images' metadata, while elevation information was extracted from the Shuttle Radar Topography Mission (SRTM) digital elevation data with 30m spatial resolution that is available in the GEE catalog (Farr et al., 2007).

The topographic correction's effectiveness and goodness were checked by comparing the illuminated and non-illuminated mountainsides of the topographic corrected and non-topographic-corrected datasets. The validation was run on two datasets created *ad hoc*. One composed of 1C-level topographically corrected K tiles and original 1C-level images for 2017, 2018, and 2019. One hundred pairs of sample points were placed within the study area on illuminated and non-illuminated correspondent areas with the same land cover. The points were manually placed using as help i) CLC and, ii) Hillshade raster generated from USGD 30m DTM (Figure 74).

The following measures were calculated:

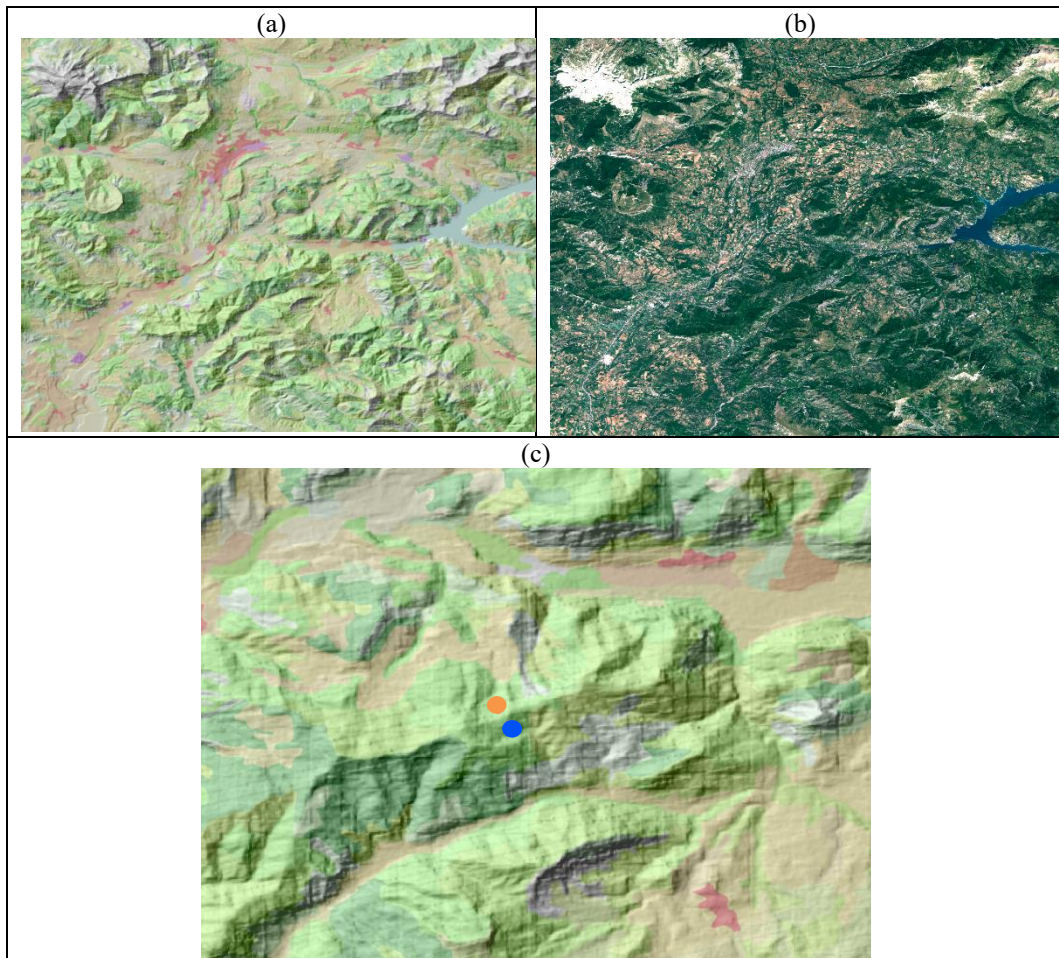
The absolute value of the difference between each illuminated point and its non-illuminated correspondents  $\Delta_{il-nil}$  for each of 1C –topographically corrected (TC) point for of band  $n$ :

$$TC\Delta_{il-nil}(n) = |DN_{i,j}^{TC-il} - DN_{i,j}^{TC-nil}| \quad [28]$$

The absolute value of the difference between each illuminated point and its non-illuminated correspondents  $\Delta_{il-nil}$  for each of 1C –topographically original points (1C), of band  $n$ :

$$1C\Delta_{il-nil}(n) = |DN_{i,j}^{1C-il} - DN_{i,j}^{1C-nil}| \quad [29]$$

Comparison of  $TC\Delta_{il-nil}(n)$  and  $1C\Delta_{il-nil}(n)$ : based on the assumption that the topographic correction should reduce the difference in the shadow of two mountainsides having the same land cover, where considered as positive validation (i.e., correct functioning of topographic correction algorithm) when  $TC\Delta_{il-nil}(n)$  is smaller than  $1C\Delta_{il-nil}(n)$ .



**Figure 74.** a) RGB visualization of a sample area; b) hillshade+CLC visualization; c) example of a pair of points on two mountainsides (orange and blue points).

It is worth mentioning that since the points placements are based on CLC (MMU 25 ha), it may be possible that the points do not sample the same LC. The results show 88% of topographic correction effectiveness. Again, the worst results are recorded for the Blue band (band 2). Table 40 reports the results of the validation.

**Table 40.** Percentage of validated topographic correction for 1C level dataset

Percentage of verified points per 1c level											
Bands	B2	B3	B4	B5	B6	B7	B8	B8A	B11	B12	total
2017	57%	74%	68%	83%	76%	71%	73%	74%	76%	70%	82%
2018	62%	74%	67%	82%	77%	76%	75%	77%	81%	77%	90%
2019	65%	79%	72%	78%	75%	73%	75%	75%	79%	72%	90%
Entire dataset	61%	76%	69%	81%	76%	74%	75%	76%	79%	73%	<b>88%</b>

The correction validity on sen2cor-corrected data was checked. Equations 28 and 29 were used to calculate and then compare  $TCA_{il-nil}(n)$  and  $2A\Delta_{il-nil}(n)$ . Table 41 shows the obtained results. From this analysis, the topographic correction on Sentinel-2 appears less effective on 2A level imagery than on 1C level imagery.

**Table 41.** Percentage of validated topographic correction for 2A level dataset

Percentage of verified points per 21A level											
Bands	B2	B3	B4	B5	B6	B7	B8	B8A	B11	B12	total
2017	33%	54%	40%	32%	56%	55%	59%	74%	78%	99%	77%
2018	36%	38%	34%	43%	53%	61%	54%	57%	53%	52%	65%
2019	48%	48%	43%	54%	65%	66%	60%	65%	66%	59%	70%
Entire dataset	39%	47%	39%	43%	58%	61%	58%	65%	66%	70%	<b>71%</b>

### ***Features extraction***

The diversification of the input information is crucial for a good classification. For example, textural elements can facilitate Land cover class discrimination (Lewiński et al., 2015) and histogram-based ones (Drzewiecki et al., 2013). Ten radiometric features, five histogram-based features, 19 textural, and one edge-detector feature were computed (Table 42). Specifically, the texture metrics from the Gray Level Co-occurrence Matrix in the 7x7 neighborhood of each pixel of 8 (Near InfraRed, NIR) were computed (Connors et al., 1984; Haralick et al., 1973; GEE, 2020). The derivate features improved the goodness of the classification but required high computational power. Indeed GEE exceeded the memory limit by running the entire code: the filtering of the Sentinel-2 data catalog, the topographic and atmospheric corrections of the filtered features, the derivative bands

computation for each epoch, and the classification itself. Thus, to slim out the classification process and reduce the classification's computational time, the correlation analysis and the layer's importance in the classification analysis were realized.










**Table 42.** Derivative features are calculated for each epoch. They are divided into 4 groups: histogram-based, radiometric, edge extractor, and textural.

	Feature	Formula/note
Radiometric	Alteration	B11/B12
	Chlorophyll IndexRedEdge CRE	$(B9/B5)-1$
	Enhanced Vegetation Index EVI	$2.5*((B9-B5)/((B9+6*B5-7.5*B1)+1))$
	HUE	$\text{Arctan}((2*V5-B3-B1)/30.5)*(B3-B1)$
	Normalized Difference Vegetation Index NDVI	$(B8-B4)/(B8+B4)$
	Soil-Adjusted Vegetation Index SAVI	$((B8-B4)/(B8+B4+L))*(1+0.5)$
	Soil Composition Index SCI	$(B11-B8)/(B11+B8)$
	Specific Leaf Area Vegetation Index SLAI	$B9/(B5+B12)$
	Wetness Index WET	$(0.1509*B2)+(0.1973*B3)+(0.3279*B4)+(0.03406*B8)-$ $(0.7112*B11)-(0.4572*B12)$
	Triangular Vegetation Index TVI	$0.5*(120*(B8-B3))-(200*(B4-B3))$
Edge	Sob	Sobel edge extractor
Histogram- based	Var	Variance
	Mean	Mean
	Skew	Skewness
	Kurt	Kurtosis
	Contr	Contrast; measures the local contrast of an image
Textural GLCM	Entr	Entropy
	Asm	Angular Second Moment; measures the number of repeated pairs
	Corr	Correlation; measures the correlation between pairs of pixels
	Var	Variance; measures how spread out the distribution of gray-levels is
	Idm	Inverse Difference Moment; measures the homogeneity
	Savg	Sum Average
	Svar	Sum Variance
	Sent	Sum Entropy
	Ent	Entropy. Measures the randomness of a gray-level distribution
	Dvar	Difference variance
	Dent	Difference entropy
	Imcorr1	Information Measure of Corr. 1
	Imcorr2	Information Measure of Corr. 2
	Maxcorr	Max Corr. Coefficient.
	Diss	Dissimilarity
	Inertia	Inertia
	Shade	Cluster Shade
Prom	Cluster prominence	

### 7.2.2. Methods

The classification is realized using 1260 training points on 9 classes (Table 43).

**Table 43.** Classes of Land Cover considered in this work.

No.	Class	Description	
1	Coniferous forest	Conifers trees areas	
2	Broadleaves forest	Broadleaves trees forests	
3	Grasslands	Includes pastures and moors	
4	Water	Internal waters	
5	Clustered bare soil areas	Clustered rocks, bare soil, and sparse vegetation. Generally in high slope mountainsides. Highly prone to erosion.	
6	Solid-rocky areas	Continuous non-clustered rocky cover. Typical of Alpine mountain peaks.	
7	Urban areas	Buildings, roads, artificial infrastructures.	
8	Glaciers	Perennial snow/ice cover. In the Alpine zone, only in areas above 3000 m a.s.l.	
9	Agricultural lands	Areas interested by agricultural activities that require tillage or present rows of fruit trees/bushes.	

### ***Training and test datasets***

The training and test datasets were generated semi-automatically through randomly sampling (stratify samples) a base layer generated from existing land cover classifications. Besides accelerating the training and test dataset creation, this approach also ensured the minimization of the subjectivity in the identification of the training points (Gromny et al., 2019). The information of ESA High-resolution Layers (VHR) 10m (Forest cover, Imperviousness, Grassland and Water and Wetness, <http://land.copernicus.eu/>) (Lefebvre et al., 2016), CORINE Land Cover (CLC) (Copernicus, 2020), and RUSLE 2015 at 100 m from ESDAC (Panagos et al., 2015) constitute the base layer. The classes of CORINE land cover, as well as other input data, were converted in classes of interest, as Table 44 shows. The base layer had 20m spatial resolution and nine classes. Using stratified sampling algorithm of Gdal, 280 pixel per class were selected from the base layer (2520 pixels in total). Each selected pixel was visually checked and eventually modified according to vicinity and representativeness criteria. The vicinity of the training pixels of same class was avoided ensuring, and the strict correspondence between class definition and training pixel evaluated (representativeness). The dataset was spilt in 50-50 for the training and the validation of the classification.

**Table 44.** Input datasets for the training layer and the translation to the reference classes.

<b>Reference classes</b>	<b>VHR mosaics 2015</b>	<b>ESDAC 2015</b>	<b>CLC</b>
Coniferous forest	Forest Type	-	312
Broadleaves forest			311
Grasslands	Grassland	-	321-231
Water	Water and Wetness	-	511,512
Clustered bare soil and sparse herbaceous vegetation areas	-	RUSLE (> 20 t/he/yr)	323-331
Solid-rocky areas	-		332
Urban areas	Imperviousness Density	-	111-133
Glaciers	-		335
Agricultural lands	-		211-244



### ***Feature selection: Correlation analysis***

The slimming out workflow was designed to reduce the computational time without losing accuracy. First, a correlation analysis was performed between the radiometric derivative features and the original bands to avoid information redundancy.

The correlation between bands was analyzed using July 2017 as a reference. The analysis was based on the DN values randomly sampled within the classes. 4 was used as a reference band. Correlation coefficients equal to 1 indicate a total correlation—this analysis considered highly-correlated variables greater or equal to 0.85 (dark green in Table 46). Then, the correlation analysis between textural bands was carried out. Since the textural bands were much less correlated to each other than the radiometric bands, the importance of textural predictors in the classification was computed by running the classification each time, excluding one different predictor. The Overall Accuracies of these classifications were considered as the importance value of the removed predictor. This indirect strategy to estimate each feature's importance within the classification was necessary because the evaluation of predictors' importance is not implemented in GEE. The importance analysis was performed on July 2017 tile. The OA of the classification computed with all textural features is 0.825. The features that exclusion caused the increasing on the OA of 0.01 points were considered less important (negatively affecting the classification). To further reduce the computational effort, the bands were normalized and then transformed into integer values (int16). Since running the normalization on GEE required too much memory was realized a “pseudo-normalization”. For each was identified the multiplicative factor that allows obtaining integer values no bigger than 32767 (max values for signed integer data format). The pseudo-normalization does not affect the classification.

### ***Classification and aggregation***

Each image was separately classified using the machine learning algorithm random forest with 50 rifle decision trees per class and four as the minimum size for terminal nodes. The same training dataset was used for each image. This means that for one image were sampled, 37 DN values in correspondence with every training point. This datum was used to train the classifier and finally to apply it to the starting image. The results are 13 classifications that were aggregated. Five different aggregation methods were tested by comparing the Overall Accuracy. The most accurate was the modal value (Table 45). Thus, the classifications were aggregated according to the most frequent pixel value between 1 and 9 (*no data* values excluded) to obtain the area's final classification. The aggregation allowed

us to minimize the single classifications' mistakes and take out from the final result, the *no data* values of the cloud masking (Nowakowski et al., 2017).

**Table 45.** Aggregation methods comparison.

Aggregation method	Overall Accuracy value
mode	0.945
median	0.940
max	0.564
min	0.647

### *Accuracy assessment*

The accuracy assessment is based on 1260 pixels and consisted in the computation of the error matrix and the derived accuracy measures for each single-epoch classification and the aggregated one. The error matrix-derived measures are the overall accuracy, the producer's accuracy, the user's accuracy, and the F1 score.

## **7.2.3. Results and discussion**

### *Feature selection*

Table 46 shows the results from the correlation analysis between radiometric-based derivative features. The correlation coefficient ranges between 0 (no correlation, light green) and 1 (total correlation, dark green) (**Table 46**). The radiometric derivative features with a correlation coefficient larger than 0.85 were excluded from the classification dataset: SLAI, NDVI, Alteration, and SAVI. The correlation between the original bands was not taken into consideration. Nevertheless, Sentinel bands 1, 2, 9, 10 were excluded from the analysis as too influenced by the atmospheric component. The final bands considered were: B4, B2, B3, B5, B6, B7, B8, B8A, B11, B12, CRE, EVI, SCI, HUE, WET, TVI. The correlation between the textural features is not particularly remarkable (**Table 47**): only the GLCM Contrast feature appears highly correlated to Dissimilarity, Variance, and Shade. Table 48 reports the results of the importance analysis of textural information: only the Shade and Prominence negatively affect the classification, as their removal increased the overall accuracy of 0.01. They were excluded from the classification dataset. The correlation and the importance of the predictors' analysis on the bands resulted in 7 highly-correlated and low-importance bands removed from the dataset (2 textural-based).

**Table 46.** Correlation analysis of radiometric-based features. The dark green cells indicate a correlation coefficient >0.85.

	B4	B2	B3	B5	B6	B7	B8	B8A	B11	B12	NDVI	ALT	CRE	EVI	SCI	HUE	SAVI	SLAI	WET	TVI
B4	Dark Green																			
B2	Dark Green	Dark Green																		
B3	Dark Green	Dark Green	Dark Green																	
B5	Dark Green	Dark Green	Dark Green	Dark Green																
B6	Light Green	Light Green	Light Green	Light Green	Dark Green															
B7	Light Green	Light Green	Light Green	Light Green	Dark Green	Dark Green														
B8	Light Green	Light Green	Light Green	Light Green	Dark Green	Dark Green	Dark Green													
B8A	Light Green	Light Green	Light Green	Light Green	Dark Green	Dark Green	Dark Green	Dark Green												
B11	Light Green	Light Green	Light Green	Light Green	Light Green	Light Green	Light Green	Light Green	Dark Green											
B12	Dark Green	Dark Green	Dark Green	Dark Green	Light Green	Light Green	Light Green	Light Green	Dark Green	Dark Green										
NDVI					Light Green	Light Green	Light Green	Light Green	Light Green	Light Green	Dark Green									
ALT					Light Green	Light Green	Light Green	Light Green	Light Green	Light Green	Dark Green	Dark Green								
CRE					Light Green	Light Green	Light Green	Light Green	Light Green	Light Green	Dark Green	Dark Green	Dark Green							
EVI	Light Green	Light Green	Light Green	Light Green	Light Green	Light Green	Light Green	Light Green	Light Green	Light Green	Light Green	Light Green	Light Green	Dark Green						
SCI	Light Green	Light Green	Light Green	Light Green	Light Green	Light Green	Light Green	Light Green	Light Green	Light Green	Light Green	Light Green	Light Green	Light Green	Dark Green					
HUE					Light Green	Light Green	Light Green	Light Green	Light Green	Light Green	Light Green	Light Green	Light Green	Light Green	Light Green	Dark Green				
SAVI					Light Green	Light Green	Light Green	Light Green	Light Green	Light Green	Light Green	Light Green	Light Green	Light Green	Light Green	Light Green	Dark Green	Dark Green		
SLAI					Light Green	Light Green	Light Green	Light Green	Light Green	Light Green	Light Green	Light Green	Light Green	Light Green	Light Green	Light Green	Light Green	Dark Green	Dark Green	
WET	Light Green	Light Green	Light Green	Light Green	Light Green	Light Green	Light Green	Light Green	Light Green	Light Green	Light Green	Light Green	Light Green	Light Green	Light Green	Light Green	Light Green	Light Green	Light Green	Dark Green
TVI	Light Green	Light Green	Light Green	Light Green	Light Green	Light Green	Light Green	Light Green	Light Green	Light Green	Light Green	Light Green	Light Green	Light Green	Light Green	Light Green	Light Green	Light Green	Light Green	Light Green

The final results are 37 bands in each one of the 13 images. The following bands used: 'B3', 'B4', 'B5', 'B6', 'B7', 'B8', 'B8A', 'B11', 'B12', 'CRE', 'EVI', 'SCI', 'HUE', 'WET', 'TVI', 'entr', 'sob', 'var', 'mean', 'skew', 'kurt', 'asm', 'contrast', 'corr', 'idm', 'maxcorr', 'var', 'svar', 'dent', 'imcorr2', 'savg', 'imcorr1', 'diss', 'sent', 'ent', 'dvar', 'inertia'.

**Table 47.** Correlation analysis of textural and edge-detector features. The dark green cells indicate a coefficient >0.85.

	Asm	Contrast	Corr	Idm	Maxcorr	Var	Svar	Dent	Imcorr2	Savg	Imcorr1	Diss	Sent	Dvar	Shade	Prom	Ent	Inertia
Asm	Dark Green																	
Contrast		Dark Green																
Corr			Dark Green															
Idm				Dark Green														
Maxcorr					Dark Green													
Var						Dark Green												
Svar							Dark Green											
Dent								Dark Green										
Imcorr2									Dark Green									
Savg										Dark Green								
Imcorr1											Dark Green							
Diss												Dark Green						
Sent													Dark Green					
Dvar														Dark Green				
Shade															Dark Green			
Prom																Dark Green		
Ent																	Dark Green	
Inertia																		Dark Green

### ***Classification***

It was not possible to perform the entire classification in one GEE script. Thus, it was carried out using some expedients. First were performed the filtering and the correction. The pre-processed dataset was then exported to the GEE personal Asset. A new script was written for the computation of the classifications in which was imported the pre-processed dataset. The slimming out tests were realized in a separate script. Finally, the single classifications were converted into int8 data format, stacked in a single image, and exported (Figure 75). Figure 76 provides some examples of the classification results in high-altitude areas (left) and lowlands (right).

**Table 48.** Importance analysis of the textural features. The features that exclusion caused increasing on the OA of 0.01 points were considered less important (negatively affecting the classification).

Excluded features	OA value
<b>All features</b>	<b>0.825</b>
entr	0.829
sob	0.826
asm	0.824
contrast	0.819
corr	0.822
var	0.822
idm	0.823
savg	0.822
svar	0.824
sent	0.827
ent	0.825
dvar	0.826
dent	0.822
imcorr1	0.824
imcorr2	0.829
maxcorr	0.825
diss	0.828
inertia	0.825
shade	<b>0.834</b>
prom	<b>0.835</b>

### ***Intra-validation***

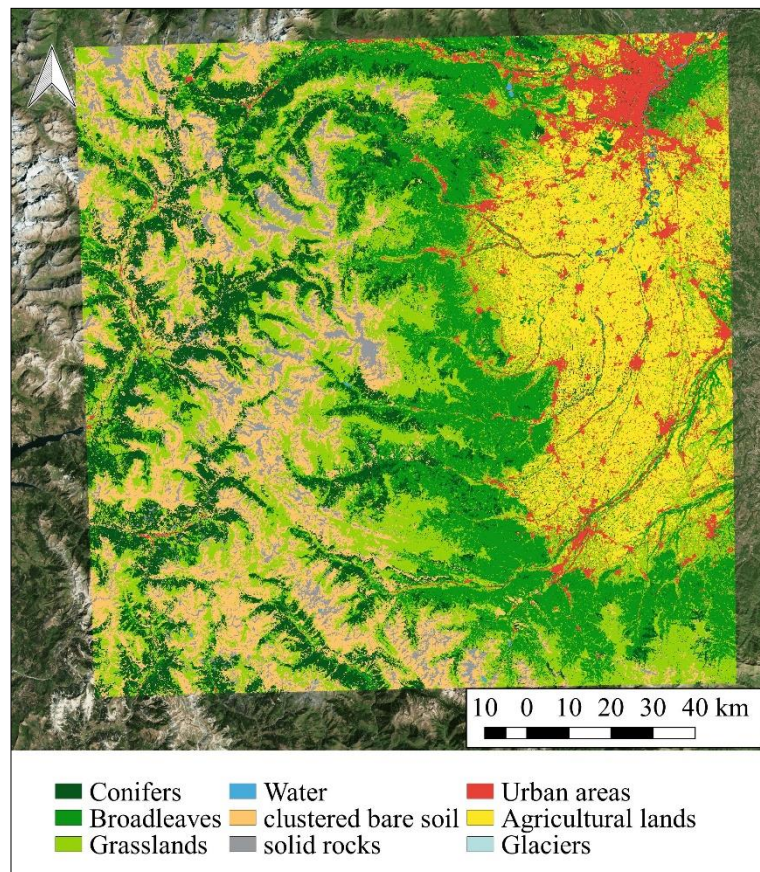
0.661 to 0.747 in the case of only radiometric derivative features and from 0.791 to 0.900 for the radiometric and textural derivative features. Table 49 reports the accuracy assessment results deriving from the classification of i) the Sentinel radiometric bands and the radiometric-based features, and ii) the Sentinel radiometric bands, the radiometric-based features, and the textural features. The F1 scores of clustered bare soil areas along with the OA accuracy values rapidly increase. The classification with the derivative features shows an overall accuracy of 86%. The OA of 94% deriving from the dataset with radiometric and textural features results from the aggregation of 13 images.

Figure 77 reports the accuracy and the F1 score for every single classification. The accuracy values have very unstable results within the classification scene. This is partially due to the incorrect classification of the areas covered by clouds (*no data*) and the pixels in the masked area's immediate surroundings that may suffer

from radiometric alteration for cloud proximity but not detected by Sentinel cloud masking.

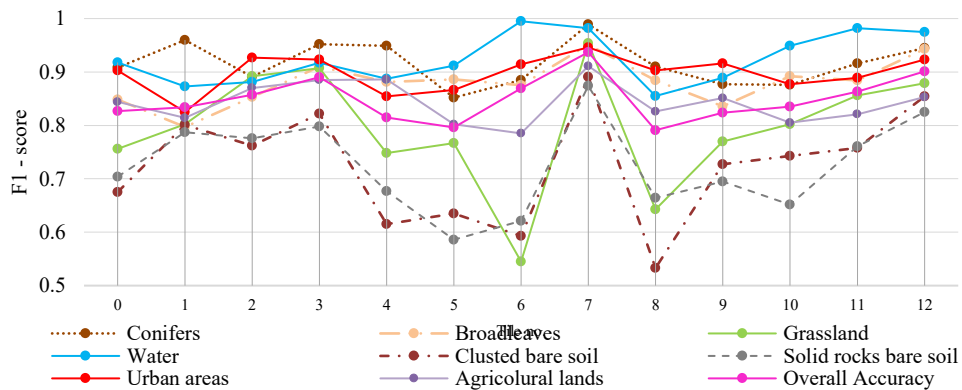
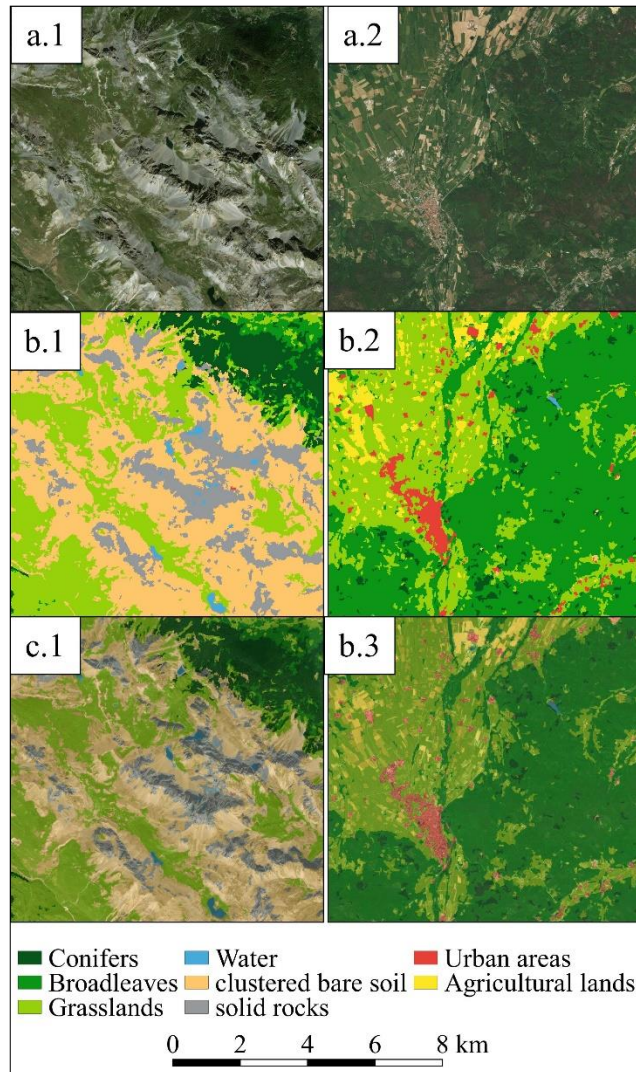
**Table 49.** Producer's and User's accuracies and F1 score for the classification with and without textural features.

	Conifers	Broad-leaves	Grassland	Water	Clustered bare soils	Solid rocky areas	Urban areas	Agri-cultural lands	OA
<b>Radiometric bands and radiometric-based features</b>									
PA	0.986	0.979	0.965	1.000	0.636	0.520	0.949	0.938	0.863
UA	0.986	0.979	0.993	0.971	0.250	0.829	0.936	0.964	
F1	0.986	0.979	0.979	0.986	0.359	0.639	0.942	0.951	
<b>Radiometric bands, radiometric-based features and textural features</b>									
PA	1.000	0.986	0.898	1.000	0.812	0.915	0.993	0.995	0.945
UA	0.993	1.000	0.993	0.979	0.957	0.771	0.950	0.946	
F1	0.996	0.993	0.943	0.989	0.879	0.837	0.971	0.970	



**Figure 75.** Classification of tile Q.

**Figure 76.** Some detail of the tile classification in high-altitude mountainous areas (left, scene 1) and lowlands (right, scene 2). Images a.1 and a.2 show the RGB orthophoto (Source: Bing Satellite); b.1 and b.2 shows the classification; c.1 and c.2 shows the overlapping of the orthophoto and the classification (low opacity).



**Figure 77.** The changes in F1-score for each class through the epochs (tile no., on the abscissae).

### **Replicability**

The replicability of the classification methodology was tested on the dataset of tile K and the overlapping area of tiles Q and K. The accuracy assessment from tile K Table 50 shows very similar results to the one of tile Q. It appears that on both tiles, the classes that describe the mountainous areas have lower F1 value. The accuracy assessment based on 700 test points (identified by stratify sampling the base layer described in 7.2.2) was realized for the overlapping area to check the stability of tiles K and Q's classifications in the most challenging areas (mountains peaks). Only 7 classes are present in the scene, but the rocky areas classes dominate the scene (Table 51).

**Table 50.** Producer's and User's accuracies and F1 score for the classification on tile K.

	Conifers	Broadleaves	Grassland	Water	Clustered bare soils	Solid rocky areas	Urban areas	Agricultural lands	Glaciers	Overall Acc.
PA	0.993	0.943	0.927	0.914	0.824	0.727	0.899	0.905	1.000	0.907
UA	0.979	0.950	0.907	0.993	0.771	0.836	0.829	0.886	0.974	
F1	0.986	0.947	0.917	0.952	0.797	0.777	0.862	0.895	0.987	

**Table 51.** Producer's and User's accuracies and F1 score for the classification on the overlapping area between tiles Q and K.

	Conifers	Broadleaves	Grassland	Water	Clustered bare soils	Solid rocky areas	Urban areas	Overall Acc.
PA	0.990	1.000	0.990	1.000	0.855	0.750	0.961	0.928
UA	1.000	0.980	1.000	0.970	0.949	0.870	0.730	
F1	0.995	0.990	0.995	0.985	0.900	0.806	0.830	

The filter for selecting only the summertime images with a very low percentage of cloud cover, on the one hand, ensured uniform illumination and atmospheric conditions; but on the other hand, impeded the use of Sentinel 2 highest processing level (2A). Besides, the classification of the 1C-level dataset achieved interesting results. The independent classification of each image and the frequency-based aggregation minimized the distortions and the errors derived from the topography



and the atmosphere. Moreover, the summertime filter reduced the variability in the meteorological and atmospheric conditions, allowing for a linear model of correction. Even if the pre-processing phase is consistent, it had a low impact on the methodology thanks to GEE cloud computing and the ease with which it is replicable in GEE. We faced some significant constraints in GEE related to the memory available for single users, the poor information regarding the available functions, and the lack of some useful functions (like layers importance). Nevertheless, it is a relatively young service that is continuously enriched with new functions and features, and our analysis was quite ambitious from the computational point of view.

Considering the results in detail, the derivative features considerably increased the goodness of the classification. It is interesting to note the role of textural bands in the discrimination of confusion between clustered soil class and solid-rocks class. Indeed, F1 scores of clustered bare soils jumped from 0.359 to 0.879 by adding the textural features to the classification (Table 49). Figure 77 clearly shows that the clustered bare soil and the solid-rocky areas are the classes with a lower F1 score in every single classification as evidence of the difficulty of separation of the two classes. Generally, a single classification accuracy shows a similar trend throughout the classes, such as image 6 (low F1 values) and classification no. 7 (high F1 values for all its classes) from Figure 77.

Regarding the aggregated classification, the overall accuracy achieves 0.945 with a clear improvement in clustered-rocky and solid-rocky areas (respectively F1-scores 0.827 and 0.890), proving the aggregation method's validity reduces the main errors from the single classifications (Table 49). The replicability analysis on tile K reported in Table 50 shows trends in clustered and solid rock classes close to the ones of tile Q. The overall accuracy of K is 0.907. The training dataset can cause the difference between K and Q overall accuracy, and it is negligible. It is worth mentioning that in tile K there is one class more: glaciers. Indeed, glaciers' land cover is relatively small and present only in K tile (in the Écrin National Park, FR). Even if the glaciers classification is excellent, some small glaciers were not detected. The overlapping area between K and Q provides promising results if we consider that the most confusing classes clustered and rocky areas are the dominant LC (Table 51).

On the other hand, the few classes present in the area provide better values of Overall accuracy. Generally, the solid-rocks are frequently misclassified as urban areas. This is attributed to the high spectral similarity of the classes and their similar textural characterization. A frequent error in Alpine areas is the classification of buildings with rocky roofs as solid-rocky areas, the same for the small rivers where

the water flow during the summertime is reduced. Also, some pixels classified as water are detected in mountainous areas, probably due to shaded rocky/snowed areas.

This study proposes a simple method for the classification of Land cover in mountainous areas in GEE platform, which includes some steps to reduce the computational effort and the time for the classification. The methodology minimizes the error introduced by the atmospheric component and the terrain inclination using only images captured during a short time range in limited cloud cover conditions and by applying atmospheric and topographic corrections. The textural derivative features played a crucial role in distinguishing the most challenging classes (clustered bare soil and solid-rocky areas). An additional positive value of the methodology is the aggregation method. Indeed, by considering the modal value of the single classifications, the final accuracy was significantly raised. All the aspects allowed us to reach good accuracies in mountain areas. Since the entire classification is performed in GEE, it can be easily modified and updated. Further investigation needs to be carried on regarding the DOS validation, for example, by considering different linear atmospheric correction models.

## Chapter 8

### Case study B: Sirba River in South-west Niger

In the Sirba River basin have been investigated the villages of Larba Birno and Tourè. These two villages are located on the river's left bank and have been selected for the analysis because particularly prone to floods and temporary water stagnation, also known as Temporary Surface Water Bodies (TSWB). In these villages were realized three classifications, one from satellite imagery and two from UAV. Namely, in this chapter will be analyzed the realization of:

- i) classification of UAV imagery for the identification of Temporary Surface Water Bodies (TSWB);
- ii) classification of UAV imagery for the definition of Land Cover (LC)
- iii) classification of Satellite imagery for identification of LC.

Table 52 reports the three classifications' main characteristics in terms of spatial, temporal, and thematic resolution.

**Table 52.** Classifications that interest the South-Niger area.

No.	Classification	Temporal	Spatial	Thematic	Reference publications
i	UAV-TSWB	Low	Very High	High	(Belcore et al., 2019; Belcore et al., 2019)
ii	UAV-LC	Low	Very High	Medium	/
iii	SAT-LC	High	Medium	Low	/

## **8.1. Classification of UAV imagery for the identification of Temporary Surface Water Bodies (TSWB)**

Temporary surface water bodies (TSWB) in sub-Saharan areas have important socio-cultural values, providing freshwater for the population and many agro-pastoral services. Indeed, the TSWB, which are temporary pools, has a crucial role in maintaining biodiversity by providing nutrients and recovery for wild species (Haas et al., 2009; WHO, 2020). They provide freshwater, grazing areas, and other ecosystem services to pastoral communities (Haas et al., 2009; Hein, 2006). Nevertheless, in urban areas, they can be a threat to human health. The TSWB within villages and cities may have adverse effects on the population's health: pools or slow-flowing standing water fosters the development of insects, including the ones vectors of diseases (Robert et al., 2016). According to the World Health Organization (WHO, 2020), the TSWB may be a sanitation and hygiene (WASH) issue: inadequate provision of WASH can lead to an increased risk of several diseases, including diarrhoea, Hepatitis A, Cholera, Typhoid, and Shigella Dysentery, Intestinal helminths, Malaria and Trachoma (WHO, 2020). Where TSWB is close to latrine sanitation facilities, residuals can rise and create an insane living environment. Moreover, temporary water bodies can cover vast areas of cities and villages, hindering the practicability of road networks. In urban areas, TSWB issues can be managed through well-designed drainage systems or channel networks. Addressing the TSWB problem at the local level is fundamental to reduce the health risk.

The health risk deriving from the TSWB is linked to the floods. Stagnant water after a floods is very common. Indeed, flood events can overload the drainage and sewage management systems, causing the rise-up of water in the drains and creating pools of standing water enriched with organic waste favourable for mosquito breeding. This is well documented in developing countries, where infectious disease outbreaks have been reported following major flood events (Few et al., 2004).

In sub-Saharan Africa, surface water resources are characterized by high variability at inter and intra year level and conditioned not only by the weather conditions and the characteristics of the soil but also by the land cover and use (Descroix et al., 2013; Gal et al., 2017; Haas et al., 2011, 2009). Due to their spatial and temporal variation, TSWB can be easily missed in mapping activities (Haas et al., 2009) that are mostly realized via remote sensing from satellite (Gardelle et al., 2010; Haas et al., 2011, 2009; Robert et al., 2016). Many events can be studied by analyzing satellite imagery, but the extracted information may be ineffective for

small-scale and punctual-shaped phenomena. Remote sensing from satellite imagery is very useful in TSWB-related studies on a large scale (Gardelle et al., 2010; Haas et al., 2011, 2009; Robert et al., 2016), although limited at the local scale by temporal and spatial resolutions of satellites. Free satellite data are available at fixed time intervals (i.e., temporal resolution), preventing a complete analysis of the TSWB for lack of data regarding the study period or bad weather conditions (Remondino, 2011).

Recent works related to the detection of stagnant water rely on aerial imagery (Suduwella et al., 2017), which is becoming prevalent thanks to the spreading of Unmanned Aerial Vehicles (UAVs). UAVs have been employed in TSWB detection too. (Amarasinghe and Wijesuriya, 2020; Carrasco-Escobar et al., 2019) identified TSWB using radiometric sensors mounted on UAV. The radiometric information is still the most common type of data used for these applications. Nevertheless, it allows identifying the stagnant water land cover at the specific time of the flight. Even if very useful, the application is compromised by the survey period, the meteorological conditions, and the intensity of the TSWB phenomenon in the season (high inter and intraseasonal variation). For a proper TSWB identification with the purpose of flood-related health risk reduction, knowing the location and the maximum potential extension of the stagnant water bodies is fundamental. The maximum seasonal extension of TSWB depends on the soil characteristics (which define the soil infiltration and runoff), the land topography, and vicinity to the aquifer. From a topographic point of view, TSWB are depressions that, because of intense rainfall (especially in sub-Saharan areas), are recharged by water. Thus, the first step in the identification of TSWB is the detailed study of land morphology. In this framework, there is a need for new technologies and methods to rapidly localize depressed zones in urban areas that may become TSWB in case of intense precipitations.

Topographic depression is generally detected from Digital Elevation Models (DEMs). Since hydro-geomorphic applications depressions are commonly removed from DEMs because they are considered human artifacts that may alter water flow simulations (Lindsay and Creed, 2006), the scientific literature is rich in depression detection from DEMs (specifically Digital Terrain Models, DTMs). Many depression-detection applications are based on high-resolution (approximately 5-1 m/pixel) DTMs are generated by LIDAR techniques (Dhun, 2011; Lindsay and Creed, 2006; Vaze et al., 2010; Wang and Liu, 2006). The most recent studies are focused on the relation between DTM resolution and topographic depressions (Burdziej and Kunz, 2007; Liu and Wang, 2008; Vaze et al., 2010; Vesakoski et al., 2014; Yang Jun and Chu Xuefeng, 2013). As far as the author knows, very few

studies were realized on topographic depressions identification from Very High Resolution (VHR) DTMs ( $< 0.5\text{m}/\text{pixel}$ ) generated by aerial photogrammetry and *Structure from Motion* technique (see paragraph 3, page 103). The goal of this work is to classify the areas of potential water stagnation from UAV very high-resolution DEM, to validate the results through the comparison with radiometric analysis and ground inspections data.

### 8.1.1. Data collection

#### *UAV flight*

The data collection consisted of the acquisition of images in visible (Red Green Blue, RGB) and infrared (Near Infrared Green Blue, NGB) spectral resolution from Unmanned Aerial Vehicles (UAVs). Using a GNSS dual-frequency receiver, the Ground Control Point for the precise georeferencing of the UAV imagery was collected. The UAV system was provided by a Nigerian enterprise based in Niamey, Drone Africa Service (DAS)<sup>5</sup>. DAS uses self-constructed and no-brand drones. A fixed-wing UAV was built explicitly by DAS to be used in this survey (Figure 78). The flight was planned and automatically controlled by the *ArduPilot* software. Two optical sensors were mounted on the system: a Sony ILCE-5100 camera (its main characteristics are described in paragraph 6, page 119) and an experimental sensor created with a Raspberry Pi computer and two Raspberry Pi 2 cameras as illustrated in paragraph 6, page 119 and in (Belcore et al., 2019). The sensors were not simultaneously used because they were too heavy to be held up together by the UAV during the same flight. Furthermore, they had different characteristics, and each camera requires specific flight settings (i.e., height and speed of flight) to ensure imagery of similar Ground Sample Distance (GSD) and the same overlapping between the pictures. The Sony camera has 23.3 megapixels of resolution.  $3.91\text{ cm}/\text{pixel}$  images were obtained in about 20 minutes of flight at 280 meters above each village's ground.

Table 53 presents the characteristics of the flights. The Raspberry camera allows the collection of Near InfraRed (NIR) information and acquires information with 5 Megapixel resolution to obtain a Ground Sample Point (GSP) of  $6.1\text{ cm}/\text{pixel}$  images was necessary to reduce the height of flight to 130 meters above the ground. To cover the same area of the Sony flight, were necessary two flights of about 30 minutes, which is the maximum duration of the UAV battery. The surveyed area covered the Niger villages of Tourè and Larba Birno, as described in paragraph 1, page 112. Six UAV flights covering a surface of about 600 hectares were performed

---

<sup>5</sup> <http://drone-africa-service.com/>

in two days (Belcore et al., 2019). In particular, were covered 320 hectares on Larba Birno and 280 hectares in Tourè; the study area includes urban areas and rural areas surrounding the villages. 579 images on Larba Birno and 507 images on Tourè were collected with the Sony camera, while 993 pictures on Larba Birno and 636 pictures on Tourè with the Raspberry NIR (Figure 79). The UAV did not power the Raspberry Pi camera, and there was no interaction between the UAV and camera. Despite the critical conditions, the sensor provided satisfactory results.



**Figure 78.** Left: UAV system built by Drone Africa Service. Right: Detail of the UAV body. It is visible that the Raspberry Pi sensor is mounted on the UAV system. 3.5 inches screen and the GPS receiver.

**Table 53.** Main characteristics of the sensors and the flights performed on Larba Birno and Tourè.

Characteristics	Sony ILCE-5100	Raspberry PI
Resolution	23.3 MP	5MP
Bands sensor	RGB	RGBN
ISO settings	1/125	1/100
Shutter frequency	Automatically set by the navigation software	1 Hz
Lateral overlap	70%	70%
Longitudinal overlap	60%	60%
Number of flight to cover each village	1	2
Average duration of flight	30 minutes	30 minutes
Height of flight from the ground	270 m	120 m
GSD	2.5 cm/pixel	6 cm/pixel



Sony ILCE-5100

Raspberry PI

**Figure 79.** Sample pictures of the same area in Larba Birno acquired by Sony-ILCE-5100 and Raspberry Pi. The SONY picture (6000x3000 pixels) has a 2.5 cm/pixel resolution and is in RGB. The raspberry picture (2592x1933 pixels) has a 6 cm/pixel resolution, and it is visualized in NIR Green Red.

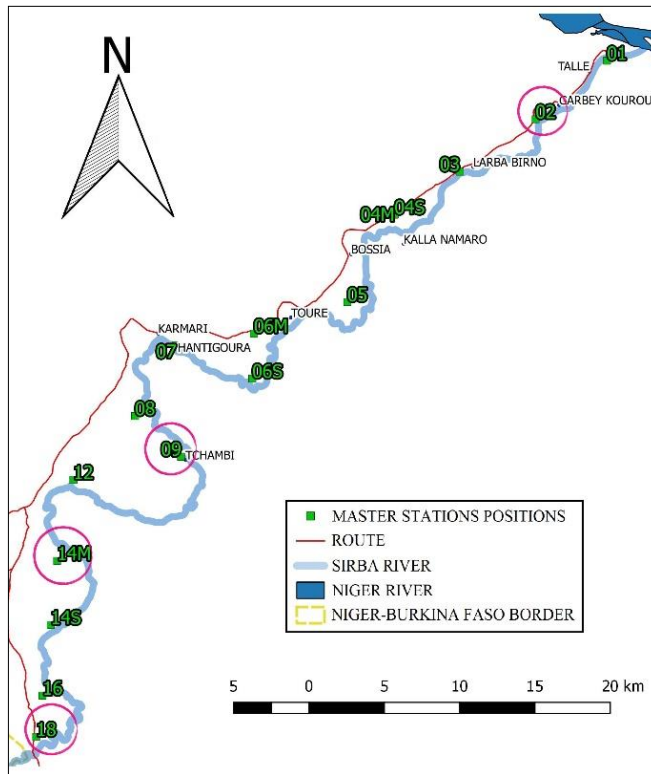
### ***GNSS survey***

In each village, a campaign of measure using two GNSS dual-frequency receivers, STONEX S10 models, in RTK rover-base modality was performed for georeferencing the data. The instruments were rented in Niamey. In RTK rover-base survey where the station master coordinates are unknown, are used two receivers: a GNSS receiver works as “master” station, storing the satellite-based measure of its position with a specific frequency (in this case, the rate was set to 1 Hz) and a receiver called “rover”, connected to the master receiver (during Sirba survey the transmission was via radio) that measures the points of interest based on its position concerning the master station (paragraph 3.1.5, page 42). The master station coordinates are estimated in post-processing using the Precise Point Positioning technique (PPP). The Up component was recorded in ellipsoidal heights and converted in orthometric heights using the EGM08 model (Pavlis et al., 2012). In Tourè, were measured 20 points, while in Larba Birno, were measured 16 points. The raw measurements were saved in the *Receiver Independent Exchange Format* (RINEX) 3.1 version with a sampling rate of 1s.

The services taken into consideration are the Canadian Spatial Reference System Precise Point Positioning tool (CSRS-PPP), the Automatic Precise Positioning Service (APPS), and the AUSPOS Online GPS processing service (AUSPOS). The precision, the convergence time (meant as the length of time required to reach centimeter-level positional solutions), and the structure and



condition of use of this paper's services. The data used for the comparison were collected in February 2018 along Sirba River (south-west Niger) in the ANADIA 2.0 project framework.



**Figure 80.** Section of Sirba River interested by the survey. The green squares identify the locations of the stations along the river. The circled ones are analysed in this contribute.

It was realized a topographic survey, which aimed to define the transversal sections along 100km of Sirba River (one section per km). Unfortunately, there are no CORS in Niger: the nearest ones are in Nigeria and Ivory Coast. Although the study area is close to the border between Niger and Nigeria, the CORS is more than 400 km from the Sirba region: this distance is too much to guarantee the requested accuracy. Besides, the closest known-coordinates points are placed in Niamey (around 200 km from the surveyed area). Considering these particular conditions, the

only feasible way to collect data was an RTK survey in a master-rover modality with a radio-modem connection. The PPP technique was used to post-process the data and to estimate the coordinates of the base stations.

The data were collected with two STONEX S10 receivers hired in Niamey. The master receiver was placed in 18 different stations along the Sirba River, and 3150 points were measured with the rover receiver. Each master station acquired data for two hours at least, considering a session length of 3 hours and 22 minutes as maximum. The high temperature (around 40°C) limited the base receiver's correct functioning that overheated and stopped the communication with the rover receiver. This prevented acquisition longer than 3 hours. The receivers' communication was even more limited by the local topography and by the abundant vegetation along the river. If the receivers were more than 3 km far from each other, the communication

stopped. In order to exploit the use of more than two GNSS constellations, the data collected by the base receiver were stored in RINEX 3.x version and then post-processed using the online free services: The Canadian Spatial Reference System (CSRS-PPP), Precise Point Positioning tool (AUSPOS) and Automatic Precise Positioning Service of the Global Differential GPS System (APPS). Table 54 describes the main characteristics of the PPP services.

**Table 54.** Summary of the main characteristics of the three services. \*calculated on 10Mb file.

	<b>CSRS-PPP</b>	<b>APPS</b>	<b>AUSPOS</b>
RINEX version	3.x	2.x	2.11
Maximum file size	Not specified	10 Mb	Not specified
Multi-file upload	No	Yes	Only via FTP
FTP	No	Yes	Yes
Height of the antenna	Automatically detected	Automatically detected	Manually set
Elevation-dependent data weighted	No	Yes	No
Cut-off angle	No	Yes	No
L1 code	No	Yes	No
Upload of pressure model	No	Yes	No
Direct results	No	Yes	No
Compulsory registration to the website	Yes	No	No
Processing time (minutes)*	20	3	20
Reference system(s) of the results	ITRF 2014, NAD83	ITRF 2014	ITRF 2014
Orthometric heights	Yes	No	Yes
Elaboration report	Yes	No	Yes
Graphic restitution of the elaborations statistics	Yes	No	Yes

*Canadian Spatial Reference System (CSRS) Precise Point Positioning tool (CSRS-PPP)*, <https://www.nrcan.gc.ca/maps-tools-publications/maps/tools-applications/10925#ppp>

The service, also described in paragraph 6.4.3, page 134, can process data in Kinematic and Static mode. It requires the selection of the reference system among NAD83 (inserting the referring epoch) or ITRF (International Terrestrial Reference Frame). Optionally, it is possibly converted ellipsoid height in geodetic height by choosing between CGDV28 (Canadian Geodetic Vertical Datum of 1928) or CGDV2013 (Canadian Geodetic Vertical Datum of 2013). The vertical datum is used to provide the user the orthometric height only if the survey is realized in Canada. The user can share his/her data with CSRS. In “more options” section, it is possible to upload an Ocean Tidal Loading (OTL) file. In August 2018, the uploading of RINEX files in version 3 has been enabled (before just in version 2.x was accepted). Only one file at a time can be processed. The results are sent by email. The results are sent by email in a compressed (ZIP format) folder. Table 55 lists the results output folder contents.

**Table 55.** Files in the CSRS-PPP results folder and their contents. The \* indicates the files available since August 2018.

<b>File format</b>	<b>Contents</b>
Portable Document Format (PDF)	Report on the processing
comma separated value (CSV) file	Positioning and clock information
text (TXT) file	Errors or warnings from the processing
position (POS) file	Positioning information for each epoch processed
summary (SUM) file*	Results of the PPP
JSON format residual file (RES)*	Solution residuals

The pdf-report contains a section summarized the essential information regarding the survey (such as starting and end time, duration of the data acquisition, antenna height). Estimated coordinates are provided in a dedicated results section in two different reference systems: WGS84 (or WGS 84 projected in UTM zones) and ITRF2014 (Altamimi et al., 2016). The  $\sigma$  values (95% confidence level) are calculated for each component (i.e., East, North, and Up). The difference in meters between the a priori coordinates and the estimated ones is also provided. The last section presents the statistic observation of the survey and the PPP (i.e., pseudo-range Residuals, Sky Distribution, Ellipsoidal Height Profile, latitude, longitude, height differences, Zenith delay, Ambiguities, tropospheric delay e Phases residuals). The

comma separated values (CSV) file contains the estimated geographical coordinates in decimal degree of each position acquired by the antenna.

*Automatic Precise Positioning Service (APPS)*,  
[https://apps.gdgps.net/apps\\_file\\_upload.php](https://apps.gdgps.net/apps_file_upload.php)

The APPS is an online free service provided by the Jet Propulsion Laboratory (JPL) of the California Institute of Technology of USA National Aeronautics and Space Administration (NASA). Its elaboration is based on the Global Differential GPS System (GDGPS) products of JPL and the software GIPSY-OASIS developed by JPL too. It applies a broad and spread geodetic structure (more than 200 stations distributed worldwide). The GDGPS operates since 2000 and declares a 99.999% reliability and precisions under 10 cm (APPS, n.d.). Without registration, users can use the reduced version of the service: indeed, it is possible to upload 5Mb at maximum to be analyzed in static mode. In order to have full access to the service, registration is compulsory (Figure 81).

Instant Positioning	
<b>APPS Options</b>	
Processing Mode	<input type="radio"/> Static <input checked="" type="radio"/> Kinematic
Measurement Type	<input type="radio"/> Single Frequency <input checked="" type="radio"/> Dual Frequency
Orbits/Clocks used	JPL Final: Data prior to <b>2018-04-21</b> JPL Rapid: Data from <b>2018-04-21</b> to <b>2018-04-25</b> JPL Ultra R/T: Data from <b>2018-04-25</b> to <b>present</b>
L1 Code	<input type="radio"/> C/A Code <input checked="" type="radio"/> P Code
Model Pressure Data?	<input checked="" type="radio"/> Yes <input type="radio"/> No
Elevation Dependent Data Weighting	<input checked="" type="radio"/> Flat <input type="radio"/> Sin <input type="radio"/> Sqrt(sin)
Advanced Options	<input type="text"/> Elevation Angle Cutoff <input type="text"/> Solution Output Rate (seconds)
<input type="button" value="Scogli file"/> Nessun file selezionato <input type="button" value="Reset"/> <input type="button" value="Upload"/>	
*A maximum of 10MB is allowed for upload.	

**Figure 81.** APPS service upload webpage.

The available options for the PPP are the processing mode (static or kinematic); the L1 code (C/A or P), if an atmospheric pressure model is requested (it can be useful for the calculation of the hydrostatic delay for the troposphere modeling), the type of weight to assign to the elevation datum (flat, sin or sqrt). The advanced options allow the user to set the value of the “cut off angle” and the output rate in seconds (clearly available just for kinematic surveys). 10 Mb is the maximum file size allowed, and the files must be in RINEX version 2.x. The results are provided

directly in the upload window. As soon as the data are uploaded, the user is readdressed to a new web page. After a few minutes, a web map of uploaded coordinates is loaded. A download link allows the user to get a compressed folder (TGZ) that contains five files: a “NINJALOG” file containing the characteristics of the survey; a “TDP” file of the coordinates converted in GIPSY format; a GIPSY STACOV file with full covariance (for static only) values; a LOG file containing GIPSY run-time messages and statistics; and finally a SUM file that summarises the results of the conversion, including the Cartesian and the geographic coordinates in and their respective  $\sigma$  values. The results folder also includes a Google Earth URL of the survey's trajectories (just in kinematic).

*AUSPOS Online GPS processing service, <https://gnss.ga.gov.au/auspos>*

It is an online free service provided by the Australian Government. It uses the relative positioning technique, which can estimate the coordinate of an unknown-positioned mark when it is over a reference station of known coordinates (Jamieson Marian and Gillins Daniel T., 2018). The coordinate correction is realized with the Bernese Software System that is very rigorous in the definition of orbital parameters, and everything concerns the modeling of the geodetic aspects (AUSPOS, 2014). The information and the parameters regarding the orbit and the Earth's orientation are obtained from the IGS, and, like the CSRS-PPP, the best ephemerids available are used. It is fundamental underlining that AUSPOS does not provide a real PPP service since the applied data correction is based on the nearest IGS and Asia Pacific Reference Frame (APREF) stations. Consequentially, the confidence of the data and the time-dependence are influenced by the distance of the reference stations used for the coordinates estimation. The service can be used without any registration. The only information needed for the elaboration is the model and the height of the antenna used, and an email address (**Figure 82**). The files must be in RINEX version 2.11. A maximum of 20 files can be uploaded simultaneously, but they must be referred to a period within seven days. The results are sent via email.

**Figure 82.** AUSPOS service upload webpage.

The conversion report of AUSPOS is a pdf file structured in five sections: User data, Processing Summary, Computed Coordinates, Ambiguity resolution, Computation Standards. The first section contains the user's data and the survey's basic information: height and type of antenna, duration of the data acquisition, number of sent files. The second section graphically shows the reference stations used for the processing and their position in the globe.

The computed coordinates section provides the processed coordinated in the ITRF2014 system and GRS80 (Geodetic Reference System 1980, adopted by Australia in 1979, Moritz, 1979), the ellipsoid and geoid heights (obtained from the Gravitational Earth Model, Pavlis et al. 2012). The percentages values of the CORS's ambiguity resolution used for the PPP and the distance between the master station and the CORS are reported in the section ambiguity resolution. The standards and the methodologies applied by AUSPOS for the data analysis are presented in the last section of the report. AUSPOS report includes warning messages and suggestions in case of low levels of confidence in the results.

The RINEX data collected along the Sirba River have been processed using the abovementioned online free services. Some attention was necessary to elaborate on the data correctly. The RINEX files version 3 were converted into RINEX version 2.11 with the RTKCONV tool that is part of the open source software RTKLIB (<http://www.rtklib.com/>), the only version supported by AUSPOS. Furthermore, the frequency rate of acquisition was reduced to one observation every 5 seconds to have less than 10 Mb size files, which is the file size limit of the APPS service. The precisions of the estimation of each service and the relative accuracy (measured as the difference between coordinates) of four sample points (02, 09, 14 e 18) (Table 56) were taken into consideration for the comparison of the results. All final coordinates have been converted into WGS84/ UTM 31N coordinates system. The APPS service provides the  $\sigma$  values with 68% confidence, while CSRS-PPP and AUSPOS calculate 95% confidence  $\sigma$ , the  $\sigma$  values of APPS were transformed in 95% confidence. The CSRS-PPP values had been taken as a reference for comparing software, as shown in Equation 30 and 31.

$$\Delta \text{ CSRS-APPS} = \text{Estimated coord. CSRS} - \text{Estimated coord. APPS} \quad [30]$$

$$\Delta \text{ CSRS-AUSPOS} = \text{Estimated coord. CSRS} - \text{Estimated coord. AUSPOS} \quad [31]$$

Where *Estimated coord. CSRS* are the North, East, and Ellipsoidal height coordinates of each sample point estimated by CSRS; and *Estimated coord. APPS*

are the North, East, and Ellipsoidal height coordinates of each sample point estimated by APPS; *Estimated coord. AUSPOS* are the North, East, and Ellipsoidal height coordinates of each sample point estimated by AUSPOS.

Moreover, three different scenarios of time acquisition were created to investigate the effectiveness of the services on short acquisition time: entire acquisition session, session of one hour, session of half-hour. The RINEX files were reduced to 1 hour and half-hour for each sample point using RTKLIB.

Table 56 reports the full acquisition times of the sample station.

Table 57 presents the values of  $\Delta$  CSRS-APPS and  $\Delta$ CSRS-AUSPOS, calculated as illustrated in equations 30 and 31. The  $\Delta$  of the samples ranged between 1 cm and 6.7 cm (that is the maximum value recorded on the longitude difference between CSRS and AUSPOS of point 02).  $\Delta$  CSRS-APPS and  $\Delta$  CSRS-AUSPOS show similar values on points 18, 14, and 09 in latitude and longitude. Station number 02 differs from other stations for the longitude and the up component. Even if the Up component's  $\sigma$  values almost reach 5 cm, the obtained results are sufficiently precise for the ANADIA 2.0 project purposes.

**Table 56.** Characteristics of the positions of the base receivers (Stations) analyzed. \* gg/mm/yyyy format

Station no.	Date of acquisition*	Session length
02	12-02-2018	1h 50m 56.00s
09	20-02-2018	2h 47m 39.00s
14	19-02-2018	2h 47m 16.00s
18	18-02-2018	3h 22m 50.00s

**Table 57.** Differences between the coordinates estimated by CSRS, APPS, and AUSPOS in WGS84/UTM 31N system for each sample station.

PPP Service	UTM 31N	STATION			
		02	18	14	09
$\Delta$ CSRS-APPS (m)	East	0.012	0.012	-0.026	-0.012
	North	0.008	-0.003	0.011	0.005
	Up	0.024	-0.001	0.015	-0.008
$\Delta$ CSRS-AUSPOS (m)	East	-0.067	0.022	-0.013	-0.008
	North	0.001	-0.002	0.004	0.002
	Up	-0.029	-0.006	0.009	-0.023

The delta of the up component ranges between 3 cm and 1 mm. The  $\sigma$  values estimated by the CSRS-PPP Canada are comparable to the ones of AUSPOS. APPS provides values that are lower than the ones of other services (Table 58).

**Table 58.**  $\sigma$ , 95% confidence, values estimated for full-time acquisitions.

PPP Service		STATION- full acquisition time			
		02 $\sigma$ (m)	18 $\sigma$ (m)	14 $\sigma$ (m)	09 $\sigma$ (m)
CSRS Canada	East	0.027	0.019	0.016	0.026
	North	0.011	0.005	0.008	0.009
	Up	0.048	0.027	0.040	0.041
APPS	East	0.006	0.0042	0.0042	0.004
	North	0.006	0.004	0.004	0.004
	Up	0.028	0.016	0.018	0.020
AUSPOS	East	0.045	0.010	0.011	0.011
	North	0.014	0.008	0.009	0.009
	Up	0.074	0.036	0.042	0.046

The higher  $\sigma$  values are recorded on the Up component by AUSPOS, which peaks to 0.074m on point 2 (Table 58). The entire acquisition session of point 02 is slightly less than the other samples. Indeed, it is 1 hour and 50 minutes, while other sample stations exceed the 2 hours of acquisition.

The precision of CSRS-PPP processing shows major bias on the East and up coordinates, while APPS and AUSPOS present very similar  $\sigma$  values on the East and North components. Station 02 is characterized by different trends from the others; this is attributable to the short stationing time. Table 59 shows the  $\sigma$  obtained from the analyses of the 1-hour acquisition time data. Again, CSRS and AUSPOS provide the higher values, even if APPS appears less confident in up component for stations 18 and 14. For example, the  $\sigma$  of point 2 calculated by AUSPOS is 0.612 m.

This specific value moves away from the equivalent of the entire acquisition time of 50 centimeters, and AUSPOS alerts users and invites them to use the corrections with caution since the provided values exceed the confidence level. The  $\sigma$  of the services on 1-hour acquisition exceed 0.095m on the up of almost every sample stations, revealing low reliability. With shorter acquisition time, the confidence levels of CSRS-PPP and APPS get closer (Table 60), while AUSPOS shows similar trends for some stations (i.e., 14 and 18) and very different for other (station 2). Figure 83 shows the values of the difference between the coordinates elaborated with the services, in WGS84/UTM31N, with 1 hour of session.



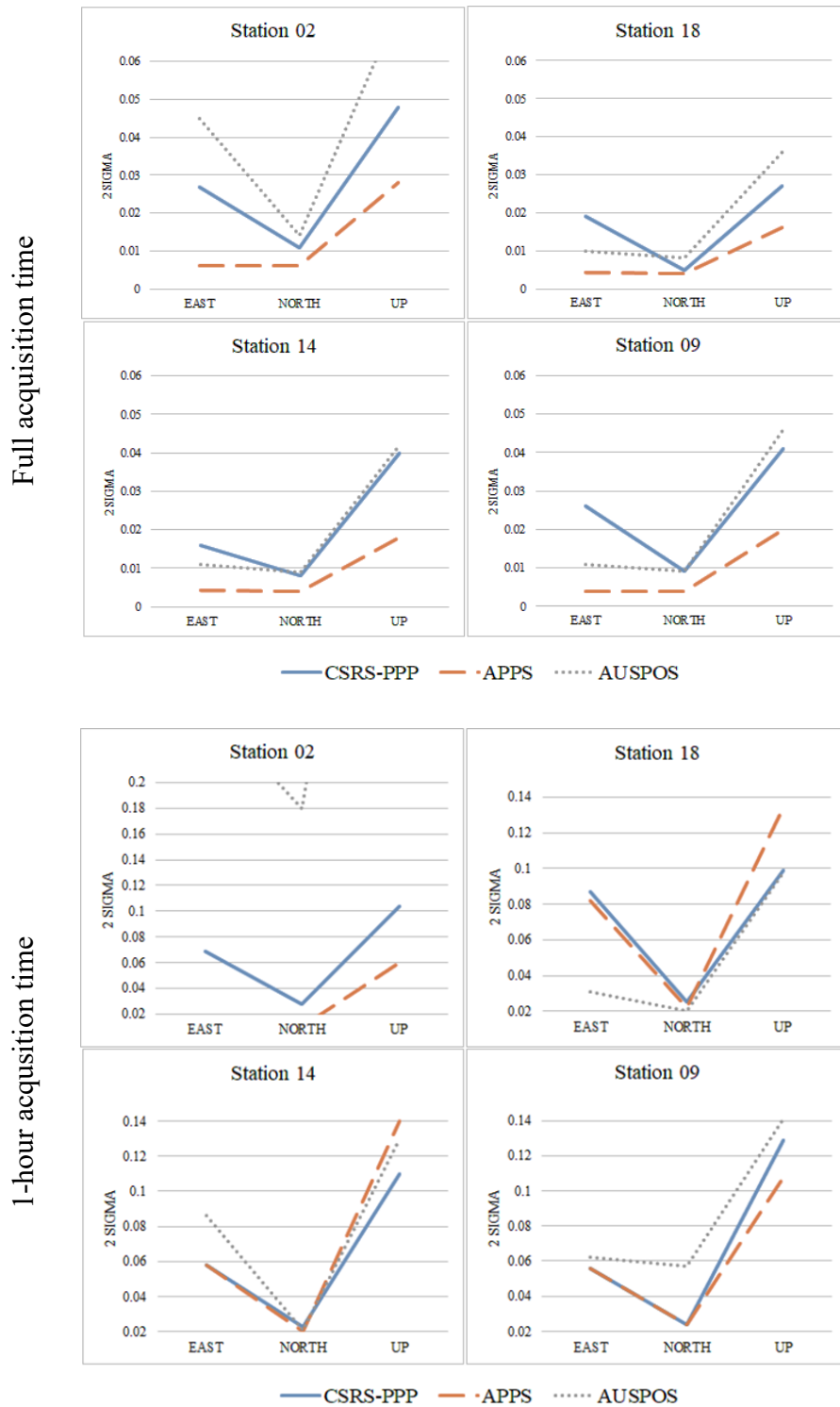
**Table 59.**  $\sigma$ , 95% confidence, estimated for acquisition time reduced to 1-hour.

PPP Service		STATION 1-hour			
		02 $\sigma$ (m)	18 $\sigma$ (m)	14 $\sigma$ (m)	09 $\sigma$ (m)
CSRS	East	0.069	0.087	0.058	0.056
	North	0.028	0.025	0.023	0.024
	Up	0.104	0.099	0.110	0.129
APPS	East	0.014	0.082	0.058	0.056
	North	0.010	0.022	0.020	0.024
	Up	0.060	0.134	0.140	0.108
AUSPOS	East	0.261	0.031	0.086	0.062
	North	0.180	0.020	0.021	0.057
	Up	0.612	0.098	0.130	0.141

The up component elaborated on one hour and the one elaborated on half-hour distance each other until 10 cm. As expected, a significant distance between the up components can be observed: the  $\Delta$  CSRS-APPS 1h of point 09 peaks 17 cm. Table 60 shows the analysis of 30 minutes-acquisition time. AUSPOS did not provide any results because one hour is the minimum acquisition time required. CSRS-PPP and APPS performances exceed in East and Up components of 20 cm (Table 61). The difference between coordinates estimated by CSRS-PPP and APPS (acquisition time of half-hour) is limited to a few millimeters, like the North component of point 09 (Table 61). An opposite scenario emerged from the Up component: points 18 and 14 reach 25 cm.

**Table 60.** Difference between the coordinates estimated by CSRS, APPS, and AUSPOS in WGS84/UTM 31N system for each sample station (1hour stationing).

PPP Service	UTM 31N	STATION 1-hour			
		02	18	14	09
$\Delta$ CSRS-APPS 1h (m)	East	0.019	-0.024	-0.004	0.025
	North	0.006	0.006	0.010	0.001
	Up	0.013	0.101	0.12	-0.010
$\Delta$ CSRS-AUSPOS 1h (m)	East	0.000	-0.018	0.052	0.290
	North	-0.024	0.005	0.018	-0.020
	Up	-0.094	0.100	0.169	-0.173



**Figure 83.** Graphical analysis of the  $\sigma$  values of East, North, and Up coordinates of the three services, obtained considering the full acquisition time.

**Table 61.**  $\sigma$  values, 95% confidence, values estimated for acquisition time reduced to 0.5-hour.

PPP Service		STATION 0,5-hour			
		02 $\sigma$ (m)	18 $\sigma$ (m)	14 $\sigma$ (m)	09 $\sigma$ (m)
CSRS	East	0.165	0.215	0.155	0.149
	North	0.072	0.068	0.060	0.061
	Up	0.202	0.260	0.245	0.362
APPS	East	0.138	0.198	0.152	0.248
	North	0.140	0.124	0.056	0.084
	Up	0.174	0.334	0.302	0.544
AUSPOS	N/A	N/A	N/A	N/A	N/A

**Table 62.** Difference between the coordinates estimated by CSRS, APPS, and AUSPOS in WGS84/UTM 31N system for each sample station (acquisition time 0.5-hour).

PPP service	UTM 31N	STATION 0,5-hour			
		02	18	14	09
$\Delta$ CSRS-APPS 0,5 h (m)	East	0.039	0.016	-0.031	-0.013
	North	-0.010	0.002	-0.008	0.006
	Up	0.016	0.247	0.139	0.043

As previously described, CORS are not available neither in the Sirba region nor in Niger. Thus, it is impossible to estimate the accuracy obtainable in this area because there are no known points for this kind of analysis, but only the precision values can be evaluated, as shown previously. One of the possible ways to analyze accuracies of PPP solutions in sub-Saharan areas is to consider CORS settled in countries close to Niger, more or less at the same latitude in order to guarantee both the mean atmospheric conditions (in terms of ionospheric and tropospheric delays) and the satellites geometry distribution. Another possible approach could be to collect 24-hours of data to obtain results independent of the satellite geometry distribution and guarantee the convergence of the solution, as described in the literature (Li and Zhang, 2014; Ren et al., 2015). However, the impossibility of realizing long-stationing sessions, due to climate effects and the lack of known-coordinates points, impeded the evaluation of the services' accuracy. Hence, to check the estimations' accuracy, raw-observations of a CORS close to the surveyed area were analyzed with PPP online services. The selected CORS was the YKRO station (Yamoussoukro Tracking Station), placed in Cote d'Ivoire and part of the IGS network (Table 63). This station was chosen because it is the closest station (considering latitude) to the investigated area, and it was operative in February

2018. This station is also away from the sea: this may ensure atmosphere conditions as similar to those of the study area. Hence, RINEX data of YKRO were downloaded for the days of the surveys. Unfortunately, data on 18 February (station no. 18) were not available. The RINEX were clipped according to the starting and end time of each acquisition. PPP coordinates estimated by online services were compared to the reference ones of the YKRO CORS (Table 64).

**Table 63.** Main characteristics of YKRO. Source: IGS website

<b>YKRO Site Information</b>	
City	Yamoussoukro
Country	Cote d'Ivoire
Tectonic Plate	African Plate
Approximate Position (ITRF)	LAT: +065214.0170 LON:-0051424.3347
Elevation ellipsoid (m)	270
Date Installed	1999-07-18

The results are never below the 15 cm on East and North components while reaching 27 cm on the Up component. It must be considered that the IGS provides the elevation of the station with a meter level of precision. It appears that the three services provide constant accuracy values.

**Table 64.** Differences between the estimated and reference (IGS) coordinates of the YKRO station

PPP Service		YKRO_02 (m)	YKRO_14 (m)	YKRO_09 (m)
CSRS Canada	East	0.193	0.210	0.210
	North	0.188	0.186	0.187
	Up	0.269	0.258	0.183
APPS	East	0.210	0.210	0.210
	North	0.170	0.180	0.180
	Up	0.260	0.257	0.254
AUSPOS	East	0.240	0.213	0.258
	North	0.175	0.188	0.197
	Up	0.261	0.276	0.235

According to the analysis performed in this paper related to the Niger area, the three services are adequate and effective for the master-rover RTK survey's post-processing corrections. APPS reveals the most precise PPP free online service among the ones investigated in this paper, followed by CSRS-PPP that guarantees satisfying performances in an easily interpretable report. Finally, AUSPOS presents less precise results, but it is incredibly intuitive. Additionally, APPS is the most rapid service in terms of data processing, and it permits the analysis of the large quantity of data (industrial application) uploading the RINEX files on an FTP provided by JPL (this option was not tested in this contribute). Nevertheless, APPS has an interface that may be complicated for non-GIPSY-expert users, and the results are not easy to be read because they are not organized in a report. CSRS-PPP is very functional because the upload process is intuitive, and the results report is easily interpretable. AUSPOS is a user-friendly service. Little information for the data elaboration is requested, and the restitution time is comparable to the one of CSRS-PPP. Even if the report is rich in the elaboration's statistical analysis, it is not complete as the one of CSRS-PPP. Nevertheless, AUSPOS results being the less precise service in this specific analysis.

The relative accuracy analysis of the services results in closer estimations of coordinates between CSRS and APPS. The coordinates estimated by AUSPOS and CSRS are up to 17 cm apart in 1-hour stationing. The analysis of the estimated coordinates of YKRO CORS has shown poor accurate results. Nevertheless, they are acceptable for the ANADIA 2.0 project.

This paragraph aims to assess PPP online service quality as free solutions for topography surveys in critical areas. Nevertheless, it was impossible to perform a complete and exhaustive statistical analysis since the available dataset is relatively low. Moreover, the lack of known-coordinates points and stationing's impossibility for more than 3 hours prevented a proper accuracy analysis of PPP services by real framework comparison.

In the ANADIA 2.0 project framework, the Canadian CSRS-PPP was used, which, although it is less precise than APPS, provides exhaustive statistics regarding the coordinates' corrections and is user-friendly. The obtained results have  $\pm 4$  cm precision and 17 cm accuracy that satisfy the ANADIA 2.0 project's needs in Niger. The CSRS-PPP was used to post-process the GNSS data collected for georeferencing the orthomosaics. Table 65 reports the final coordinates used for the master station in Larba and Tourè to collect the GCPs.

**Table 65.** Description of the characteristics of the GNSS surveys in Larba Birno and Tourè. The Delta is the difference between the base station's measured coordinates and the estimated coordinates by Precise Point Positioning.

<b>Larba Birno</b>	DATE	14/09/2018		
	STARTING TIME	13:06:02.00		
	END TIME	14:15:40.00		
	H ANTENNA (m)	1.81		
		<b>LAT (+n)</b>	<b>LONG (+e)</b>	<b>ELL.HEIGHT</b>
	ESTIMATED COORD, geographic	13° 42' 12.62923"	1° 32' 54.87735"	235.28
	ESTIMATED COORD, cartographic (m)	1515407.211	343045.802	235.262
	2SIGMA (m)	0.014	0.045	0.054
	DELTA (m)	-0.062	0.663	0.3235
	<b>Tourè</b>	DATE	13/09/2018	
STARTING TIME		14:24:41.00		
END TIME		17:00:28.00		
H ANTENNA (m)		1.89		
		<b>LAT (+n)</b>	<b>LONG (+e)</b>	<b>ELL.HEIGHT</b>
ESTIMATED COORD, geographic		13° 36' 49.66473"	1° 26' 24.00953"	238.339
ESTIMATED COORD, cartographic (m)		1505555.569	331238.476	238.339
2SIGMA (m)		0.004	0.012	0.024
DELTA (m)		0.154	0.327	0.677

### 8.1.2. Data pre-processing

#### *Orthophoto and DEM generation*

The data collected were processed according to a traditional Structure from Motion (SfM) workflow (paragraph 3, page 103). The results are one Digital Terrain Model (DTM) and one multiband orthophoto in Red Green Blue Near InfraRed. The images collected with the Raspberry and the Sony sensors were elaborated using the software Photoscan version 1.3.3 (see paragraph 6.4.2, page 134), and two multiband orthomosaics for each study village were generated. Figure 84 reports the workflow of the orthophoto generation. The pictures captured by each camera were analyzed on a separate set. The software automatically aligned each set, then the sparse cloud generated and georeferenced using the points measured with the GNSS receivers. Eight points out of 20 were used as checkpoints (CPs) in

Larba, and 6 points out of 16 were used as CPs in Tourè. After the cloud's densification, the point clouds of the RGB and RGN datasets were aligned based on the Ground Control Points (GCPs) locations.

Table 66 shows the final RMSE (Root Mean Square Error) values obtained for the GCPs for each village, while Table 67 shows the ones for the CPs.

**Figure 84.** The workflow of the orthophoto and Digital Terrain model generation.

**Table 66.** RMSE value of the ground control points (GCPs)

Errors (cm)	Larba Birno		Tourè	
	Sony ILCE RGB	Raspberry RGN	Sony ILCE RGB	Raspberry RGN
X error-easting	4.80	4.21	3.52	5.40
Y error-northing	7.48	4.75	3.77	5.05
Z error-altitude	4.66	2.64	3.79	2.93
Total error	10.03	6.88	6.40	7.95

**Table 67.** RMSE value of the checkpoints (CPs)

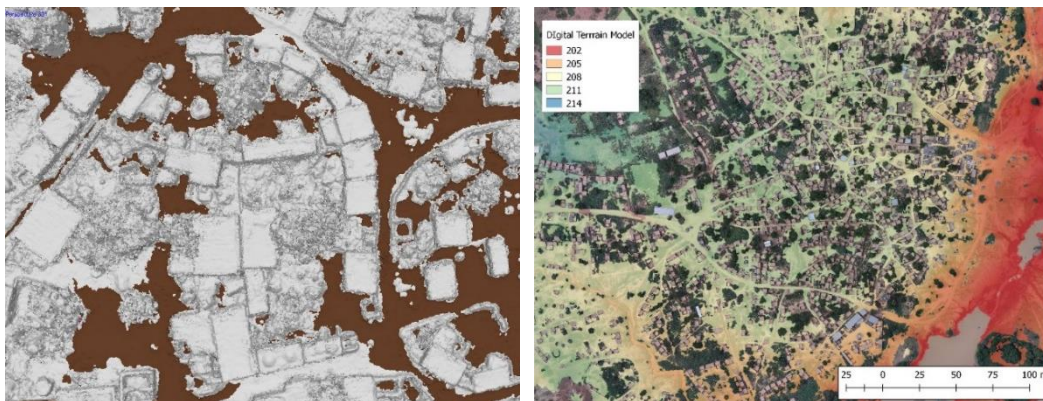
Errors (cm)	Larba Birno		Tourè	
	Sony ILCE RGB	Raspberry RGN	Sony ILCE RGB	Raspberry RGN
X error-easting	1.83	5.88	3.75	5.41
Y error-northing	6.89	7.21	3.81	6.54
Z error-altitude	4.84	4.17	7.90	3.03
Total error	8.62	10.20	5.67	9.02

Once the sparse cloud was georeferenced, the “high quality” dense cloud was generated. It was then created an interpolated mesh of the point cloud, the texture, and finally, the orthomosaic. The same process was followed for the photos acquired by the raspberry Pi camera and the Sony ILCE. The final orthophotos have a resolution of 4 cm in RGB and 6 cm in NGB. The Sony ILCE point cloud was used to extrapolate The DTM because of the higher spatial resolution than the Raspberry-point cloud. For each dataset, the dense cloud was cropped into a “high interest” area that coincides to the village's centre The cropped dense cloud was classified using a specific ground classification tool inbuilt in Photoscan to identify the ground points. The classification is automatic and based on three parameters: Maximum Degree Angle, Maximum Distance, and Cell size. Table 68 shows the settings used for the ground classification in each village.

**Table 68.** The parameters set of the ground classification algorithm. Maximum degree angle describes the maximum slope of the study area expressed in degree; Maximum distance in the maximum distance between the ground and the highest feature in the scene; Cell size in the side size of the most extended cell in which are no detectable ground points (i.e. very dense woods, big buildings).

	<b>Larba Birno</b>	<b>Tourè</b>
Maximum degree angle [degree]	1	1.5
Maximum Distance [meters]	20	25
Cell size [meters]	30	30

The ground points were used for generating the DTM with 7.81 cm/pixel of resolution and 164 points/m<sup>2</sup> in Tourè and Larba Birno. The DTM was not interpolated. This means that there is no elevation information in correspondence of buildings and permanent water, where the DTM has a NULL value. Two reasons can justify this choice: i) the final goal is to identify the depressed area on the ground as potential areas of waterlogging and water stagnation; thus, no water stagnation can occur in the presence of buildings or other permanent land covers; ii) interpolation produced false positive in TSWB analysis. The resulting DTM is a raster reporting the orthometric heights of the study area only where available (i.e., where the point cloud has information regarding the ground) and no-data values were unavailable (Figure 85).



**Figure 85.** On the left, a detail of the ground classification was performed on the point cloud on Tourè. The brown area is the one classified as “ground” by the Photoscan algorithm. Right: extract of the non-interpolated DTM of Tourè.

### 8.1.3. Methods

#### *Identification of topographic depressions*

The detection of potential seasonal water bodies was based on the assumption that all depressed areas can fetch (and store) water after precipitation regardless of

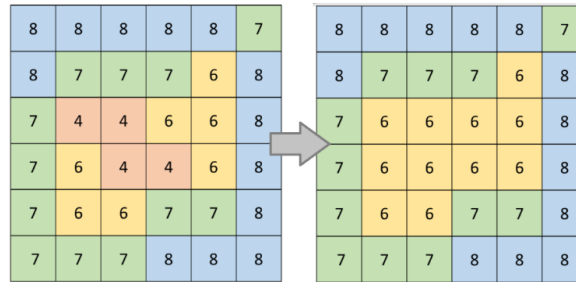


the type of soil, the vegetation cover, and the permeability. Based on this assumption, the localization of the depressed areas corresponds to the potential TSWB. The detection of Potential TSWB was performed using a fill sinks algorithm (Li and Wong, 2010; Liu and Wang, 2008; “On depressional storages,” 2006; Vaze et al., 2010; Yang Jun and Chu Xuefeng, 2013) on the non-interpolated DTM.

Fill sinks algorithms are commonly used in hydrology analysis to modify and calculate the water flow direction of a DEMs (Digital Elevation Models) layer (Wang and Liu, 2006). Filling sinks allows for the removal of any local depressions from DEMs. This operation reduces the inaccuracy when determining channel networks. Otherwise, the catchment area is considered flow accumulation and prevents stream-flow patterns (Lindsay and Creed, 2006). Modern GIS platforms provide, within the hydrologic analysis toolbox, fill sinks algorithm tools. Many algorithms lead to similar results though different ways: most of the algorithms identify the local minima and fills them from the bottom to the top by using the outlet's values of their neighborhood (Planchon et Darboux, 2002; Wang and Liu, 2006). Quantum GIS and SAGA GIS under hydrologic analysis tools propose three algorithms: Fill Sinks (Planchon et Darboux, 2002), Fill Sinks (Wang & Liu, 2006) and Fill Sinks XXL (Wang et Liu, 2006). Regardless of the fill sinks algorithm, the results are very similar (Wang et Liu, 2006): the depressed are identified and filled, meaning that the raster values of the depression are pushed to the surrounding areas' values (Figure 86). The main difference between the algorithms is processing time. Fill sinks by (Planchon et Darboux, 2002) is generally slower than the Wang et Liu (2006) one. The fill sinks XXL is based on (Wang et Liu, 2006)'s algorithm but modified and designed for large datasets.

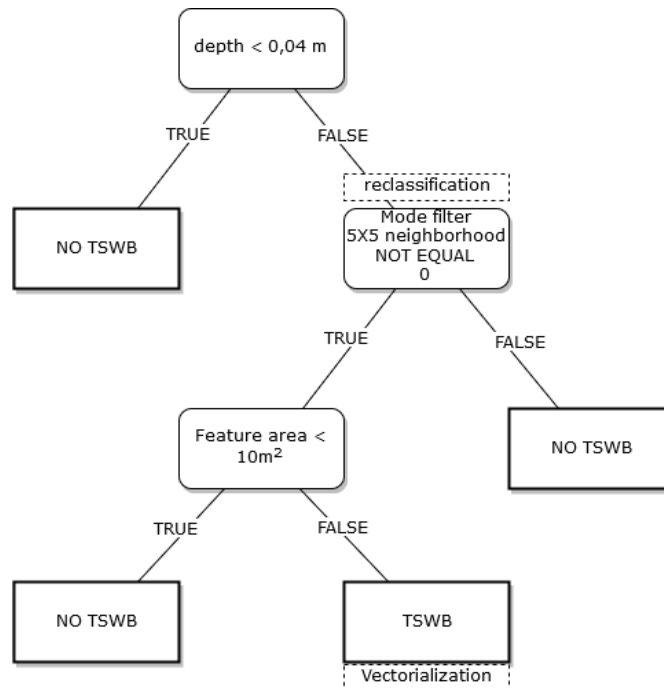
This application used the fill sinks algorithm designed by (Wang et Liu, 2006) to identify the depressions by subtracting the filled-DTM from the original DTM. The input parameters are the input DTM, the slope degree, and optional parameters for the generation of flow direction and watershed basin that were not considered in this analysis. It is worth underlying that depressions in very high resolution (VHR) DTMs are attributable to natural terrain roughness. The topographic depressions detected from VHR DTM can be spurious or real terrain features (Vesakoski et al., 2014). Indeed, the spreading of high-precision and high-accuracy DTMs leads to a very detailed topographic representation of the terrain, describing also not significant features, as well as noticeable in Figure 88. (Lindsay and Creed, 2006) underline how artifacts and actual depressions should be distinguished in DTMs. For this purpose, the topographic depressions characterized by low depth and small extension were considered natural terrain roughness. 10 m<sup>2</sup> and 4 cm are

the thresholds selected respectively for the extension and the depth. These specific requirements are valid in the study area and, generally, in similar sub-Saharan environments. Only deeper depressions may maintain water for a more extended period than the less deep ones that are more affected by the evapotranspiration process. The same parameters may results ineffective in different environments, such as temperate areas (Lindsay and Creed, 2006).



**Figure 86.** Simplified representation of fill sinks algorithms functioning, the depressed areas (i.e., DN value 4) are rise up based on the neighborhood. Depending on the algorithm used, the number of neighbor cells considered may vary.

The relevant water depressions were identified through a basic decision tree classifier composed of two nested levels (Figure 87).



**Figure 87.** Graphic restitution of the decision tree structure applied for the identification of TSWB.

The analysis was realized with SAGA 2.3.2 and Qgis 3.4.8. First, the pixels with DN value (depth expressed in meters) larger than 0.04 were selected, and the raster converted in binary format when 0 value is given to DN smaller than 0.04 and 1 to the others. A mode 5x5 filter was then applied to delete smaller features caused by soil roughness (mode value equals 0) and smooth the raster. Finally, using the Saga Sieve module were deleted the groups of adjacent cells smaller than 10 m<sup>2</sup>.

#### **8.1.4. Accuracy assessment**

(Lindsay and Creed, 2006) recognize five approaches for the validation of DTM-derived depressions: i) comparison to ground inspection data; ii) Examination of the source data; iii) Classification; iv) Knowledge-based approaches; and v) Modelling. In this research, the TSWB were validated through a double approach based on ground inspection data and comparison to TSWB extracted from radiometric analysis (knowledge-based approach).

##### ***Ground inspection validation***

The results obtained were checked against the data collected in the field on the 14<sup>th</sup> of August 2018 (one month earlier than the UAV survey) by governmental staff. The ground data were collected using a Garmin GPS receiver in the center of Larba Birno and Tourè villages. The local staff mapped nine waterlogged areas in Larba Birno. Only the biggest stagnations (according to local staff) were considered. The average size of the provided ponds is 820 m<sup>2</sup>. In Tourè, only one TSWB was reported, but it was not mapped.

##### ***Radiometry-based validation***

The detected topographic depressions were compared to the spectral data collected by the NIR sensor. The orthophoto obtained from the Raspberry Pi acquisitions elaboration was used to calculate the Normalized Difference Water Index (NDWI) by (McFeeters, 2013), equation 32.

$$\text{NDWI} = (\text{Green} - \text{NIR}) / (\text{Green} + \text{NIR}) \quad [32]$$

The NDWI provides values between 1 and -1, where surface cover by water has values near 1, while soil or dry surface presents values around -1. Values between 1 and 0 indicate waterlogged or wet areas (El-Asmar and Hereher, 2011; Memon et al., 2015; Qiao et al., 2012; Yang et al., 2017). A specific classification

was created for these values, considering that the River Sirba NDWI water presents mean DN 0.05 (Table 69). In this study, 1,34% of pixels in Larba show values bigger than 0.025, while in Tourè, 8.86% (classes 6 and 7) (Table 69). The pixels belong to classes 6 and 7, considered the one of water and intense waterlogging. Pixel groups larger than 10m<sup>2</sup> were vectorized and compared to the DTM-based model.

**Table 69.** Pixels distribution (percentage) of the NDWI raster within the identified classification. Column 1 shows the class's name, column two the interval of values describing the class (low-value ≤ DN < higher-value), in column three, are reported the pixel distribution in each class in Tourè village analysis, while the fourth column presents the NDWI pixels distribution of Larba Birno.

Class	NDWI interval	Percentage of cover in Tourè (%)	Percentage of cover in Larba (%)
1	-1 – -0.112	1.66	4.35
2	-0.112 – -0.069	8.06	20.59
3	-0.069 – -0.026	28.15	35.68
4	-0.026 – 0.005	41.09	31.68
5	0.005 – 0.025	11.17	6.25
6	0.025 – 0.030	7.16	0.45
7	0.030 – 1	2.70	0.89

### 8.1.5. Results

The filled sinks raster results in a model of little roughness and uniform Digital Numbers (DN) values. The surface depressions were calculated as the difference between the filled DTM and the original one. The result is a raster of the same resolution and extension of the non-interpolated DTM that contains the “depth” of the depressions and, in flat areas, a DN 0 value. The depth ranges between 0.005 and 0.1 m.

**Table 70.** DN distribution within the reclassified raster of depressions for the villages of Tourè and Larba Birno

Class	Depth interval (m)	Percentage of cover in Tourè (%)	Percentage of cover in Larba (%)
1	0.005 – 0.04	94.16	78.94
2	0.04 – 0.05	2.50	9.18
3	>0.05	3.34	11.88

The relevant depression resulting from the decision tree classifier are 240 features in Larba Birno, for an average extension of 32 m<sup>2</sup>. While in Tourè 167 depressions were detected with 19 m<sup>2</sup> average extension.

#### ***Validation: ground inspection***

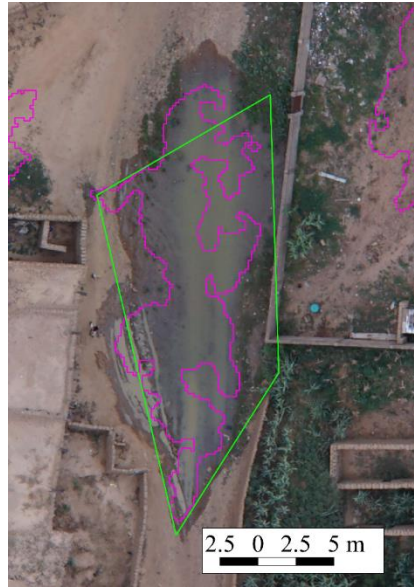
In Larba Birno the local staff mapped nine water ponds. Five ponds matched the DTM analysis. The omitted ponds are located in NULL values zones of the DTM, which means that those areas were considered non-ground during the points cloud classification. It is worth mentioning that no detailed information regarding the methodology used for the mapping activities was available. The TSWB estimated from the DTM-analysis are smaller than the TSWB identified by ground inspection (Table 71). The difference in extension reaches 862 m<sup>2</sup>. This aspect must be considered with caution because of the unknown precision and accuracy of the validation data. The local staff did not map the TSWB in Tourè, but they only report a temporary secondary branch of Sirba River.

#### ***Validation: radiometric analysis***

The NDWI analysis in Larba Birno resulted in only one TSWB that satisfied the extension requirements. Some other areas with high NDWI values were detected, but they corresponded to the bank river. The DTM-based analysis matches the NDWI-based TSWB (Figure 90). Even though the location of the TSWB matches, the extensions are slightly different. The NDWI-based TSWB extends 89 m<sup>2</sup>, while the TSWB extends 122 m<sup>2</sup>.

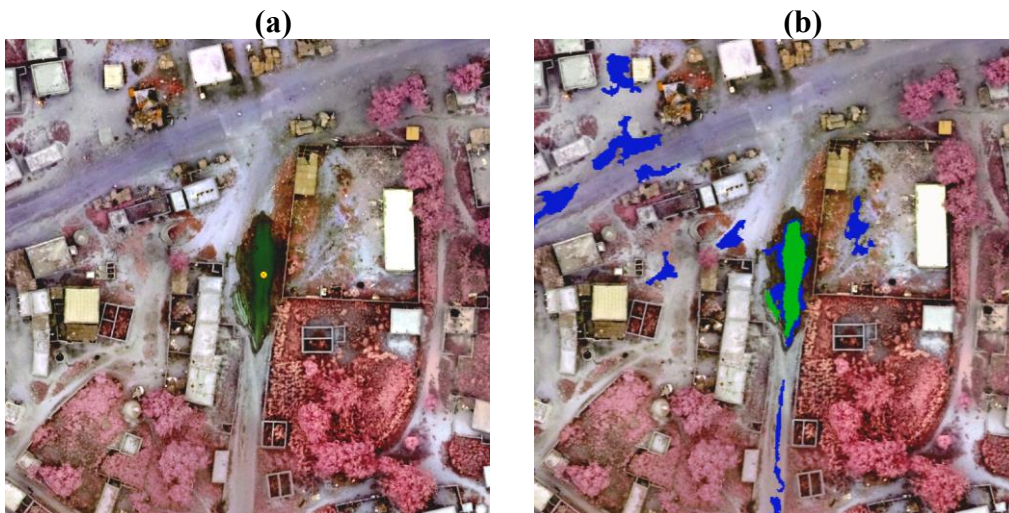


**Figure 88.** Detail of the depressions identified through the DTM analysis in Larba Birno. The small and shallow depressions are DTM artifacts created by the roughness of the soil. Some depressions are well defined (blue spots), while others are noisy due to irregularities on the ground due to mud and water.

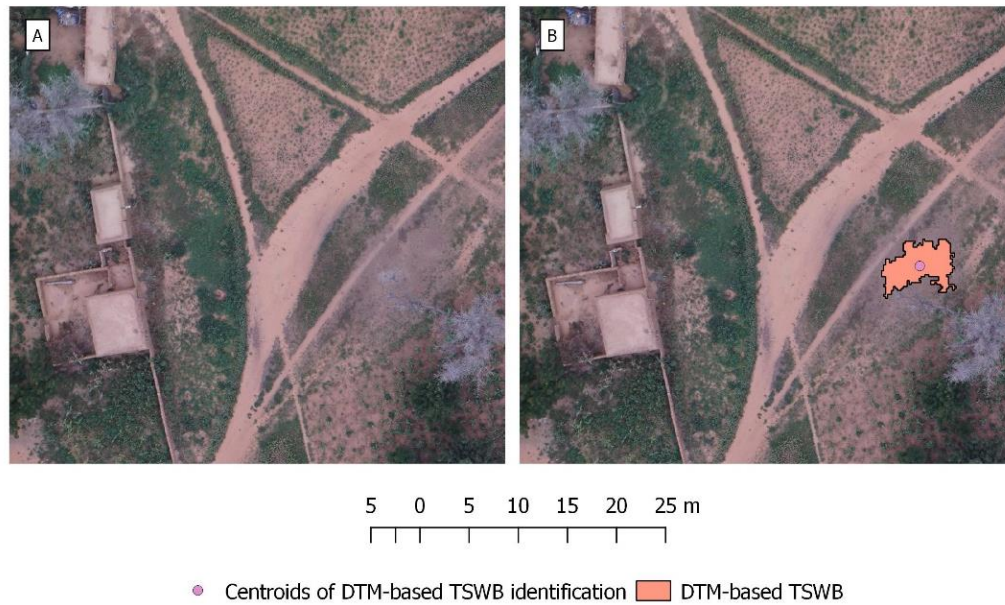


**Figure 89.** Example of matched TSWB between the ground inspection (green polygon) the DTM-derived (pink polygon).

In Tourè, six TSWB were detected by radiometric analysis. Only one partially matches the DTM-based TSWB. The remaining are omitted. It worth underling that the NDWI method is not sensitive enough to detect mud and wet areas, such as the example in Figure 91.



**Figure 90.** a) RGN visualization of the Temporary Surface Water Body (TSWB) in Larba Birno. b) Match of NDWI-based (green) and DTM-based (blue) TSWBs.



**Figure 91.** Sample TSWB in Larba Birno. A scene is extracted from the orthophoto. B scene shows the information originated from the DTM analysis. In this case, the NDWI analysis results in the total absence of water. From picture A, it is possible to identify the loam residuals in correspondence with the potential TSWB. Moreover, the path seems to be created in order to avoid TSWB.

**Table 71.** Larba: comparison between ground inspection TSWB and DTM-detected

ID	Ground measure area (m <sup>2</sup> )	DTM-derived area (m <sup>2</sup> )	Difference area (m <sup>2</sup> )
1	1153	290	862
2	359	20	340
3	521	Not detected	/
4	302	Not detected	/
5	399	Not detected	/
6	530	139	391
7	211	122	88
8	666	166	499
9	3242	Not detected	/

### 8.1.6. Discussion and conclusion

The proposed method efficiently identifies the topographic depression from Very High-Resolution Digital Terrain Model. It is a fast and straightforward method for potential temporary surface water bodies (TSWB) detection. The results demonstrate the validity of the method that detected most of the existing TSWB in

the 2018 rainy season. Nevertheless, this approach still needs to be tuned and improved. The ground inspections emerge that four out of nine TSWB in Larba Birno were not detected because they are located outside the non-interpolated DTM. This underlines two primary limits of the method related to the ground points' classification and the DTM quality. The method considers as non-depressed all areas covered by buildings, infrastructures, but also the vegetation. This is an imprecision since TSWB can also be in densely vegetated areas. The second consideration regards the quality of UAV-generated DTM. Contrary to LiDAR data, UAV-based point clouds hardly provide users with ground data in dense tree cover. Consequentially, even if the vegetate areas are potentially TSWB, it would be impossible to detect them from UAV-derived data.

The comparison to the ground truth should be carefully interpreted. The information regarding the ground data collection methodology is inferior and base only on local staff impression. Furthermore, the data are poorly detailed and mapped with a low-precision GPS receiver. Nevertheless, the DTM analysis tends to underestimate the TSWB extension from the ground inspection validation. This leads to assuming that additional analysis should be carried on to understand the possible connection between close TSWBs.

It must be considered that such analysis was complicated by the topography, the land cover, and use of the study area. Indeed, both villages are characterized by a very low difference in height and homogeneous land cover environment: the low density of buildings, absence of woods, and not intense cultivation. These characteristics, on the one hand, facilitate the extraction of ground information with modern photogrammetry software. On the other hand, the nature of the area leads to many outliers in DTM analysis. For example, some latrines (present in almost every households 'yards) without roof or cover were recognized as depressions. However, the small size of the latrine-depression made them easily removable from the dataset.

One of the most significant limit of the DTM analysis is related to the detection of the TSWB already present since they are not detected as depression by the software, Figure 92 shows.

This limitation can be overcome by the parallel reading of the radiometric and DTM information, which permits total and complete information during the rainy season. The DTM analysis is fundamental in identifying the potential temporary water bodies in the dry season or low precipitation years.

The results of the comparison reveal DTM-based detection quite an effective method. It can help identify the maximum potential extension of temporary water bodies, crucial information for health-risk reduction plans. It is hard to correctly



analyze the results' goodness because of the lack of precise and complete information regarding the ground truth. Similarly, the radiometric comparison is not exhaustive since it only describes the TSWB present at the acquisition time, without providing the information about the potential extension. It must be considered that the occurrence of surface water is related to the amount and distribution of rainfall and the catchment characteristics that influence runoff generation. Indeed, this work aims to be the first step through an in-depth study of temporary surface water bodies, their identification, and localization. Further consideration should be done regarding the type of soil and its infiltration capacity related to the precipitation distribution and intensity, along with the ground classification methodology and the orthomosaic quality.

It is worth stressing that the ratio behind this work is the lack of high-resolution radiometric information of TSWB maximum extension. Indeed, within the ANADIA 2.0 project, it was impossible to realize the UAV survey in mid-August, the period in which the TSWB are in their maximum extension.



**Figure 92.** TSWB detected by NDWI analysis (green features) and partially developed under a tree crown. It was not detected by the DTM method.

## 8.2. Satellite

Sub-Saharan Africa is exceptionally vulnerable to Climate Change-induced phenomena, such as floods, erosion, droughts, which have dramatically increased in the past years. Therefore, frequent information regarding the Land Cover of this area is crucial to land management, as these maps provide users with information related to terrestrial ecosystems and livelihoods (Li et al., 2020). Sub-Saharan areas' classification is one of the most challenging due to the landscape's complexity and the low spectral variability within the covers. Moreover, the sand dust particulates in the atmosphere may alter the Earth's surface's spectral response and further exacerbate the difficulty of the classification (paragraph 6.2, page 115). These are some of the reasons that contribute to the data scarcity of this area. Indeed, to date, few very high-resolution Land Cover maps of sub-Saharan areas exist. Examples are the Africa LC by ESA and FROM-GLC10 (Li et al., 2020). Although these LC maps are incredibly complex to realize, most of them do not provide great thematic detail and, because of their nature, they are hard to update significantly in terms of training dataset due to the large quantity of time and manual work this task requires. The case study of the ANADIA 2.0 project, being in southern Niger, faces all the sub-Saharan LC mapping limitations and an updated, high-detailed LC map of the area is not available. In this application, the Land Cover map of the southwest Niger has been realized using nine classes over 16 features. The entire process was realized in the Google Earth Engine platform, and two multi-temporal approaches for classification were tested and compared.

### 8.2.1. Materials and methods

#### *Satellite Imagery filtering and pre-processing*

The images sensed by Sentinel-2 (both Sentinel-2A and Sentinel-2B satellites) were filtered by location and sensing date. The study area includes the segment of Sirba River that lies in Niger country for about 100 km length. The period covers all the acquisitions between 2017 and 2019. An additional filtering parameter regards the cloud cover percentage, which must be less than 10% over a single scene. Only images sensed during the rainy season (from August to October) were selected to maximize the classes' spectral variability, especially to better distinguish between the vegetation classes and the bare soils and to identify water. Sentinel-2 level 1C dataset was used for this classification since only one image from the corrected dataset of Sentinel-2 level 2A satisfied the filter mentioned above parameters (see paragraph 5.1, page 94 for more information regarding the satellite correction levels). The selected images from the 1C level are 16 (Table 72).

The dataset was atmospherically corrected applying the Dark Object Subtraction (DOS) (Chavez, 1988), which is a linear atmospheric correction model that performs similarly to radiative transfer models on homogeneous surfaces (Lantzanakis et al., 2017), was applied as already illustrated for the Alps case in paragraph 7.2, page 162.

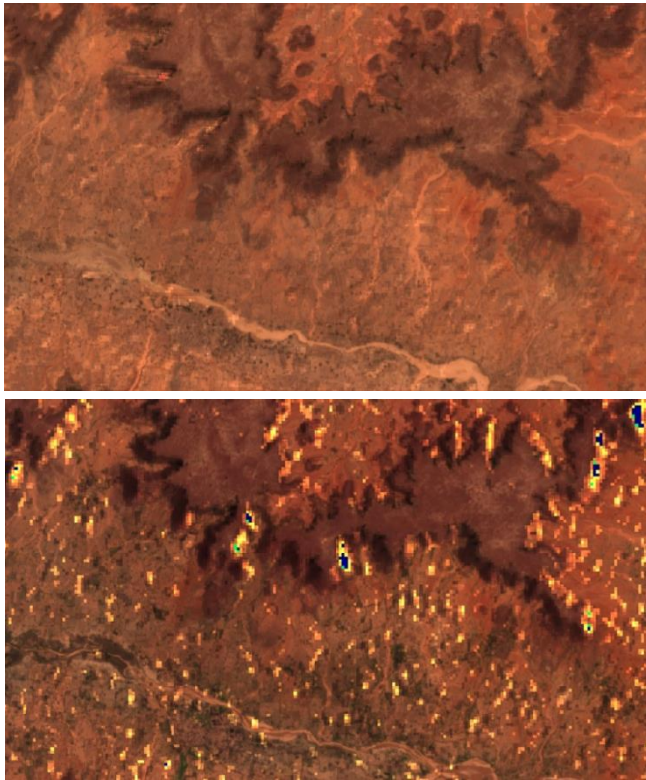
**Table 72.** List of Sentinel-2 images used in the classification.

Year	No.	Sentinel Image Identification Code
2017	0	20170815T102021_20170815T102513_T31PCR
	1	20170924T102021_20170924T102649_T31PCR
	2	20170926T101009_20170926T102049_T31PCR
2018	3	20180815T102019_20180815T102918_T31PCR
	4	20180820T102021_20180820T103538_T31PCR
	5	20180911T101019_20180911T101438_T31PCR
	6	20180911T101019_20180911T102702_T31PCR
	7	20180916T101021_20180916T101512_T31PCR
	8	20180921T101019_20180921T101647_T31PCR
	9	20180924T102019_20180924T102602_T31PCR
	10	20180929T102021_20180929T103112_T31PCR
2019	11	20190812T101031_20190812T102016_T31PCR
	12	20190911T101021_20190911T102116_T31PCR
	13	20190921T101031_20190921T102426_T31PCR
	14	20190926T101029_20190926T102551_T31PCR
	15	20190929T102029_20190929T102700_T31PCR

Knowing that DOS can affect the classification's results differently depending on the geographical area (and land cover), the classification was performed over the DOS-corrected dataset and the non-corrected dataset, and then the Overall Accuracies of the classifications were compared to check the influence of DOS on the final result.

The topographical correction of the images was initially applied to reduce the effects of elevation over the plateaux areas, using the code originally implemented in GEE by Patrick Burns and Matt Macander (paragraph 7.2, page 162). Nevertheless, the correction introduced noise in the dataset, most probably because the plateaux slopes do not interfere with the soil's spectral response, and the Digital

Elevation Model applied is not resolute enough. Thus, the dataset was not topographically corrected.



(a)

**Figure 93.** (a) RGB mosaic on sentinel 1C data, DOS applied; (b) RGB mosaic on sentinel 1C data, DOS applied, and topographically corrected. The correction excessively alters the data over the plateaux, but also in the plane areas.

(b)


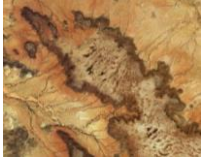


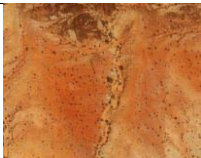




### *Identification of classes*

Nine classes describe the classification system, as Table 73 illustrates. They have been selected according to the needs of the project ANADIA 2.0.

### *Training and test datasets*

The training dataset is constituted of 2500 points, 300 points for each class except for the class of the Urban areas, which is constitute only by 100 points. The choice of unbalancing the training is due to the low percentage of urban areas cover. Since the Urban areas class covers the smallest portion of the study area and the Random Forest classifier tends to promote the more represented classes in training, few samples of the Urban area were used to train the classifier. The validation dataset is composed of 1800 points, 200 for each class. The training and validation dataset were manually created using a 2017 map as a ground reference.

**Table 73.** Classes on the classification in South Niger.

No.	Class	Description	Picture
1	Water	Internal waters	
2	Plateaux	Elevated areas over the dry savannah. They influence the water catchment, the erosion process, and present peculiar plant species.	
3	Riparian vegetation	The thickly vegetated area along the rivers. It is usually composed of trees and bushes.	
4	Urban areas	Villages and main roads.	
5	Red bare soils	Red soils rich in ferric oxides which characterized the savannah soil landscape.	
6	Sandy bare soils	Sand natural deposits.	
7	Vegetation of the plateaux	Vegetation on the plateaux. It grows along the drainage canals. It is mostly composed of herbaceous species.	
8	Irrigated agricultural lands	Areas interested by intense agricultural activity that require tillage, and irrigated generally through channel systems.	
9	Non-irrigated agricultural lands and pastures	Areas interested by moderate agricultural activities that require tillage or pastures.	

### ***Feature extraction and selection***

The feature extraction consisted of the computation of 6 spectral features, 4 histogram-based features, 18 textural, 2 elevation-derived features, and 1 edge-detector feature added to the 12 spectral bands Sentinel 2. The features were computed on the NearInfrared band. Specifically, the Gray Level Co-occurrence Matrix's texture metrics were computed over a 9x9 neighborhood while the histogram-based features on a 3x3 filter. (Connors et al., 1984; Haralick et al., 1973; GEE, 2020). Table 74 lists the extracted features.

The feature selection phase is fundamental to reduce the computational time of the classification without losing accuracy. In mid-2020, the function *SmileRandomForest* was introduced in the GEE coding platform. Unlike its predecessor *RandomForest* function, it allows the computation of the layer importance, which is based on the GINI impurity system (see paragraph 4.3.2, page 63). A simplified description of the GINI gain defines it as the sum of impurity decreases from two nodes and the parent node. The GINI is calculated for each variable of the classifier. The variables that have high GINI gain (so they have less impurity) are more important.

The features with less than 50 of GINI gain were removed from the input dataset. The threshold value was selected according to the maximum accuracy achievable. As realized for the Alpine Arch case study, a “pseudo-normalization” was carried out.

### ***Classification and multi-temporal strategies comparison***

Two different multi-temporal approaches were compared: aggregated multi-temporal and stacked multi-temporal methods. These methods are described in detail in paragraph 4.2.1, page 54. Figure 94 shows the classification workflow.

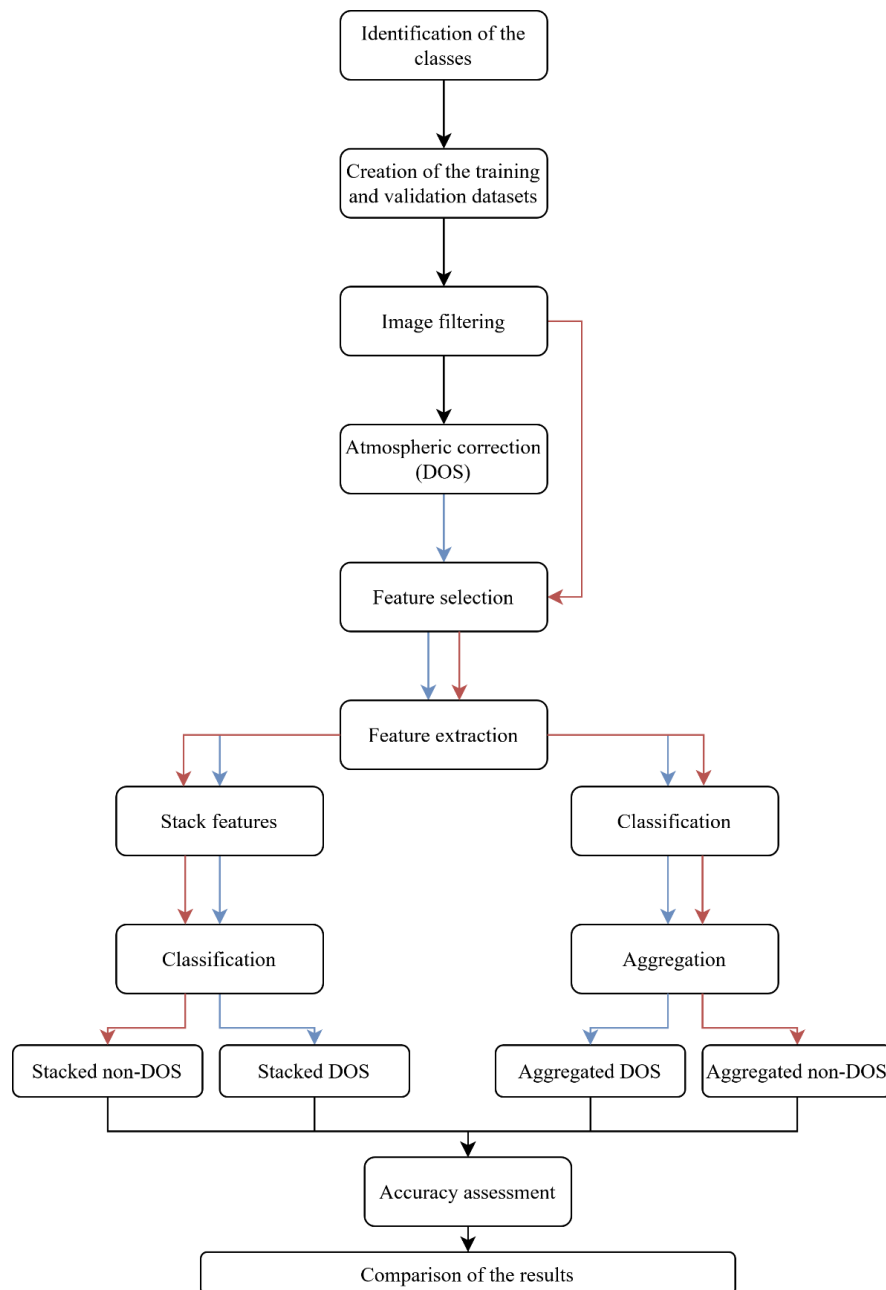
In the aggregated multi-temporal each image was separately classified using the machine learning algorithm random forest with 100 rifle decision trees per class and 2 as the minimum size for terminal nodes. The same training dataset was used for each image. The results are 16 classifications that were aggregated according to the modal value. Only the more accurate classifications (more than 0.94 of overall accuracy) were used in the final aggregation. Differently, the stack multi-temporal approach consisted of one classification over a dataset composed of all the features from different epochs ensembled. In this case, the images were stacked together and classified with Random forest algorithm (200 rifle decision trees per class and 4 as the minimum size for terminal nodes). Due to GEE's limitation on the available memory, only 2018 and 2019 data were considered.

**Table 74.** Derivative features are calculated for each epoch. They are divided into 5 groups: histogram-based, radiometric, edge extractor, textural. And elevation.

	<b>Feature</b>	<b>Formula/note</b>
<b>Spectral</b>	Chlorophyll IndexRedEdge, CRE	$(B9/B5)-1$
	Enhanced Vegetation Index, EVI	$2.5*((B9-B5)/((B9+6*B5-7.5*B1)+1))$
	HUE	$\text{Arctan}((2*V5-B3-B1)/30.5)*(B3-B1)$
	Soil Composition Index, SCI	$(B11-B8)/(B11+B8)$
	Wetness Index, WET	$(0.1509*B2)+(0.1973*B3)+(0.3279*B4)+$ $(0.03406*B8)-(0.7112*B11)-$ $(0.4572*B12)$
	Triangular Vegetation Index, TVI	$0.5*(120*(B8-B3))-(200*(B4-B3))$
<b>Edge</b>	Sob	Sobel edge extractor
<b>Histogram-Based</b>	Var	Variance
	Mean	Mean
	Skew	Skewness
	Kurt	Kurtosis
	Entr	Entropy
<b>Textural GLCM</b>	Asm	Angular Second Moment; measures the number of repeated pairs
	Corr	Correlation; measures the correlation between pairs of pixels
	Var	Variance; measures how spread out the distribution of gray-levels is
	Idm	Inverse Difference Moment; measures the homogeneity
	Savg	Sum Average
	Svar	Sum Variance
	Sent	Sum Entropy
	Ent	Entropy. Measures the randomness of a gray-level distribution
	Dvar	Difference variance
	Dent	Difference entropy
	Imcorr1	Information Measure of Corr. 1
	Imcorr2	Information Measure of Corr. 2
	Maxcorr	Max Corr. Coefficient.
	Diss	Dissimilarity
	Inertia	Inertia
	Shade	Cluster Shade
	Prom	Cluster prominence
<b>Elevation</b>	DSM	Digital Surface Model
	Height model, HM	DSM-DTM

### *Accuracy assessment*

The classifications' accuracy was assessed based on the error matrix-derived measures: the overall accuracy, the producer's accuracy, the user's accuracy, and the F1 score.



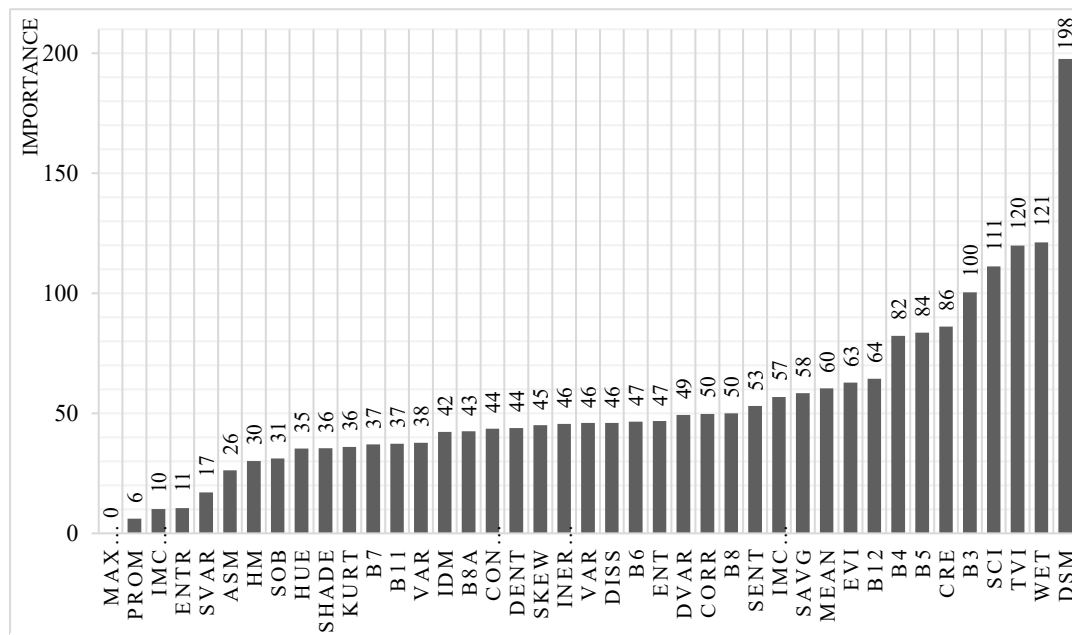
**Figure 94.** The workflow of the classification. Red arrows indicate the DOS processing, while the blue ones indicated the processing without DOS correction.



## 8.2.2. Results

### *Feature extraction and selection*

Figure 95 shows the results of the GINI importance analysis. The bands per image (that initially were 44) were reduced to 16 according to the maximum achievable accuracy (Table 75) computed by considering five scenarios with reduced input features. Scenario 3 revealed better OA (0.85) and little out of bag error (0.07).



**Figure 95.** GINI importance of the extracted features.

**Table 75.** Tests run over five scenarios that differ in the number of input features in the classification selected according to their importance value (see Figure 95). The parameters considered for the best scenario evaluation are the out-of-bag error (oob) and the overall accuracy (OA).

	<b>GINI threshold</b>	<b>oob</b>	<b>OA</b>
Scenario 1	none	0.08	0.846
Scenario 2	>40	0.07	0.846
Scenario 3	>50	0.07	0.854
Scenario 4	>60	0.08	0.849
Scenario 5	>80	0.08	0.842

### *Classification and multi-temporal strategies comparison*

The aggregated multi-temporal classification was performed separately in 16 images with 16 features for each. Table 76 provides the OA values calculated for each classification. Classification with OA less than 0.94 were not used for the modal aggregation. The stacked multi-temporal classification was realized using as input dataset the features from different epochs together. The period considered was 2018 and 2019. The input features of the stack multi-temporal classification were 76.

**Table 76.** OA achieved on single classification. The underlined classifications were excluded from the aggregation

<b>Classification no.</b>	<b>OA</b>
1	0.97
2	0.95
3	0.96
<b>4</b>	<b><u>0.85</u></b>
<b>5</b>	<b><u>0.94</u></b>
<b>6</b>	<b><u>0.83</u></b>
7	<b><u>0.85</u></b>
<b>8</b>	<b><u>0.92</u></b>
9	0.95
10	0.95
<b>11</b>	<b><u>0.92</u></b>
12	0.95
13	0.95
<b>14</b>	<b><u>0.94</u></b>
15	0.95
16	0.96

To further optimize the process, the GINI importance was computed for the 76 bands. Four scenarios for the slimming out were considered (Table 77), but the best results are provided by scenario number 12, which does not remove any feature from the classification. The atmospheric correction's influence on the classifications was checked by comparing the accuracy of the same classification model applied to corrected and non-corrected input datasets. The DOS has little influence on the

aggregated multi-temporal classification's goodness: it shifts the OA from 0.971 (non-corrected dataset) to 0.975 (corrected dataset). Similarly, the DOS showed little influence on the stacked method too. Indeed it shifts the OA from 0.955 (non-corrected) to 0.960 (corrected), Table 78.

**Table 77.** Tests run over 5 scenarios that differ in the number of input features in the classification selected according to their importance value. The parameters considered for the best scenario evaluation are the out-of-bag error (OOB) and the overall accuracy (OA).

	<b>GINI threshold</b>	<b>OOB</b>	<b>OA</b>
Scenario 1	none	0.019	0.960
Scenario 2	>9	0.020	0.958
Scenario 3	>10	0.020	0.955
Scenario 4	>20	0.023	0.951

**Table 78.** DOS influences over the classifications.

	<b>No correction</b>	<b>DOS</b>
OA of Aggregated multi-temporal	0.971	0.975
OA of Stack multi-temporal	0.955	0.960

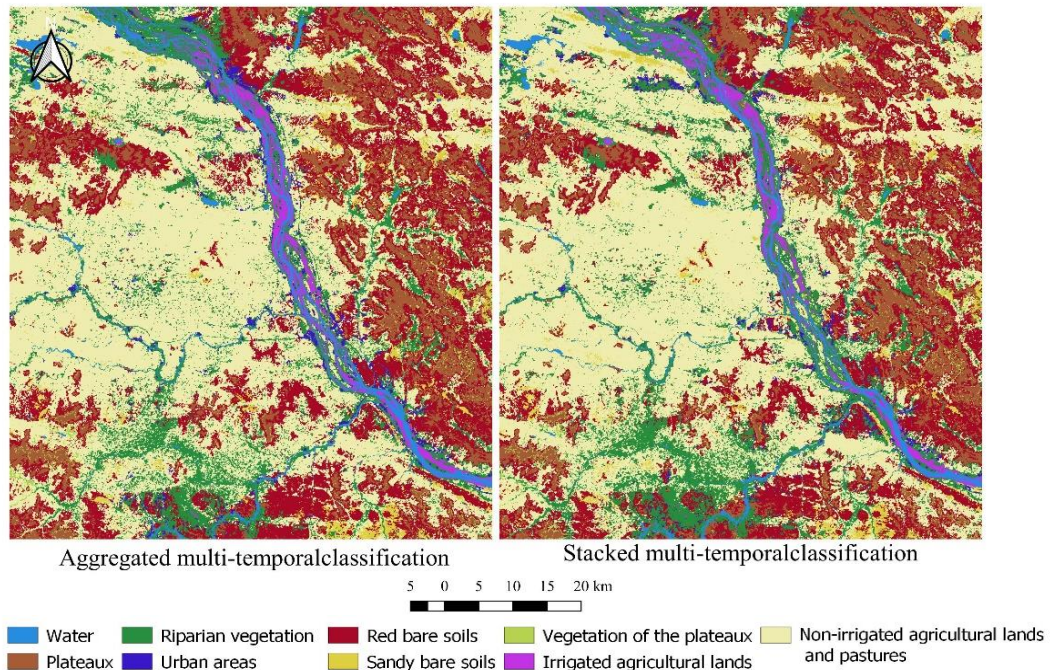
### *Accuracy assessment*

The error matrices give the goodness of the classification. Both multi-temporal approaches resulted in high accuracy values. For what concerns the aggregated approach, Table 79 shows that the User's and Producer's accuracies are always above 0.95. The *Plateaux* class appears to be less accurate, although its F1 score reaches 0.95. The model correctly identifies sandy bare soils and irrigated land classes. Regarding the stacked classification, the accuracy values are slightly lower than the one on the aggregate multi-temporal classification. As Table 80 shows, the *plateaux* class reaches 0.947 of F1-score, which is the less accurate class along the non-irrigated lands and pastures. The overall accuracy is 0.96, only 0.05 points of difference from the aggregated methods.

Although the high accuracy value, some salt-and-pepper effect is present all over the scene, thus, for aesthetic reasons, some post-processing operations were carried out. Specifically, erosion (size 4) and dilation (size 3) were realized in class *Urban areas* (Figure 96).

**Table 79.** Error matrix of the aggregated multi-temporal classification.

	Water	Plateaux	Forest bushes	Urban areas	Red bare soils	Sandy bare soil	Vegetation (plateaux)	Irrigated agricultura	Non-irrigated	TOT
Water	200	0	0	0	0	0	0	0	0	200
Plateaux	0	189	0	0	0	0	11	0	0	200
Forest bushes	0	0	200	0	0	0	0	0	0	200
Urban areas	0	0	7	193	0	0	0	0	0	200
Redc bare soils	0	8	0	0	188	0	0	0	4	200
Sandy bare soil	0	0	0	0	1	197	0	0	2	200
Vegetation (plateaux)	0	0	0	0	0	0	200	0	0	200
Irrigated agricultural lands	0	0	0	0	0	0	0	200	0	200
Non-irrigated lands and pastures	0	0	6	5	1	0	0	0	188	200
<b>TOT</b>	<b>200</b>	<b>197</b>	<b>213</b>	<b>198</b>	<b>190</b>	<b>197</b>	<b>211</b>	<b>200</b>	<b>194</b>	
Producer's accuracy	1.000	0.959	0.939	0.975	0.989	1.000	0.948	1.000	0.969	OA= 0.975
User's accuracy	1.000	0.945	1.000	0.965	0.940	0.985	1.000	1.000	0.940	
F1-score	1.000	0.952	0.969	0.970	0.964	0.992	0.973	1.000	0.954	



**Figure 96.** Example of the aggregated multi-temporal classification (left) and the stacked multi-temporal classification (right).

**Table 80.** Error matrix of the stacked multi-temporal classification.

	Water	Plateaux	Forest bushes	Urban areas	Red bare soils	Sandy bare soil	Vegetation (plateaux)	Irrigated agricultura	Non-irrigated	TOT
Water	183	0	0	0	0	0	0	0	0	183
Plateaux	0	180	0	0	0	0	10	0	0	190
Forest bushes	1	0	191	0	0	0	1	3	0	196
Urban areas	0	0	6	161	0	0	0	0	0	167
Redc bare soils	0	9	0	2	174	0	0	0	8	193
Sandy bare soil	4	0	0	0	0	178	0	0	1	183
Vegetation (plateaux)	0	1	0	0	0	0	195	0	0	196
Irrigated agricultural lands	3	0	6	0	0	0	0	171	0	180
Non-irrigated lands and pastures	0	0	8	4	0	0	0	0	177	189
<b>TOT</b>	<b>191</b>	<b>190</b>	<b>211</b>	<b>167</b>	<b>174</b>	<b>178</b>	<b>206</b>	<b>174</b>	<b>186</b>	
Producer's accuracy	0.958	0.947	0.905	0.964	1.000	1.000	0.947	0.983	0.952	OA= 0.960
User's accuracy	1.000	0.947	0.974	0.964	0.902	0.973	0.995	0.950	0.937	
F1-score	0.979	0.947	0.939	0.964	0.948	0.986	0.970	0.966	0.944	

### 8.2.3. Discussion and conclusions

The classification shows very positive results. The GINI importance analysis allows the lightening of the classification process and improves the classification's goodness. Although this was not true for the stacked classification, reducing the dataset reduces the OA. It is worth underlining that in this case, the importance analysis was applied twice. The DOS correction has little influence on the final accuracy results for both multi-temporal approaches. This is an unexpected result since most relevant literature underlines the importance of atmospheric correction in multi-temporal approaches, especially in stacked ones.

The little influence might be caused by the short period and the very similar meteorological condition of the analyzed dataset. Also, the classifier Random Forest, which is little sensitive to non-normalized datasets, might contribute to such results. Although the little influence of DOS in the results, it was maintained in the classification workflow mainly because of its lightweight on the processing time. More complex atmospheric correction models can require more computational power and processing time. Thus, further and more detailed analysis needs to be realized in this direction. Little distance also emerges from the comparison of the

two multi-temporal approaches. The aggregated multi-temporal classification overcomes the stacked one for only 0.015 points of OA (regardless of the atmospheric correction). The F1 score of some classes of the aggregated multi-temporal approach is 1 (water and irrigated lands). In the stacked multi-temporal approaches, the F1 score shows some differences: irrigated land class is not one of the most accurate class, but bare soil is. This method seems to penalize the irrigated class, which is often confused with forest or water. Despite some little differences, in this case, the two methods are perfectly exchangeable for this specific application. In terms of time to apply one or the other, again, there is a little difference. If classifications of around-hundred a feature realized using local machine require high computational power, using GEE this is not required anymore. Nevertheless, there is a strong possibility of running out of memory in additional features or a vast area. Indeed data from 2017 were taken out. In this specific application, the classification of the aggregated multi-temporal method was used because of the slightly higher accuracy and the less scarcity of salt-and-pepper effect all over the scene.

### **8.3. Land Cover using UAV imagery**

Extreme floods are a severe natural threat for many sub-Saharan areas (Tiepolo et al., 2019a) that can cause conspicuous losses. In the last twenty years, countries have suffered from the effects of heavy rains and devastating floods in many parts of the Niger basin (Descroix et al., 2013; Fiorillo et al., 2018; Tamagnone et al., 2019). In these areas, a complete flood risk assessment is particularly important for risk management (Siejka et al., 2018), and it is one of the goal of the ANADIA project (Paragraph 1, page 112). In this framework, the Land-cover maps provide essential data to describe the flood risk and develop flood risk management plans (Kalantar et al., 2017).

On the one hand, the Land Cover influences the flood itself. Covers, such as urban areas, bare soil, arable lands, and shrubs, have different permeability. Consequentially, the dominance of one over the other, or generally an unbalance in their distribution, strongly affects floods. The land cover also defines the surface roughness, which plays a crucial role in the runoff. For example, (Booth et al., 2002) demonstrate that grass-dominated landscapes exhibit larger peak flows than forest-dominated landscapes with impervious areas. The increase of the runoff in a water basin is a direct consequence of reducing the discharge time and, therefore, of the possibility of foods (Tamagnone et al., 2019).

On the other hand, mapping the land cover provides information regarding the items exposed to flood risks, such as infrastructures, agricultural lands, and human

settlements. Although, as (Siejka et al., 2018) underline, the Land cover in the vicinity of rivers is rarely taken into account in assessing the flood risk. When considered, it is often detected from the photointerpretation of low spatial-resolution data or semi-automatic classification algorithms. Nevertheless, high-detailed information can add a further level of information by detecting the particularly endangered items by the floods. For example, the houses are built with non-water resistant material, like in south-west Niger where traditional houses are built of earth and wood poles.

For images with very high resolution, such as those captured using Unmanned Aerial Vehicles (UAV) systems, object-oriented classification methods are more efficient in classifying the land cover (see paragraph 4.2, page 51). Although UAV data usually have low spectral resolution and, consequentially, the features to be classified have a relatively similar spectral response, they can be separated using spatial, texture, and contextual information (Kalantar et al., 2017). A typical case is represented by the concrete roofs and parking lots, which usually have a similar spectral signature, but they differ in texture and shape. Low spectral detail limitation is often reduced by incorporating texture features, elevation features, and/or robust classifiers.

Several studies have been conducted using different approaches and models for Land Cover classification. These studies have primarily varied according to the technique used, the training sample size, and the input dataset. (Zhang et al., 2017) developed a classification framework based on deep-learning, and OBIA proposed to classify UAV RGB imagery with 5 cm resolution into five categories. They use spatial, spectral, and texture features for 280 training objects. The classification achieved an overall accuracy of 97%.

Similarly, Sameen et al. (Sameen et al., 2018) classified an RGB orthomosaic with a 10 cm resolution of urban areas using Convolutional Neural Network (CNN). They achieved promising results, although the training dataset was pretty large compare to one of the other researches, and they identified seven classes with relatively low thematic detail. (Liu and Abd-Elrahman, 2018) propose seven high-thematic detail categories classification of wetlands from six-centimeter resolution UAV imagery using multi-view information. They used 2800 training objects and reached an overall accuracy of 80.4%. A novel method was developed by (Kalantar et al., 2017) that uses a fuzzy unordered rule. Their method reached a 91% overall accuracy. Other authors investigated the optimization of UAV imagery classification, such as (Ma et al., 2017a). The latter researched the optimum number of input features in the Random Forest (RF) and Support Vector Machine (SVM) classification of UAV RGB imagery (with 0.2 m resolution). They identified for

RF 8 features for 300 training objects. (De Luca et al., 2019) identified five classes from RGB and NIR information achieving 97% of overall accuracy using the Random Forest algorithm and 150 objects for each class. Most of these studies analyzed RGB imagery. Even though they generally obtain good results, they consider few classes with relatively low thematic detail. Moreover, none of them analyzed the goodness of the segmentation from a geometric point of view.

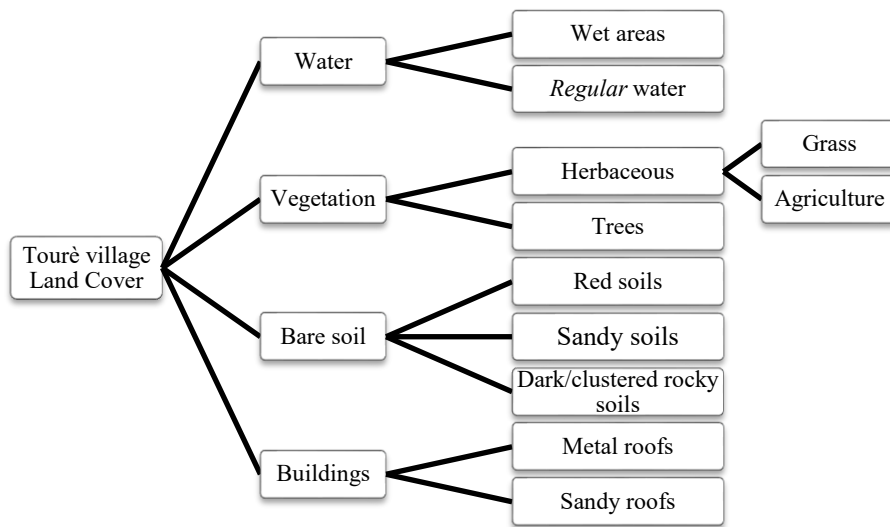
This classification aims to identify nine high-thematic classes from an RGB-NIR dataset using supervised OBIA-RF classification. Particular attention is given to the definition of classes to satisfy the flood risk management requirements and correctly identify, from a geometrical point of view too, the flood exposed buildings. A geometric validation for the segmentation is carried out for the buildings. The data collection, the pre-processing phase, and the generation of the orthomosaics are the same applied for identifying Temporary Surface Water Bodies (TSWB) as illustrated in paragraphs 8 and 8.1.2, pages 195-211.

### **8.3.1. Classes identification**

The classification system consists of four macro-classes (Water, vegetation, Bare soil, and Buildings); 9 classes; and two sub-classes (Figure 97).

The macro-class “buildings” is divided into two classes according to the material of the roofs: Brick roof (or sandy roofs) and metal roofs. The separation of the roof types is due to two reasons. First, these classes are differently affected by floods; indeed, houses with metal roofs are generally built with concrete bricks (as per the author’s experience) and thus less prone to be damaged by floods. On the contrary, sandy brick roofs are typical of traditional building techniques that consist of sun-dried bricks sustained by wooden poles and kept together by mud. Floods significantly damage these buildings. Even though they are very similar from a categorical point of view, the two classes strongly differ in the spectral response. Similar reasons exist behind the choice of the bare soil classes. Indeed, each type of soil has specific permeability and roughness that differently impact floods. Each soil type within the study areas has a specific spectral response that differs from other soils’ spectral responses. This is particularly true for the red soils and the sandy ones in the study area. The class of Agricultural land and the buildings are a significant class for the risk management plan. Agriculture is the main source of income for the local population of Tourè, and the damage of agricultural fields would be a consistent economic loss that can treat the food security of many households. Finally, the Wet Lands class is another class of interest for flood risk management because it represents an extremely variable class; it allows the analyst to define the limit of watered areas.





**Figure 97.** Classification legend structure composed of 4 macro-classes (Buildings, Bares soils, Vegetation, and Water); 10 classes and two sub-classes (Grass and agricultural lands).

### 8.3.2. Methods

#### *Features extraction*

Additional features can improve the quality of the classification (paragraph 2.3, page 56). The input dataset was enriched with derivative features, namely, spectral, textural, and elevation-based features. The extraction of features was based on the literature classification research (paragraph 2.3, page 56) and the author's personal experience. Ten features were extracted from the RGB and RGN datasets and used for the segmentation process: two spectral features, one edge-extractor feature, five GLCM textural features, and one Digital Surface Model.

Since the OBIA approach allows the analyst to introduce into the classification model features regarding the segmented objects' geometric characteristics and their relationship with the neighborhood's objects, 39 features were computed for each object. Table 81 reports the used measures for segmentation and classification.

#### *Segmentation*

The segmentation was carried out in three steps, each of which focused on identifying specific objects. First, the image was segmented with a multiresolution algorithm and threshold to separate the buildings. Then, the vegetated areas were divided into trees and herbaceous vegetation. The classes defined during the segmentation were then deleted to perform the Random Forest classification. Table 82 shows the eCognition ruleset used for the segmentation.

**Table 81.** Features selected for the segmentation and the classification

Feature Group	Feature Name	Note	Software	Segmentation	Classification
Spectral	Normalized Difference Water Index (NDWI)	(McFeeters, 1996)	Orfeo toolbox	X	X Mean value
	Enhanced Vegetation Index (EVI)		Orfeo toolbox	X	X Mean value
	HUE	Calculated on RGB	eCognition		X
	HUE	Calculate on NIR	eCognition		X
	Normalized Difference Water Index (NDWI)		eCognition		X Standard deviation to neighborhood
	Enhanced Vegetation Index (EVI)		eCognition		X Standard deviation to neighborhood
	Brightness		eCognition		X
Edge-extractor	Sobel		eCognition		X Mean value
	Sobel		eCognition		X Standard deviation to neighborhood
Textural (Haralick et al., 1973)	Grey Level Co-occurrence Matrix (GLCM) Sum Variance	Calculated on NIR channel	Orfeo toolbox	X	X Mean value
	Grey Level Co-occurrence Matrix (GLCM) Dissimilarity	Calculated on Green Channel	Orfeo toolbox	X	X Mean value
	Grey Level Co-occurrence Matrix (GLCM) Sum Average	Calculated on Green Channel	Orfeo toolbox	X	X Mean value
	Grey Level Co-occurrence Matrix (GLCM) Sum Variance	Calculated on Green Channel	Orfeo toolbox	X	X Mean value
	Grey Level Co-occurrence Matrix (GLCM) Dissimilarity	Calculated on NIR channel	Orfeo toolbox	X	X Mean value
	Grey Level Co-occurrence Matrix (GLCM) Sum Variance		eCognition		X Standard deviation to neighborhood
	Grey Level Co-occurrence Matrix (GLCM) Dissimilarity		eCognition		X Standard deviation to neighborhood
	Grey Level Co-occurrence Matrix (GLCM) Sum Average		eCognition		X Standard deviation to neighborhood
Continues in the following page					

	Grey Level Co-occurrence Matrix (GLCM) Sum Variance		eCognition		X Standard deviation to neighborhood
	Grey Level Co-occurrence Matrix (GLCM) Dissimilarity		eCognition		X Standard deviation to neighborhood
Elevation	Digital Surface Model	Calculated on RGB	/	X	X Mean value
	Digital Surface Model	Calculated on RGB	eCognition		X Standard deviation to neighborhood
	Slope				
RGB dataset	Red	/	/	X	X Mean value
	Green	/	/	X	X Mean value
	Blue	/	/	X	X Mean value
	Red	/	eCognition		X Standard deviation to neighborhood
	Green	/	eCognition		X Standard deviation to neighborhood
	Blue	/	eCognition		X Standard deviation to neighborhood
NIR dataset	Red_2	/	/	X	X Mean value
	Green_2	/	/	X	X Mean value
	NIR	/	/	X	X Mean value
	Red_2	/	eCognition		X Standard deviation to neighborhood
	Green_2	/	eCognition		X Standard deviation to neighborhood
	NIR	/	eCognition		X Standard deviation to neighborhood
Relation to neighbours	Mean difference to neighbors	Calculated on DSM	eCognition		X
Geometric	Length/Width		eCognition		X
	Rectangular fit		eCognition		X
	Radius of the smaller enclosing ellipse		eCognition		X
	Compactness		eCognition		X

**Table 82.** Segmentation ruleset applied for the Land Cover OBIA classification of Touré village

Algorithm	Parameters	Values	Computing time	Layers (weight) and conditions
Houses				
Multiresolution segmentation	Scale parameter	60	1:19	DSM (1) GLCM_NIR_3 (1) Glc_m_rgb_3 (2) Glc_m_rgb_5 (1) Green_rgb (1) Nir (1)
	Shape	0.2		
	Compactness	0.8		
Assign class	Use class	unclassified	0:27	Mean GLCM_adv_3_rgb >= 3.5 and Mean NDWI < 0.05 and Mean DSM >= 200 And Mean diff. to neighbors DSM (0) >= 0.2 Mean GLCM_adv_3_rgb >= 3.5 And Mean NDWI < 0.05 And Mean DSM >= 200 And Mean diff. to neighbors DSM (0) >= 0.2
	Assign class	Houses		
Assign class	Use class	unclassified	0:0.06	Rel. border to houses > 0.6
	Assign class	Houses		
Merge Region	Use class	Houses	0:0.04	
Multiresolution segmentation	Scale parameter	100	1:40	Only Houses GLCM_NIR_3 (1) Glc_m_rgb_3 (2) Glc_m_rgb_5 (1)
	Shape	0.8		
	Compactness	0.2		
Trees				
Merge Region	Use class	uncli	0:03	
Multiresolution segmentation	Scale parameter	80	2:17	Only Unclassified DSM (1) GLCM_NIR_3 (1) Glc_m_rgb_3 (1) Glc_m_rgb_5 (1) Green_rgb (1) NDWI (1) Nir (1)
	Shape	0.1		
	Compactness	0.5		
Assign class	Use class	unclassified	0:21	Mean diff. to neighbors DSM (0) > 1 and Mean NDWI < 0.03
	Assign class	Trees		
Merge Region	Use class	Trees	0:01	
Continues in the following page				

Grass				
Merge Region	Use class	unclassified	2:55	
Multiresolution segmentation	Scale parameter	200	2:37	Only Unclassified DSM (1) Glcm_rgb_5 (1) Green_rgb (1) NDWI (1) Nir (1) Red (NIR dataset) (1) Red (RGB dataset) (1)
	Shape	0.25		
	Compactness	0.2		

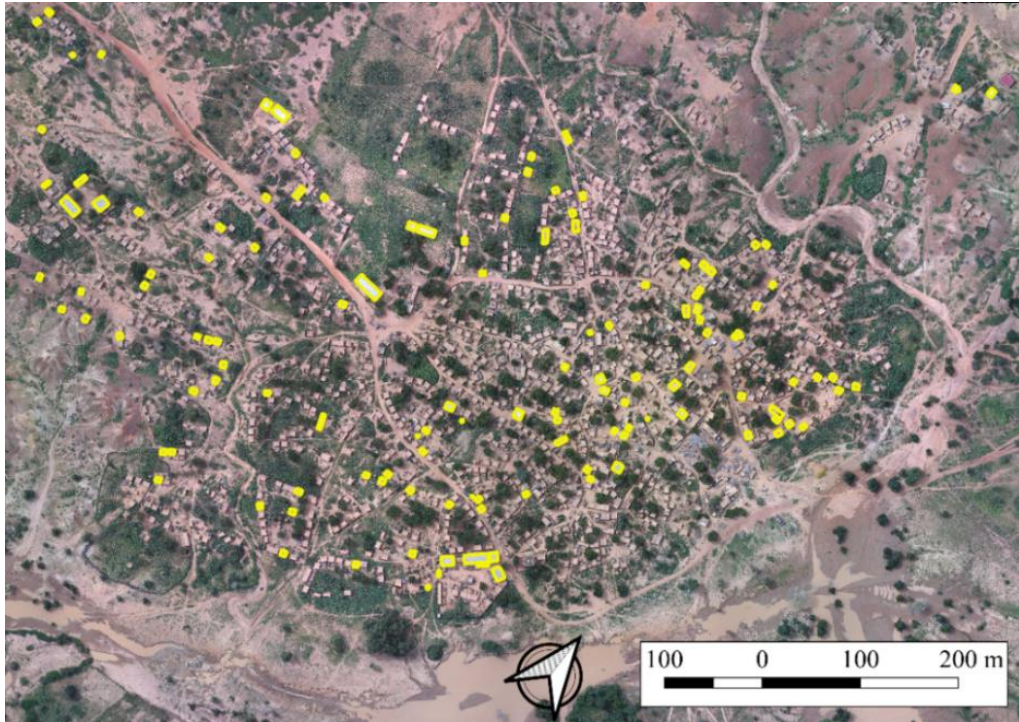
### ***Training selection and classification model***

The training and test dataset comprises 3046 objects: 200 sample objects for each class, except for classes 9 (Gullies) and 10 (Metal roofs) that have respectively 108 and 78. The difference in the number of objects reflects classes' covering within the study scene and objects' size. The selection of the training and test objects was randomized as much as possible by spreading random points within the scene and labeling them. The number of points within the classes was balanced by manually adding the missing points. The geometries on which the points lay were used to train and the model in proportion 50-50 (i.e. 1523 training objects and 1523 validation objects).

The model was trained in eCognition environment, with 100 Depth, 4 minimum sample count, and maximum tree number 50.

### ***Accuracy assessment***

Regarding the assessment of the segmentation (see paragraphs 4.5.1 and 4.5.2, pages 87-90), only the buildings were taken into account. Indeed the correct segmentation and location of these objects were considered more relevant than others for flood risk management. Namely, a visual evaluation and quantitative metrics were realized, in indices and RMSE forms both. The validation used for the segmentation is a two levels-accuracy assessment. The first level is based on (Ke and Quackenbush, 2011), and it consists of a simple visual evaluation. While the second level assessment is a quantitative method that compares several variables, and it assesses the under-segmentation and over-segmentation. Both accuracy assessment levels use as reference 133 objects randomly selected, but manually delineated (Figure 98).



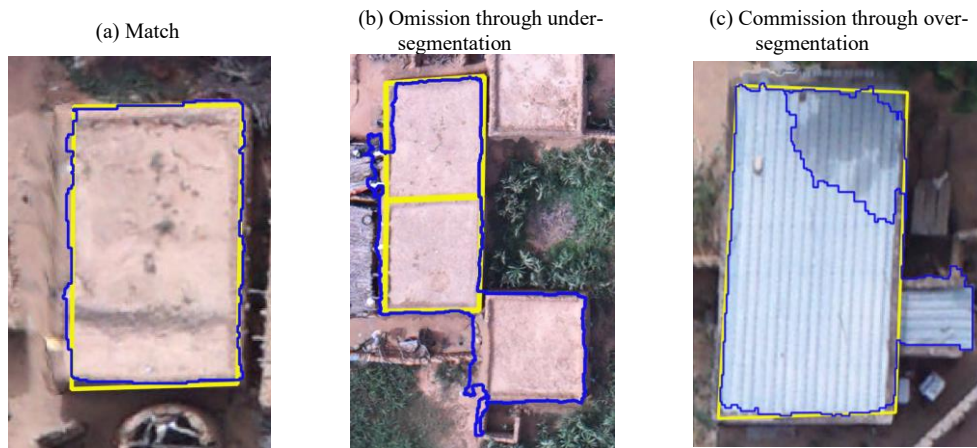
**Figure 98.** Position of the reference objects within the study area.

The accuracy was evaluated in terms of correspondence between the reference houses and the segmented ones. The goodness of the segmentation was assessed in two steps, as realized for the Alpine case study, see paragraph 7.1.3, page 146.

The situation shown in Figure 99a was considered as matching objects (M), while the relations of reference and segmented objects in Figure 99b and Figure 99c were considered as non-matching houses. The segmented houses were counted based on their overlap with the reference houses. For example, the segmented houses in Figure 99c are one, and in Figure 99d are three. Even if significant, these measures provide a partial view of the goodness of the segmentation. The Omission and Commission errors can describe more precisely the goodness of the segmentation. As illustrated by (Ke and Quackenbush, 2011), three possible cases of the relation between the reference dataset and the segmented one were taken into consideration: i) Match, ii) Omission through under-segmentation, and iii) Commission through over-segmentation, (Figure 99).

As qualitative measures to assess the goodness of the segmentation, the areal difference, the perimeter, the centroid's distance, the Under-segmentation index, the Over-segmentation index, and the completeness index were evaluated. The Root Mean Square Error (RMSE) was calculated for the area and the perimeter.

The classification goodness was evaluated using the overall accuracy, producer's accuracy, User's accuracy, and F1 score metrics, as described in paragraph 4.5.1, page 87.



**Figure 99.** Possible relations between reference crowns (yellow outline) and segmented crowns (blue outline)

### 8.3.3. Results

The complete segmentation was realized in 11 hours<sup>6</sup>, and it is composed of 34439 objects, while the classification was carried out in approximately 4 hours, Figure 100.



**Figure 100.** a) example of segmentation in a sample area, and b) its classification.

---

<sup>6</sup> These data should be considered carefully, since the analysis is machine-dependant. It was realised using a laptop with 16 GB RAM and 2.7 GHz processor.

### *Accuracy assessment*

The visual assessment reveals a tendency to over-segmenting (14 over-segmented objects against 7 under-segmented objects), Table 83. 84% of the houses were detected (112 matches over 133 references). The F1 score, which related user's and producer's accuracies, is 70%.

**Table 83.** Visual assessment metrics of the segmentation of the buildings in Niger case study

Visual validation	No. objects
No. References	133
No. Segmented	185
Matches	112
Omission Through Under-Segmentation	7
Commission Through Over-Segmentation	14
Producer's Accuracy	0.842
User's Accuracy	0.605
F1 Score	0.704

The area-based measures do not confirm the tendency of the segmentation method to over-segmenting. The median value on the over-segmentation average is only 0.32, while the under-segmentation index is 0.63. Although the difference between the indices is small, it is unneglectable. The completeness index (D) provides extremely positive information (0.069) along with the Jaccard index, which is 0.88 and reflects the F1 score of visual assessment (Table 84).

**Table 84.** Area-based quantitative assessment of the segmentation of the buildings in Niger case study. \* lower values means better segmentation.

	Over Segmentation Index*	Under Segmentation Index*	D*	Jaccard Index
Average	0.063	0.122	0.113	0.830
Min	0.000	0.002	0.009	0.181
Max	0.473	0.786	0.560	1.000
Median	0.032	0.063	0.069	0.882

Table 85 reports the RMSE measures, which indicates the precision of the extension of the segmented houses over the reference ones. The error over the Area is, on average, 2.29 m<sup>2</sup>, which represents the 6% on the average house extension. On the contrary, the RMSE of the perimeter is slightly higher, and it reaches 18% of error over the average perimeter extension.



**Table 85.** Root Mean Square Error of the Area and the Perimeters of the house objects in Niger study area

Metric	RMSE	Average value	%	u.m.
Area	2.289	40.594	6%	m2
Perimeter	4.368	24.778	18%	m

The classification assessment results picture good classification. The overall accuracy is over 94% (Table 86). The ten classes have user's accuracy of over 90% except for Grassland and Dark clustered rocky soils classes. Indeed the two classes are less accurate.

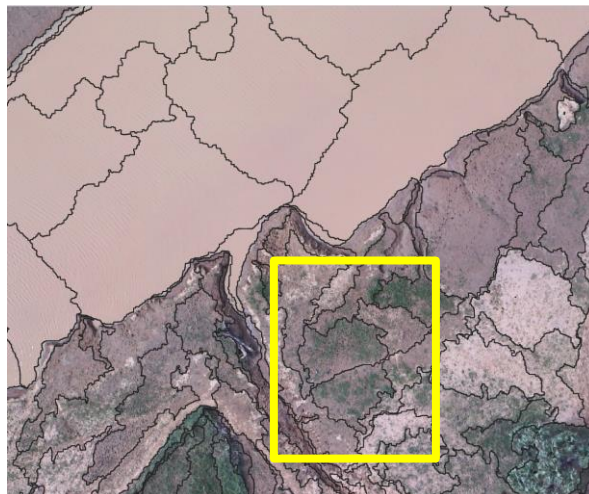
**Table 86.** Error matrix of Object-bases classification of Tourè along Sirba River (Niger).

	Wetland	Water	Grassland	Agricultural	Trees	Sandy soil	Clustered rocky dark soil	Gullies	Metal roofs houses	Bricks roofs houses	TOT
Wet land	<b>100</b>	0	0	0	0	0	0	0	0	0	<b>100</b>
Water	1	<b>98</b>	0	0	1	0	0	0	0	0	<b>100</b>
Grassland	6	0	<b>85</b>	6	1	0	1	1	0	0	<b>100</b>
Agricultural	0	0	0	<b>97</b>	1	1	0	1	0	0	<b>100</b>
Trees	0	0	0	1	<b>99</b>	1	0	0	0	0	<b>101</b>
Sandy soil	0	0	0	0	0	<b>93</b>	1	1	0	5	<b>100</b>
Clusted rocky dark soil	1	0	3	0	0	4	<b>86</b>	5	0	0	<b>99</b>
Gullies	0	0	0	0	0	1	1	<b>74</b>	0	3	<b>79</b>
Metal roofs houses	0	0	0	0	0	0	0	0	<b>44</b>	0	<b>44</b>
Bricks roofs houses	0	0	0	0	0	2	1	0	1	<b>96</b>	<b>100</b>
<b>TOT</b>	<b>108</b>	<b>98</b>	<b>88</b>	<b>104</b>	<b>102</b>	<b>102</b>	<b>90</b>	<b>82</b>	<b>45</b>	<b>104</b>	
Producer's acc.	0.926	1.000	0.966	0.933	0.971	0.912	0.956	0.902	0.978	0.923	OA= 0.945
user'acc	1.000	0.980	0.850	0.970	0.980	0.930	0.869	0.937	1.000	0.960	
F1-score	0.962	0.990	0.904	0.951	0.975	0.921	0.910	0.919	0.989	0.941	

### 8.3.4. Discussion and conclusions

The assessment of the houses' segmentation provides outstanding results. Indeed over 84% of the houses were correctly detected, and a low number of objects were under-segmented. Over segmentation is a frequent error, although apparently, the most common condition is the correct segmentation of the houses in terms of extension (testify by the low RMSE aver the area, 6%), described by more than one object. This may be caused by the roofs' spectral variation due mainly to shadows or damaged roofs, or objects on the roofs. Figure 99c is an example of over-segmentation caused by shaded roofs. Also, it appears from visual interpretation of aerial images that some households stock woods/straw covered by black plastic tissues on the roofs, interfering with the segmentation process. This frequent condition may also explain the higher RMSE over the perimeter in respect of the area. Even if the over-segmentation demonstrates the segmentation to be low-accurate, it is worth mentioning that it is partially overcome in the classification phase since the different segments are classified as “buildings” and later merged.

In regards to the classification, the Random Forest algorithm provided accurate results. The class Grassland has been classified as agricultural land and wet areas mainly. The confusion between Grassland and Agricultural land can be explained by the spectral similarity between them and the lack of textural distinction. It is worth underlining that some agricultural land does not have the typical cultivation pattern of plants on lines, thus not always detected by the textural information. At the same time, the confusion between grassland and wet areas depends on the presence of transition cover between the two, as Figure 101 shows.



**Figure 101.** Detail of the segmentation process. The yellow square indicates two objects of mixed class: grassland and wet areas.

The clustered rocky soil is confused with gullies. The main feature that distinguishes them is the DSM and its difference between the neighboring objects. As the wet areas and the grassland, some mixed classes between sandy and clustered soils exist. The main challenges faced during the classification are related to two main aspects: the high variability of the land cover within the village and the class definitions. The first is related to various objects in households ‘yards that are part of everyday life, such as Figure 102 (pot, dishes, plastic tissues, bottles, etc.). These objects have a significantly different spectral response since they are made of various materials, and thus, they create noise in the classification, altering the spectral values and the texture of these areas. Basically, this class is not fully represented in the classification system, and it was classified as bare soil. The other challenging aspect regards the confusion between agricultural areas and grasslands. The two classes are separated mainly by textural features based on the regular distribution of plants in rows. Nevertheless, this is not always true, some plots are rich in weeds, and the regular row pattern is imprecise since the agricultural works are not mechanized.

It is worth underlying that, according to the literature, the training dataset is relatively small, only 100 samples describe each class, but it is revealed to be sufficient for acceptable results. Similarly, some classes are underrepresented (less training objects), although this unbalance mirrors the area's real cover conditions. Such unbalances in the training datasets must be considered regular for classifications of relatively small areas and very specific classes such as the gullies and rocky-clustered areas. The same unbalance is present on the test dataset. Besides the inaccuracy related to the particularity of the area, the classification provides good results for DRR plans.



**Figure 102.** Example of land cover spectral variability within households ‘yards.

## 8.4. Comparison to existing LC classifications

As mentioned in paragraph 2.1 (page 9), many Land Cover maps deriving from the interpretation of Satellite data exist. The most used LC information for the European region is the Corine Land Cover, produced by the Copernicus programme. The latest version of Corine Land Cover (CLC) is referred to 2018 and it is based on Sentinel-2 data. It has 100 m spatial resolution and, at level 3 of detail, 40 classes. CLC classes includes land covers and use classes (i.e. recreation urban areas) (Falt'an et al., 2020). Having many classes of land cover and use makes the CLC adaptable to different applications.

For any LC production in Europe at high level of detail, a comparison with CLC is due. Such comparison requires the translation of the CLC classes into the target LC classification and the comparison of the LC maps according validation points or region.

The Alpine region LC classification from Sentinel 2 data tile Q (from now on named Alpine LC) was compared to CLC 2018. The class translation was realized according the CLC classes of **Table 44**, and each pixel of the map compared. An error matrix using CLC as reference was produced (Table 87). Four Land use classes of the CLC were not considered in the analysis because hardly translatable in the LC Alpine classification: 141 - Green urban areas; 142 - Sport and leisure facilities; 244 - Agro-forestry areas, 411 - Inland marshes. Globally, they cover 28 km<sup>2</sup>, less than the 0.5% of the analysed area (0.24%), which is a negligible cover for the comparison purposes.

Generally, there is good accordance between the two classifications. Indeed, the overall accuracy reaches 56%. *Conifers*, *Broadleaves* and *Agricultural land* are the classes that show better agreement between the LC classification (F1 score of 0.68, 0.70 and 0.68 respectively). As expected, the main incongruities are registered on the *Grasslands*, *Clustered-bare soils and sparse vegetation areas* and *Rocks* classes. Indeed, these three classes differ significantly in the thematic definition of CLC and Alpine LC. *Clustered-bare soils* are defined in Alpine LC as areas characterized by being prone to erosion. Indeed the class was trained using the USLE data (paragraph 7.2.2, page 180). This definition includes many alpine sparsely vegetated grasslands. Consequentially many pixels labeled *Grasslands* in Corine are in *Clustered-bare soils* class in Alpine LC. Similarly, the *Rocks* class of Corine includes the clustered rocky areas, which are typical of alpine environments, but, being interested by erosive activity, are part of the *Clustered-bare soils* class in LC alpine classification. Additional attention should be given to the differences of the spatial resolution and the detail of the classifications. Alpine LC has spatial

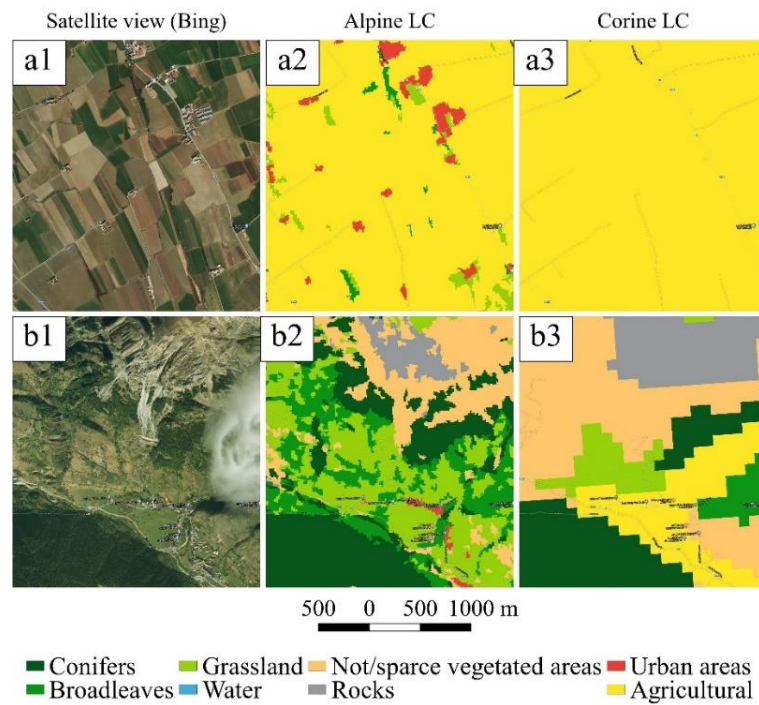
resolution ten times more detail than the CLC, which has pixel size of 100 m and a MMU of 25 hectares. The Alpine LC has spatial resolution of 10 m and the MMU is 100 m<sup>2</sup>. Large MMU, such the CLC MMU, may penalize the LC classes characterised by small and discontinuous cover distribution. As example, 25 ha MMU of CLC does not detect the isolated farms of Italian lowlands (Pianura Padana), which are well described by Alpine CLC. Surely the Urban areas and Water are the classes most penalized by lower spatial resolution of CLC. Small ponds, streams, farms, roads and railways are not represented (Figure 103).

**Table 87.** Error matrix of the CLC 2018 (reference) and Alpine Classification. To facilitate the reading, the values are reported in square kilometres.

	Conifers	Broadleaves	Grasslands	Water	Clustered bare soils and sparse vegetation	Rocks	Urban areas	Agricultural	Total
Conifers	1138	187	171	1	131	31	1	0	1661
Broadleaves	159	1469	203	1	14	3	10	7	1866
Grasslands	91	109	942	1	219	16	10	26	1415
Water	1	1	0	7	0	0	2	1	13
Clustered-bare soils	215	210	1011	4	846	123	21	4	2434
Rocks	7	1	50	5	702	332	1	0	1098
Urban areas	11	26	73	4	14	6	388	16	538
Agricultural	50	320	701	4	27	3	300	1575	2981
Total	1673	2323	3152	27	1954	515	734	1629	
PA	0.680	0.632	0.299	0.247	0.433	0.645	0.529	0.967	OA
UA	0.685	0.787	0.666	0.537	0.348	0.303	0.720	0.528	0.558
F1	0.683	0.701	0.413	0.339	0.386	0.412	0.610	0.683	

Concerning the Niger LC map, today there is no official product of Land Cover and use that can be considered a shared and trusted reference. Despite the large availability of satellite source data no harmonised LC product at high resolution exist. In 2017 ESA created a land cover classification map of Africa at 20m resolution using 180000 Copernicus Sentinel-2 images captured between December 2015 and December 2016 (ESA, 2016). The map is still a prototype and only eleven classes are described (i.e. Trees, Shrubs, Grasslands, Croplands, Aquatic Vegetation, Sparse Vegetation, Bare Areas, Built-Up Snow An Open Waters). The lack of thematic detail is compensate by the 20m spatial resolution, which make it unique in LC data of Niger. Although still a prototype only partiality validated, it

was used as reference LC map for the comparison of LC map of Sirba River generated with the stacked approach. The classes of the two LC systems are hardly harmonized, thus the translation required the creation of a target common classification for LC Africa ESA and LC of Sirba area, as **Table 88** shows.

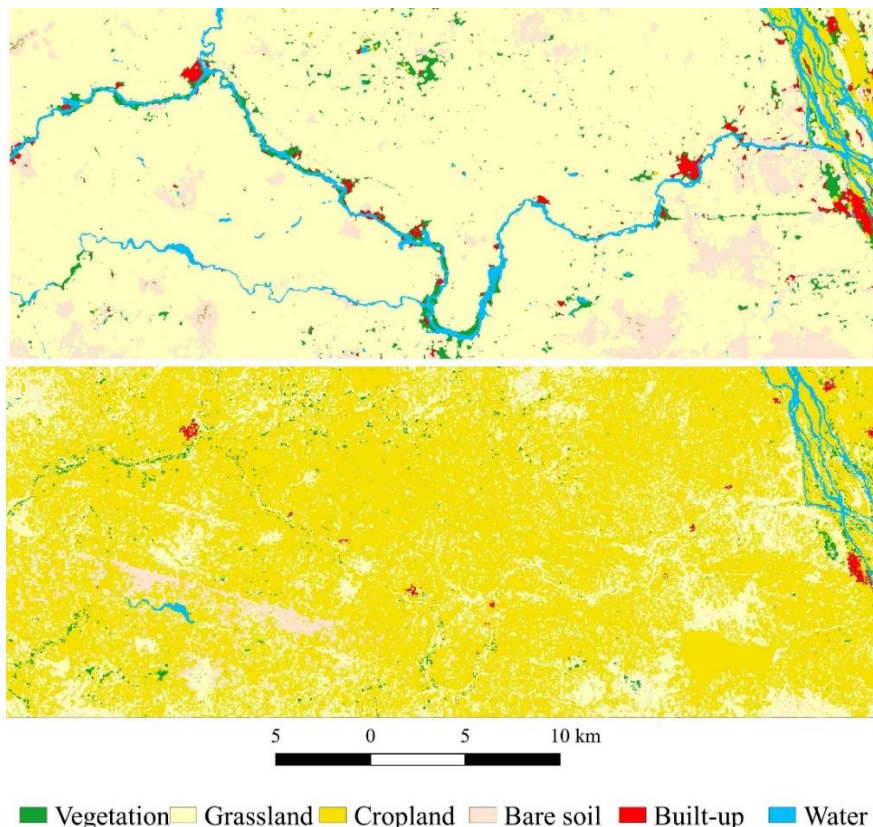


**Figure 103.** Examples of Alpine LC and Corine LC in plane area and mountainous zone; a1. Bing satellite view with Google labels of Padana plain; a2. Alpine LC classification and Google labels; a3. CLC2018 classification and Google labels. b1. Bing satellite view with Google labels of montaneous area (Valle Stura di Demonte, Italy); b2. Alpine LC classification and Google labels; b3. CLC2018 classification and Google labels.

**Table 88.** Conversion classes between ESA Africa LC and Sirba LC.

Common classes	ESA Africa LC	Sirba LC
1- Vegetation	1- Trees, 2 - Shrubs, 6 - Sparse vegetation	3 - Forest and bushes, 8- Plateaux vegetation
2- Grassland	3 - Grasslands	10 – non-irrigated agricultural lands and pastures
3- Cropland	4 - Cropland	9 – Irrigated agricultural lands
4 - Bare areas	7- Bare areas	5 – Red bare soils, 6 - Sandy soils, 2 - Plateaux
5 - Built-up	8- Built-up	4 – Urban areas
6 - Waters	5 Aquatic vegetation, 10 - Open waters	1 – Water bodies

Then a pixel by pixel comparison reveals low overall accuracy (0.203) despite the two classification have similar spatial resolution (10m and 20m). The major issue regards the confusion between *Grassland*, *Cropland* and *Bare areas*. The majority of pixels classified as *Grassland* in Sirba LC are labelled as *Bare areas* in the ESA Africa LC (**Table 89**). Similarly, most of the croplands of the Sirba LC are classified *Grassland* in the ESA LC. Indeed the F1 score of *Cropland* is only 0.056. Such results are ascribable to the nature of the definitions of pastures, grasslands and bare soils. In fact, pastures are considered *Agricultural land* in ESA LC, and *Grassland* in Sirba LC. This is clearly detectable from the visual comparison between the classifications (Figure 104). Sirba River and most of seasonal ponds and lakes are detected in Sirba LC and not in ESA LC, because of the dataset of the classifications. Sirba LC is a rainy season LC (only summer months on 2017-2019), while ESA LC is bases on one year observations. This influences also the vegetation class, which is captured in its maximum during the rainy season. A good overlap is present between the other classes. It is worth underling that the ESA Africa LC is a prototype and it is was validated using Crowdsourcing only for Kenya, Gabon, Ivory Coast and South Africa.



**Figure 104.** Sirba River area classified according Sirba LC (top) and ESA LC (bottom).

**Table 89.** Error matrix of the ESA LC Africa (reference) and Sirba Classification. To facilitate the reading, the values are reported in square kilometres.

	Vegetation	Grassland	Cropland	Bare areas	Built-up	Waters	Total
Vegetation	1068	1497	101	1568	56	97	4387
Grassland	2451	8908	105	34992	1103	787	48348
Cropland	7819	29140	1503	10711	1792	722	51686
Bare areas	36	1407	2	11037	19	113	12614
Built-up	58	4	66	59	584	12	783
Waters	10	0	101	4	0	1109	1224
Total	11442	40956	1879	58369	3554	2841	
PA	0.093	0.218	0.800	0.189	0.164	0.390	OA
UA	0.244	0.184	0.029	0.875	0.745	0.906	0.203
F1	0.135	0.200	0.056	0.311	0.269	0.546	

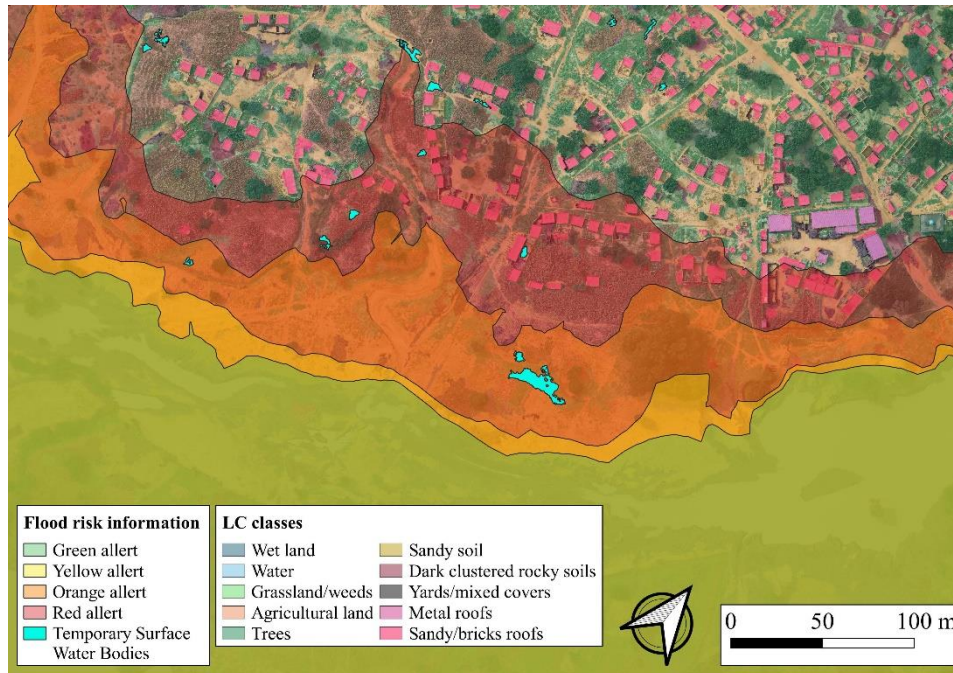
## 8.5. Atlas applications in Disaster Risk Reduction planning

The five classifications described in the previous chapters constitute the final Atlas, which provide information at different spatial and thematic resolution, and it is specifically though for Disaster Risk Reduction plans related to rockfall (Alps) and floods (Niger).

The Satellite classification of the Niger case study was used in flood risk analysis to map the Sirba riverbed and to detect the villages and settlements that lay along its banks. Moreover, the GNSS survey processed with PPP technique was used as base for the generation of a High Resolution DTM, which calibrated the hydraulic model. In major detail, hydraulic flood risk model derived from the hydraulic model allowed the definition of four risk levels. This information was disseminated via Atlas of flood risk (Massazza et al., 2020) and a web GIS (<http://www.slapis-niger.org/fr>) created by ANADIA 2.0 project. Moreover, the ANADIA project include also Plans for flood risk reduction at village level for Tourè and Larba Birno. In the definition of these plans the TSWB, the flood risk and the classified buildings were cross-examined to identify the elements exposed



to different levels of risk and quantify the potential losses. The planners integrated the TSWB information into the analysis for evaluating the post-flood health risk related to infectious diseases.



**Figure 105.** Extract from Tourè village (Niger) flood risk analysis considering the buildings exposed to four level of flood risk (Green, Yellow, Orange and Red) and water stagnation.

The Alpine case study offers a starting point for future application in rockfall risk analysis. The satellite Alpine LC classification allows the characterization of protection forests by cross-analysing the information regarding land morphology, the forest cover, its proximity to rocks and erosion-prone areas, and the urban areas. It is worth underling that this represent an approximate analysis since roads and railways are generally not detected in the classification since smaller than the MMU (100 m<sup>2</sup>). The individual tree crown map provides planners with forest parameters for rockfall modelling, and the main dendrometric parameters can be derived from ITD. Also, it can provide a basemap for the identification of past avalanches and rockfalls events.

# Chapter 9

## Conclusion and future vision

This research aims to investigate the existing methodology for the generation of Land Cover maps at Very High Resolution (VHR). The aspects examined concern the entire generation process: from the data acquisition and final result accuracy analysis.

The most innovative tool for the acquisition of VHR optical imagery is the Unmanned Aerial Vehicles (UAV), which are incredibly versatile for the data collection of environmental critical areas. They overcome the satellite data in terms of spatial and temporal resolution, and the recent introduction of UAV-embeddable hyperspectral and multispectral cameras makes UAV technology superior in terms of spectral resolution. Nevertheless, the satellite still dominates the optical data collection on extensive areas, and there is no comparison between the satellite historical dataset (which starts from 1972 with the Landsat mission) and the UAV's one. The UAV can be integrated with many different sensors according to the need of the survey. Simple devices for data acquisition can be created, such as the Raspberry InfraRed camera that, although extremely simple and cheap, allowed the photogrammetric reconstruction of flood-endangered areas. On the other hand, the UAV systems require quite long pre-classification processing and background knowledge about photogrammetry and positioning.

Precise georeferencing of the UAV-derived orthomosaics require additional time for the pre-classification phase, and, unlike satellite optical imagery, GNSS dual-frequency receivers are compulsory to have centimeter-level accuracy. The GNSS survey can have several limitations in geodetic depressed areas, but techniques such as PPP are now very accessible, thanks to high-performant platforms, for example, the CSRS-PPP.

Both UAV and satellite data require high-computational power for the analysis. Although new on-cloud processing platforms exist, such as Google Earth Engine (GEE), they provide only satellite optical datasets. GEE performs exceptionally well; nevertheless, it is still immature for detailed Land Cover analyses. The principal limit is the limited memory available for a single user and poor

documentation regarding the algorithms. Even if existing algorithms are regularly implemented (as an example, the GINI importance analysis has been recently introduced for the Random Forest algorithm), many functionalities and parameters are still missing.

Concerning the classification process, the machine learning overcomes the parametric classifiers since they can deal with non-Gaussian distributions and data of different kinds and nature can be easily integrated into the input dataset. For example, data from different optical sensors mounted on the UAV, as it was realized in Alpine arch and Sub-Saharan UAV case studies. The Random Forest algorithm is extremely performant for small training datasets, as the over 90% Overall accuracy of the five classifications of the Atlas testifies. Its limited sensitivity to the data distribution and its ensemble nature can be two of the causes related to the little influence of atmospheric correction (both the radiative and linear models, as tested over the Alpine case study) over the satellite images. Another factor influencing the low impact of atmospheric correction over the classification accuracy can be the little time span considered for the classifications.

The increase of the spatial and thematic resolution is directly proportional to the need for additional input features. The textural information was revealed to be fundamental in the classification and segmentation phases. Indeed, Grey Level Co-occurrence Matrix (GLCM)-derived measures, such as the ones proposed by Haralick, improve the classification of 10% in the Alpine satellite case study, and more specifically, it helps in the distinguish of high thematic detail classes, such as clustered bare soils in Alps classification and Urban areas in Sub-saharan. Textural information was revealed to have also a strong influence over the segmentation process.

Due to the high-spectral heterogeneity of VHR imagery, the single pixel of a specific feature of the scene can have enormous spectral variation. This is the main reason behind the spread of object-oriented (OBIA) techniques in their classification. The segmentation is still strongly-dependant on the analyst's experience, and many different approaches exist. The texture has been revealed to have a crucial role in the segmentation process too. Textural information resulting from multifractality analysis has proven to simplify the segmentation of homogeneous spectral areas, such as forests. In VHR OBIA classification, the assessment for the classes in a pixel-based approach is not enough. The need for assessing the segmentation is unneglectable. Additional research needs to be realized to find a shared and efficient geometric validation approach from this point of view.

The final Land Cover Maps of the Atlas satisfy most of Anderson's criteria listed in Table 3: the satellite classifications and the UAV LC map of Tourè have over 85% accuracy; the accuracy is almost equal for each class; the methodology has been proven to be repeatable and applicable over extensive areas (at least over the Alpine areas), and the classes structure is well defined and can be aggregated if needed. The satellite classifications do not satisfy criterion 6, which states that the classification system should be applicable over different time of the year, was not tested since the selection of specific time of the year is one of the factors that made

possible the separation of certain classes (agricultural land and bare soils along the Sirba river). The Individual Tree crown Detection and the Temporary Surface Water Bodies detection are hard to evaluate in terms of Anderson's criteria because they are focused on the segmentation of the image and the identification of a single specific class.

Besides being geographically and environmentally far from each other, the two case studies are bounded by being hard-to-map and endangered by natural hazards. The analysis and the methodology applied for the classification demonstrate that similar processing and treatments lead to good precisions and accuracy. For example, the textural information in both cases facilitates segmentation and classification. Similarly, the aggregated multi-temporal approach proposed to reduce the variability of the images led to high-accuracy classification. In both cases, selecting a limited period for the satellite classification allowed the maximization of the seasonal characterization. It increased the separability of some hard-to-map classes (clustered bare soils from solid rock, Nigerienne urban areas from bare soils and pastures).

The Atlas maps were created through supervised classification systems that require massive human work to create the training and test datasets. Additional research should be done to reduce this time. A possible solution to test and improve can be using stratified samples of already existing LC maps, as realized over the Alpine arch satellite case study. Today technologies, tools, and algorithms cannot only allow the atomization of the process, but they can also lead to more detailed classification using less expensive tools in economic terms. Future research should focus on the optimization of the classification process to reduce the costs related to the sensors for data acquisition, the pre-processing, and the classification itself.

# References

- Abdullah S, S., Tahar, K.N., Rashid, M.F.A., Osoman, M.A., 2019. Capabilities of UAV-Based Watershed Segmentation Method for Estimating Tree Crown: A Case Study of Oil Palm Tree. *IOP Conf. Ser.: Earth Environ. Sci.* 385, 012015. <https://doi.org/10.1088/1755-1315/385/1/012015>
- Achard, F., Eva, H., Mayaux, P., n.d. Tropical forest mapping from coarse spatial resolution satellite data: production and accuracy assessment issues 23.
- Aden, S.T., Bialas, J.P., Champion, Z., Levin, E., McCarty, J.L., 2014. Low cost infrared and near infrared sensors for UAVs. *ISPRS - International Archives of the Photogrammetry, Remote Sensing and Spatial Information Sciences XL-1*, 1–7. <https://doi.org/10.5194/isprsarchives-XL-1-1-2014>
- Agarwal, S., Snavely, N., Seitz, S.M., Szeliski, R., 2010. Bundle adjustment in the large, in: *Proceedings of the 11th European Conference on Computer Vision: Part II, ECCV'10*. Springer-Verlag, Heraklion, Crete, Greece, pp. 29–42.
- Agrawal, N., Singhal, S., 2015. Smart drip irrigation system using raspberry pi and arduino, in: *Communication Automation International Conference on Computing*. Presented at the *Communication Automation International Conference on Computing*, pp. 928–932. <https://doi.org/10.1109/CCAA.2015.7148526>
- Aich, V., Koné, B., Hattermann, F.F., Paton, E.N., 2016. Time Series Analysis of Floods across the Niger River Basin. *Water* 8, 165. <https://doi.org/10.3390/w8040165>
- Akhloufi, M.A., Bendada, A., 2013. Fusion of active and passive infrared images for face recognition, in: *Thermosense: Thermal Infrared Applications XXXV*. Presented at the *Thermosense: Thermal Infrared Applications XXXV*, International Society for Optics and Photonics, p. 87050B. <https://doi.org/10.1117/12.2017942>
- Aksoy, S., Koperski, K., Tusk, C., Marchisio, G., 2009. Land Cover Classification with Multi-Sensor Fusion of Partly Missing Data [WWW Document]. <https://doi.org/info:doi/10.14358/PERS.75.5.577>
- Aleksandrowicz, S., Wawrzaszek, A., Drzewiecki, W., Krupinski, M., 2016. Change Detection Using Global and Local Multifractal Description. *IEEE Geosci. Remote Sensing Lett.* 13, 1183–1187. <https://doi.org/10.1109/LGRS.2016.2574940>
- Al-Saddik, H., Simon, J.C., Cointault, F., 2019. Assessment of the optimal spectral bands for designing a sensor for vineyard disease detection: the case of ‘Flavescence dorée.’ *Precision Agric* 20, 398–422. <https://doi.org/10.1007/s11119-018-9594-1>
- Altamimi, Z., Rebischung, P., Métivier, L., Collilieux, X., 2016. ITRF2014: A new release of the International Terrestrial Reference Frame modeling nonlinear station motions. *Journal of Geophysical Research: Solid Earth* 121, 6109–6131. <https://doi.org/10.1002/2016JB013098>
- Al-Wassai, F.A., Kalyankar, N.V., 2013. Major Limitations of Satellite images. *arXiv:1307.2434 [cs]*.
- Amarasinghe, A., Wijesuriya, V.B., 2020. Drones vs Dengue: A Drone-Based Mosquito Control System for Preventing Dengue, in: *2020 RIVF International Conference on Computing and Communication Technologies*

- (RIVF). Presented at the 2020 RIVF International Conference on Computing and Communication Technologies (RIVF), pp. 1–6. <https://doi.org/10.1109/RIVF48685.2020.9140773>
- Anderson, G.P., Felde, G.W., Hoke, M.L., Ratkowski, A.J., Cooley, T.W., Chetwynd Jr, J.H., Gardner, J.A., Adler-Golden, S.M., Matthew, M.W., Berk, A., 2002. MODTRAN4-based atmospheric correction algorithm: FLAASH (Fast Line-of-sight Atmospheric Analysis of Spectral Hypercubes), in: Algorithms and Technologies for Multispectral, Hyperspectral, and Ultraspectral Imagery VIII. International Society for Optics and Photonics, pp. 65–71.
- Anderson, J.R., 1976. A Land Use and Land Cover Classification System for Use with Remote Sensor Data. U.S. Government Printing Office.
- APPS, n.d. Automatic Precise Positioning Service - APPS [WWW Document]. URL <http://apps.gdgps.net/index.php> (accessed 9.4.19).
- AUSPOS, A.G., 2014. AUSPOS - Online GPS Processing Service [WWW Document]. URL <https://www.ga.gov.au/scientific-topics/positioning-navigation/geodesy/auspos> (accessed 9.4.19).
- Baamonde, S., Cabana, M., Sillero, N., Penedo, M.G., Naveira, H., Novo, J., 2019. Fully automatic multi-temporal land cover classification using Sentinel-2 image data. *Procedia Computer Science, Knowledge-Based and Intelligent Information & Engineering Systems: Proceedings of the 23rd International Conference KES2019* 159, 650–657. <https://doi.org/10.1016/j.procs.2019.09.220>
- Baluja, J., Diago, M.P., Balda, P., Zorer, R., Meggio, F., Morales, F., Tardaguila, J., 2012. Assessment of vineyard water status variability by thermal and multispectral imagery using an unmanned aerial vehicle (UAV). *Irrig Sci* 30, 511–522. <https://doi.org/10.1007/s00271-012-0382-9>
- Banu, T.P., Borlea, G.F., Banu, C., 2016. The Use of Drones in Forestry. *Journal of Environmental Science and Engineering B* 5. <https://doi.org/10.17265/2162-5263/2016.11.007>
- Belcore, E., Pezzoli, A., Calvo, A., 2019a. Analysis of gender vulnerability to climate-related hazards in a rural area of Ethiopia. *The Geographical Journal* 0. <https://doi.org/10.1111/geoj.12321>
- Belcore, E., Pezzoli, A., Massazza, G., Rosso, M., Piras, M., 2019b. Raspberry Pi 3 multispectral low-cost sensor for UAV-based remote sensing. Case study in south-west Niger. *Int. Arch. Photogramm. Remote Sens. Spatial Inf. Sci. XLII-2/W13*, 207–214. <https://doi.org/10.5194/isprs-archives-XLII-2-W13-207-2019>
- Belcore, E., Piras, M., Pezzoli, A., Massazza, G., Rosso, M., 2019c. Detection of temporary surface water bodies in Niger using high resolution imagery.
- Belcore, E., Piras, M., Wozniak, E., 2020. Specific alpine environment land cover classification methodology: Google Earth Engine processing for Sentinel-2 data. *Int. Arch. Photogramm. Remote Sens. Spatial Inf. Sci. XLIII-B3-2020*, 663–670. <https://doi.org/10.5194/isprs-archives-XLIII-B3-2020-663-2020>
- Belcore, Elena, Wawrzaszek, A., Wozniak, E., Grasso, N., Piras, M., 2020. Individual Tree Detection from UAV Imagery Using Hölder Exponent. *Remote Sensing* 12, 2407. <https://doi.org/10.3390/rs12152407>
- Belgiu, M., Drăguț, L., 2016. Random forest in remote sensing: A review of applications and future directions. *ISPRS Journal of Photogrammetry and Remote Sensing* 114, 24–31. <https://doi.org/10.1016/j.isprsjprs.2016.01.011>

- Berberoğlu, S., Akin, A., Atkinson, P.M., Curran, P.J., 2010. Utilizing image texture to detect land-cover change in Mediterranean coastal wetlands. *International Journal of Remote Sensing* 31, 2793–2815. <https://doi.org/10.1080/01431160903111077>
- Berie, H.T., Burud, I., 2018. Application of unmanned aerial vehicles in earth resources monitoring: focus on evaluating potentials for forest monitoring in Ethiopia. *European Journal of Remote Sensing* 51, 326–335. <https://doi.org/10.1080/22797254.2018.1432993>
- Berni, J.A.J., Zarco-Tejada, P.J., Suárez, L., González-Dugo, V., Fereres, E., n.d. REMOTE SENSING OF VEGETATION FROM UAV PLATFORMS USING LIGHTWEIGHT MULTISPECTRAL AND THERMAL IMAGING SENSORS 6.
- Biau, G., Scornet, E., 2016. A random forest guided tour. *TEST* 25, 197–227. <https://doi.org/10.1007/s11749-016-0481-7>
- Bigi, V., Pezzoli, A., Rosso, M., 2018. Past and Future Precipitation Trend Analysis for the City of Niamey (Niger): An Overview. *Climate* 6, 73. <https://doi.org/10.3390/cli6030073>
- Bisnath, S., Gao, Y., 2009. Current State of Precise Point Positioning and Future Prospects and Limitations, in: Sideris, M.G. (Ed.), *Observing Our Changing Earth*, International Association of Geodesy Symposia. Springer, Berlin, Heidelberg, pp. 615–623. [https://doi.org/10.1007/978-3-540-85426-5\\_71](https://doi.org/10.1007/978-3-540-85426-5_71)
- Bisnath, S., Wells, D., Dodd, D., 2003. Evaluation of Commercial Carrier-Phase-Based WADGPS Services for Marine Applications. Presented at the Proceedings of the 16th International Technical Meeting of the Satellite Division of The Institute of Navigation (ION GPS/GNSS 2003), pp. 17–27.
- Blaschke, T., 2010. Object based image analysis for remote sensing. *ISPRS Journal of Photogrammetry and Remote Sensing* 65, 2–16. <https://doi.org/10.1016/j.isprsjprs.2009.06.004>
- Booth, D.B., Hartley, D., Jackson, R., 2002. FOREST COVER, IMPERVIOUS-SURFACE AREA, AND THE MITIGATION OF STORMWATER IMPACTS. *J Am Water Resources Assoc* 38, 835–845. <https://doi.org/10.1111/j.1752-1688.2002.tb01000.x>
- Bottai, L., Arcidiaco, L., Chiesi, M., Maselli, F., 2013. Application of a single-tree identification algorithm to LiDAR data for the simulation of stem volume current annual increment. *JARS* 7, 073699. <https://doi.org/10.1117/1.JRS.7.073699>
- Bowles, J.H., Mike, n.d. The Two Most Important Algorithms in Predictive Modeling Today: Strata 2012 - O'Reilly Conferences, February 28 - March 01, 2012, Santa Clara, CA [WWW Document]. URL <https://conferences.oreilly.com/strata/strata2012/public/schedule/detail/22658> (accessed 5.26.20).
- Breiman, L., 2001. Random Forests. *Machine Learning* 45, 5–32. <https://doi.org/10.1023/A:1010933404324>
- Bruce, C.M., Hilbert, D.W., Cooperative Research Centre for Tropical Rainforest Ecology and Management, CSIRO (Australia), Tropical Forest Research Centre, 2006. Pre-processing methodology for application to Landsat TM/ETM+ imagery of the wet tropics. Rainforest CRC, Cairns, Qld.
- Burdziej, J., Kunz, M., 2007. Effect of digital terrain model resolution on topographic parameters calculation and spatial distribution of errors 12.
- Burton, I., Kates, R.W., White, G.F., 1993. *The environment as hazard*, 2nd ed. ed. Guilford Press, New York.

- Campbell, J.B., Wynne, R.H., 2011. *Introduction to remote sensing*, 5th ed. ed. Guilford Press, New York.
- Carrasco, L., O’Neil, A.W., Morton, R.D., Rowland, C.S., 2019. Evaluating Combinations of Temporally Aggregated Sentinel-1, Sentinel-2 and Landsat 8 for Land Cover Mapping with Google Earth Engine. *Remote Sensing* 11, 288. <https://doi.org/10.3390/rs11030288>
- Carrasco-Escobar, G., Manrique, E., Ruiz-Cabrejos, J., Saavedra, M., Alava, F., Bickersmith, S., Prussing, C., Vinetz, J.M., Conn, J.E., Moreno, M., Gamboa, D., 2019. High-accuracy detection of malaria vector larval habitats using drone-based multispectral imagery. *PLOS Neglected Tropical Diseases* 13, e0007105. <https://doi.org/10.1371/journal.pntd.0007105>
- Chaudhuri, P., Ghosh, A.K., Oja, H., 2009. Classification Based on Hybridization of Parametric and Nonparametric Classifiers. *IEEE Transactions on Pattern Analysis and Machine Intelligence* 31, 1153–1164. <https://doi.org/10.1109/TPAMI.2008.149>
- Chavez, P.S., 1988. An improved dark-object subtraction technique for atmospheric scattering correction of multispectral data. *Remote Sensing of Environment* 24, 459–479. [https://doi.org/10.1016/0034-4257\(88\)90019-3](https://doi.org/10.1016/0034-4257(88)90019-3)
- Chisholm, R.A., Cui, J., Lum, S.K.Y., Chen, B.M., 2013. UAV LiDAR for below-canopy forest surveys. *J. Unmanned Veh. Sys.* 01, 61–68. <https://doi.org/10.1139/juvs-2013-0017>
- Chuvieco, E., 2016. *Fundamentals of satellite remote sensing: an environmental approach*, Second edition. ed. CRC Press, Taylor & Francis Group, Boca Raton.
- Clarke, K., 2001. *Proceedings of the 20th International Cartographic Conference, ICC 2001 Beijing China August 6-10, 2001: Mapping the 21st century. Cartography in a mobile internet age.* The Society, Beijing.
- Clinton, N., Holt, A., Scarborough, J., Yan, L., Gong, P., 2010. Accuracy Assessment Measures for Object-based Image Segmentation Goodness [WWW Document]. <https://doi.org/info:doi/10.14358/PERS.76.3.289>
- Collins, P., Bisnath, S., 2011. Issues in Ambiguity Resolution for Precise Point Positioning. Presented at the Proceedings of the 24th International Technical Meeting of the Satellite Division of The Institute of Navigation (ION GNSS 2011), pp. 679–687.
- Colomina, I., Molina, P., 2014. Unmanned aerial systems for photogrammetry and remote sensing: A review. *ISPRS Journal of Photogrammetry and Remote Sensing* 92, 79–97. <https://doi.org/10.1016/j.isprsjprs.2014.02.013>
- Connors, R.W., Trivedi, M.M., Harlow, C.A., 1984. Segmentation of a high-resolution urban scene using texture operators. *Computer Vision, Graphics, and Image Processing* 25, 273–310. [https://doi.org/10.1016/0734-189X\(84\)90197-X](https://doi.org/10.1016/0734-189X(84)90197-X)
- Copernicus, n.d. CORINE Land Cover (CLC) — Copernicus Land Monitoring Service [WWW Document]. URL <https://land.copernicus.eu/user-corner/publications/clc-flyer> (accessed 3.16.20).
- Corcoran, J.M., Knight, J.F., Gallant, A.L., 2013. Influence of Multi-Source and Multi-Temporal Remotely Sensed and Ancillary Data on the Accuracy of Random Forest Classification of Wetlands in Northern Minnesota. *Remote Sensing* 5, 3212–3238. <https://doi.org/10.3390/rs5073212>
- Cowell, R., 1997. Stretching the Limits: Environmental Compensation, Habitat Creation and Sustainable Development. *Transactions of the Institute of British Geographers* 22, 292–306.



- Dale, V.H., 1997. The Relationship Between Land-Use Change and Climate Change. *Ecological Applications* 7, 753–769. <https://doi.org/10.2307/2269433>
- Danila, E., Hahuie, V., Georgescu, P.L., Moraru, L., 2019. SURVEY OF FOREST COVER CHANGES BY MEANS OF MULTIFRACTAL ANALYSIS. *Carpath. J. Earth Environ. Sci.* 14, 51–60. <https://doi.org/10.26471/cjees/2019/014/057>
- De Luca, G., N. Silva, J.M., Cerasoli, S., Araújo, J., Campos, J., Di Fazio, S., Modica, G., 2019. Object-Based Land Cover Classification of Cork Oak Woodlands using UAV Imagery and Orfeo ToolBox. *Remote Sensing* 11, 1238. <https://doi.org/10.3390/rs11101238>
- DeFries, R.S., Chan, J.C.-W., 2000. Multiple Criteria for Evaluating Machine Learning Algorithms for Land Cover Classification from Satellite Data. *Remote Sensing of Environment* 74, 503–515. [https://doi.org/10.1016/S0034-4257\(00\)00142-5](https://doi.org/10.1016/S0034-4257(00)00142-5)
- Delalay, M., Tiwari, V., Ziegler, A.D., Gopal, V., Passy, P., 2019. Land-use and land-cover classification using Sentinel-2 data and machine-learning algorithms: operational method and its implementation for a mountainous area of Nepal. *JARS* 13, 014530. <https://doi.org/10.1117/1.JRS.13.014530>
- Descroix, L., Moussa, I.B., Genthon, P., Sighomnou, D., Mahé, G., Mamadou, I., Vandervaere, J.-P., Gautier, E., Maïga, O.F., Rajot, J.-L., Abdou, M.M., Dessay, N., Ingatan, A., Noma, I., Yéro, K.S., Karambiri, H., Fensholt, R., Albergel, J., Olivry, J.-C., 2013. Impact of Drought and Land – Use Changes on Surface – Water Quality and Quantity: The Sahelian Paradox. Current Perspectives in Contaminant Hydrology and Water Resources Sustainability. <https://doi.org/10.5772/54536>
- Dhun, K., 2011. APPLICATION OF LIDAR DEMS TO THE MODELLING OF SURFACE DRAINAGE PATTERNS IN HUMAN MODIFIED LANDSCAPES.
- Dietz, A.J., Hu, Z., Tsai, Y.-L., 2018. REMOTE SENSING OF SNOW COVER IN THE ALPS - AN OVERVIEW OF OPPORTUNITIES AND CONSTRAINTS 2.
- D’Oleire-Oltmanns, S., Marzoff, I., Peter, K.D., Ries, J.B., 2012. Unmanned Aerial Vehicle (UAV) for Monitoring Soil Erosion in Morocco. *Remote Sensing* 4, 3390–3416. <https://doi.org/10.3390/rs4113390>
- Dong, T., Zhang, X., Ding, Z., Fan, J., 2020. Multi-layered tree crown extraction from LiDAR data using graph-based segmentation. *Computers and Electronics in Agriculture* 170, 105213. <https://doi.org/10.1016/j.compag.2020.105213>
- Dorren, L.K.A., Maier, B., Seijmonsbergen, A.C., 2003. Improved Landsat-based forest mapping in steep mountainous terrain using object-based classification. *Forest Ecology and Management* 183, 31–46. [https://doi.org/10.1016/S0378-1127\(03\)00113-0](https://doi.org/10.1016/S0378-1127(03)00113-0)
- Drzewiecki, W., Wawrzaszek, A., Aleksandrowicz, S., Krupiński, M., Bernat, K., 2013. Comparison of selected textural features as global content-based descriptors of VHR satellite image, in: 2013 IEEE International Geoscience and Remote Sensing Symposium - IGARSS. Presented at the 2013 IEEE International Geoscience and Remote Sensing Symposium - IGARSS, pp. 4364–4366. <https://doi.org/10.1109/IGARSS.2013.6723801>
- Du, P., Samat, A., Waske, B., Liu, S., Li, Z., 2015. Random Forest and Rotation Forest for fully polarized SAR image classification using polarimetric and

- spatial features. *ISPRS Journal of Photogrammetry and Remote Sensing* 105, 38–53. <https://doi.org/10.1016/j.isprsjprs.2015.03.002>
- Duda, R.O., Hart, P.E., Stork, D.G., 2012. *Pattern Classification*. John Wiley & Sons.
- Dundar, M., Ehlmann, B.L., Leask, E.K., 2019. Machine-Learning-Driven New Geologic Discoveries at Mars Rover Landing Sites: Jezero and NE Syrtis. *arXiv:1909.02387 [astro-ph, stat]*.
- EGA, 2019. European GNSS Agency [WWW Document]. URL <https://www.gsa.europa.eu/> (accessed 9.30.19).
- Eisavi, V., Homayouni, S., Yazdi, A.M., Alimohammadi, A., 2015. Land cover mapping based on random forest classification of multitemporal spectral and thermal images. *Environ Monit Assess* 187, 291. <https://doi.org/10.1007/s10661-015-4489-3>
- El-Asmar, H.M., Hereher, M.E., 2011. Change detection of the coastal zone east of the Nile Delta using remote sensing. *Environmental Earth Sciences* 62, 769–777. <https://doi.org/10.1007/s12665-010-0564-9>
- Elmezayen, A., El-Rabbany, A., 2019. Precise Point Positioning Using World's First Dual-Frequency GPS/GALILEO Smartphone. *Sensors* 19, 2593. <https://doi.org/10.3390/s19112593>
- El-Mowafy, A., 2012. *Precise Real-Time Positioning Using Network RTK. Global Navigation Satellite Systems: Signal, Theory and Applications*. <https://doi.org/10.5772/29502>
- Eren Kamil, Uzel Turgut, Gulal Engin, Yildirim Omer, Cingoz Ayhan, 2009. Results from a Comprehensive Global Navigation Satellite System Test in the CORS-TR Network: Case Study. *Journal of Surveying Engineering* 135, 10–18. [https://doi.org/10.1061/\(ASCE\)0733-9453\(2009\)135:1\(10\)](https://doi.org/10.1061/(ASCE)0733-9453(2009)135:1(10))
- ESA, 2019. ESA [WWW Document]. European Space Agency. URL <https://www.esa.int/ESA> (accessed 9.30.19).
- ESA, 2016. ESA CCI LAND COVER – S2 prototype Land Cover 20m map of Africa 2016 [WWW Document]. URL <http://2016africallandcover20m.esrin.esa.int/> (accessed 4.12.21).
- Eslami, M., Mohammadzadeh, A., 2017. A novel method for urban land cover mapping based on new vegetation indices and texture-spectral information from fused visible and hyperspectral thermal infrared airborne data. *European Journal of Remote Sensing* 50, 320–331. <https://doi.org/10.1080/22797254.2017.1328645>
- Falt'an, V., Petrovič, F., O'ahel', J., Feranec, J., Druga, M., Hruška, M., Nováček, J., Solár, V., Mechurová, V., 2020. Comparison of CORINE Land Cover Data with National Statistics and the Possibility to Record This Data on a Local Scale—Case Studies from Slovakia. *Remote Sensing* 12, 2484. <https://doi.org/10.3390/rs12152484>
- FAO, 2000. *LAND COVER CLASSIFICATION SYSTEM* [WWW Document]. URL <http://www.fao.org/3/x0596e/x0596e01e.htm> (accessed 9.29.19).
- Farda, N.M., 2017. Multi-temporal Land Use Mapping of Coastal Wetlands Area using Machine Learning in Google Earth Engine. *IOP Conf. Ser.: Earth Environ. Sci.* 98, 012042. <https://doi.org/10.1088/1755-1315/98/1/012042>
- Farr, T.G., Rosen, P.A., Caro, E., Crippen, R., Duren, R., Hensley, S., Kobrick, M., Paller, M., Rodriguez, E., Roth, L., Seal, D., Shaffer, S., Shimada, J., Umland, J., Werner, M., Oskin, M., Burbank, D., Alsdorf, D., 2007. The Shuttle Radar Topography Mission. *Reviews of Geophysics* 45. <https://doi.org/10.1029/2005RG000183>

- Feng, Q., Liu, J., Gong, J., 2015. UAV Remote Sensing for Urban Vegetation Mapping Using Random Forest and Texture Analysis. *Remote Sensing* 7, 1074–1094. <https://doi.org/10.3390/rs70101074>
- Few, R., Ahern, M., Matthies, F., Kovats, S., 2004. Floods, health and climate change: a strategic review 139.
- Fiorillo, E., Crisci, A., Issa, H., Maracchi, G., Morabito, M., Tarchiani, V., 2018. Recent Changes of Floods and Related Impacts in Niger Based on the ANADIA Niger Flood Database. *Climate* 6, 59. <https://doi.org/10.3390/cli6030059>
- Fischler, M.A., Bolles, R.C., 1981. Random sample consensus: a paradigm for model fitting with applications to image analysis and automated cartography. *Commun. ACM* 24, 381–395. <https://doi.org/10.1145/358669.358692>
- Fonstad, M.A., Dietrich, J.T., Courville, B.C., Jensen, J.L., Carbonneau, P.E., 2013. Topographic structure from motion: a new development in photogrammetric measurement. *Earth Surface Processes and Landforms* 38, 421–430. <https://doi.org/10.1002/esp.3366>
- Forsyth, D., Ponce, J., 2012. *Computer vision: a modern approach*, 2nd ed. ed. Pearson, Boston.
- Foundation, R.P., n.d. *Raspberry Pi — Teach, Learn, and Make with Raspberry Pi* [WWW Document]. Raspberry Pi. URL <https://www.raspberrypi.org> (accessed 3.20.19).
- Franklin, S.E., Wulder, M.A., 2002. Remote sensing methods in medium spatial resolution satellite data land cover classification of large areas. *Progress in Physical Geography: Earth and Environment* 26, 173–205. <https://doi.org/10.1191/0309133302pp332ra>
- Gal, L., Grippa, M., Hiernaux, P., Pons, L., Kergoat, L., 2017. The paradoxical evolution of runoff in the pastoral Sahel: analysis of the hydrological changes over the Agoufou watershed (Mali) using the KINEROS-2 model. *Hydrology and Earth System Sciences* 21, 4591–4613. <https://doi.org/10.5194/hess-21-4591-2017>
- Gao, B., 1996. NDWI—A normalized difference water index for remote sensing of vegetation liquid water from space. *Remote Sensing of Environment* 58, 257–266. [https://doi.org/10.1016/S0034-4257\(96\)00067-3](https://doi.org/10.1016/S0034-4257(96)00067-3)
- Gao, B.-C., Davis, C., Goetz, A., 2006. A Review of Atmospheric Correction Techniques for Hyperspectral Remote Sensing of Land Surfaces and Ocean Color, in: 2006 IEEE International Symposium on Geoscience and Remote Sensing. Presented at the 2006 IEEE International Symposium on Geoscience and Remote Sensing, pp. 1979–1981. <https://doi.org/10.1109/IGARSS.2006.512>
- Gao, J., Liao, W., Nuytens, D., Lootens, P., Vangeyte, J., Pižurica, A., He, Y., Pieters, J.G., 2018. Fusion of pixel and object-based features for weed mapping using unmanned aerial vehicle imagery. *International Journal of Applied Earth Observation and Geoinformation* 67, 43–53. <https://doi.org/10.1016/j.jag.2017.12.012>
- Gao, Y., Chen, K., 2004. Performance Analysis of Precise Point Positioning Using Real-Time Orbit and Clock Products. *Positioning* 1, 0–0.
- Gao, Y., Harima, K., Shen, X., 2003. Real-Time Kinematic Positioning Based on Un-differenced carrier Phase Data Processing, in: *Proceedings of the 2003 National Technical Meeting of The Institute of Navigation*. Presented at the

- National Technical Meeting of The Institute of Navigation, Anaheim, CA, pp. 362–368.
- Gao, Y., Shen, X., 2002. A New Method for Carrier-Phase-Based Precise Point Positioning. *Navigation* 49, 109–116. <https://doi.org/10.1002/j.2161-4296.2002.tb00260.x>
- Gardelle, J., Hiernaux, P., Kergoat, L., Grippa, M., 2010. Less rain, more water in ponds: a remote sensing study of the dynamics of surface waters from 1950 to present in pastoral Sahel (Gourma region, Mali). *Hydrol. Earth Syst. Sci.* 16.
- Gastellu-Etchegorry, J.P., Martin, E., Gascon, F., 2004. DART: a 3D model for simulating satellite images and studying surface radiation budget. *International Journal of Remote Sensing* 25, 73–96. <https://doi.org/10.1080/0143116031000115166>
- Gavish, Y., O’Connell, J., Benton, T.G., 2018. Quantifying and modelling decay in forecast proficiency indicates the limits of transferability in land-cover classification. *Methods in Ecology and Evolution* 9, 235–244. <https://doi.org/10.1111/2041-210X.12870>
- Ge, M., Gendt, G., Rothacher, M., Shi, C., Liu, J., 2008. Resolution of GPS carrier-phase ambiguities in Precise Point Positioning (PPP) with daily observations. *J Geod* 82, 389–399. <https://doi.org/10.1007/s00190-007-0187-4>
- GEE, n.d. Google Earth Engine [WWW Document]. URL <https://earthengine.google.com/platform/> (accessed 3.9.20).
- Ghamisi, P., Rasti, B., Yokoya, N., Wang, Q., Hofle, B., Bruzzone, L., Bovolo, F., Chi, M., Anders, K., Gloaguen, R., Atkinson, P.M., Benediktsson, J.A., 2019. Multisource and Multitemporal Data Fusion in Remote Sensing: A Comprehensive Review of the State of the Art. *IEEE Geoscience and Remote Sensing Magazine* 7, 6–39. <https://doi.org/10.1109/MGRS.2018.2890023>
- Ghosh, A., Joshi, P.K., 2014. A comparison of selected classification algorithms for mapping bamboo patches in lower Gangetic plains using very high resolution WorldView 2 imagery. *International Journal of Applied Earth Observation and Geoinformation* 26, 298–311. <https://doi.org/10.1016/j.jag.2013.08.011>
- Giordan, D., Manconi, A., Remondino, F., Nex, F., 2017. Use of unmanned aerial vehicles in monitoring application and management of natural hazards. *Geomatics, Natural Hazards and Risk* 8, 1–4. <https://doi.org/10.1080/19475705.2017.1315619>
- Gislason, P.O., Benediktsson, J.A., Sveinsson, J.R., 2006. Random Forests for land cover classification. *Pattern Recognition Letters, Pattern Recognition in Remote Sensing (PRRS 2004)* 27, 294–300. <https://doi.org/10.1016/j.patrec.2005.08.011>
- Goldblatt, R., Rivera Ballesteros, A., Burney, J., 2017. High Spatial Resolution Visual Band Imagery Outperforms Medium Resolution Spectral Imagery for Ecosystem Assessment in the Semi-Arid Brazilian Sertão. *Remote Sensing* 9, 1336. <https://doi.org/10.3390/rs9121336>
- Gorelick, N., Hancher, M., Dixon, M., Ilyushchenko, S., Thau, D., Moore, R., 2017. Google Earth Engine: Planetary-scale geospatial analysis for everyone. *Remote Sensing of Environment, Big Remotely Sensed Data: tools, applications and experiences* 202, 18–27. <https://doi.org/10.1016/j.rse.2017.06.031>

- Grejner-Brzezinska Dorota A., Kashani Israel, Wielgosz Pawel, Smith Dru A., Spencer Paul S. J., Robertson Douglas S., Mader Gerald L., 2007. Efficiency and Reliability of Ambiguity Resolution in Network-Based Real-Time Kinematic GPS. *Journal of Surveying Engineering* 133, 56–65. [https://doi.org/10.1061/\(ASCE\)0733-9453\(2007\)133:2\(56\)](https://doi.org/10.1061/(ASCE)0733-9453(2007)133:2(56))
- Gromny, E., Lewiński, S., Rybicki, M., Malinowski, R., Krupiński, M., Nowakowski, A., Jenerowicz, M., 2019. Creation of training dataset for Sentinel-2 land cover classification, in: Romaniuk, R.S., Linczuk, M. (Eds.), *Photonics Applications in Astronomy, Communications, Industry, and High-Energy Physics Experiments 2019*. Presented at the Photonics Applications in Astronomy, Communications, Industry, and High-Energy Physics Experiments 2019, SPIE, Wilga, Poland, p. 106. <https://doi.org/10.1117/12.2536773>
- Grömping, U., 2009. Variable Importance Assessment in Regression: Linear Regression versus Random Forest. *The American Statistician* 63, 308–319. <https://doi.org/10.1198/tast.2009.08199>
- Grznárová, A., Mokroš, M., Surový, P., Slavík, M., Pondelík, M., Merganič, J., 2019. THE CROWN DIAMETER ESTIMATION FROM FIXED WING TYPE OF UAV IMAGERY. *Int. Arch. Photogramm. Remote Sens. Spatial Inf. Sci.* XLII-2/W13, 337–341. <https://doi.org/10.5194/isprs-archives-XLII-2-W13-337-2019>
- Guan, H., Li, J., Chapman, M., Deng, F., Ji, Z., Yang, X., 2013. Integration of orthoimagery and lidar data for object-based urban thematic mapping using random forests. *International Journal of Remote Sensing* 34, 5166–5186. <https://doi.org/10.1080/01431161.2013.788261>
- Haas, E.M., Bartholomé, E., Combal, B., 2009. Time series analysis of optical remote sensing data for the mapping of temporary surface water bodies in sub-Saharan western Africa. *Journal of Hydrology* 370, 52–63. <https://doi.org/10.1016/j.jhydrol.2009.02.052>
- Haas, E.M., Bartholomé, E., Lambin, E.F., Vanacker, V., 2011. Remotely sensed surface water extent as an indicator of short-term changes in ecohydrological processes in sub-Saharan Western Africa. *Remote Sensing of Environment* 115, 3436–3445. <https://doi.org/10.1016/j.rse.2011.08.007>
- Hadjimitsis, D.G., Clayton, C.R.I., Hope, V.S., 2004. An assessment of the effectiveness of atmospheric correction algorithms through the remote sensing of some reservoirs. *International Journal of Remote Sensing* 25, 3651–3674. <https://doi.org/10.1080/01431160310001647993>
- Hadjimitsis, D.G., Papadavid, G., Agapiou, A., Themistocleous, K., Hadjimitsis, M.G., Retalis, A., Michaelides, S., Chrysoulakis, N., Toullos, L., Clayton, C.R.I., 2010. Atmospheric correction for satellite remotely sensed data intended for agricultural applications: impact on vegetation indices. *Nat. Hazards Earth Syst. Sci.* 10, 89–95. <https://doi.org/10.5194/nhess-10-89-2010>
- Haralick, R.M., Shanmugam, K., Dinstein, I., 1973. Textural Features for Image Classification. *IEEE Transactions on Systems, Man, and Cybernetics SMC*-3, 610–621. <https://doi.org/10.1109/TSMC.1973.4309314>
- Harris, S., Veraverbeke, S., Hook, S., 2011. Evaluating Spectral Indices for Assessing Fire Severity in Chaparral Ecosystems (Southern California) Using MODIS/ASTER (MASTER) Airborne Simulator Data. *Remote Sensing* 3, 2403–2419. <https://doi.org/10.3390/rs3112403>

- Hartley, R., Zisserman, A., 2003. *Multiple View Geometry in Computer Vision*. Cambridge University Press.
- Hein, L., 2006. The impacts of grazing and rainfall variability on the dynamics of a Sahelian rangeland. *Journal of Arid Environments* 64, 488–504. <https://doi.org/10.1016/j.jaridenv.2005.06.014>
- Hepinstall-Cymerman, J., Coe, S., Alberti, M., 2009. Using Urban Landscape Trajectories to Develop a Multi-Temporal Land Cover Database to Support Ecological Modeling. *Remote Sensing* 1, 1353–1379. <https://doi.org/10.3390/rs1041353>
- Herold, M., Mayaux, P., Woodcock, C.E., Baccini, A., Schmullius, C., 2008. Some challenges in global land cover mapping: An assessment of agreement and accuracy in existing 1 km datasets. *Remote Sensing of Environment* 112, 2538–2556. <https://doi.org/10.1016/j.rse.2007.11.013>
- Hobbs, S.W., Paull, D.J., Clarke, J.D.A., 2016. DEVELOPING AND TESTING OF A LOW-COST SPECTROMETER FOR ROBOTICS 2.
- Houze, R.A., 2012. Orographic effects on precipitating clouds. *Reviews of Geophysics* 50. <https://doi.org/10.1029/2011RG000365>
- Hruska, R., Mitchell, J., Anderson, M., Glenn, N.F., 2012. Radiometric and Geometric Analysis of Hyperspectral Imagery Acquired from an Unmanned Aerial Vehicle. *Remote Sensing* 4, 2736–2752. <https://doi.org/10.3390/rs4092736>
- Hu, Y., Dong, Y., Batunacun, 2018. An automatic approach for land-change detection and land updates based on integrated NDVI timing analysis and the CVAPS method with GEE support. *ISPRS Journal of Photogrammetry and Remote Sensing* 146, 347–359. <https://doi.org/10.1016/j.isprsjprs.2018.10.008>
- Huete, A., Justice, C., Liu, H., 1994. Development of vegetation and soil indices for MODIS-EOS. *Remote Sensing of Environment* 49, 224–234. [https://doi.org/10.1016/0034-4257\(94\)90018-3](https://doi.org/10.1016/0034-4257(94)90018-3)
- Huete, A.R., 1988. A soil-adjusted vegetation index (SAVI). *Remote Sensing of Environment* 25, 295–309. [https://doi.org/10.1016/0034-4257\(88\)90106-X](https://doi.org/10.1016/0034-4257(88)90106-X)
- Hurni, K., Heinimann, A., Würsch, L., 2017. Google Earth Engine Image Pre-processing Tool: Background and Methods 12.
- Hussain, M., Chen, D., Cheng, A., Wei, H., Stanley, D., 2013. Change detection from remotely sensed images: From pixel-based to object-based approaches. *ISPRS Journal of Photogrammetry and Remote Sensing* 80, 91–106. <https://doi.org/10.1016/j.isprsjprs.2013.03.006>
- Hussin, Y.A., Gilani, H., van Leeuwen, L., Murthy, M.S.R., Shah, R., Baral, S., Tsendbazar, N.-E., Shrestha, S., Shah, S.K., Qamer, F.M., 2014. Evaluation of object-based image analysis techniques on very high-resolution satellite image for biomass estimation in a watershed of hilly forest of Nepal. *Appl Geomat* 6, 59–68. <https://doi.org/10.1007/s12518-014-0126-z>
- Iglhaut, J., Cabo, C., Puliti, S., Piermattei, L., O'Connor, J., Rosette, J., 2019. Structure from Motion Photogrammetry in Forestry: a Review. *Curr Forestry Rep* 5, 155–168. <https://doi.org/10.1007/s40725-019-00094-3>
- IGS, 2019. IGS Network [WWW Document]. URL <http://www.igs.org/network> (accessed 9.4.19).
- IPCC 2012: *Managing the Risks of Extreme Events and Disasters to Advance Climate Change Adaptation*. A Special Report of Working Groups I and II of the Intergovernmental Panel on Climate Change [Field, C.B., V. Barros, T.F. Stocker, D. Qin, D.J. Dokken, K.L. Ebi, M.D. Mastrandrea, K.J. Mach,

- G.-K. Plattner, S.K. Allen, M. Tignor, and P.M. Midgley (eds.)). Cambridge University Press, Cambridge, UK. [WWW Document], 2012. . European Environment Agency. URL <https://www.eea.europa.eu/data-and-maps/indicators/global-and-european-temperature-1/ipcc-2012-managing-the-risks> (accessed 9.30.19).
- Itten, K.I., Meyer, P., 1993. Geometric and radiometric correction of TM data of mountainous forested areas. *IEEE Transactions on Geoscience and Remote Sensing* 31, 764–770. <https://doi.org/10.1109/36.239898>
- Jaboyedoff, M., Horton, P., Derron, M.-H., Longchamp, C., Michoud, C., 2013. Monitoring Natural Hazards, in: Bobrowsky, P.T. (Ed.), *Encyclopedia of Natural Hazards*. Springer Netherlands, Dordrecht, pp. 686–696. [https://doi.org/10.1007/978-1-4020-4399-4\\_354](https://doi.org/10.1007/978-1-4020-4399-4_354)
- Jamieson Marian, Gillins Daniel T., 2018. Comparative Analysis of Online Static GNSS Postprocessing Services. *Journal of Surveying Engineering* 144, 05018002. [https://doi.org/10.1061/\(ASCE\)SU.1943-5428.0000256](https://doi.org/10.1061/(ASCE)SU.1943-5428.0000256)
- Jawak, S.D., Devliyal, P., Luis, A.J., 2015. A Comprehensive Review on Pixel Oriented and Object Oriented Methods for Information Extraction from Remotely Sensed Satellite Images with a Special Emphasis on Cryospheric Applications. *Advances in Remote Sensing* 04, 177. <https://doi.org/10.4236/ars.2015.43015>
- Jenerowicz, M., Wawrzaszek, A., Krupiński, M., Aleksandrowicz, S., Drzewiecki, W., 2019. Comparison of mathematical morphology with the local multifractal description applied to the image samples processing, in: Romaniuk, R.S., Linczuk, M. (Eds.), *Photonics Applications in Astronomy, Communications, Industry, and High-Energy Physics Experiments 2019*. Presented at the Photonics Applications in Astronomy, Communications, Industry, and High-Energy Physics Experiments 2019, SPIE, Wilga, Poland, p. 29. <https://doi.org/10.1117/12.2536408>
- Jensen, J.R., Lulla, D.K., 1987. Introductory digital image processing: A remote sensing perspective. *Geocarto International* 2, 65–65. <https://doi.org/10.1080/10106048709354084>
- Jin, Y., Liu, X., Chen, Y., Liang, X., 2018. Land-cover mapping using Random Forest classification and incorporating NDVI time-series and texture: a case study of central Shandong. *International Journal of Remote Sensing* 39, 8703–8723. <https://doi.org/10.1080/01431161.2018.1490976>
- Jog, S., Dixit, M., 2016. Supervised classification of satellite images, in: 2016 Conference on Advances in Signal Processing (CASP). Presented at the 2016 Conference on Advances in Signal Processing (CASP), pp. 93–98. <https://doi.org/10.1109/CASP.2016.7746144>
- Jones, E., Mills, F., Doran, B., Caprarelli, G., Clarke, J., 2011. Initial results from a GIS-based unsupervised classification study of the Martian surface, in: *Proceedings of the 10th Australian Space Science Conference Brisbane 27-30 September 2010*. National Space Society of Australia.
- Kalantar, B., Mansor, S.B., Sameen, M.I., Pradhan, B., Shafri, H.Z.M., 2017. Drone-based land-cover mapping using a fuzzy unordered rule induction algorithm integrated into object-based image analysis. *International Journal of Remote Sensing* 38, 2535–2556. <https://doi.org/10.1080/01431161.2016.1277043>
- Kaufman, Y.J., Sendra, C., 1988. Algorithm for automatic atmospheric corrections to visible and near-IR satellite imagery. *International Journal of Remote Sensing* 9, 1357–1381. <https://doi.org/10.1080/01431168808954942>

- Kavzoglu, T., Mather, P.M., 2003. The use of backpropagating artificial neural networks in land cover classification. *International Journal of Remote Sensing* 24, 4907–4938. <https://doi.org/10.1080/0143116031000114851>
- Ke, Y., Quackenbush, L.J., 2011. A comparison of three methods for automatic tree crown detection and delineation from high spatial resolution imagery. *International Journal of Remote Sensing* 32, 3625–3647. <https://doi.org/10.1080/01431161003762355>
- Kelcey, J., Lucieer, A., 2012. Sensor Correction of a 6-Band Multispectral Imaging Sensor for UAV Remote Sensing. *Remote Sensing* 4, 1462–1493. <https://doi.org/10.3390/rs4051462>
- Keller, J.M., Chen, S., Crownover, R.M., 1989. Texture description and segmentation through fractal geometry. *Computer Vision, Graphics, and Image Processing* 45, 150–166. [https://doi.org/10.1016/0734-189X\(89\)90130-8](https://doi.org/10.1016/0734-189X(89)90130-8)
- Khatami, R., Mountrakis, G., Stehman, S.V., 2016. A meta-analysis of remote sensing research on supervised pixel-based land-cover image classification processes: General guidelines for practitioners and future research. *Remote Sensing of Environment* 177, 89–100. <https://doi.org/10.1016/j.rse.2016.02.028>
- Kim, M., Seo, J., Lee, J., 2014. A Comprehensive Method for GNSS Data Quality Determination to Improve Ionospheric Data Analysis. *Sensors* 14, 14971–14993. <https://doi.org/10.3390/s140814971>
- Kingston, D., Beard, R., n.d. Real-Time Attitude and Position Estimation for Small UAVs Using Low-Cost Sensors, in: AIAA 3rd “Unmanned Unlimited” Technical Conference, Workshop and Exhibit. American Institute of Aeronautics and Astronautics. <https://doi.org/10.2514/6.2004-6488>
- Kouba, J., Héroux, P., 2001. Precise Point Positioning Using IGS Orbit and Clock Products. *GPS Solutions* 5, 12–28. <https://doi.org/10.1007/PL00012883>
- Kumar, L., Mutanga, O., 2018. Google Earth Engine Applications Since Inception: Usage, Trends, and Potential. *Remote Sensing* 10, 1509. <https://doi.org/10.3390/rs10101509>
- Kustas, W.P., Norman, J.M., 1996. Use of remote sensing for evapotranspiration monitoring over land surfaces. *Hydrological Sciences Journal* 41, 495–516. <https://doi.org/10.1080/02626669609491522>
- Lacaux, J.-P., Tourre, Y.M., Vignolles, C., Ndione, J.-A., Lafaye, M., 2007. Classification of ponds from high-spatial resolution remote sensing: Application to Rift Valley Fever epidemics in Senegal [WWW Document]. URL /paper/Classification-of-ponds-from-high-spatial-remote-to-Lacaux-Tourre/dde8fa0f53c86ea97c9df70f0afa063acdcf5970 (accessed 6.8.20).
- Lacoste, H., Ouwehand, L., European Space Agency (Eds.), 2008. Proceedings of the 2nd MERIS/ (A)ATSR user workshop: 22-26 September 2008, ESRIN, Frascati, Italy, EUROPEAN SPACE AGENCY -PUBLICATIONS- ESA SP. ESA Communication Production Office, ESTEC, Noordwijk, The Netherlands.
- Langley, S.K., Cheshire, H.M., Humes, K.S., 2001. A comparison of single date and multitemporal satellite image classifications in a semi-arid grassland. *Journal of Arid Environments* 49, 401–411. <https://doi.org/10.1006/jare.2000.0771>
- Lantzanakis, G., Mitraka, Z., Chrysoulakis, N., 2017. Comparison of Physically and Image Based Atmospheric Correction Methods for Sentinel-2 Satellite Imagery, in: Karacostas, T., Bais, A., Nastos, P.T. (Eds.), Perspectives on



- Atmospheric Sciences, Springer Atmospheric Sciences. Springer International Publishing, pp. 255–261.
- Lary, D.J., Alavi, A.H., Gandomi, A.H., Walker, A.L., 2016. Machine learning in geosciences and remote sensing. *Geoscience Frontiers* 7, 3–10. <https://doi.org/10.1016/j.gsf.2015.07.003>
- Laurent, V.C.E., Verhoef, W., Clevers, J.G.P.W., Schaepman, M.E., 2011. Estimating forest variables from top-of-atmosphere radiance satellite measurements using coupled radiative transfer models. *Remote Sensing of Environment* 115, 1043–1052. <https://doi.org/10.1016/j.rse.2010.12.009>
- Lefebvre, A., Sannier, C., Corpetti, T., 2016. Monitoring Urban Areas with Sentinel-2A Data: Application to the Update of the Copernicus High Resolution Layer Imperviousness Degree. *Remote Sensing* 8, 606. <https://doi.org/10.3390/rs8070606>
- LEONE, A.P., WRIGHT, G.G., CORVES, C., 1995. The application of satellite remote sensing for soil studies in upland areas of Southern Italy. *International Journal of Remote Sensing* 16, 1087–1105. <https://doi.org/10.1080/01431169508954465>
- Lewiński, S., Aleksandrowicz, S., Banaszekiewicz, M., 2015. Testing Texture of VHR Panchromatic Data as a Feature of Land Cover Classification. *Acta Geophys.* 63, 547–567. <https://doi.org/10.2478/s11600-014-0250-5>
- Li, J., Wong, D.W.S., 2010. Effects of DEM sources on hydrologic applications. *Computers, Environment and Urban Systems* 34, 251–261. <https://doi.org/10.1016/j.compenvurbsys.2009.11.002>
- Li, P., Zhang, X., 2014. Integrating GPS and GLONASS to accelerate convergence and initialization times of precise point positioning. *GPS Solut* 18, 461–471. <https://doi.org/10.1007/s10291-013-0345-5>
- Li, Q., Qiu, C., Ma, L., Schmitt, M., Zhu, X.X., 2020. Mapping the Land Cover of Africa at 10 m Resolution from Multi-Source Remote Sensing Data with Google Earth Engine. *Remote Sensing* 12, 602. <https://doi.org/10.3390/rs12040602>
- Lindsay, J.B., Creed, I.F., 2006. Distinguishing actual and artefact depressions in digital elevation data. *Computers & Geosciences* 32, 1192–1204. <https://doi.org/10.1016/j.cageo.2005.11.002>
- Liu, H., Wang, L., 2008. Mapping detention basins and deriving their spatial attributes from airborne LiDAR data for hydrological applications. *Hydrological Processes* 22, 2358–2369. <https://doi.org/10.1002/hyp.6834>
- Liu, K., Shi, W., Zhang, H., 2011. A fuzzy topology-based maximum likelihood classification. *ISPRS Journal of Photogrammetry and Remote Sensing* 66, 103–114. <https://doi.org/10.1016/j.isprsjprs.2010.09.007>
- Liu, T., Abd-Elrahman, A., 2018. Multi-view object-based classification of wetland land covers using unmanned aircraft system images. *Remote Sensing of Environment* 216, 122–138. <https://doi.org/10.1016/j.rse.2018.06.043>
- Long, J.A., Lawrence, R.L., Greenwood, M.C., Marshall, L., Miller, P.R., 2013. Object-oriented crop classification using multitemporal ETM+ SLC-off imagery and random forest. *GIScience & Remote Sensing* 50, 418–436. <https://doi.org/10.1080/15481603.2013.817150>
- Lopes, R., Betrouni, N., 2009. Fractal and multifractal analysis: A review. *Medical Image Analysis* 13, 634–649. <https://doi.org/10.1016/j.media.2009.05.003>
- Lorimer, N.D., Haight, R.G., Leary, R.A., 1994. The fractal forest: fractal geometry and applications in forest science. General Technical Report NC-170. St.

- Paul, MN: U.S. Dept. of Agriculture, Forest Service, North Central Forest Experiment Station 170.
- Lu, D., Weng, Q., 2007. A survey of image classification methods and techniques for improving classification performance. *International Journal of Remote Sensing* 28, 823–870. <https://doi.org/10.1080/01431160600746456>
- Ma, L., Fu, T., Blaschke, T., Li, M., Tiede, D., Zhou, Z., Ma, X., Chen, D., 2017a. Evaluation of Feature Selection Methods for Object-Based Land Cover Mapping of Unmanned Aerial Vehicle Imagery Using Random Forest and Support Vector Machine Classifiers. *ISPRS International Journal of Geo-Information* 6, 51. <https://doi.org/10.3390/ijgi6020051>
- Ma, L., Li, M., Ma, X., Cheng, L., Du, P., Liu, Y., 2017b. A review of supervised object-based land-cover image classification. *ISPRS Journal of Photogrammetry and Remote Sensing* 130, 277–293. <https://doi.org/10.1016/j.isprsjprs.2017.06.001>
- Magliocca, N.R., Rudel, T.K., Verburg, P.H., McConnell, W.J., Mertz, O., Gerstner, K., Heinimann, A., Ellis, E.C., 2015. Synthesis in land change science: methodological patterns, challenges, and guidelines. *Reg Environ Change* 15, 211–226. <https://doi.org/10.1007/s10113-014-0626-8>
- Maglione, P., 2016. Very High Resolution Optical Satellites: An Overview of the Most Commonly used. *American Journal of Applied Sciences* 13, 91–99. <https://doi.org/10.3844/ajassp.2016.91.99>
- Magnard, C., Morsdorf, F., Small, D., Stilla, U., Schaepman, M.E., Meier, E., 2016. Single tree identification using airborne multibaseline SAR interferometry data. *Remote Sensing of Environment* 186, 567–580. <https://doi.org/10.1016/j.rse.2016.09.018>
- Maier, B., Tiede, D., Dorren, L., 2008. Characterising mountain forest structure using landscape metrics on LiDAR-based canopy surface models, in: Blaschke, T., Lang, S., Hay, G.J. (Eds.), *Object-Based Image Analysis: Spatial Concepts for Knowledge-Driven Remote Sensing Applications*, Lecture Notes in Geoinformation and Cartography. Springer Berlin Heidelberg, Berlin, Heidelberg, pp. 625–643. [https://doi.org/10.1007/978-3-540-77058-9\\_34](https://doi.org/10.1007/978-3-540-77058-9_34)
- MALLICK, D.I.J., 1987. A review of: “Image Interpretation in Geology”. By S. A. DRURY. (London: Allen & Unwin, 1987.) [Pp. 243.] Price £40·00 (hardback), £17·95 (paperback). *International Journal of Remote Sensing* 8, 1399–1400. <https://doi.org/10.1080/01431168708954782>
- Mandelbrot, B.B., 1982. *The fractal geometry of nature*. San Francisco: W.H. Freeman, 1982, Revised edition of: *Fractals* (1977).
- Martins, V.S., Barbosa, C.C.F., De Carvalho, L.A.S., Jorge, D.S.F., Lobo, F.D.L., Novo, E.M.L. de M., 2017. Assessment of Atmospheric Correction Methods for Sentinel-2 MSI Images Applied to Amazon Floodplain Lakes. *Remote Sensing* 9, 322. <https://doi.org/10.3390/rs9040322>
- Maschler, J., Atzberger, C., Immitzer, M., 2018. Individual Tree Crown Segmentation and Classification of 13 Tree Species Using Airborne Hyperspectral Data. *Remote Sensing* 10, 1218. <https://doi.org/10.3390/rs10081218>
- Massazza, G., Belcore, E., Ibrahim, M.H., Tarchiani, V., Tiepolo, M., Souradji Issa, Pezzoli, A., Rosso, M., 2020. Atlas cartographique des zones inondables de la Rivière Sirba. <https://doi.org/10.13140/RG.2.2.18592.61446>
- Massazza, G., Tamagnone, P., Pezzoli, A., Housseini, M., Belcore, E., Tiepolo, M., Rosso, M., 2018. Améliorations sur le système d’observation du bassin de

- la Rivière Sirba pour la gestion des risques naturels, in: Colloque International AMMA-CATCH. AMMA CATCH.
- Massazza, G., Tamagnone, P., Wilcox, C., Belcore, E., Pezzoli, A., Vischel, T., Panthou, G., Housseini Ibrahim, M., Tiepolo, M., Tarchiani, V., Rosso, M., 2019. Flood Hazard Scenarios of the Sirba River (Niger): Evaluation of the Hazard Thresholds and Flooding Areas. *Water* 11, 1018. <https://doi.org/10.3390/w11051018>
- Maxwell, A.E., Warner, T.A., Fang, F., 2018. Implementation of machine-learning classification in remote sensing: an applied review. *International Journal of Remote Sensing* 39, 2784–2817. <https://doi.org/10.1080/01431161.2018.1433343>
- McFeeters, S.K., 2013. Using the Normalized Difference Water Index (NDWI) within a Geographic Information System to Detect Swimming Pools for Mosquito Abatement: A Practical Approach. *Remote Sensing* 5, 3544–3561. <https://doi.org/10.3390/rs5073544>
- Mejias, L., Lai, J., Bruggemann, T., 2015. Sensors for Missions, in: Valavanis, K.P., Vachtsevanos, G.J. (Eds.), *Handbook of Unmanned Aerial Vehicles*. Springer Netherlands, Dordrecht, pp. 385–399. [https://doi.org/10.1007/978-90-481-9707-1\\_6](https://doi.org/10.1007/978-90-481-9707-1_6)
- Memon, A.A., Muhammad, S., Rahman, S., Haq, M., 2015. Flood monitoring and damage assessment using water indices: A case study of Pakistan flood-2012. *The Egyptian Journal of Remote Sensing and Space Science* 18, 99–106. <https://doi.org/10.1016/j.ejrs.2015.03.003>
- Meneguzzo, D.M., Liknes, G.C., Nelson, M.D., 2013. Mapping trees outside forests using high-resolution aerial imagery: a comparison of pixel- and object-based classification approaches. *Environ Monit Assess* 185, 6261–6275. <https://doi.org/10.1007/s10661-012-3022-1>
- Merciol, F., Balem, T., Lefèvre, S., 2019. Efficient and large-scale land cover classification using multiscale image analysis 5.
- Mielcarek, M., Stereńczak, K., Khosravipour, A., 2018. Testing and evaluating different LiDAR-derived canopy height model generation methods for tree height estimation. *International Journal of Applied Earth Observation and Geoinformation* 71, 132–143. <https://doi.org/10.1016/j.jag.2018.05.002>
- Mills, S., McLeod, P., 2013. Global seamline networks for orthomosaic generation via local search. *ISPRS Journal of Photogrammetry and Remote Sensing* 75, 101–111. <https://doi.org/10.1016/j.isprsjprs.2012.11.003>
- Mireault, Y., Tétrault, P., Lahaye, F., Héroux, P., Kouba, J., 2008. Online precise point positioning: A new, timely service from natural resources Canada. *GPS World* 19, 59–64.
- Moawad, M.B., Aziz, A.O.A., Mamtimin, B., 2016. Flash floods in the Sahara: a case study for the 28 January 2013 flood in Qena, Egypt. *Geomatics, Natural Hazards and Risk* 7, 215–236. <https://doi.org/10.1080/19475705.2014.885467>
- Moe, K.T., Owari, T., Furuya, N., Hiroshima, T., 2020. Comparing Individual Tree Height Information Derived from Field Surveys, LiDAR and UAV-DAP for High-Value Timber Species in Northern Japan. *Forests* 11, 223. <https://doi.org/10.3390/f11020223>
- Mohamed, S.A., El-Raey, M.E., 2019. Land cover classification and change detection analysis of Qaroun and Wadi El-Rayyan lakes using multi-temporal remotely sensed imagery. *Environ Monit Assess* 191, 229. <https://doi.org/10.1007/s10661-019-7339-x>

- Mohammed, J., Bingley, R.M., Moore, T., Hill, C., 2018. An Assessment of the Precise Products on Static Precise Point Positioning using Multi-Constellation GNSS. Presented at the 2018 IEEE/ION Position, Location and Navigation Symposium (PLANS), pp. 634–641.
- Mohan, M., Silva, C.A., Klauberg, C., Jat, P., Catts, G., Cardil, A., Hudak, A.T., Dia, M., 2017. Individual Tree Detection from Unmanned Aerial Vehicle (UAV) Derived Canopy Height Model in an Open Canopy Mixed Conifer Forest. *Forests* 8, 340. <https://doi.org/10.3390/f8090340>
- NASA, 2019. NASA [WWW Document]. NASA. URL <http://www.nasa.gov/index.html> (accessed 9.30.19).
- Natural Resources Canada, 2016. Natural Resources Canada [WWW Document]. URL <https://webapp.geod.nrcan.gc.ca/geod/tools-outils/ppp.php> (accessed 9.4.19).
- Nebiker, S., Annen, A., Scherrer, M., Oesch, D., 2008. A LIGHT-WEIGHT MULTISPECTRAL SENSOR FOR MICRO UAV – OPPORTUNITIES FOR VERY HIGH RESOLUTION AIRBORNE REMOTE SENSING 8.
- Nex, F., Remondino, F., 2014. UAV for 3D mapping applications: a review. *Appl Geomat* 6, 1–15. <https://doi.org/10.1007/s12518-013-0120-x>
- NOAA, N.O. and A.A., 2019. NOAA's National Ocean Service [WWW Document]. URL <https://oceanservice.noaa.gov/welcome.html> (accessed 9.30.19).
- Nowakowski, A., Rybicki, M., Kukawska, E., Malinowski, R., Krupiński, M., Lewinski, S., 2017. Aggregation of Sentinel-2 time series classifications as a solution for multitemporal analysis, in: Bruzzone, L., Bovolo, F., Benediktsson, J.A. (Eds.), *Image and Signal Processing for Remote Sensing XXIII*. Presented at the Image and Signal Processing for Remote Sensing, SPIE, Warsaw, Poland, p. 11. <https://doi.org/10.1117/12.2277976>
- Oguntunde, P.G., Lischeid, G., Abiodun, B.J., 2018. Impacts of climate variability and change on drought characteristics in the Niger River Basin, West Africa. *Stoch Environ Res Risk Assess* 32, 1017–1034. <https://doi.org/10.1007/s00477-017-1484-y>
- Oliveira, D., Pereira Neves dos Reis, W., Morandin Junior, O., 2019. A Qualitative Analysis of a USB Camera for AGV Control. *Sensors* 19, 4111. <https://doi.org/10.3390/s19194111>
- On depression storages: The effect of DEM spatial resolution, 2006. *Journal of Hydrology* 318, 138–150. <https://doi.org/10.1016/j.jhydrol.2005.06.010>
- Ostad-Ali-Askari, K., Qasemy, Z., Eslamian, S., Pirnazar, M., Namadi, A., Singh, V.P., Dalezios, N.R., Matouq, M., Ghane, M., Khani, S., 2017. Preparing A Land Cover Map with Emphasis on Green Space (Grass, Tree, Agriculture): by using Image Texture Filters in Panchromatic Band, Iran. *International Journal of Constructive Research in Civil Engineering* 3. <https://doi.org/10.20431/2454-8693.0304012>
- Pádua, L., Vanko, J., Hruška, J., Adão, T., Sousa, J.J., Peres, E., Morais, R., 2017. UAS, sensors, and data processing in agroforestry: a review towards practical applications. *International Journal of Remote Sensing* 38, 2349–2391. <https://doi.org/10.1080/01431161.2017.1297548>
- Pan, S., Chen, W., Jin, X., Shi, X., He, F., 2015. Real-Time PPP Based on the Coupling Estimation of Clock Bias and Orbit Error with Broadcast Ephemeris. *Sensors* 15, 17808–17826. <https://doi.org/10.3390/s150717808>
- Panagiotidis, D., Abdollahnejad, A., Surový, P., Chiteculo, V., 2017. Determining tree height and crown diameter from high-resolution UAV imagery.

- International Journal of Remote Sensing 38, 2392–2410.  
<https://doi.org/10.1080/01431161.2016.1264028>
- Panagos, P., Borrelli, P., Poesen, J., Ballabio, C., Lugato, E., Meusburger, K., Montanarella, L., Alewell, C., 2015. The new assessment of soil loss by water erosion in Europe. *Environmental Science & Policy* 54, 438–447.  
<https://doi.org/10.1016/j.envsci.2015.08.012>
- Pandey, P.C., Koutsias, N., Petropoulos, G.P., Srivastava, P.K., Dor, E.B., 2019. Land use/land cover in view of earth observation: data sources, input dimensions, and classifiers—a review of the state of the art. *Geocarto International* 0, 1–32. <https://doi.org/10.1080/10106049.2019.1629647>
- Paneque-Gálvez, J., McCall, M.K., Napoletano, B.M., Wich, S.A., Koh, L.P., 2014. Small Drones for Community-Based Forest Monitoring: An Assessment of Their Feasibility and Potential in Tropical Areas. *Forests* 5, 1481–1507.  
<https://doi.org/10.3390/f5061481>
- Pavlis, N.K., Holmes, S.A., Kenyon, S.C., Factor, J.K., 2012. The development and evaluation of the Earth Gravitational Model 2008 (EGM2008). *Journal of Geophysical Research: Solid Earth* 117.  
<https://doi.org/10.1029/2011JB008916>
- Pearse, G.D., Dash, J.P., Persson, H.J., Watt, M.S., 2018. Comparison of high-density LiDAR and satellite photogrammetry for forest inventory. *ISPRS Journal of Photogrammetry and Remote Sensing* 142, 257–267.  
<https://doi.org/10.1016/j.isprsjprs.2018.06.006>
- Pearson, R.L., Miller, L.D., U.S. International Biological Program, International Symposium on Remote Sensing of Environment, 1972. Remote mapping of standing crop biomass for estimation of the productivity of the shortgrass prairie, Pawnee National Grasslands, Colorado. Dept. of Watershed Sciences, College of Forestry and Natural Resources, Colorado State University, Fort Collins, Colo.
- Pelletier, C., Valero, S., Inglada, J., Dedieu, G., Champion, N., 2016. An assessment of image features and random forest for land cover mapping over large areas using high resolution Satellite Image Time Series, in: 2016 IEEE International Geoscience and Remote Sensing Symposium (IGARSS). Presented at the 2016 IEEE International Geoscience and Remote Sensing Symposium (IGARSS), pp. 3338–3341.  
<https://doi.org/10.1109/IGARSS.2016.7729863>
- Persello, C., Bruzzone, L., 2010. A Novel Protocol for Accuracy Assessment in Classification of Very High Resolution Images. *IEEE Transactions on Geoscience and Remote Sensing* 48, 1232–1244.  
<https://doi.org/10.1109/TGRS.2009.2029570>
- Pinty, B., Verstraete, M.M., 1992. GEMI: a non-linear index to monitor global vegetation from satellites. *Vegetatio* 101, 15–20.  
<https://doi.org/10.1007/BF00031911>
- Piras, M., Belcore, E., Pezzoli, A., Massazza, G., Rosso, M., 2019. Raspberry PI Camera for high resolution 3D modelling in remote areas. Case study in South-West Niger. *Geophysical Research Abstracts*, EGU2019-19068 21, 1.
- Piras, M., Marucco, G., Charqane, K., 2010. Statistical analysis of different low cost GPS receivers for indoor and outdoor positioning, in: IEEE/ION Position, Location and Navigation Symposium. Presented at the IEEE/ION Position, Location and Navigation Symposium, pp. 838–849.  
<https://doi.org/10.1109/PLANS.2010.5507325>

- Poortinga, A., Tenneson, K., Shapiro, A., Nquyen, Q., San Aung, K., Chishtie, F., Saah, D., 2019. Mapping Plantations in Myanmar by Fusing Landsat-8, Sentinel-2 and Sentinel-1 Data along with Systematic Error Quantification. *Remote Sensing* 11, 831. <https://doi.org/10.3390/rs11070831>
- Pouliot, D.A., King, D.J., Bell, F.W., Pitt, D.G., 2002. Automated tree crown detection and delineation in high-resolution digital camera imagery of coniferous forest regeneration. *Remote Sensing of Environment* 82, 322–334. [https://doi.org/10.1016/S0034-4257\(02\)00050-0](https://doi.org/10.1016/S0034-4257(02)00050-0)
- Pyke, C.R., Andelman, S.J., 2007. Land use and land cover tools for climate adaptation. *Climatic Change* 80, 239–251. <https://doi.org/10.1007/s10584-006-9110-x>
- Qadri, S., Khan, D.M., Ahmad, F., Qadri, S.F., Babar, M.E., Shahid, M., Ul-Rehman, M., Razzaq, A., Shah Muhammad, S., Fahad, M., Ahmad, S., Pervez, M.T., Naveed, N., Aslam, N., Jamil, M., Rehmani, E.A., Ahmad, N., Akhtar Khan, N., 2016. A Comparative Study of Land Cover Classification by Using Multispectral and Texture Data [WWW Document]. *BioMed Research International*. <https://doi.org/10.1155/2016/8797438>
- Qiao, C., Luo, J., Sheng, Y., Shen, Z., Zhu, Z., Ming, D., 2012. An Adaptive Water Extraction Method from Remote Sensing Image Based on NDWI. *Journal of the Indian Society of Remote Sensing* 40, 421–433. <https://doi.org/10.1007/s12524-011-0162-7>
- Qiu, L., Jing, L., Hu, B., Li, H., Tang, Y., 2020. A New Individual Tree Crown Delineation Method for High Resolution Multispectral Imagery. *Remote Sensing* 12, 585. <https://doi.org/10.3390/rs12030585>
- Radoux, J., Defourny, P., 2007. A quantitative assessment of boundaries in automated forest stand delineation using very high resolution imagery. *Remote Sensing of Environment, ForestSAT Special Issue* 110, 468–475. <https://doi.org/10.1016/j.rse.2007.02.031>
- Raguram, R., Frahm, J.-M., Pollefeys, M., 2008. A Comparative Analysis of RANSAC Techniques Leading to Adaptive Real-Time Random Sample Consensus, in: Forsyth, D., Torr, P., Zisserman, A. (Eds.), *Computer Vision – ECCV 2008, Lecture Notes in Computer Science*. Springer, Berlin, Heidelberg, pp. 500–513. [https://doi.org/10.1007/978-3-540-88688-4\\_37](https://doi.org/10.1007/978-3-540-88688-4_37)
- RAHMAN, H., DEDIEU, G., 1994. SMAC: a simplified method for the atmospheric correction of satellite measurements in the solar spectrum. *International Journal of Remote Sensing* 15, 123–143. <https://doi.org/10.1080/01431169408954055>
- Ramachandra, V., 2019. Deep Clustering for Mars Rover image datasets. [arXiv:1911.06623 \[astro-ph\]](https://arxiv.org/abs/1911.06623).
- Rastner, P., Bolch, T., Notarnicola, C., Paul, F., 2014. A Comparison of Pixel- and Object-Based Glacier Classification With Optical Satellite Images. *IEEE Journal of Selected Topics in Applied Earth Observations and Remote Sensing* 7, 853–862. <https://doi.org/10.1109/JSTARS.2013.2274668>
- Remondino, F., 2011. Heritage Recording and 3D Modeling with Photogrammetry and 3D Scanning. *Remote Sensing* 3, 1104–1138. <https://doi.org/10.3390/rs3061104>
- Ren, X., Choy, S., Harima, K., Zhang, X., 2015. Multi-constellation GNSS precise point positioning using GPS, GLONASS and BeiDou in Australia. Presented at the International Global Navigation Satellite Systems (IGNSS)

- Symposium, International Global Navigation Satellite Systems Society, pp. 1–13.
- Richards, J.A., 2013. *Remote Sensing Digital Image Analysis*. Springer Berlin Heidelberg, Berlin, Heidelberg. <https://doi.org/10.1007/978-3-642-30062-2>
- Richardson, A.J., 1977. Distinguishing Vegetation from Soil Background Information 12.
- Richter, R., 1990. A fast atmospheric correction algorithm applied to Landsat TM images. *International Journal of Remote Sensing* 11, 159–166. <https://doi.org/10.1080/01431169008955008>
- Rizeei, H.M., Saharkhiz, M.A., Pradhan, B., Ahmad, N., 2016. Soil erosion prediction based on land cover dynamics at the Semenyih watershed in Malaysia using LTM and USLE models. *Geocarto International* 31, 1158–1177. <https://doi.org/10.1080/10106049.2015.1120354>
- Rizos, C., 2007. Alternatives to current GPS-RTK services and some implications for CORS infrastructure and operations. *GPS Solutions* 3, 151–158. <https://doi.org/10.1007/s10291-007-0056-x>
- Robert, E., Grippa, M., Kergoat, L., Pinet, S., Gal, L., Cochonneau, G., Martinez, J.-M., 2016. Monitoring water turbidity and surface suspended sediment concentration of the Bagre Reservoir (Burkina Faso) using MODIS and field reflectance data. *International Journal of Applied Earth Observation and Geoinformation* 52, 243–251. <https://doi.org/10.1016/j.jag.2016.06.016>
- Rodriguez-Galiano, V.F., Chica-Rivas, M., 2014a. Evaluation of different machine learning methods for land cover mapping of a Mediterranean area using multi-seasonal Landsat images and Digital Terrain Models. *International Journal of Digital Earth* 7, 492–509. <https://doi.org/10.1080/17538947.2012.748848>
- Rodriguez-Galiano, V.F., Chica-Rivas, M., 2014b. Evaluation of different machine learning methods for land cover mapping of a Mediterranean area using multi-seasonal Landsat images and Digital Terrain Models. *International Journal of Digital Earth* 7, 492–509. <https://doi.org/10.1080/17538947.2012.748848>
- Rogan, J., Chen, D., 2004. Remote sensing technology for mapping and monitoring land-cover and land-use change. *Progress in Planning* 61, 301–325. [https://doi.org/10.1016/S0305-9006\(03\)00066-7](https://doi.org/10.1016/S0305-9006(03)00066-7)
- Rouse, J.W., 1973. Monitoring the vernal advancement and retrogradation of natural vegetation. NASA/GSFCT Type Report.
- Sáčkov, I., Bucha, T., Király, G., Brolly, G., Raši, R., 2014. Individual tree and crown identification in the danube floodplain forests based on airborne laser scanning data 7.
- Salah, M., 2017a. A survey of modern classification techniques in remote sensing for improved image classification 11, 21.
- Salah, M., 2017b. A survey of modern classification techniques in remote sensing for improved image classification 11, 21.
- Sameen, M.I., Pradhan, B., Aziz, O.S., 2018. Classification of Very High Resolution Aerial Photos Using Spectral-Spatial Convolutional Neural Networks [WWW Document]. *Journal of Sensors*. <https://doi.org/10.1155/2018/7195432>
- Seitz, S.M., Curless, B., Diebel, J., Scharstein, D., Szeliski, R., 2006. A Comparison and Evaluation of Multi-View Stereo Reconstruction Algorithms, in: 2006 IEEE Computer Society Conference on Computer Vision and Pattern Recognition - Volume 1 (CVPR'06). Presented at the 2006 IEEE Computer

- Society Conference on Computer Vision and Pattern Recognition - Volume 1 (CVPR'06), IEEE, New York, NY, USA, pp. 519–528. <https://doi.org/10.1109/CVPR.2006.19>
- Sekertekin, A., Marangoz, A.M., Akcin, H., 2017. PIXEL-BASED CLASSIFICATION ANALYSIS OF LAND USE LAND COVER USING SENTINEL-2 AND LANDSAT-8 DATA. *Int. Arch. Photogramm. Remote Sens. Spatial Inf. Sci.* XLII-4/W6, 91–93. <https://doi.org/10.5194/isprs-archives-XLII-4-W6-91-2017>
- Sene, K., 2013. *Flash Floods: Forecasting and Warning*. Springer Netherlands.
- Sensefly, 2014. *User Manual: multiSPEC 4C camera* 28.
- Shalaby, A., Tateishi, R., 2007. Remote sensing and GIS for mapping and monitoring land cover and land-use changes in the Northwestern coastal zone of Egypt. *Applied Geography* 27, 28–41. <https://doi.org/10.1016/j.apgeog.2006.09.004>
- Shelestov, A., Lavreniuk, M., Kussul, N., Novikov, A., Skakun, S., 2017. Exploring Google Earth Engine Platform for Big Data Processing: Classification of Multi-Temporal Satellite Imagery for Crop Mapping. *Front. Earth Sci.* 5. <https://doi.org/10.3389/feart.2017.00017>
- Shepherd, J.D., Dymond, J.R., 2010. Correcting satellite imagery for the variance of reflectance and illumination with topography. *International Journal of Remote Sensing*. <https://doi.org/10.1080/01431160210154029>
- Sidhu, N., Pebesma, E., Câmara, G., 2018. Using Google Earth Engine to detect land cover change: Singapore as a use case. *European Journal of Remote Sensing* 51, 486–500. <https://doi.org/10.1080/22797254.2018.1451782>
- Siejka, M., Mika, M., Salata, T., Leń, P., 2018. Algorithm of land cover spatial data processing for the local flood risk mapping. *Survey Review* 50, 397–403. <https://doi.org/10.1080/00396265.2017.1287620>
- Singh, A., Bansal, R.K., Jha, N., 2015. Open Source Software vs Proprietary Software. *IJCA* 114, 26–31. <https://doi.org/10.5120/20080-2132>
- Skoglar, P., Orguner, U., Törnqvist, D., Gustafsson, F., 2012. Road Target Search and Tracking with Gimballed Vision Sensor on an Unmanned Aerial Vehicle. *Remote Sensing* 4, 2076–2111. <https://doi.org/10.3390/rs4072076>
- Snively, K.N., 2008. *Scene Reconstruction and Visualization from Internet Photo Collections*.
- Sobota, J., Pišl, R., Balda, P., Schlegel, M., 2013. Raspberry Pi and Arduino boards in control education. *IFAC Proceedings Volumes, 10th IFAC Symposium Advances in Control Education* 46, 7–12. <https://doi.org/10.3182/20130828-3-UK-2039.00003>
- Sobrino, J.A., Raissouni, N., 2000. Toward remote sensing methods for land cover dynamic monitoring: Application to Morocco. *International Journal of Remote Sensing* 21, 353–366. <https://doi.org/10.1080/014311600210876>
- Soenen, S.A., Peddle, D.R., Coburn, C.A., 2005. SCS+C: a modified Sun-canopy-sensor topographic correction in forested terrain. *IEEE Transactions on Geoscience and Remote Sensing* 43, 2148–2159. <https://doi.org/10.1109/TGRS.2005.852480>
- Sokal, R.R., 1974. Classification: purposes, principles, progress, prospects. *Science* 185, 1115–1123. <https://doi.org/10.1126/science.185.4157.1115>
- Sola, I., García-Martín, A., Sandonís-Pozo, L., Álvarez-Mozos, J., Pérez-Cabello, F., González-Audicana, M., Montorio Llovería, R., 2018. Assessment of atmospheric correction methods for Sentinel-2 images in Mediterranean



- landscapes. *International Journal of Applied Earth Observation and Geoinformation* 73, 63–76. <https://doi.org/10.1016/j.jag.2018.05.020>
- Song, C., Woodcock, C.E., Seto, K.C., Lenney, M.P., Macomber, S.A., 2001. Classification and Change Detection Using Landsat TM Data. *Remote Sensing of Environment* 75, 230–244. [https://doi.org/10.1016/S0034-4257\(00\)00169-3](https://doi.org/10.1016/S0034-4257(00)00169-3)
- Stojić, T., Reljin, I., Reljin, B., 2006a. Adaptation of multifractal analysis to segmentation of microcalcifications in digital mammograms. *Physica A: Statistical Mechanics and its Applications* 367, 494–508.
- Stojić, T., Reljin, I., Reljin, B., 2006b. Adaptation of multifractal analysis to segmentation of microcalcifications in digital mammograms. *Physica A: Statistical Mechanics and its Applications* 367, 494–508. <https://doi.org/10.1016/j.physa.2005.11.030>
- Suduwella, C., Amarasinghe, A., Nirosan, L., Elvitigala, C., De Zoysa, K., Keppetiyagama, C., 2017. Identifying Mosquito Breeding Sites via Drone Images, in: *Proceedings of the 3rd Workshop on Micro Aerial Vehicle Networks, Systems, and Applications - DroNet '17*. Presented at the the 3rd Workshop, ACM Press, Niagara Falls, New York, USA, pp. 27–30. <https://doi.org/10.1145/3086439.3086442>
- Sun, W., Xu, G., Gong, P., Liang, S., 2006. Fractal analysis of remotely sensed images: A review of methods and applications. *International Journal of Remote Sensing* 27, 4963–4990. <https://doi.org/10.1080/01431160600676695>
- S.V.S.Prasad, M., Savithri, D.T.S., Krishna, D.I.V.M., 2015. Techniques in Image Classification; A Survey. *Global Journal of Research In Engineering*.
- Talukdar, S., Singha, P., Mahato, S., Shahfahad, Pal, S., Liou, Y.-A., Rahman, A., 2020. Land-Use Land-Cover Classification by Machine Learning Classifiers for Satellite Observations—A Review. *Remote Sensing* 12, 1135. <https://doi.org/10.3390/rs12071135>
- Tamagnone, P., Massazza, G., Pezzoli, A., Rosso, M., 2019. Hydrology of the Sirba River: Updating and Analysis of Discharge Time Series. *Water* 11, 156. <https://doi.org/10.3390/w11010156>
- Tang, L., Shao, G., 2015. Drone remote sensing for forestry research and practices. *J. For. Res.* 26, 791–797. <https://doi.org/10.1007/s11676-015-0088-y>
- Teillet, P.M., Guindon, B., Goodenough, D.G., 1982. On the Slope-Aspect Correction of Multispectral Scanner Data. *Canadian Journal of Remote Sensing* 8, 84–106. <https://doi.org/10.1080/07038992.1982.10855028>
- Thanh Noi, P., Kappas, M., 2018. Comparison of Random Forest, k-Nearest Neighbor, and Support Vector Machine Classifiers for Land Cover Classification Using Sentinel-2 Imagery. *Sensors* 18, 18. <https://doi.org/10.3390/s18010018>
- Thyagarajan, K.K., Vignesh, T., 2019. Soft Computing Techniques for Land Use and Land Cover Monitoring with Multispectral Remote Sensing Images: A Review. *Arch Computat Methods Eng* 26, 275–301. <https://doi.org/10.1007/s11831-017-9239-y>
- Tiepolo, M., Bacci, M., Braccio, S., 2018. Multihazard Risk Assessment for Planning with Climate in the Dosso Region, Niger. *Climate* 6, 67. <https://doi.org/10.3390/cli6030067>
- Tiepolo, M., Rosso, M., Massazza, G., Belcore, E., Issa, S., Braccio, S., 2019a. Flood Assessment for Risk-Informed Planning along the Sirba River, Niger. *Sustainability* 11, 4003. <https://doi.org/10.3390/su11154003>

- Tiepolo, M., Rosso, M., Massazza, G., Belcore, E., Issa, S., Braccio, S., 2019b. Flood Assessment for Risk-Informed Planning along the Sirba River, Niger. *Sustainability* 11, 4003. <https://doi.org/10.3390/su11154003>
- Topouzelis, K., Psyllos, A., 2012. Oil spill feature selection and classification using decision tree forest on SAR image data. *ISPRS Journal of Photogrammetry and Remote Sensing* 68, 135–143. <https://doi.org/10.1016/j.isprsjprs.2012.01.005>
- Torresan, C., Berton, A., Carotenuto, F., Gennaro, S.F.D., Gioli, B., Matese, A., Miglietta, F., Vagnoli, C., Zaldei, A., Wallace, L., 2017. Forestry applications of UAVs in Europe: a review. *International Journal of Remote Sensing* 38, 2427–2447. <https://doi.org/10.1080/01431161.2016.1252477>
- Torres-Sánchez, J., López-Granados, F., Peña, J.M., 2015. An automatic object-based method for optimal thresholding in UAV images: Application for vegetation detection in herbaceous crops. *Computers and Electronics in Agriculture* 114, 43–52. <https://doi.org/10.1016/j.compag.2015.03.019>
- Towler, J., Krawiec, B., Kochersberger, K., 2012. Radiation Mapping in Post-Disaster Environments Using an Autonomous Helicopter. *Remote Sensing* 4, 1995–2015. <https://doi.org/10.3390/rs4071995>
- Townshend, J.R., Latham, J., Arino, O., 2008. Integrated Global Observations of the Land: an IGOS-P Theme.
- Triggs, B., McLauchlan, P.F., Hartley, R.I., Fitzgibbon, A.W., 2000. Bundle Adjustment — A Modern Synthesis, in: Triggs, B., Zisserman, A., Szeliski, R. (Eds.), *Vision Algorithms: Theory and Practice*, Lecture Notes in Computer Science. Springer, Berlin, Heidelberg, pp. 298–372. [https://doi.org/10.1007/3-540-44480-7\\_21](https://doi.org/10.1007/3-540-44480-7_21)
- Tulldahl, H.M., Bissmarck, F., Larsson, H., Grönwall, C., Tolt, G., 2015. Accuracy evaluation of 3D lidar data from small UAV, in: *Electro-Optical Remote Sensing, Photonic Technologies, and Applications IX*. Presented at the Electro-Optical Remote Sensing, Photonic Technologies, and Applications IX, International Society for Optics and Photonics, p. 964903. <https://doi.org/10.1117/12.2194508>
- Turner, B.L., Lambin, E.F., Reenberg, A., 2007. The emergence of land change science for global environmental change and sustainability. *PNAS* 104, 20666–20671. <https://doi.org/10.1073/pnas.0704119104>
- Turner, D., Lucieer, A., Watson, C., 2012. An Automated Technique for Generating Georectified Mosaics from Ultra-High Resolution Unmanned Aerial Vehicle (UAV) Imagery, Based on Structure from Motion (SfM) Point Clouds. *Remote Sensing* 4, 1392–1410. <https://doi.org/10.3390/rs4051392>
- Turner, M.G., Gardner, R.H., 2015. *Landscape Ecology in Theory and Practice: Pattern and Process*, 2nd ed. Springer-Verlag, New York. <https://doi.org/10.1007/978-1-4939-2794-4>
- Turner, M.J., Blackledge, J.M., Andrews, P.R., 1998. *Fractal geometry in digital imaging*. Academic Press, San Diego, Calif.
- UN, U.N., 2016. *The New Urban Agenda*. United Nations.
- UNDRR, U.N.O. for D.R.R., 2015. *Sendai Framework for Disaster Risk Reduction 2015 - 2030*. United Nations Office for Disaster Risk Reduction (UNDRR), Geneva.
- van Blyenburgh, P., 1999. UAVs: an overview. *Air & Space Europe* 1, 43–47. [https://doi.org/10.1016/S1290-0958\(00\)88869-3](https://doi.org/10.1016/S1290-0958(00)88869-3)
- Vastaranta, M., Kankare, V., Holopainen, M., Yu, X., Hyypä, J., Hyypä, H., 2012. Combination of individual tree detection and area-based approach in

- imputation of forest variables using airborne laser data. *ISPRS Journal of Photogrammetry and Remote Sensing* 67, 73–79. <https://doi.org/10.1016/j.isprsjprs.2011.10.006>
- Vaze, J., Teng, J., Spencer, G., 2010. Impact of DEM accuracy and resolution on topographic indices. *Environmental Modelling & Software* 25, 1086–1098. <https://doi.org/10.1016/j.envsoft.2010.03.014>
- Véhel, J.L., Mignot, P., 1994. MULTIFRACTAL SEGMENTATION OF IMAGES. *Fractals* 02, 371–377. <https://doi.org/10.1142/S0218348X94000466>
- Vepakomma, U., Cormier, D., Thiffault, N., 2015. POTENTIAL OF UAV BASED CONVERGENT PHOTOGRAMMETRY IN MONITORING REGENERATION STANDARDS. *Int. Arch. Photogramm. Remote Sens. Spatial Inf. Sci. XL-1/W4*, 281–285. <https://doi.org/10.5194/isprsarchives-XL-1-W4-281-2015>
- Vermote, E.F., Vermeulen, A., 1999. Atmospheric correction algorithm: spectral reflectances (MOD09). *ATBD version 4*, 1–107.
- Vesakoski, J.-M., Alho, P., Hyypä, J., Holopainen, M., Flener, C., Hyypä, H., 2014. Nationwide Digital Terrain Models for Topographic Depression Modelling in Detection of Flood Detention Areas. *Water* 6, 271–300. <https://doi.org/10.3390/w6020271>
- Vieira, G. da S., Rocha, B.M., Soares, F., Lima, J.C., Pedrini, H., Costa, R., Ferreira, J., 2019. Extending the Aerial Image Analysis from the Detection of Tree Crowns, in: 2019 IEEE 31st International Conference on Tools with Artificial Intelligence (ICTAI). Presented at the 2019 IEEE 31st International Conference on Tools with Artificial Intelligence (ICTAI), pp. 1681–1685. <https://doi.org/10.1109/ICTAI.2019.00247>
- Voorons, M., Germain, M., Benie, G.B., Ko Fung, 2003. Segmentation of high resolution images based on the multifractal analysis, in: *IGARSS 2003. 2003 IEEE International Geoscience and Remote Sensing Symposium. Proceedings (IEEE Cat. No.03CH37477)*. Presented at the *IGARSS 2003. 2003 IEEE International Geoscience and Remote Sensing Symposium. Proceedings (IEEE Cat. No.03CH37477)*, pp. 3531–3533 vol.6. <https://doi.org/10.1109/IGARSS.2003.1294844>
- Wallace, L., Lucieer, A., Watson, C., Turner, D., 2012. Development of a UAV-LiDAR System with Application to Forest Inventory. *Remote Sensing* 4, 1519–1543. <https://doi.org/10.3390/rs4061519>
- Wang, F., Li, J.-W., Shi, W., Liao, G.-P., 2013. Leaf image segmentation method based on multifractal detrended fluctuation analysis. *Journal of Applied Physics* 114, 214905. <https://doi.org/10.1063/1.4839815>
- Wang, L., Li, Z., Ge, M., Neitzel, F., Wang, Z., Yuan, H., 2018. Validation and Assessment of Multi-GNSS Real-Time Precise Point Positioning in Simulated Kinematic Mode Using IGS Real-Time Service. *Remote Sensing* 10, 337. <https://doi.org/10.3390/rs10020337>
- Wang, L., Liu, H., 2006. An efficient method for identifying and filling surface depressions in digital elevation models for hydrologic analysis and modelling. *International Journal of Geographical Information Science* 20, 193–213. <https://doi.org/10.1080/13658810500433453>
- Wang, X.-H., Zhang, Y.-Z., Xu, M.-M., 2019. A Multi-Threshold Segmentation for Tree-Level Parameter Extraction in a Deciduous Forest Using Small-Footprint Airborne LiDAR Data. *Remote Sensing* 11, 2109. <https://doi.org/10.3390/rs11182109>

- Warner, T.T., 2004. Desert Meteorology by Thomas T. Warner [WWW Document]. Cambridge Core. <https://doi.org/10.1017/CBO9780511535789>
- Wawrzaszek, A., Aleksandrowicz, S., Krupiński, M., Drzewiecki, W., 2014. Influence of Image Filtering on Land Cover Classification when using Fractal and Multifractal Features. *Photogrammetrie - Fernerkundung - Geoinformation* 2014, 101–115. <https://doi.org/10.1127/1432-8364/2014/0212>
- White, J.C., Wulder, M.A., Vastaranta, M., Coops, N.C., Pitt, D., Woods, M., 2013. The Utility of Image-Based Point Clouds for Forest Inventory: A Comparison with Airborne Laser Scanning. *Forests* 4, 518–536. <https://doi.org/10.3390/f4030518>
- Whiteside, T.G., Boggs, G.S., Maier, S.W., 2011. Comparing object-based and pixel-based classifications for mapping savannas. *International Journal of Applied Earth Observation and Geoinformation* 13, 884–893. <https://doi.org/10.1016/j.jag.2011.06.008>
- WHO, 2020. World Health Organization, WHO [WWW Document]. URL <https://www.who.int> (accessed 7.22.20).
- Wiegand, C.L., Richardson, A.J., Escobar, D.E., Gerbermann, A.H., 1991. Vegetation indices in crop assessments. *Remote Sensing of Environment* 35, 105–119. [https://doi.org/10.1016/0034-4257\(91\)90004-P](https://doi.org/10.1016/0034-4257(91)90004-P)
- Wolf, B.-M., Heipke, C., 2007. Automatic extraction and delineation of single trees from remote sensing data. *Machine Vision and Applications* 18, 317–330. <https://doi.org/10.1007/s00138-006-0064-9>
- Wu, C., Agarwal, S., Curless, B., Seitz, S.M., 2012. Schematic Surface Reconstruction, in: *IEEE Conference on Computer Vision and Pattern Recognition*.
- Wu, C., Agarwal, S., Curless, B., Seitz, S.M., 2011. Multicore bundle adjustment, in: *CVPR 2011. Presented at the CVPR 2011*, pp. 3057–3064. <https://doi.org/10.1109/CVPR.2011.5995552>
- Wu, H., Li, Z.-L., 2009. Scale Issues in Remote Sensing: A Review on Analysis, Processing and Modeling. *Sensors* 9, 1768–1793. <https://doi.org/10.3390/s90301768>
- Yang Jun, Chu Xuefeng, 2013. Effects of DEM Resolution on Surface Depression Properties and Hydrologic Connectivity. *Journal of Hydrologic Engineering* 18, 1157–1169. [https://doi.org/10.1061/\(ASCE\)HE.1943-5584.0000731](https://doi.org/10.1061/(ASCE)HE.1943-5584.0000731)
- Yang, X., Zhao, S., Qin, X., Zhao, N., Liang, L., 2017. Mapping of Urban Surface Water Bodies from Sentinel-2 MSI Imagery at 10 m Resolution via NDWI-Based Image Sharpening. *Remote Sensing* 9, 596. <https://doi.org/10.3390/rs9060596>
- Yao, W., Krzystek, P., Heurich, M., 2012. Tree species classification and estimation of stem volume and DBH based on single tree extraction by exploiting airborne full-waveform LiDAR data. *Remote Sensing of Environment* 123, 368–380. <https://doi.org/10.1016/j.rse.2012.03.027>
- Yigit, C.O., Gikas, V., Alcay, S., Ceylan, A., 2014. Performance evaluation of short to long term GPS, GLONASS and GPS/GLONASS post-processed PPP. *Survey Review* 46, 155–166. <https://doi.org/10.1179/1752270613Y.00000000068>
- Young, N.E., Anderson, R.S., Chignell, S.M., Vorster, A.G., Lawrence, R., Evangelista, P.H., 2017. A survival guide to Landsat preprocessing. *Ecology* 98, 920–932. <https://doi.org/10.1002/ecy.1730>

- Yu, Le, Liang, L., Wang, J., Zhao, Y., Cheng, Q., Hu, L., Liu, S., Yu, Liang, Wang, X., Zhu, P., Li, Xueyan, Xu, Y., Li, C., Fu, W., Li, Xuecao, Li, W., Liu, C., Cong, N., Zhang, H., Sun, F., Bi, X., Xin, Q., Li, D., Yan, D., Zhu, Z., Goodchild, M.F., Gong, P., 2014. Meta-discoveries from a synthesis of satellite-based land-cover mapping research. *International Journal of Remote Sensing* 35, 4573–4588. <https://doi.org/10.1080/01431161.2014.930206>
- Yuan, H., Van Der Wiele, C.F., Khorram, S., 2009. An Automated Artificial Neural Network System for Land Use/Land Cover Classification from Landsat TM Imagery. *Remote Sensing* 1, 243–265. <https://doi.org/10.3390/rs1030243>
- Yurtseven, H., Akgul, M., Coban, S., Gulci, S., 2019. Determination and accuracy analysis of individual tree crown parameters using UAV based imagery and OBIA techniques. *Measurement* 145, 651–664. <https://doi.org/10.1016/j.measurement.2019.05.092>
- Zaforemska, A., Xiao, W., Gaulton, R., 2019. INDIVIDUAL TREE DETECTION FROM UAV LIDAR DATA IN A MIXED SPECIES WOODLAND. *Int. Arch. Photogramm. Remote Sens. Spatial Inf. Sci.* XLII-2/W13, 657–663. <https://doi.org/10.5194/isprs-archives-XLII-2-W13-657-2019>
- Zarco-Tejada, P.J., Ustin, S.L., 2001. Modeling canopy water content for carbon estimates from MODIS data at land EOS validation sites, in: IGARSS 2001. Scanning the Present and Resolving the Future. Proceedings. IEEE 2001 International Geoscience and Remote Sensing Symposium (Cat. No.01CH37217). Presented at the IGARSS 2001. Scanning the Present and Resolving the Future. Proceedings. IEEE 2001 International Geoscience and Remote Sensing Symposium, IEEE, Sydney, NSW, Australia, pp. 342–344. <https://doi.org/10.1109/IGARSS.2001.976152>
- Zeide, B., Pfeifer, P., 1991. A Method for Estimation of Fractal Dimension of Tree Crowns. *for sci* 37, 1253–1265. <https://doi.org/10.1093/forestscience/37.5.1253>
- Zha, Y., Gao, J., Ni, S., 2003. Use of normalized difference built-up index in automatically mapping urban areas from TM imagery. *International Journal of Remote Sensing* 24, 583–594. <https://doi.org/10.1080/01431160304987>
- Zhai, Y., Qu, Z., Hao, L., 2018. Land Cover Classification Using Integrated Spectral, Temporal, and Spatial Features Derived from Remotely Sensed Images. *Remote Sensing* 10, 383. <https://doi.org/10.3390/rs10030383>
- Zhang, X., Chen, G., Wang, W., Wang, Q., Dai, F., 2017. Object-Based Land-Cover Supervised Classification for Very-High-Resolution UAV Images Using Stacked Denoising Autoencoders. *IEEE Journal of Selected Topics in Applied Earth Observations and Remote Sensing* 10, 3373–3385. <https://doi.org/10.1109/JSTARS.2017.2672736>
- Zhang, X., Friedl, M.A., Schaaf, C.B., Strahler, A.H., Hodges, J.C.F., Gao, F., Reed, B.C., Huete, A., 2003. Monitoring vegetation phenology using MODIS. *Remote Sensing of Environment* 84, 471–475. [https://doi.org/10.1016/S0034-4257\(02\)00135-9](https://doi.org/10.1016/S0034-4257(02)00135-9)
- Zumberge, J.F., Heflin, M.B., Jefferson, D.C., Watkins, M.M., Webb, F.H., 1997. Precise point positioning for the efficient and robust analysis of GPS data from large networks. *Journal of Geophysical Research: Solid Earth* 102, 5005–5017. <https://doi.org/10.1029/96JB03860>

# PhD publications

- Belcore, E., Pezzoli, A., Calvo, A., 2019.** Analysis of gender vulnerability to climate-related hazards in a rural area of Ethiopia. *The Geographical Journal* 0. <https://doi.org/10.1111/geoj.12321>
- Belcore, E., Piras, M., Pezzoli, A., Massazza, G., Rosso, M., 2019.** Raspberry Pi 3 multispectral low-cost sensor for UAV-based remote sensing. Case study in south-west Niger. *Int. Arch. Photogramm. Remote Sens. Spatial Inf. Sci.* XLII-2/W13, 207–214. <https://doi.org/10.5194/isprs-archives-XLII-2-W13-207-2019>
- Belcore, E., Piras, M., Wozniak, E., 2020.** Specific alpine environment land cover classification methodology: Google Earth Engine processing for Sentinel-2 data. *Int. Arch. Photogramm. Remote Sens. Spatial Inf. Sci.* XLIII-B3-2020, 663–670. <https://doi.org/10.5194/isprs-archives-XLIII-B3-2020-663-2020>
- Belcore, E., Wawrzaszek, A., Wozniak, E., Grasso, N., Piras, M., 2020.** Individual Tree Detection from UAV Imagery Using Hölder Exponent. *Remote Sensing* 12, 2407. <https://doi.org/10.3390/rs12152407>
- Massazza, G., Tamagnone, P., Wilcox, C., **Belcore, E., Pezzoli, A., Vischel, T., Panthou, G., Housseini Ibrahim, M., Tiepolo, M., Tarchiani, V., Rosso, M., 2019.** Flood Hazard Scenarios of the Sirba River (Niger): Evaluation of the Hazard Thresholds and Flooding Areas. *Water* 11, 1018. <https://doi.org/10.3390/w11051018>
- Tiepolo, M., Rosso, M., Massazza, G., **Belcore, E., Issa, S., Braccio, S., 2019a.** Flood Assessment for Risk-informed Planning Along the Sirba River, Niger. *SUSTAINABILITY* 11, 1–21.

# Appendix A

List of parameters for ITD validation

Ruleset	Algorithm	Parameters	Values	Computing time
RGN spectral information	Contrast split segmentation	Minimum threshold	40000	7' 54''
		Maximum threshold	100000	
		Step size	500	
		Stepping type	Add	
		Layer	NIR	
		Class for bright objects	Trees	
		Class for dark objects	Other	4' 56''
	Multiresolution segmentation	Scale parameter	1200	
		Layer	NIR, RED, GREEN	
		Shape	0.05	
	Compactness	0.5		
	Remove object	Condition	Area < 80Px	1' 43''
NDVI	Contrast split segmentation	Minimum threshold	0.18	11' 29''
		Maximum threshold	0.25	
		Step size	5	
		Stepping type	Add	
		Layer	NDVI	
		Class for bright objects	Trees	
		Class for dark objects	Other	6''
	Remove object	Condition	Area < 80Px	
	Contrast split segmentation	Minimum threshold	0.25	7' 89''
		Maximum threshold	1.00	
		Step size	5	
		Stepping type	Add	
		Layer	NDVI	
		Class for bright objects	Other	
	Class for dark objects	Trees	4' 28''	
Multiresolution segmentation	Scale parameter	11		
	Layer	NDVI		
	Shape	0.05		
	Compactness	0.5		
CHM	Contrast split segmentation	Tile size	1500	5' 42''
		Minimum threshold	0.4	
		Maximum threshold	1	
		Step size	5	
		Stepping type	Add	
		Layer	CHM	
		Class for bright objects	Other	
		Class for dark objects	Trees	

	Multiresolution segmentation	Scale parameter	11	5' 31''
		Layer	CHM	
		Shape	0.05	
		Compactness	0.5	
	Remove object	Condition	Area < 80Px	<0,001''
Sum Variance GLCM	Contrast split segmentation	Tile size	1500	5' 42''
		Minimum threshold	1	
		Maximum threshold	10	
		Step size	5	
		Stepping type	Add	
		Layer	Sum Variance	
		Class for bright objects	Trees	
		Class for dark objects	Other	
	Multiresolution segmentation	Scale parameter	12	5' 31''
		Layer	Sum variance	
		Shape	0.05	
		Compactness	0.5	
	Remove object	Condition	Area < 80Px	<0,001''
Hybrid approach	Contrast split segmentation	Tile size	1500	
		Minimum threshold	5	
		Maximum threshold	100	
		Step size	5	
		Stepping type	Add	
		Layer	CHM	
		Class for bright objects	Trees	
		Class for dark objects	Other	
	Multiresolution segmentation	Scale parameter	12	
		Layer	Sum Variance with CHM local maxima as input thematic layer	
		Shape	0.05	
		Compactness	0.5	
	Remove object	Condition	Area < 80Px	



# Appendix B

## Google Earth engine code

### Image filtering, DOS, topographic correction and training samples import

```
var sentinel21c = ee.ImageCollection("COPERNICUS/S2") //import SENTINEL 2 dataset, 1C level
    .filterBounds(study_area) // filter on my astusdy area boundaries
    .filterDate('2017-01-01', '2019-12-31'); //time interval (aaaa-mm-gg format)

print('Filtered (by date) Image Count: ', sentinel21c.size()); //number of images within the time range
//print('available data description', sentinel2); // feature-->list of the images of the collection: from older (0) to
most recent (N).

var cloudBitMask1c = ee.Number(2).pow(10).int();
var cirrusBitMask1c = ee.Number(2).pow(11).int();
// Simple cloudMask function for Sentinel-2 based on QA band
function cloudmask(sentinel21c) {
  var qa1c = sentinel21c.select('QA60');
  // Both flags should be set to zero, indicating clear conditions.
  var mask1c = qa1c.bitwiseAnd(cloudBitMask1c).eq(0).and(
    qa1c.bitwiseAnd(cirrusBitMask1c).eq(0));
  return sentinel21c.updateMask(mask1c);
}

var masked1c = sentinel21c.map(cloudmask);
//print(masked.sort('CLOUDY_PIXEL_PERCENTAGE'), 'available data, ordered by cloud cover
percentage:');

var filteredmasked1c = masked1c.filterMetadata('CLOUDY_PIXEL_PERCENTAGE','less_than',10);
print('list of images with less than 10% of cloud cover from 1C level:', filteredmasked1c);

//select only the images taken during summer months
var collection0 = filteredmasked1c
    .filter(ee.Filter.calendarRange(6,8,'month'))
    .select(['B1', 'B2', 'B3','B4', 'B5', 'B6','B7', 'B8', 'B8A','B9', 'B11','B12']);
print('list of SUMMER images with less than 10% of cloud cover from 1C level:', collection0);

//var median1c = collection0.reduce(ee.Reducer.median());
//Map.addLayer(median1c, {bands:['B4_median','B3_median','B2_median'], min: 0, max: 3500}, 'true color
scene of median 1c');

//////////ATOMSPHERIC CORRECTION, Dark Object Subtraction, DOS (Chavez, 1996)//////////

var collection = collection0.map(DOScorrection); //apply DOS correction function to the collection with
masked clouds

//DOS function start
function DOScorrection(img){

//clipping out edge of the scenes
var image = ee.Image(img.clip(img.geometry().buffer(-10000)));
```

```

//extract the minimum values for each band of each scene
var atm0 = img.reduceRegion({
  reducer: ee.Reducer.min(),
  geometry: img.geometry(),
  scale: 20,
  maxPixels: 1e9
});

//subtract minimum value to each band (CORRECTION)

var B1 = img.select('B1').subtract(ee.Number(atm0.get('B1'))).max(0).int16();
var B2 = img.select('B2').subtract(ee.Number(atm0.get('B2'))).max(0).int16();
var B3 = img.select('B3').subtract(ee.Number(atm0.get('B3'))).max(0).int16();
var B4 = img.select('B4').subtract(ee.Number(atm0.get('B4'))).max(0).int16();
var B5 = img.select('B5').subtract(ee.Number(atm0.get('B5'))).max(0).int16();
var B6 = img.select('B6').subtract(ee.Number(atm0.get('B6'))).max(0).int16();
var B7 = img.select('B7').subtract(ee.Number(atm0.get('B7'))).max(0).int16();
var B8 = img.select('B8').subtract(ee.Number(atm0.get('B8'))).max(0).int16();
var B8A = img.select('B8A').subtract(ee.Number(atm0.get('B8A'))).max(0).int16();
var B9 = img.select('B9').subtract(ee.Number(atm0.get('B9'))).max(0).int16();
var B11 = img.select('B11').subtract(ee.Number(atm0.get('B11'))).max(0).int16();
var B12 = img.select('B12').subtract(ee.Number(atm0.get('B12'))).max(0).int16();

//create the atmosphere corrected image
var imageDOS = ee.Image(B1.addBands(B2).addBands(B3).addBands(B4).addBands(B5).addBands(B6).addBands(B7).addBands(B8).addBands(B8A).addBands(B9).addBands(B11).addBands(B12));

return imageDOS.copyProperties(img);
}

//var medianDOS = collection.reduce(ee.Reducer.median());
//Map.addLayer(medianDOS, {bands:['B4_median','B3_median','B2_median'], min: 0, max: 3500, gamma: 1.35}, 'true color scene of median DOS');

//////////////////////////////////TOPOGRAPHIC ILLUMINATION CORRECTION//////////////////////////////////

var scale = 300;

// get terrain layers
var dem = ee.Image("USGS/SRTMGL1_003");
var degree2radian = 0.01745;

var terrainCorrection = function(collection) {

  collection = collection.map(illuminationCondition);
  collection = collection.map(illuminationCorrection);

  return(collection);

//////////////////////////////////
// Function to calculate illumination condition (IC). Function by Patrick Burns and Matt Macander
function illuminationCondition(img){

// Extract image metadata about solar position
var SZ_rad = ee.Image.constant(ee.Number(img.get('MEAN_SOLAR_ZENITH_ANGLE'))).multiply(3.14159265359).divide(180).clip(img.geometry().buffer(10000));

```

```

var SA_rad = ee.Number(3.14159265359).multiply(3.14159265359).divide(180).clip(img.geometry().buffer(10000));
ee.Image.constant(ee.Number(3.14159265359).multiply(3.14159265359).divide(180)).clip(img.geometry().buffer(10000));
// Creat terrain layers
var slp = ee.Terrain.slope(dem).clip(img.geometry().buffer(10000));
var slp_rad = ee.Terrain.slope(dem).multiply(3.14159265359).divide(180).clip(img.geometry().buffer(10000));
var asp_rad = ee.Terrain.aspect(dem).multiply(3.14159265359).divide(180).clip(img.geometry().buffer(10000));

// Calculate the Illumination Condition (IC)
// slope part of the illumination condition
var cosZ = SZ_rad.cos();
var cosS = slp_rad.cos();
var slope_illumination = cosS.expression("cosZ * cosS",
    {'cosZ': cosZ,
     'cosS': cosS.select('slope')});
// aspect part of the illumination condition
var sinZ = SZ_rad.sin();
var sinS = slp_rad.sin();
var cosAziDiff = (SA_rad.subtract(asp_rad)).cos();
var aspect_illumination = sinZ.expression("sinZ * sinS * cosAziDiff",
    {'sinZ': sinZ,
     'sinS': sinS,
     'cosAziDiff': cosAziDiff});
// full illumination condition (IC)
var ic = slope_illumination.add(aspect_illumination);

// Add IC to original image
var img_plus_ic = ee.Image(img.addBands(ic.rename('IC')).addBands(cosZ.rename('cosZ')).addBands(cosS.rename('cosS')).addBands(slp.rename('slope')));
return img_plus_ic;
}

// Function to apply the Sun-Canopy-Sensor + C (SCSc) correction method to each image.
// Function by Patrick Burns and Matt Macander

function illuminationCorrection(img){
  var props = img.toDictionary();
  var st = img.get('system:time_start');

  var img_plus_ic = img;
  var mask1 = img_plus_ic.select('B8').gt(-0.1);
  var mask2 = img_plus_ic.select('slope').gte(5)
    .and(img_plus_ic.select('IC').gte(0))
    .and(img_plus_ic.select('B8').gt(-0.1));
  var img_plus_ic_mask2 = ee.Image(img_plus_ic.updateMask(mask2));

  // Specify Bands to topographically correct
  var bandList = ['B1', 'B2', 'B3', 'B4', 'B5', 'B6', 'B7', 'B8', 'B8A', 'B9', 'B11', 'B12'];
  var compositeBands = img.bandNames();
  var nonCorrectBands = img.select(compositeBands.removeAll(bandList));

  var geom = ee.Geometry(img.get('system:footprint')).bounds().buffer(10000);

  function apply_SCScorr(band){
    var method = 'SCSc';
    var out = img_plus_ic_mask2.select('IC', band).reduceRegion({
      reducer: ee.Reducer.linearFit(), // Compute coefficients: a(slope), b(offset), c(b/a)

```

```

    geometry: ee.Geometry(img.geometry().buffer(-5000)), // trim off the outer edges of the image for linear
relationship
    scale: 300,
    maxPixels: 1000000000
  });

  if (out === null || out === undefined) {
    return img_plus_ic_mask2.select(band);
  }

  else {
    var out_a = ee.Number(out.get('scale'));
    var out_b = ee.Number(out.get('offset'));
    var out_c = out_b.divide(out_a);
  // Apply the SCS correction
    var SCS_output = img_plus_ic_mask2.expression(
      "((image * (cosB * cosZ + cvalue)) / (ic + cvalue))", {
        'image': img_plus_ic_mask2.select(band),
        'ic': img_plus_ic_mask2.select('IC'),
        'cosB': img_plus_ic_mask2.select('cosS'),
        'cosZ': img_plus_ic_mask2.select('cosZ'),
        'cvalue': out_c
      });

    return SCS_output;
  }
}

var img_SCScorr = ee.Image(bandList.map(apply_SCScorr)).addBands(img_plus_ic.select('IC'));
var bandList_IC = ee.List([bandList, 'IC']).flatten();
img_SCScorr = img_SCScorr.unmask(img_plus_ic.select(bandList_IC)).select(bandList);

return img_SCScorr.addBands(nonCorrectBands)
  .setMulti(props)
  .set('system:time_start',st);
}

};

var collection = terrainCorrection(collection);
print('list of SUMMER images with less than 10% of cloud cover and topographically corrected from 1C level:',
collection);

var median1cTC = collection.reduce(ee.Reducer.median());
Map.addLayer(median1cTC, {bands:['B4_median','B3_median','B2_median'], min: 0, max: 3500, gamma:
1.35}, 'true color scene corrected');
print(median1cTC, 'median1cTC');

////////////////////////////////////TRAINING DATASET////////////////////////////////////

Map.centerObject(study_area);

//import training dataset

Map.addLayer(trainingdef, {min:0,max:11,palette: ['grey','white']}, 'training');

print(trainingdef, 'training');

```

```

//Create the training points by randomly inserting 250 points for each class of the training dataset (then
downloaded and MANUALLY modified on GIS sftw)
//REMOVE THE ONES FROM CLASSES 0 AND 11 (non classifiable and not defined)

var training_points = trainingdef.addBands(ee.Image.pixelLonLat())
  .stratifiedSample({
    numPoints: 250,
    classBand: 'b1',
    projection: 'EPSG:32631',
    scale: 10,
    region: training
  })
  .map(function(f) {
return f.setGeometry(ee.Geometry.Point([f.get('longitude'), f.get('latitude')]));
  }).filterMetadata('b1', "not_equals", 0).filterMetadata('b1', "not_equals", 11);

print (training_points.reduceColumns(ee.Reducer.frequencyHistogram(),['class']));
Map.addLayer(training_points, {color: 'blue'}, 'training_points, blue');

print(training_points,'training_points');

Export.table.toDrive({
  collection: training_points,
  description:'training_points',
  fileFormat: 'CSV'
});

var test_points = trainingdef.addBands(ee.Image.pixelLonLat())
  .stratifiedSample({
    numPoints: 250,
    classBand: 'b1',
    projection: 'EPSG:32631',
    seed: 1,
    scale: 10,
    region: training
  })
  .map(function(f) {
    return f.setGeometry(ee.Geometry.Point([f.get('longitude'), f.get('latitude')]));
  }).filterMetadata('b1', "not_equals", 0).filterMetadata('b1', "not_equals", 11);

print (test_points.reduceColumns(ee.Reducer.frequencyHistogram(),['class']));
Map.addLayer(test_points, {color: 'red'}, 'test_points, red');

print(test_points, 'test_points');
print(training_points_def, 'training_points_def');
Map.addLayer(training_points_def, {color: 'blue'}, 'training_points_def');

/////classification/////
var classifier_q = ee.Classifier.randomForest({numberOfTrees: 40, minLeafPopulation: 4}).train({
  features: 'training_points_def',
  classProperty: 'class',
});
return image.classify(classifier_q).copyProperties(image);
};

var classification_q = collection_indices.select(class_bands).map(classified_q);

/////VALIDATION /////

```

```

var test_points_q = test_points_def.filterMetadata('class', "not_equals", 10);
var validation_q = function(image){
var accuracy_points = image.sampleRegions({
  collection: test_points,
  properties : ['b1'],
  scale:10,
  tileScale: 4,
});
return accuracy_points;
};

var accuracy_points_q = classification_q.map(validation_q);

var errormatrixloop_q = function (fc){
  var EM2 = ee.FeatureCollection(fc).errorMatrix('b1', 'classification');
  var EM3 = EM2.accuracy();
  return ee.Feature(null).set('AEM', EM3).set('EM', EM2);
};

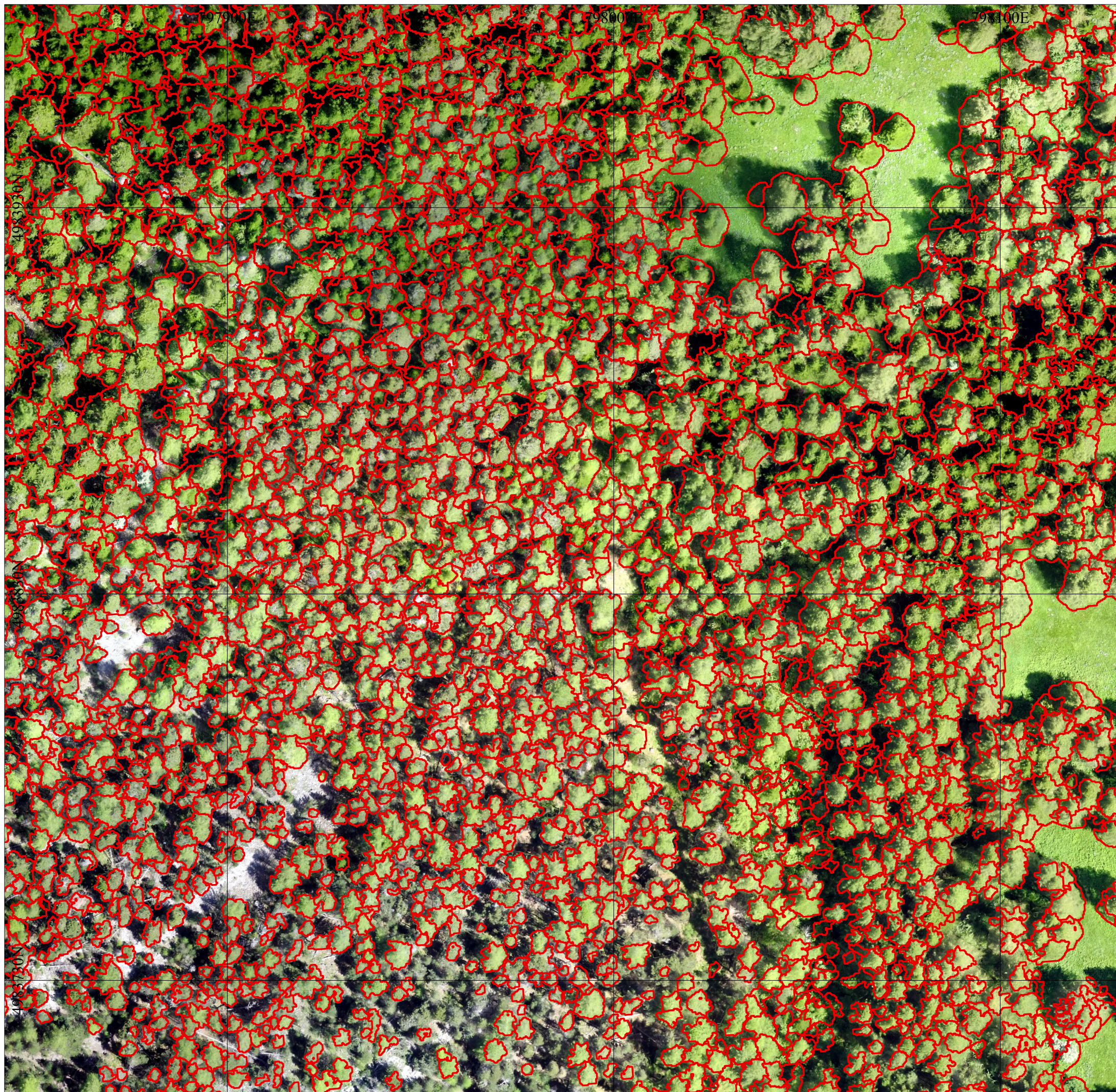
var lists = ee.FeatureCollection(accuracy_points_q.map(errormatrixloop_q));
print(lists);

//////////////////////////////////////CREATE STACK IMAGE OF THE CLASSIFICATIONS//////////////////////////////////////

var stack_classes = classification_q.toBands().clip(q_geometry).int8();
print(stack_classes);

Export.image.toDrive({
  image: stack_classes,
  description: 'classification_q_cor',
  maxPixels: 1E13,
  fileNamePrefix: 'class_q-cor',
  fileFormat: 'geoTIFF'});

```



POLITECNICO  
DI TORINO



UNIVERSITÀ  
DEGLI STUDI  
DI TORINO



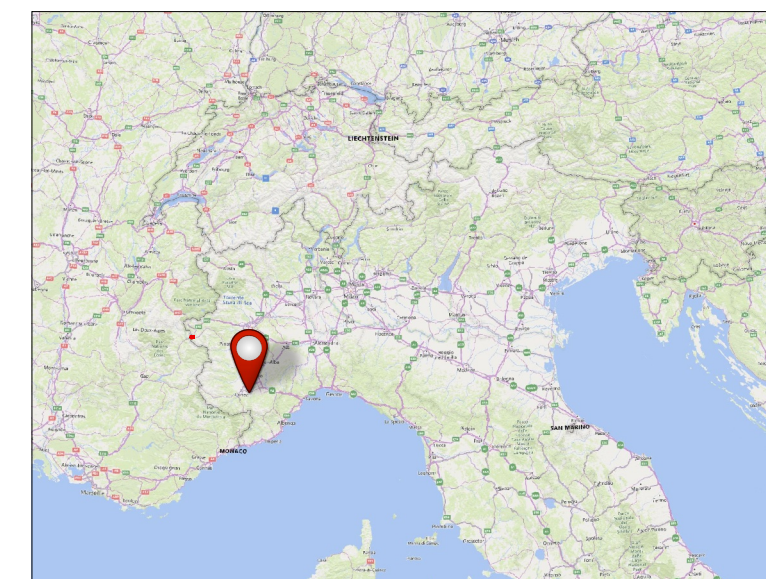
Dipartimento Interateneo di Scienze, Progetto e Politiche del Territorio

## Land Cover Atlas of environmental critic zones

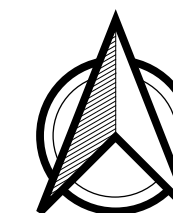
Map number: 01

SCALE 1:1000

*Alpine case study, Cesana Torinese Italy*




25 0 25 50 m



Reference system: WGS 84/UTM zone 32N

Data source: Unmanned Aerial Vehicles image,  
RGB spatial resolution: 0,10m/pixel  
RGN spatial resolution: 0,10m/pixel

### Legend

 crowns outline identified with Holder exponent  
RGB orthomosaic, UAV, 2017

Segmentation Producer's accuracy: 79%

Segmentation User's accuracy: 69%

Segmentation F1-score-mean: 73%

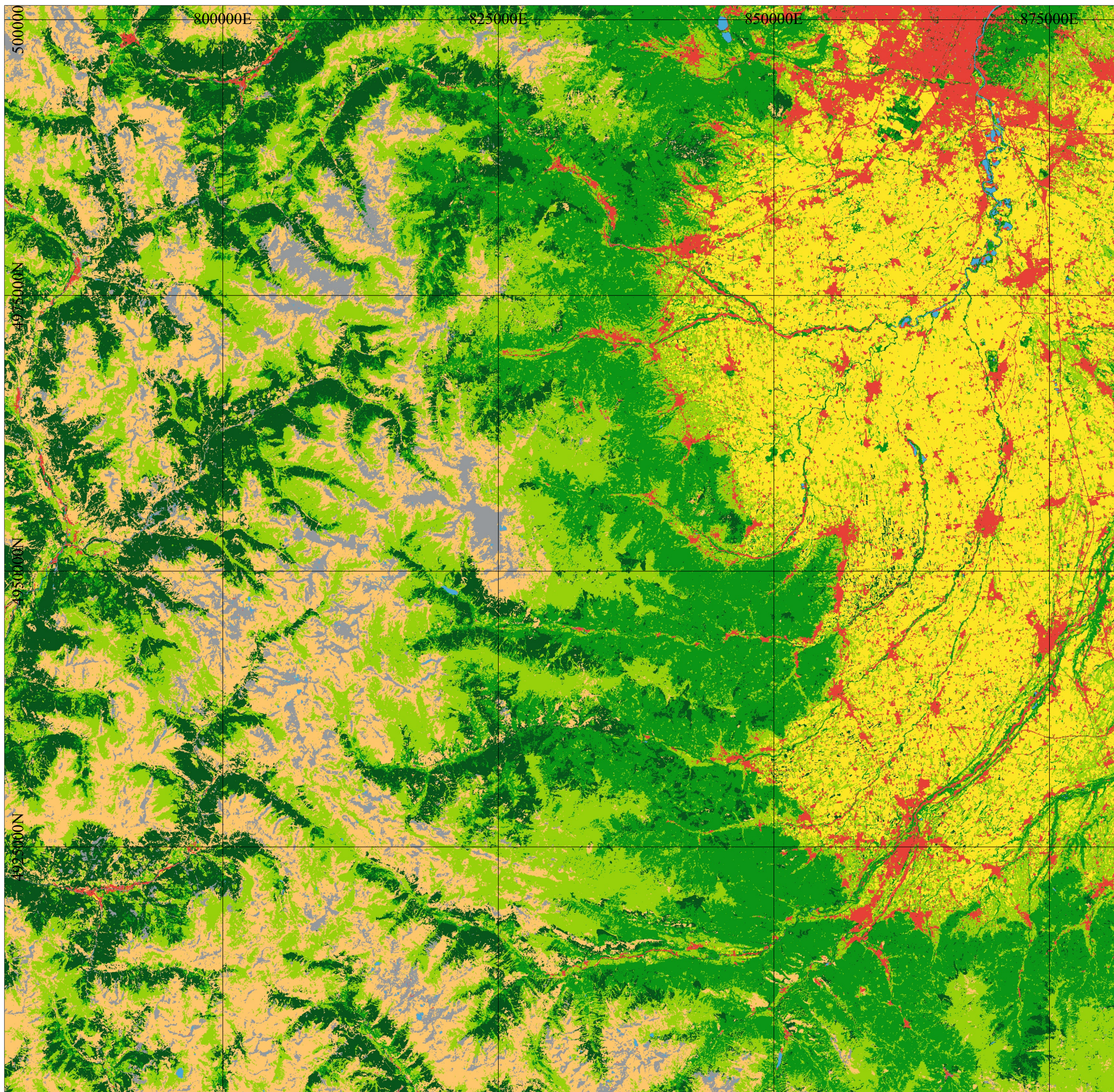
Over-segmentation index: 0.06

Under-segmentation index: 0.21

Completeness index: 0,18

Jaccard index: 0.72

Centroid distance: 0,46



POLITECNICO  
DI TORINO



UNIVERSITÀ  
DEGLI STUDI  
DI TORINO



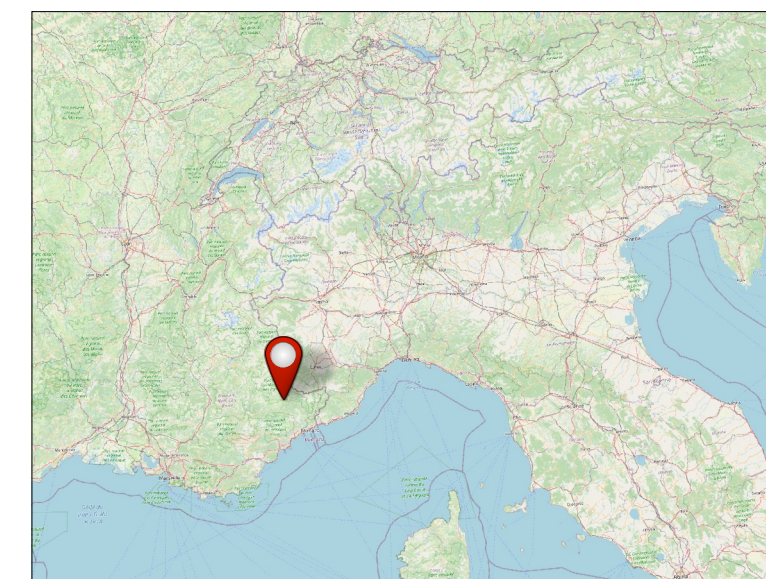
Dipartimento Interateneo di Scienze, Progetto e Politiche del Territorio

## Land Cover Atlas of environmental critic zones

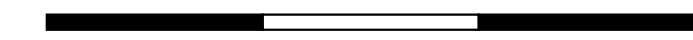
Map number: 02 (a)

SCALE 1:350000

*Alpine case study*



10 0 10 20 km













Reference system: WGS 84/UTM zone 32N

Data source: Sentinel-2 mission, 2017-2019

RGB spatial resolution: 10 m/pixel

Multispectral spatial resolution: 20 m/pixel

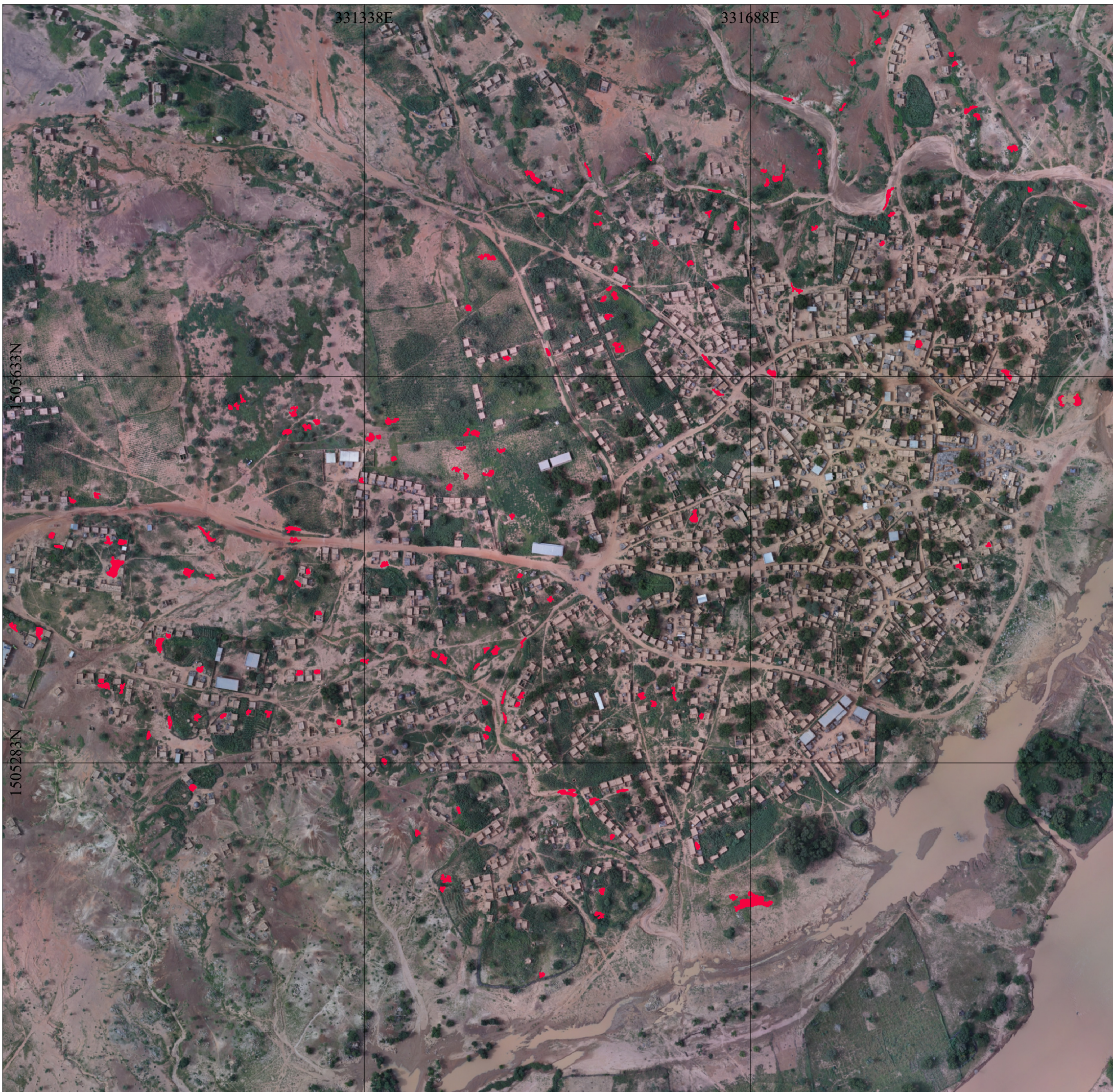
### Legend

- |  |  |
|--|--|
|  Coniferous                       |  Rocks        |
|  Broadleaf                        |  Urban areas  |
|  Grassland                        |  Dead woods   |
|  Water                            |  Agricultural |
|  Not vegetated areas<br>(EROSION) |  Glaciers     |

Classification Overall Accuracy: 94%

Classification F1-score-mean: 95%





POLITECNICO  
DI TORINO



UNIVERSITÀ  
DEGLI STUDI  
DI TORINO



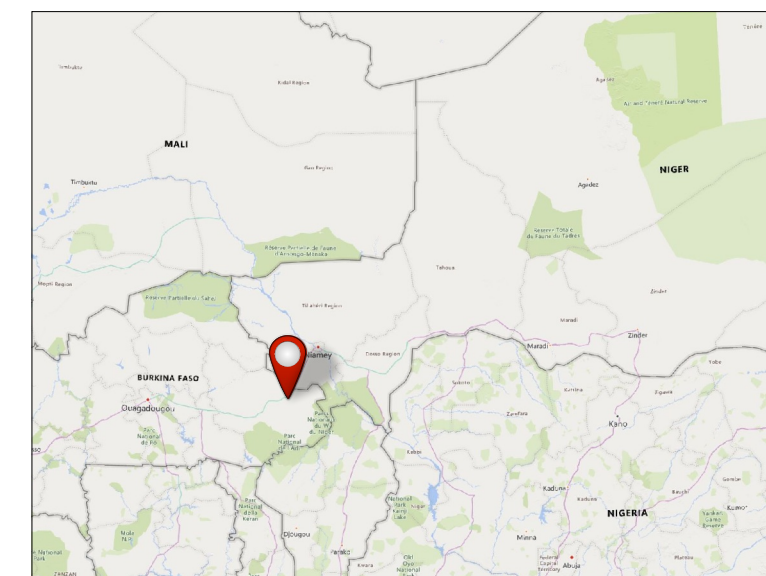
Dipartimento Interateneo di Scienze, Progetto e Politiche del Territorio

## Land Cover Atlas of environmental critic zones

Map number: 03 (a)

SCALE 1:3500

*Niger case study, Tourè village*



100 0 100 200 m



Reference system: WGS 84/UTM zone 31N

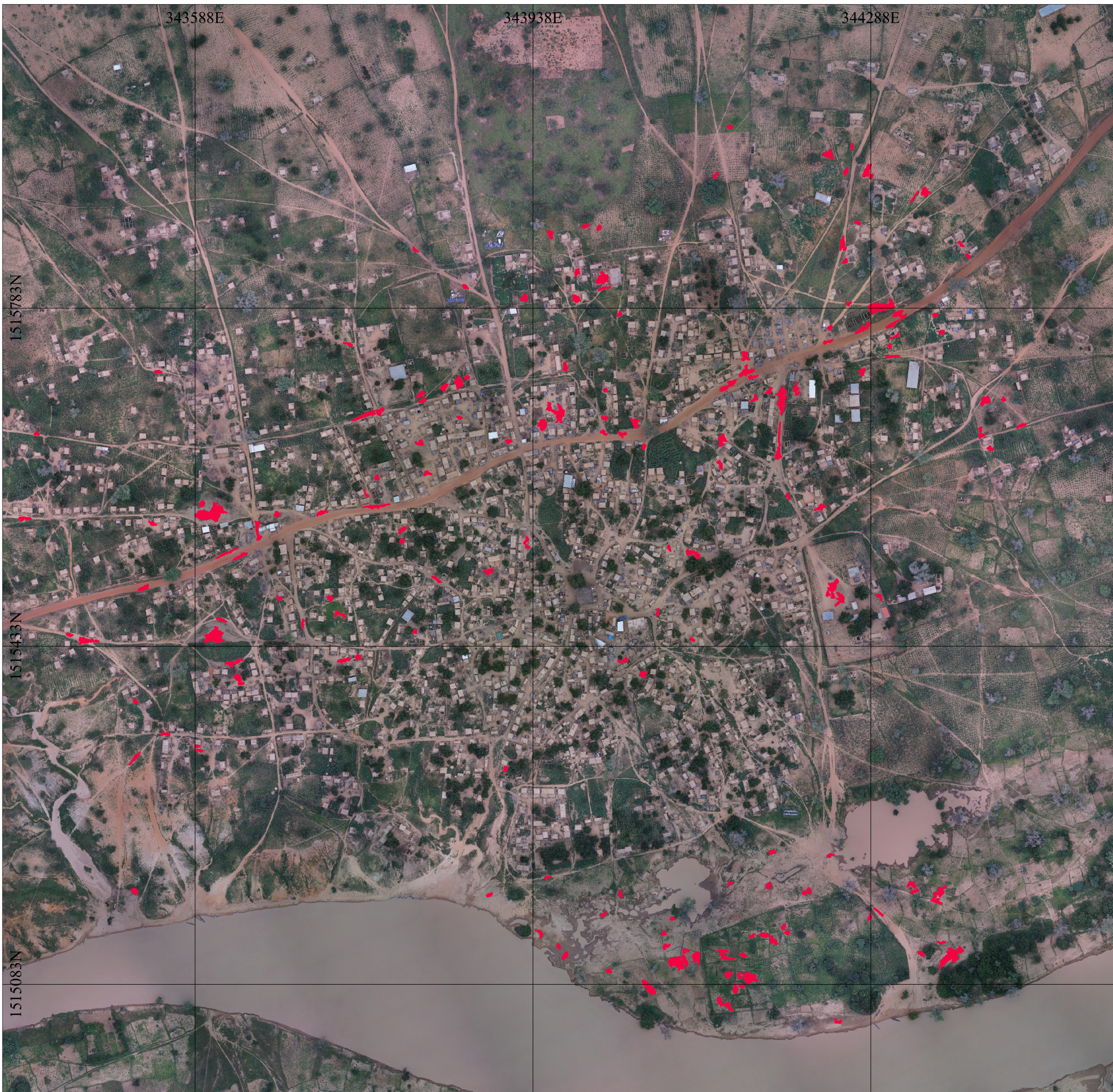
Data source: Unmanned Aerial Vehicles image,  
RGB spatial resolution: 0,04m/pixel

### Legend

■ Temporary Surface Water Bodies (TSWB)  
extracted from DTM analysis

Tourè Unmanned Aerial Vehicles (UAV) orthomosaic, 2017

From comparison to NDWI data 1 out of 6 TSWBs were detected.  
Comparison to ground inspection data was not possible.



POLITECNICO  
DI TORINO



UNIVERSITÀ  
DEGLI STUDI  
DI TORINO



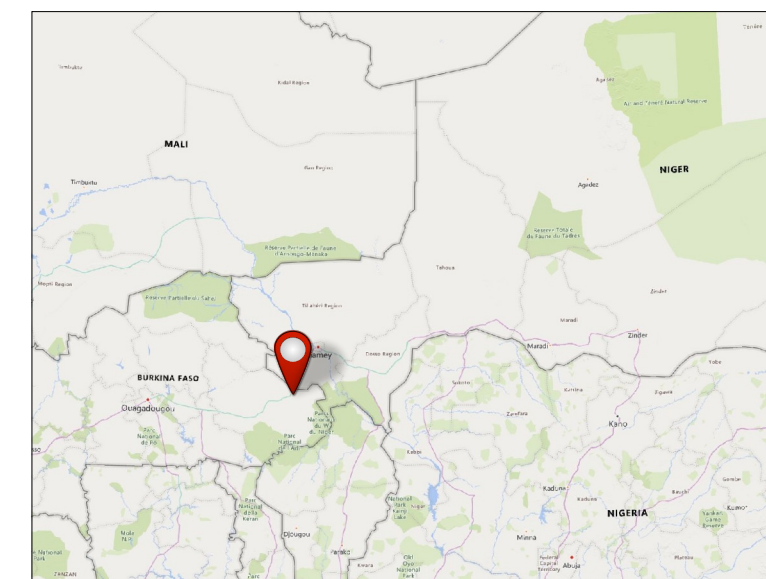
Dipartimento Interateneo di Scienze, Progetto e Politiche del Territorio

## Land Cover Atlas of environmental critic zones

Map number: 03 (b)

SCALE 1:3500

*Niger case study, Larba Birno village*



100 0 100 200 m



Reference system: WGS 84/UTM zone 31N

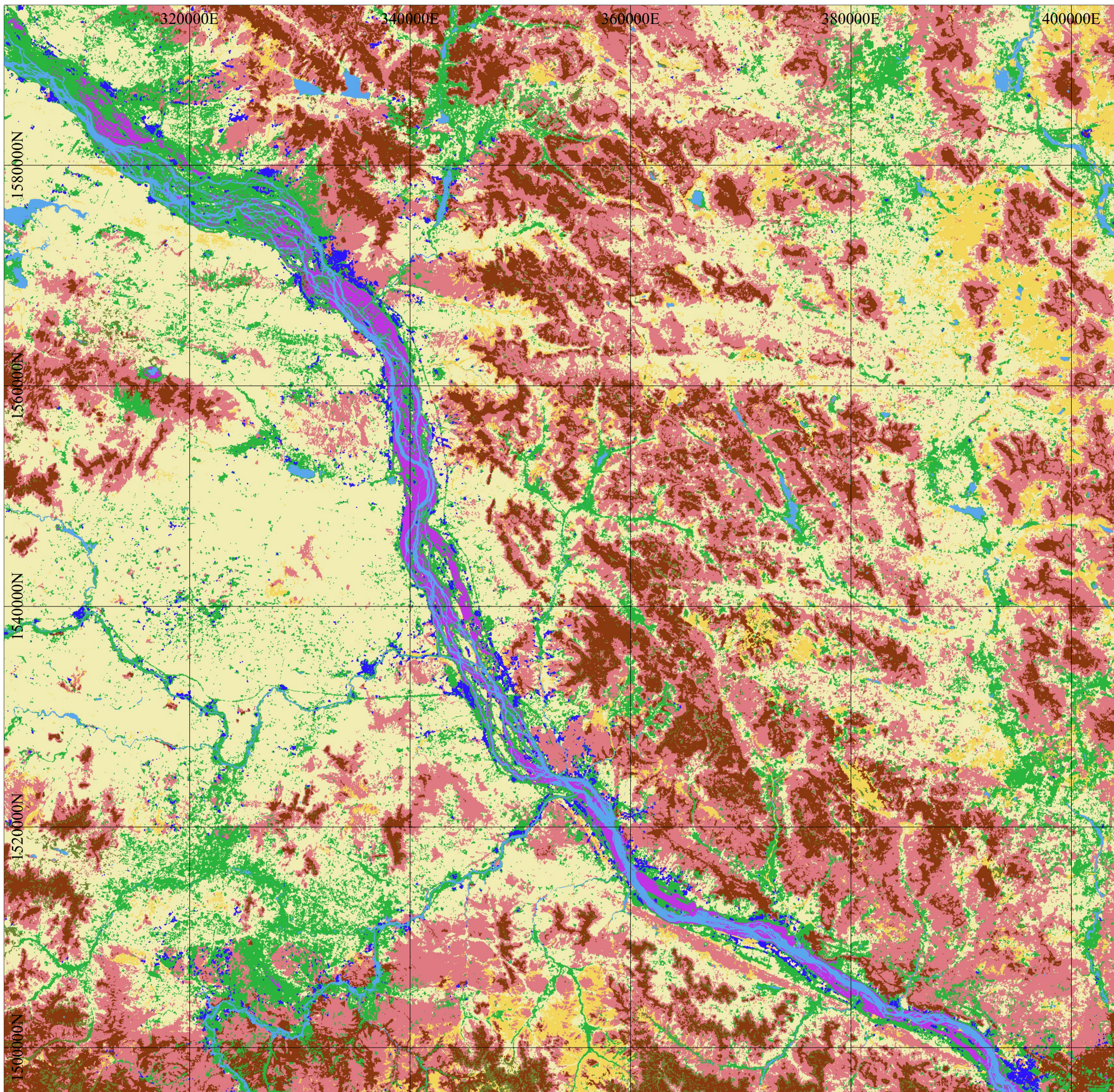
Data source: Unmanned Aerial Vehicles image,  
RGB spatial resolution: 0,04m/pixel

### Legend

■ Temporary Surface Water Bodies (TSWB)  
extracted from DTM analysis

Larba Birno Unmanned Aerial Vehicles (UAV)  
orthomosaic, 2017

From comparison to NDWI data 1 out of 6 TSWBs were detected.  
From comparison to ground inspection data 5 out of 9 TSWBs  
were detected.



POLITECNICO  
DI TORINO



UNIVERSITÀ  
DEGLI STUDI  
DI TORINO



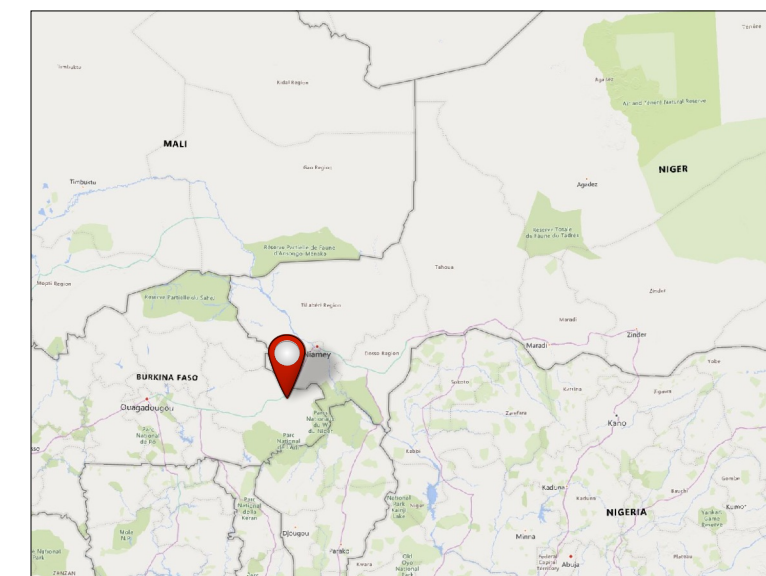
Dipartimento Interateneo di Scienze, Progetto e Politiche del Territorio

## Land Cover Atlas of environmental critic zones

Map number: 04

SCALE 1:35000

*Niger case study*



10 0 10 20 km












Reference system: WGS 84/UTM zone 31N

Data source: Sentinel-2 mission, 2017-2019

RGB spatial resolution: 10 m/pixel

Multispectral spatial resolution: 20 m/pixel

### Legend

- |  |   |
|--|---|
|  Water          |  Sandy bare soils                              |
|  Plateaux       |  Herbaceous vegetation of the plateaux         |
|  Woods          |  Irrigated agricultural lands                  |
|  Urban areas    |  Non-irrigated agricultural lands and pastures |
|  Red bare soils |   |

Classification Overall Accuracy: 96%

Classification F1-score-mean: 96%



POLITECNICO  
DI TORINO



UNIVERSITÀ  
DEGLI STUDI  
DI TORINO



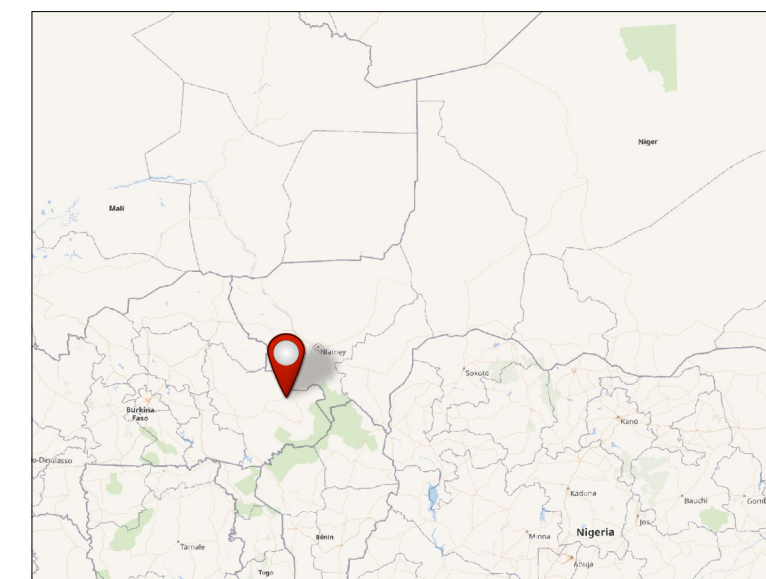
Dipartimento Interateneo di Scienze, Progetto e Politiche del Territorio

## Land Cover Atlas of environmental critic zones

Map number: 05

SCALE 1:2500

*Niger case study, Tourè village*



50 0 50 100 150 m



Reference system: WGS 84/UTM zone 31N

Data source: Unmanned Aerial Vehicles image,  
RGB spatial resolution: 0,04m/pixel  
RGN spatial resolution: 0,08m/pixel

### Legend

Wet land	Sandy soil
Water	Dark clustered rocky soils
Grassland/weeds	Yards/mixed covers
Agricultural land	Metal roofs
Trees	Sandy/bricks roofs

Classification Overall Accuracy: 94%  
Classification F1-score-mean: 95%